Liège Université

Faculté des Sciences appliquées

Department of Chemical Engineering

Development of new catalysts for proton exchange membrane fuel cells (PEMFCs)

Anthony Zubiaur

Supervisor:
Nathalie Job

A thesis submitted in fulfillment of the requirements
for the degree of Doctor of Philosophy in Engineering

2017

Acknowledgements

I want to thank Prof. Nathalie Job, the supervisor of this thesis, for proposing this thesis subject to me, and also for her availability, her meticulous proofreading and her patience.

I also want to thank Dr. Sandrine Berthon-Fabry from MINES ParisTech, Prof. Sophie Hermans from Université Catholique de Louvain, Dr. Isotta Cerri from Toyota Motor Europe, as well as Dr. Stéphanie Lambert and Prof. Angélique Léonard from Liège Université for accepting to be part of the thesis jury.

I would like to thank the people from the Laboratoire d'Electrochimie et de Physicochimie des Matériaux et des Interfaces (LEPMI) of Université de Grenoble for their welcome. In particular, I want to thank Prof. Marian Chatenet and Dr. Frédéric Maillard for teaching me the basis of electrochemical measurements with a three electrode cell and for discussions about the obtained results, not forgetting Dr. Laetitia Dubau for TEM, STEM, and EDX measurements and discussions.

I want to thank people who helped me with physicochemical measurements: Martine Dejeneffe from Liège Université for TEM measurements and discussions, Prof. Bénédicte Vertruyen from Liège Université for XRD measurements and discussions, Anne Iserentant from Université Catholique de Louvain for ICP-AES measurements, and Dr. Yan Busby from Université de Namur for XPS measurements.

I would also like to thank Alice Dubus from Liège Université, our glass blower, who did an excellent work with the three electrode cell setup and was always available when glass broke.

Obviously, I would like to thank all the people from the Department of Chemical Engineering of Liège Université and, particularly, the people from the so-called 'carbon group' for the good work atmosphere and discussions (not especially about work). I will not cite everyone but you will stay in my memory.

I would like to thank Dr. Ir. Pierre-Yves Olu for fruitful discussions.

Finally, I thank my friends and family, which are always there for me when needed. Special thanks to Clémentine for her daily help and support.

Abstract

In this thesis, the synthesis and the physicochemical and electrochemical characterization of carbon xerogel-supported electrocatalysts for proton exchange membrane fuel cells (PEMFCs) were studied. It is structured around three axes: (i) the synthesis and characterization of catalysts constituted of Pt nanoparticles deposited on carbon xerogel (Pt/CX catalysts) with high Pt loading and the streamlining of the synthesis process in order to speed up the synthesis method and avoid Pt losses; (ii) the synthesis and characterization of (solid and hollow) PtCo nanoparticles deposited on carbon xerogel (PtCo/CX catalysts); and (iii) the durability study of the best catalysts synthesized in the two previous parts, in a three electrode cell (liquid electrolyte) and in a PEMFC, through accelerated stress tests (ASTs).

First, the strong electrostatic adsorption (SEA) method was adapted in order to synthesize Pt/CX catalysts with Pt loading up to 25 wt.% with as low Pt losses as possible. The resulting Pt/CX catalysts, obtained by multiple impregnation-drying-reduction cycles, display small Pt nanoparticles (*ca.* 2-3 nm) with a narrow particle size distribution. The electrochemical properties of these Pt/CX catalyst, *i.e.* the electroactive Pt surface area and the specific and mass activity for the oxygen reduction reaction (ORR), are constant, whatever the Pt loading. To avoid any Pt losses during the synthesis of Pt/CX catalysts and to speed up the synthesis process, a streamlining of the method was performed. Multiple-step methods, *e.g.* charge enhanced dry impregnation (CEDI) and reduction of Pt ions by sodium borohydride, and one-step methods, *e.g.* reduction of Pt ions by formic acid and Pt colloid synthesis, were studied. From this investigation, the best Pt/CX catalysts for the ORR are those synthesized by SEA, CEDI, and formic acid reduction methods. They exhibit higher activity for the ORR than a commercial Pt/HSAC catalyst. Only the last synthesis method is a one-step method. It allows depositing in a single step up to at least 37 wt.% of Pt particles with average diameter around 3-4 nm.

Then, methods to synthesize PtCo/CX catalysts were developed. Indeed, the alloying of Pt with transition metal, Co in this case, allows increasing the catalytic activity for the ORR. The first method is based on the SEA method. It consists in successive or simultaneous deposition of Pt and Co. However, only the successive

deposition of Pt followed by that of Co yields bimetallic catalyst. Even so, the two metals deposited on the CX were not alloyed. As a result, no activity enhancement was observed. The other method is based on the colloid method. It yields hollow PtCo nanoparticles, with an average particle size of *ca.* 50 nm, deposited on CX. These hollow PtCo/CX catalysts exhibit very high activity (specific activity between 14 and 20 times as high and mass activity around 7 times as high as that of a commercial Pt/HSAC reference catalyst).

Finally, the durability of the best synthesized catalysts (formic acid-reduced Pt/CX and hollow PtCo/CX catalysts) was studied in a three electrode cell (liquid electrolyte) and in PEMFC, using ASTs which consist in cycling the potential of the working electrode (*i.e.* the catalytic layer) between 0.6 and 1.0 V *vs.* RHE. The major result of the durability study is that, contrary to Pt/CX and Pt/HSAC catalysts, the hollow PtCo/CX catalysts exhibit very good morphology stability during the ASTs. Moreover, in PEMFC, the activity of hollow PtCo/CX catalysts stabilizes quickly and no degradation of performance could be seen between 10,000 and 30,000 AST cycles, contrary to pure Pt catalysts which exhibit a continuous decrease in performance.

Résumé

Cette thèse consiste en l'étude de la synthèse d'électrocatalyseurs supportés sur xérogel de carbone pour piles à combustible à membrane échangeuse de protons (PEMFCs) ainsi que leur caractérisation physicochimique et électrochimique. Elle comporte trois parties: (i) la synthèse et la caractérisation de catalyseurs constitués de nanoparticules de Pt déposées sur un xérogel de carbone (Pt/CX); (ii) la synthèse et la caractérisation de catalyseurs constitués de nanoparticules (pleines ou creuses) de PtCo déposées sur un xérogel de carbone (PtCo/CX); (iii) l'étude de la durabilité des catalyseurs les plus performants synthétisés lors des deux premières parties, durant des essais de dégradation accélérée (ou "accelerated stress tests", ASTs), en cellule à trois électrodes (électrolyte liquide) ainsi qu'en PEMFC.

D'abord, la méthode dite de "strong electrostatic adsorption" (SEA) a été adaptée afin de synthétiser des catalyseurs Pt/CX présentant des teneurs en Pt jusqu'à 25 $\%_{\text{mass.}}$ tout en limitant les pertes de Pt autant que possible. Les catalyseurs Pt/CX obtenus sont composés de petites particules de Pt d'environ 2-3 nm avec une distribution de taille étroite. Les propriétés électrochimiques de ces catalyseurs Pt/CX, c'est-à-dire la surface spécifique de Pt ainsi que l'activité spécifique et massique pour la réduction de l'oxygène (ORR), sont constantes quelle que soit la teneur en Pt. Afin d'éviter toute perte de Pt durant la synthèse et d'accélérer cette dernière, une rationalisation du procédé a été effectuée. Des méthodes de dépôt de Pt en plusieurs étapes, comme la technique dite de "charge enhanced dry impregnation" (CEDI) ou un procédé utilisant le borohydrure de sodium comme réducteur des ions Pt, ainsi que des techniques de dépôt de Pt en une seule étape, comme la méthode utilisant l'acide formique comme réducteur des ions Pt ou le procédé colloïdal, ont été étudiées. Les meilleures performances pour l'ORR ont été obtenues par synthèse SEA, CEDI ou *via* réduction du précurseur de Pt par l'acide formique. Seule cette dernière méthode est réalisée en une seule étape. Elle permet de déposer, en une seule opération, jusqu'à au moins 37 $\%_{\text{mass.}}$ de particules de Pt de 3-4 nm de diamètre.

Ensuite, des synthèses de catalyseurs PtCo/CX ont été développées. En effet, la présence d'alliage Pt-métal de transition, dans ce cas-ci du Co, permet d'augmenter l'activité pour l'ORR des catalyseurs. La première se base sur la méthode SEA.

Elle consiste en une déposition successive ou simultanée de Pt et de Co. Cependant, seul le dépôt successif de Pt suivi de celui de Co a permis d'obtenir des catalyseurs bimétalliques. Malgré la présence des deux métaux sur le support, aucun alliage n'a pu être formé, et les performances des catalyseurs n'ont donc pas été améliorées. La seconde et dernière méthode étudiée est basée sur la formation d'un colloïde métallique (similaire au colloïde de Pt précédemment évoqué). Cette méthode a permis d'obtenir des catalyseurs constitués de particules creuses de PtCo d'environ 50 nm de diamètre supportées sur xérogel de carbone. L'activité de ces catalyseurs PtCo/CX à particules creuses est la plus élevée de cette thèse (une activité spécifique 14 à 20 fois plus élevée que celle du catalyseur commercial Pt/HSAC de référence ainsi qu'une activité massique environ 7 fois plus élevée).

Finalement, la durabilité des catalyseurs les plus performants synthétisés précédemment (le catalyseur Pt/CX réduit par l'acide formique ainsi que le catalyseur PtCo/CX à particules creuses) à été étudiée en cellule à trois électrodes (électrolyte liquide) ainsi qu'en PEMFC, sur base d'ASTs. Ces ASTs consistent à faire cycler le potentiel de l'électrode de travail (autrement dit, le potentiel de la couche catalytique) entre 0,6 et 1,0 V *vs.* RHE. Le résultat le plus marquant de cette étude de durabilité est que, contrairement aux catalyseurs Pt/CX et Pt/HSAC, les catalyseurs PtCo/CX à particules creuses montrent une très bonne stabilité morphologique durant les ASTs. De plus, en PEMFC, l'activité de ces catalyseurs se stabilise rapidement et aucune dégradation de l'activité n'a pu être observée entre 10.000 et 30.000 cycles, contrairement aux catalyseurs de Pt pur, dont les performances continuent de décroître avec le nombre de cycles.

Contents

Introduction

Context

World population grows every day. In developed and developing countries, this growth causes a dramatic increase in the world energy consumption. To fulfill the worldwide energy demand, our current power supply system must change. Indeed, the fossil fuels, *i.e.* oil, gas, and coal, which provide *ca.* 85% of the world energy, are available in limited quantity. Moreover, their combustion impacts the environment, by emitting greenhouse gases, which take part in climate change, as well as particles and unburned fuel, which cause pollution.

A possible solution to decrease the impact of energy consumption is to diversify and increase the efficiency of the power generation systems. Particular attention should be paid to renewable energies. Biomass, hydro, thermal, wind, and solar electricity are among the most promising sustainable energies [1]. However, the technologies producing these sustainable energies are not mature enough or are too expensive to fully replace the use of fossil fuels in the short term. One major drawback for the wide-spreading of sustainable energy is the intermittence of some of these power sources.

To overcome this problem, the development of storage systems is necessary to store the excess of power produced during peak hours in order to deliver energy when needed. Particularly interesting storage devices are electrochemical systems, such as batteries or electrolyzers and fuel cells. The last two are electrochemical storage devices (electrolyzers) coupled with electrochemical conversion systems (fuel cells). The coupling operates as follows: electrolyzers transform electrical energy into chemical energy, *i.e. via* water electrolysis, while fuel cells convert back the chemical energy into electrical energy [2]. This coupling exhibits a remarkable advantage: the fuel (usually H_2) containing the energy can be stored for a very long time. Indeed, electrolyzers can produce H_2 from renewable electricity, *e.g.* hydro, solar, or wind electricity. Produced H_2 can then be stored in tanks and transported towards the energy consumer, where fuel cells convert back the chemical energy of H_2 into electricity. The transport between the source and the consumer can also be carried

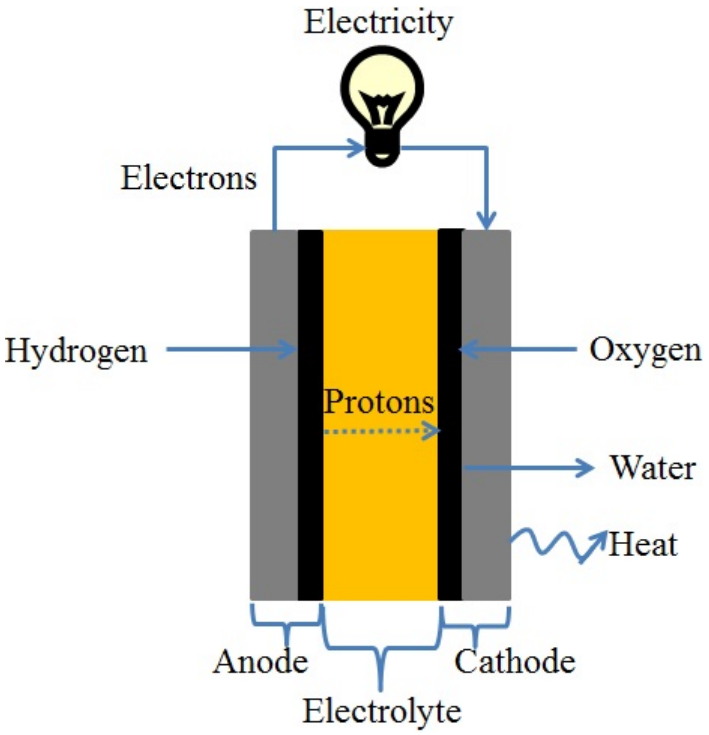

Figure 1: Schematic representation of an acidic medium fuel cell.

out by H_2 pipelines or networks of pipes. As electrolyzers and fuel cells are based on the same principles, one operates as the reverse of the other. For this process to function with as little loss as possible, the two devices must display high efficiencies.

Fuel cells

Focusing on the energy conversion system, *i.e.* the fuel cell, Figure 1 illustrates the production of electricity from H_2 molecules in an acidic medium. The description of the fuel cell functioning will be explained on the basis of H_2-fueled acidic medium cells, as this thesis is focused on this very common fuel cell type. For the other kinds of fuel cells, the base principles are the same but some parameters change, *e.g.* the utilized fuel (CH_4, alcohol, *etc.*) or the electrolytic medium. For instance, in the case of alkaline fuel cells, the half reactions are different, the charge carrier is OH^-, and the water is produced at the anode.

As any electrochemical cell, a fuel cell is constituted of (i) an anode, where oxidation takes place, (ii) a cathode, where the reduction occurs, and (iii) an electrolyte, which electrically insulates the anode from the cathode but allows the ions to cross from one side to the other. In the case of an acidic fuel cell, H_2 molecules enter the (porous) anode, where they are reduced into protons, yielding electrons according to the hydrogen oxidation reaction (HOR):

$$H_2 \longrightarrow 2H^+ + 2e^- \tag{1}$$

The produced electrons leave the anode through the external circuit, to power an electrical device. The protons leave the anode, cross the electrolyte, and react at the cathode with electrons and oxygen molecules, producing water according to the oxygen reduction reaction (ORR):

$$O_2 + 4H^+ + 4e^- \longrightarrow 2H_2O \tag{2}$$

In addition to water and electricity, fuel cells also produce heat during operation as the system is, of course, not thermodynamically ideal.

Many kinds of fuel cells are currently developed and some of them are already commercialized. Table 1 (adapted from Reference [3]) shows the main characteristics of different types of fuel cells. This list is non-exhaustive, since other types of fuel cells can be emerging but are still under research nowadays. Briefly, these fuel cells can be distinguished from each other on the basis of the electrolyte (solid or liquid), of their working temperature, and of the fuel used. Solid oxide fuel cells use O^{2-}-conductive electrolyte at temperature above 1000 K. Molten carbonate fuel cells include liquid CO_3^{2-}-conductive electrolyte (*i.e.* molten carbonate salts) at 873-973 K. Phosphoric acid fuel cells are based on liquid H^+-conductive electrolyte at 433-493 K. These three kind of fuel cells, which work at high temperature, are already commercialized for stationary applications, such as micro-combined heat and power, emergency power systems, or uninterruptible power supplies. Alkaline fuel cells, where the electrolyte is an alkaline solution (usually KOH in water), *i.e.* the mobile species is OH^-, exhibit a wide range of temperature and pressure operating conditions, leading to a wide application range, from the above-mentioned stationary applications to mobile and portable devices. For example, they were already used during the Apollo space program in the 1960s. However, their sensitivity to CO and CO_2 prevents their utilization in town (due to CO and CO_2 from the air) and their fueling from H_2 produced by steam methane reforming (as it also produces CO and CO_2). Direct borohydride fuel cells are an emerging kind of mobile and portable alkaline fuel cells, fueled with sodium borohydride ($NaBH_4$). Enzymatic fuel cells decompose organic matter (glucose) to produce electricity. These fuel cells are mainly used as power sources for implantable medical micro-sensors and devices. Proton exchange membrane fuel cells (PEMFCs) are fueled by H_2 and use a polymer membrane as electrolyte. They are one of the most studied fuel cells types because of (i) their temperature and pressure operating ranges, which are closer to the ambient, and because of (ii) their higher power density and their better dynamic characteristics than other types of fuel cells [4]. Their functioning is described with more details in the next section. Other types of fuel cells derive from PEMFCs: (i) direct alcohol fuel cells, which use methanol, ethanol, and other alcohols as a fuel; (ii) direct formic acid fuel cells, which are fueled with formic acid; and (iii) high-temperature proton exchange membrane fuel cells, which work at higher temperature than the classic PEMFCs. Researchers are still developing PEMFCs but they are already commercialized from above-mentioned stationary applications to mobile applications, *e.g.* cars or buses.

Table 1: Fuel cell types and main characteristics (adapted from Reference [3]).

Fuel cell type	Fuel	Charge carrier	Operation temperature K	Application	Commercialized
Solid oxide	CH_4	O^{2-}	1073-1273	Stationary	Yes
Molten carbonate	CH_4	CO_3^{2-}	873-973	Stationary	Yes
Alkaline	H_2	OH^-	Below 273-503	Stationary Miniaturized Mobile	Yes
Phosphoric acid	H_2	H^+	433-493	Stationary	Yes
High-temperature proton exchange membrane	H_2	H^+	383-453	Stationary Mobile	Yes
Direct alcohol	Methanol, ethanol	H^+	Ambient-393	Miniaturized Mobile	Yes
Direct borohydride	Sodium borohydride ($NaBH_4$)	Na^+ / OH^-	293-358	Miniaturized Mobile	No
Low-temperature proton exchange membrane	H_2	H^+	333-353	Stationary Mobile	Yes
Direct formic acid	Formic acid (HCOOH)	H^+	303-333	Miniaturized Mobile	No
Enzymatic	Organic matter (glucose)	H^+	293-333	Miniaturized	No

Proton exchange membrane fuel cells (PEMFCs)

The proton exchange membrane fuel cell (PEMFC) is a versatile device with a lot of possible uses. PEMFCs components and their roles are described hereafter. Figure 2 is a picture of classic components of a PEMFC.

The core of a PEMFC device is the membrane electrode assembly (MEA). The MEA is composed of a polymer membrane covered by catalytic layers on both sides. The polymer membrane, usually made of perfluorosulfonic acid (PFSA), named Nafion® when distributed by Du Pont de Nemours, is an electric insulator but a proton conductor when properly hydrated. It is sandwiched between the two catalytic layers, which constitute the electrodes (anode and cathode). PFSA is composed of long polytetrafluoroethylene (PTFE) backbones, grafted with perfluorovinyl ether groups terminated by a sulfonate function which is the acidic site allowing proton conduction. Figure 3 shows the chemical structure of a PFSA membrane.

To speed up the oxidation and reduction reactions, catalytic layers are present on both sides of the polymer electrolyte membrane (PEM) and constitute the electrodes of the cell; the HOR occurs at the anode, whereas the ORR occurs at the cathode. Both electrodes are often manufactured from the same components: (i) catalytic sites, usually platinum or platinum-based nanoparticles, which catalyze both reactions (HOR and ORR); (ii) a porous support for these catalytic sites, usually high surface area carbon (HSAC), which maintains the dispersion of the catalytic sites,

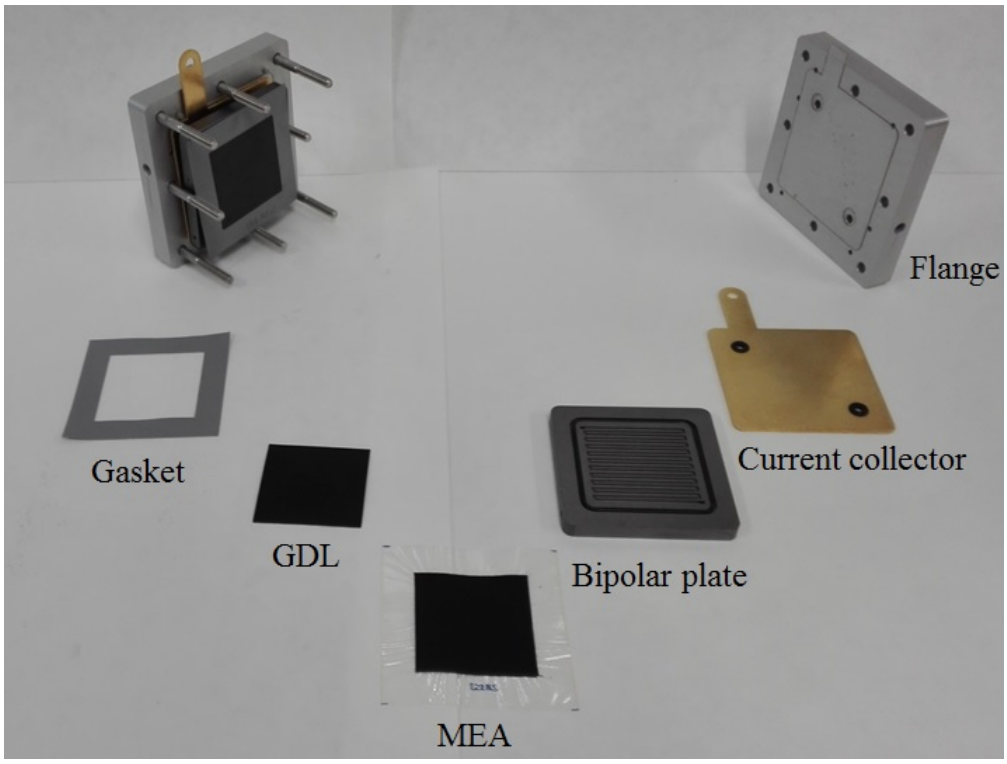

Figure 2: Picture of fuel cell components.

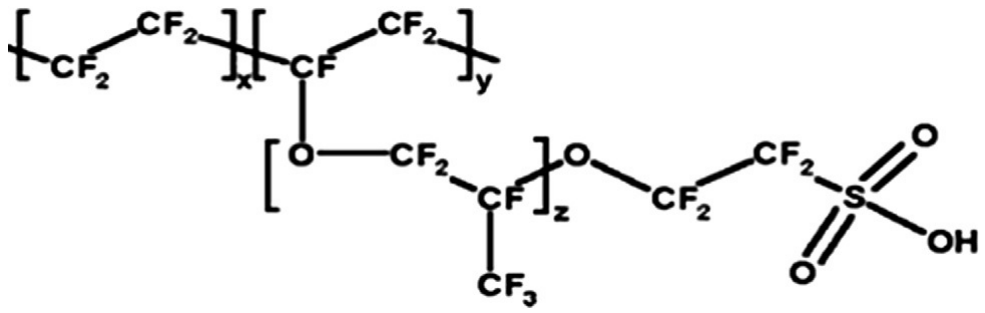

Figure 3: Chemical structure of a perfluorosulfonic acid (PFSA) membrane [5].

conducts electrons from or towards the active sites, and exhibits porosity so that the gaseous reactive species and the product (H_2, O_2, and water) can diffuse towards or from the active sites; and (iii) an ionomer, usually Nafion®, which conducts protons between the active sites and the PEM.

The assembly of the fuel cell components is schematized in Figure 4a for a mono-cell configuration. As for Figure 4b, it schematizes the cathode catalytic layer, while Figure 4c zooms in on a platinum nanoparticle deposited on the carbon support. In order that the ORR reaction occurs, as shown by Equation (2), all the reactants must be in contact with the active sites. In other words, (i) O_2 molecules, usually from air, must be able to access platinum nanoparticles by diffusion through the porosity of the catalytic layer and through the ionomer; (ii) protons must access platinum nanoparticles by transport through the ionomer network within the electrode; (iii) electrons must access platinum nanoparticles through the conductive carbon support; and (iv) produced water molecules must be able to leave the platinum particles by diffusion through the ionomer and through the porosity of the catalytic layer. Besides these contact issues, the reaction pathway of the ORR is very complex and involves a lot of adsorbed intermediate species. Stamenkovic *et al.* proposed the following schematic pathway [6]

$$\begin{array}{ccccccc} O_2 & \longrightarrow & O_{2,ad} & \underset{}{\overset{k_1}{\rightleftharpoons}} & H_2O_{2,ad} & \xrightarrow{k_2} & H_2O \\ & & & & \Big\| \, {\scriptstyle k_3}^{\uparrow}_{\downarrow}{\scriptstyle k_{-3}} & & \\ & & & & H_2O_2 & & \end{array} \tag{3}$$

where the rate-determining step is the first charge transfer happening after the adsorption of O_2 on the platinum surface:

$$O_{2,ad} + e^- \longrightarrow O_{2,ad}^- \tag{4}$$

Gas diffusion layers (GDLs), usually constituted of carbon cloth impregnated by poly-vinylidene fluoride (PVDF) and covered by a layer of microporous carbon, are

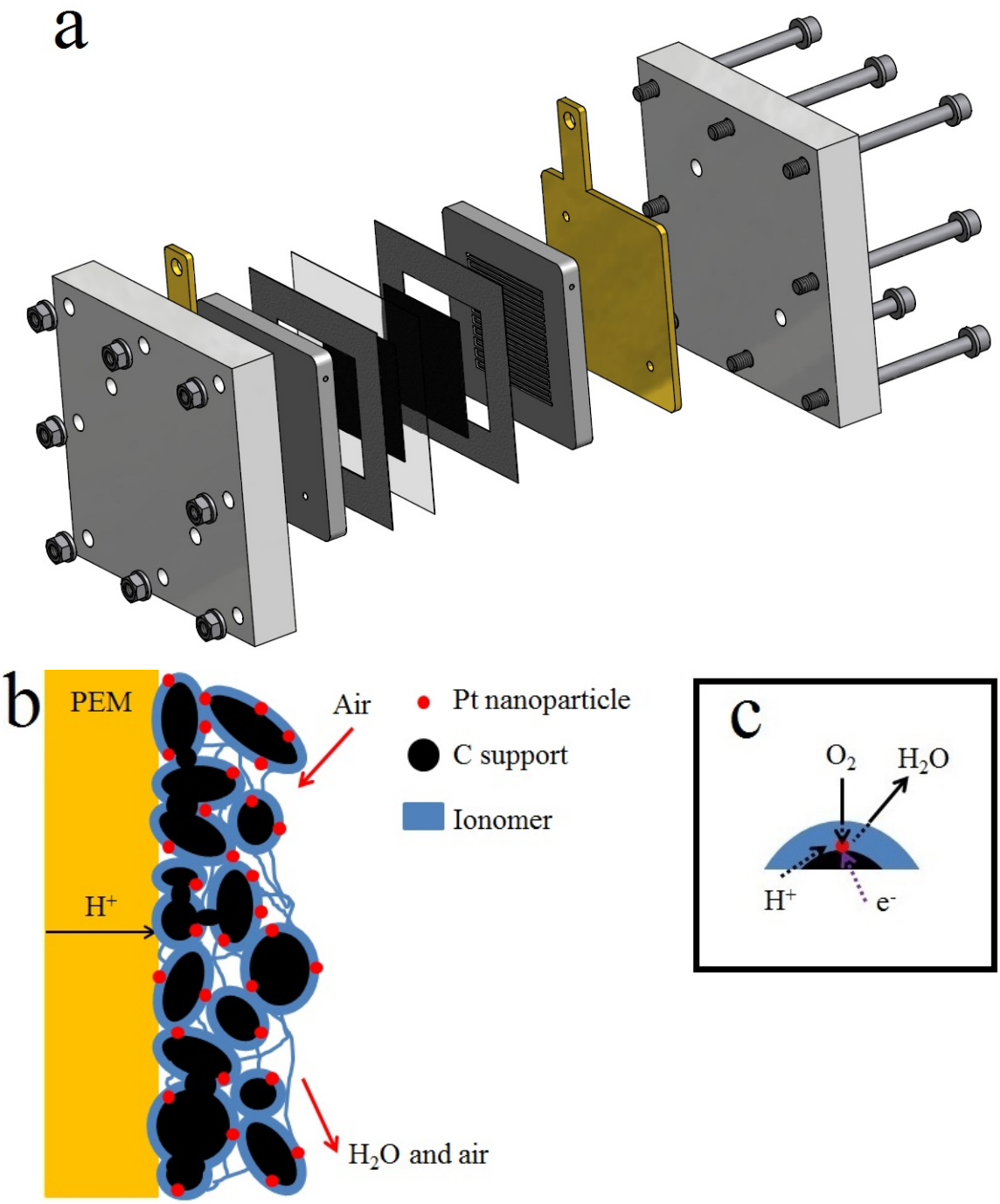

Figure 4: Schematic representation of a PEMFC (a), of the cathode catalytic layer (b), and enlargement of a platinum nanoparticle (c).

placed on both sides of the MEA. The roles of the GDLs are (i) to spread the reactive gases all over the catalytic layers, (ii) to help to evacuate the excess water produced by the cell, and (iii) to conduct electrons between the catalytic layer and the next component, the bipolar plates. Bipolar plates, usually constituted of graphite, metal (stainless steel, titanium, *etc.*), or composites, display engraved channels, which distribute the reactive gases over the GDLs. Moreover, these electrically conductive plates allow the electrons to cross from the GDLs to the current collectors, the latter being connected to the external electrical device to be powered. Finally, gaskets are placed around GDLs, between the MEA and the bipolar plates, in order to prevent gas leaks, especially H_2. All the components are held together and pressed by two flanges and screws.

The voltage of one single PEMFC is limited by thermodynamics. The maximum cell voltage, given by the Nernst equation, is equal to 1.23 V at 298 K and under standard conditions. At usual operating conditions (temperature around 343-353 K and pressure around 1-2 bar), the equilibrium cell voltage decreases to 1.17 V. This voltage can never be reached during operation, as it corresponds to the ideal voltage, *i.e.* to the voltage performed when no current is produced. In fact, when a cell produces electricity, the system is not ideal anymore, leading to a loss of electrical work in the form of heat. This conversion of chemical energy into heat instead of electricity results in voltage losses, also called overpotentials. These overpotentials cause the *ca.* 1 V of maximal tension that one single fuel cell can usually display. In order to increase the total voltage, fuel cells are piled up, forming the so-called fuel cell stacks (Figure 5). The voltage of a fuel cell stack is then the sum of the voltage of all the piled-up cells. The geometrical surface area of the cells can also be increased to produce higher current.

Drawbacks of PEMFCs

PEMFCs still exhibit several limitations hampering their extensive worldwide commercialization, *e.g.* the manufacturing of the components, the assembly of the elements, the heat and water management, the production, distribution, and storage of H_2, *etc.* Besides these limitations, the cell components can also be improved. For example, the catalytic layers display properties which are still not optimal, such as (i) their relatively low activity, (ii) their low stability (especially at the cathode), and (iii) their non-optimal architecture. Commonly used catalysts are platinum nanoparticles deposited on high surface area carbon (Pt/HSAC). Platinum nanoparticles are used in order to speed up the sluggish ORR. However, platinum does not exhibit the optimal activity for this specific reaction. Indeed, in order to display good activity for chemical reactions which involve adsorbates, *e.g.* ORR which involves the adsorption of O_2 molecules and oxygenated intermediates, catalytic sites must exhibit an optimal binding energy with the reactive species. In other words, the binding energy between active sites and adsorbates must be neither too weak (otherwise the adsorbates cannot adsorb on the active sites and the reaction does not occurs) nor

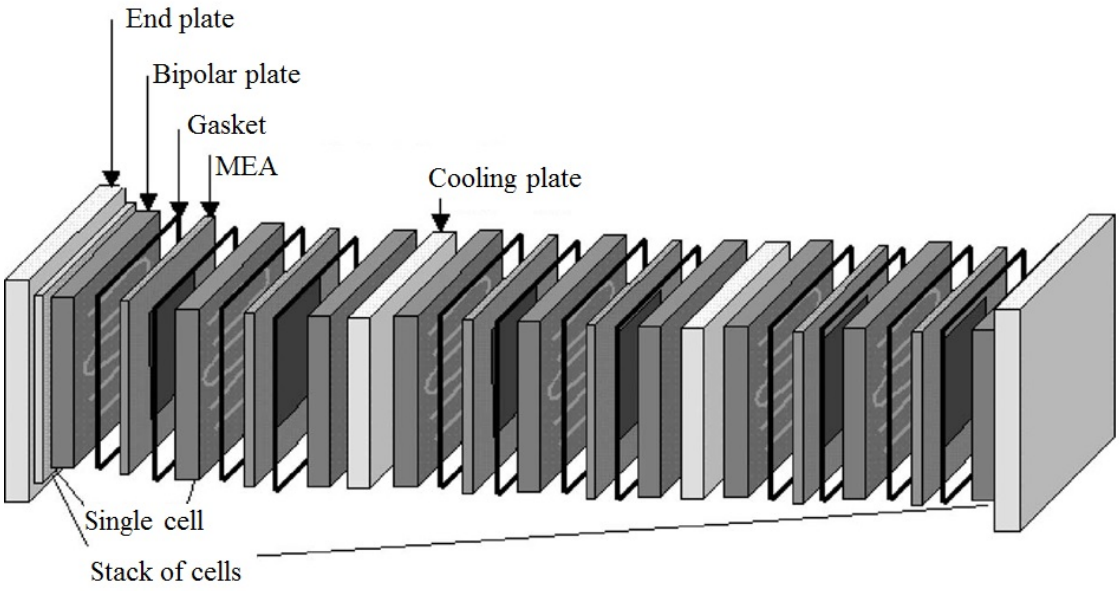

Figure 5: Scheme of a fuel cell stack (adapted from Reference [7]).

too strong (otherwise the adsorbed species stay on the active sites and do not dissociate, leading to a poisoning of the active sites), following the well-known Sabatier's principle. When considering the binding of O_2 molecules and oxygenated intermediates, among all the pure metals, platinum exhibits the best activity for ORR, as shown by Figure 6 illustrating Sabatier's principle in this case [8]. However, the binding energy between platinum atoms and the oxygenated intermediates of the ORR is *ca.* 0.2-0.3 eV too high [8, 9], which leads to kinetic limitations.

Another limitation is the instability of Pt/HSAC catalysts under PEMFC conditions [10–13]. When focusing on the degradation of platinum nanoparticles, several phenomena can occur. First, platinum atoms from small particles can dissolve, diffuse, and redeposit on large ones. This phenomenon is called the electrochemical Ostwald ripening. This process is driven by the diminution of the surface energy of the particles when transferred from small to large ones. Second, platinum crystallites can migrate at the surface of the carbon support and coalesce with others. Third, platinum particles can detach from the carbon support or agglomerate. This is generally induced by carbon corrosion (oxidation into CO_2) which occurs upon PEMFC operation. Finally, platinum atoms can dissolve from crystallites and reprecipitate in the ionomer or in the membrane. These particles do not participate to the electrochemical reactions anymore, as they are isolated from the electron-conductive carbon support.

The architecture of the catalytic layers also plays an important role in the complex system of PEMFCs. Indeed, diffusion of reactants and products directly impacts the quantity of produced current. Diffusional limitations are more pronounced in the cathode catalytic layer. Actually, at the cathode, the ORR involves three re-

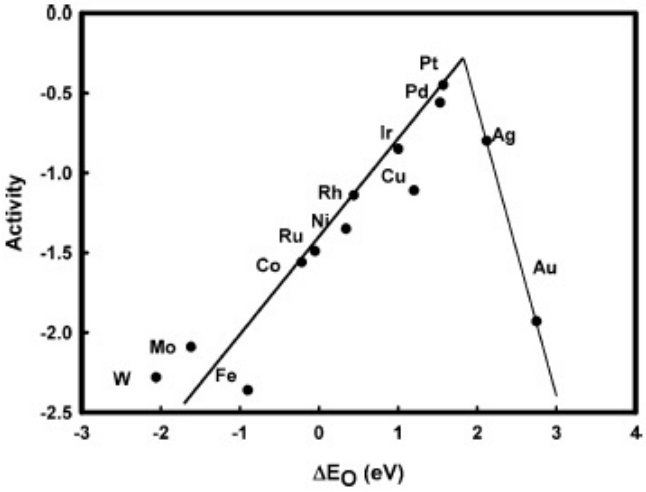

Figure 6: Representation of Sabatier's principle in the case of the oxygen reduction activity of metals (values are expressed as a difference from the theoretical maximum activity for oxygen reduction) as a function of the oxygen binding energy, ΔE_O (reproduced from Reference [8]).

actants and one product (see Equation (2)), which have to diffuse to/from the active sites situated at the surface of the platinum nanoparticles (see Figure 4b and c). If any of these four species can not reach or leave active sites, these sites at the surface of platinum nanoparticles do not participate in the ORR, leading to useless platinum particles. This is why, in order to produce sufficiently active catalytic layers, manufacturers use catalysts with high platinum loading (up to 70 wt.%), despite the expensiveness and the supply limitations of platinum. Indeed, the high platinum loading has two major impacts on the PEMFC performance: (i) the high amount of platinum particles ensures that enough catalytic sites are truly active (*i.e.* in contact with the carbon support and the ionomer and accessible by reactants through the pore texture) and (ii) the use of highly loaded catalysts allows to decrease the thickness of the catalytic layer (down to several µm), while keeping the same platinum loading on the layer, leading to a diminution of the diffusional limitations.

The impact of the above-mentioned problems can be illustrated by the voltage-current curve of PEMFCs (Figure 7). Every limitation leads to a voltage decrease, the so-called overpotentials. These overpotentials represent the loss of electrical work resulting from the conversion of chemical energy into heat. The voltage decrease of a fuel cell stem from three limitations: (i) the sharp decrease at high voltage and low current, η_{ORR}, is due to the sluggish kinetics of the ORR, catalyzed by platinum particles, *i.e.* the activation energy of the reaction is transformed into heat instead of electrical work; (ii) the linear decrease at moderate voltage and current, η_{Ohm}, is due to the resistance of the cell, *e.g.* the ionic resistance of the proton exchange membrane, which causes the conversion of chemical energy into heat by Joule effect; and (iii) the decrease at low voltage and high current is due to mass-transport limitations, *e.g.* the O_2 diffusion inside the catalytic layer, leading again to energy (*i.e.* voltage) loss, η_{diff}.

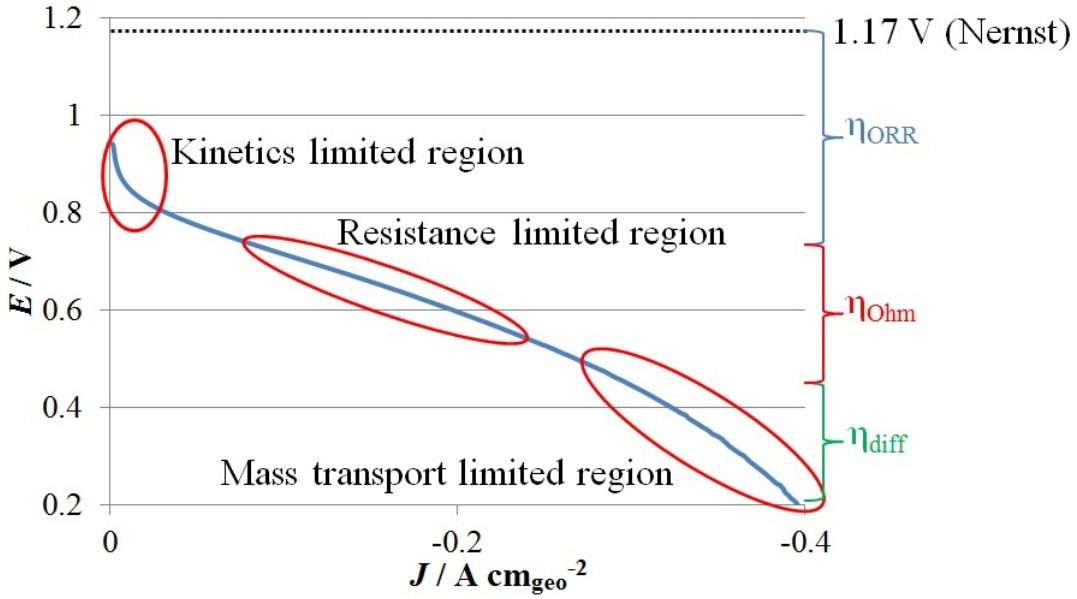

Figure 7: Voltage-current curve of a commercial PEMFC.

Solutions

For the last decades, researchers investigated possible solutions to overcome the limitations of PEMFCs. In particular, significant resources were dedicated to the design of the catalysts for the ORR.

First, the catalytic activity of Pt/HSAC was improved. To do so, the deposition of platinum particles onto the carbon support had to be optimized. Indeed, the platinum particle size directly impacts the catalyst activity for the ORR, as the ORR is structure-sensitive [14–16]. Large platinum particles exhibit high specific activity for the ORR, *i.e.* high activity per platinum surface area. This high specific activity is due to large terraces, *i.e.* large facets, of platinum atoms at the surface of the particles which, like for bulk platinum, weakly bind the oxygenated intermediates of the ORR. When decreasing the particle size, the size of these terraces of platinum atoms decreases, leading to a higher proportion of platinum atoms at the edge sites, *i.e.* sites situated at the border of two facets, than at the terrace sites. The edge platinum atoms, which are low coordinated adsorption sites, bind more strongly the oxygenated intermediates of the ORR leading to a decrease of the activity. This is why the specific activity decreases with the size of the platinum particle, *i.e.* when increasing the proportion of edge platinum atoms [14–16]. However, another property of the platinum particles impacts the activity when focusing on the mass activity for the ORR, *i.e.* the activity expressed by mass unit of platinum. This property is the dispersion of platinum, *i.e.* the ratio between the number of platinum atoms at the surface of the particles and the total number of platinum atoms. The dispersion increases when the particle size decreases, leading to a higher proportion of platinum atoms at the particle surface, and so a higher number of active sites for

the same amount of platinum. As the specific activity of platinum particles and the platinum dispersion are inversely related with the platinum particle size, the mass activity for the ORR, which is the combination of both phenomena, must reach a maximum with regard to the platinum particle size. This optimum is close to 3-4 nm [17, 18].

In order to further improve the activity for the ORR, the strength of the bond between the surface platinum atoms and the oxygenated intermediates of the ORR can be weakened by alloying platinum to transition metals (PtM), such as Cu, Co, Ni, *etc.* Indeed, as their atomic radius is smaller than that of platinum atoms, the introduction of transition metals within the platinum lattice leads to its contraction. The smaller platinum lattice parameter and the modified electronic structure of platinum atoms by the neighbour transition metal atoms lead to a widening of the *d*-band of platinum and a decrease of the average energy of the band, *i.e.* the *d*-band center [19–21]. This phenomenon, also called the strain-ligand effect, impacts the adsorption properties of oxygenated species, such as the oxygenated intermediates of the ORR, by modifying the platinum *5d*-band [9, 22]. As explained in previous paragraphs, decreasing the energy of the bond between platinum active sites and oxygenated intermediates leads to an increase in the ORR activity.

On this basis, two different ways of improvement of the activity for the ORR of PtM catalysts were explored by researchers. On the one hand, the increase in activity due to extended surface and well-defined facet catalysts was investigated. This way of improvement is based on Stamenkovic and co-workers' study [23] which evidences the huge activity for the ORR of the Pt_3Ni (1 1 1) facet. Stemming from this result, a lot of studies about very active structures with well-defined facets were conducted, *e.g.* octahedra [24, 25], nanoframes [26], nanostructured thin films [27], *etc.* On the other hand, researchers worked on the increase in activity by increasing the density of structural defects. These structural defects lead to the formation of low and high coordination active sites (schematically represented in Figure 8) and contracted and dilated structures. These particular active sites exhibit modified adsorption properties for the oxygenated species [28, 29]. As an example, low coordination active sites can strongly bind oxygenated intermediates of the ORR, leading on a decrease of the activity for the ORR, whereas high coordination active sites weakly bind the oxygenated intermediates, leading to an increase of the activity [30]. In order to increase the density of structural defects of particles, particular structures of nanoparticles were synthesized, such as nanoporous particles [31, 32], sponge particles [32–34], and hollow nanoparticles [32, 35–37].

After the catalytic activity for the ORR, the second property to improve was the stability of the catalysts, especially that of the metal nanoparticles. In order to investigate if alloying platinum with a transition metal, besides increasing the activity, impacts the durability of the catalyst, many durability studies were performed on PtM catalysts [33, 34, 38–42]. From these studies, it is shown that the alloying of platinum with transition metals lowers the amount of dissolved platinum atoms, which leads to a mitigation of the particle dissolution, growth, and migration [12]. However, PtM catalysts may suffer from other stability issues. The major issue is

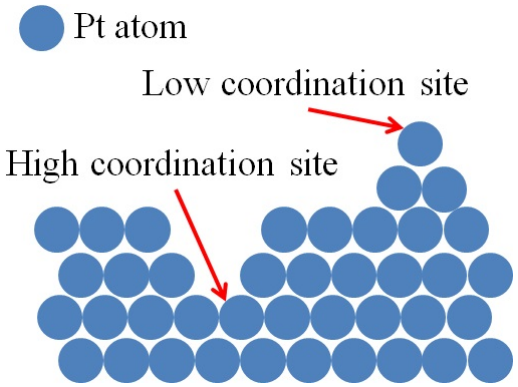

Figure 8: Schematic representation of low and high coordination platinum sites.

the dissolution of the transition metal. When PtM catalysts are used in PEMFCs, this dissolution can decrease the performance of the fuel cell, as the transition metal atoms, responsible for the strain-ligand effect, are dissolved and leave the nanoparticles [13]. Moreover, the dissolved transition metal cations, which are not able to be reduced in PEMFCs medium, strongly interact with the sulfonated groups of the ionomer and the membrane. This strong interaction induces two major effects: (i) the proton-transport properties of the ionomer and the membrane degrade; and (ii) the mass-transport limitations of O_2 molecules through the ionomer towards the active sites worsen [13, 43]. These impacts are mainly due to the blocking of the proton-conductive sites by the metal cations and to the degradation of the polymer, which is accelerated by metal cations. However, the morphology and structure of the nanoparticles after the dissolution of the transition metal can change, leading to particular types of structure and morphology [26, 31–34, 36, 37, 44–48]. These morphologies, such as hollow nanoparticles, display very good stability under PEMFC conditions, as they are formed after thousands of hours of PEMFC operation [35,49]. The combination of the good stability under PEMFC condition and the high ORR activity of such nanostructures, predominantly due to a high density of structural defects, pushed researchers to develop direct synthesis of nanostructured particles, such as hollow nanoparticles [32, 36, 37, 50, 51].

Concerning the architecture of the cathode catalytic layer, one possible solution is to replace the usual carbon supports, which are not optimal for the application in PEMFCs, by nanostructured carbons. Indeed, the diffusion of O_2 molecules towards the active site of platinum particles is a key problem in PEMFCs (as already discussed in the previous section: Drawbacks of PEMFCs). The O_2 diffusion properties are strongly dependent of the pore texture of the catalytic layer, which stems from the structure of the carbon support and the manufacture conditions of the MEA (*e.g.* hot-pressing). The highly microporous structures of commonly used high surface area carbons are not optimal for the O_2 diffusion within the catalytic layer. In order to improve mass transport inside this layer, other types of highly porous carbon support can be considered. For example, carbon xerogels (CXs) may be promising materials. CXs are meso-macroporous synthetic carbons with a pore texture which can be tuned from the synthesis variables. The synthesis of CXs *via*

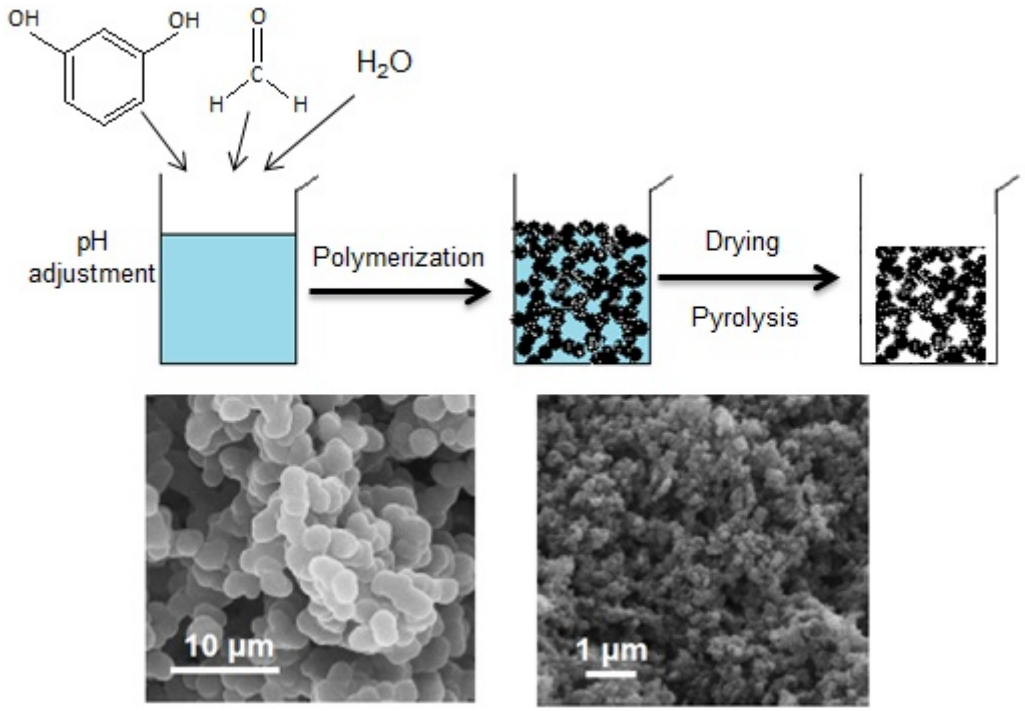

Figure 9: Schematic representation of the synthesis of carbon xerogel and SEM micrographs of two carbon xerogels with different textures. The micrographs are reproduced from Reference [60].

a sol-gel process is schematized in Figure 9 and can be summarized in four steps: (i) the polycondensation of resorcinol and formaldehyde in aqueous solution; (ii) the aging of the gel; (iii) the drying of the gel; and (iv) the pyrolysis of the polymer. Figure 9 also shows scanning electron microscopy (SEM) micrographs of two CXs with different textures. As a synthetic material, CXs exhibit high purity and controllable and reproducible pore texture [52]. When CXs are used as carbon support for PEMFC catalysts, their controllable and reproducible pore texture leads to catalytic layers with tailored architecture. This leads mitigating mass-transport limitations within the catalytic layer, resulting in better performance in PEMFCs [53]. Moreover, previous works have demonstrated that CXs are excellent supports to deposit metals, especially platinum, with high dispersion [53–59].

Objectives of the thesis

The aim of this thesis is to combine several of the above-mentioned solutions in order to overcome the limitations of the ORR catalysts currently used at the cathode of PEMFCs. So, this thesis focused on the improvement of the PEMFC cathode catalytic layer performance by: (i) using a carbon support with a pore texture suitable for the catalytic layer; (ii) developing synthesis methods for platinum nanoparticles supported on carbon xerogel (Pt/CX catalysts) with high platinum

loading; (iii) developing synthesis methods for bimetallic PtCo nanoparticles supported on carbon xerogel (PtCo/CX catalysts); and (iv) analyzing the activity and the durability of these catalysts both in liquid electrolyte and in real PEMFC.

To improve the mass-transport properties of the cathodic catalytic layer, a carbon xerogel (CX) with appropriate pore texture was used as support for the catalytic particles. The deposition of platinum onto CX was then studied with the aim to synthesize highly loaded catalysts, *i.e.* 30-40 wt.% of platinum, with good dispersion, *i.e.* platinum particle size around 3-4 nm, by means of the simplest possible synthesis method, *i.e.* which could be easily scaled up. In order to increase the catalytic activity for the ORR, methods to synthesize PtCo nanoparticles deposited on CX were then investigated. In particular, the synthesis of hollow PtCo/CX catalysts, which are supposed to exhibit high performance for the ORR and high durability in PEMFCs, was carried out. Finally, the activity for the ORR of the synthesized Pt/CX and PtCo/CX catalysts was measured in a three-electrode cell and the durability of the catalysts with the best performance was investigated in both a three-electrode cell system and a full PEMFC assembly.

Thesis outline

This thesis is structured around three axes: (i) the synthesis of platinum nanoparticles deposited on carbon xerogel (Pt/CX catalysts) for the oxygen reduction reaction (ORR) and its streamlining; (ii) the synthesis of PtCo nanoparticles (solid and hollow) deposited on carbon xerogel (PtCo/CX catalysts) for the ORR; and (iii) the study of the durability of the best catalysts synthesized in the two previous parts. Each axis is divided into two consecutive chapters.

- In the first chapter, the platinum deposition on carbon xerogel *via* the so-called strong electrostatic adsorption (SEA) is studied. Based on previous works [54, 56–59], the synthesis of Pt/CX catalysts was modified in order to increase the platinum loading of the catalysts and decrease the platinum losses during the synthesis.

- The second chapter focuses on a further streamlining of the platinum deposition process. Several Pt/CX synthesis methods were performed with the purpose of decreasing, or even avoiding completely, the platinum losses during the catalyst synthesis and/or speeding up the procedure. The electrochemical properties of these catalysts were compared to those of a commercial catalyst.

- Chapter 3 concerns the synthesis of PtCo particles deposited on carbon xerogel (PtCo/CX catalysts) based on the SEA method.

- In Chapter 4, the synthesis of hollow PtCo/CX catalysts is investigated and their electrochemical performance is compared to the same commercial catalyst as above.

- The penultimate chapter is dedicated to the durability study of the catalysts with the best performance for the ORR analyzed in the previous chapters. The durability of Pt/CX and hollow PtCo/CX catalysts was compared to that of the commercial catalyst in a three-electrode cell setup.
- Finally, in Chapter 6, the durability of the catalysts with the best performance for the ORR is studied *in situ*, *i.e.* in full PEMFC assembly, and compared to that of two commercial catalysts assembled in the same conditions.

After the six chapters, a general conclusion and an outlook summarize the thesis and the future works to perform. At the end of the manuscript, an appendix introduces the reader to the electrochemical measurements (in three electrode cell or in PEMFC) performed all over the chapters.

This thesis regroups results either already published, submitted for publication, or in preparation for publication. Chapter 1 was published in *Fuel cells* [61]. Some of the results of Chapter 2 were published in *Catalysts* [62]. Chapter 2 has recently been submitted in its entirety to *Applied Catalysis B: Environmental*. Chapters 4 and 5 are in preparation for submission. Chapter 3 is not considered publishable as such and Chapter 6 has to be extended before publication since it mainly consists of preliminary results. As a consequence, the six chapters of this thesis can be read independently of each other, as each chapter is structured as an article.

References

[1] H. Ibrahim and A. Ilinca, Techno-Economic Analysis of Different Energy Storage Technologies, in *Energy Storage - Technologies and Applications*, edited by A. Zobaa, chapter 1, InTech, 2013.

[2] I. Katsounaros, S. Cherevko, A. R. Zeradjanin, and K. J. J. Mayrhofer, *Angewandte Chemie - International Edition* **53**, 102 (2014).

[3] O. Z. Sharaf and M. F. Orhan, *Renewable and Sustainable Energy Reviews* **32**, 810 (2014).

[4] Y. Wang, K. S. Chen, J. Mishler, S. C. Cho, and X. C. Adroher, *Applied Energy* **88**, 981 (2011).

[5] G. Forozani, P. Shamshiri, and N. Sheikh, *Journal of Fuel Cell Science and Technology* **9**, 034501 (2012).

[6] V. Stamenković, T. J. Schmidt, P. N. Ross, and N. M. Marković, *The Journal of Physical Chemistry B* **106**, 11970 (2002).

[7] V. Mehta and J. S. Cooper, *Journal of Power Sources* **114**, 32 (2003).

[8] J. K. Nørskov, J. Rossmeisl, A. Logadottir, L. Lindqvist, J. R. Kitchin, T. Bligaard, and H. Jónsson, *J. Phys. Chem. B.* **108**, 17886 (2004).

[9] I. E. L. Stephens, A. S. Bondarenko, U. Grønbjerg, J. Rossmeisl, and I. Chorkendorff, *Energy & Environmental Science* **5**, 6744 (2012).

[10] Y. Shao-Horn, W. C. Sheng, S. Chen, P. J. Ferreira, E. F. Holby, and D. Morgan, *Topics in Catalysis* **46**, 285 (2007).

[11] X. Z. Yuan, H. Li, S. Zhang, J. Martin, and H. Wang, *Journal of Power Sources* **196**, 9107 (2011).

[12] S. Zhang, X. Z. Yuan, J. N. C. Hin, H. Wang, J. Wu, K. A. Friedrich, and M. Schulze, *Journal of Power Sources* **195**, 1142 (2010).

[13] L. Dubau, L. Castanheira, F. Maillard, M. Chatenet, O. Lottin, G. Maranzana, J. Dillet, A. Lamibrac, J. C. Perrin, E. Moukheiber, A. Elkaddouri, G. De Moor, C. Bas, L. Flandin, and N. Caqué, *Wiley Interdisciplinary Reviews: Energy and Environment* **3**, 540 (2014).

[14] M. Nesselberger, S. Ashton, J. C. Meier, I. Katsounaros, K. J. J. Mayrhofer, and M. Arenz, *Journal of the American Chemical Society* , 17428 (2011).

[15] F. J. Perez-Alonso, D. N. McCarthy, A. Nierhoff, P. Hernandez-Fernandez, C. Strebel, I. E. L. Stephens, J. H. Nielsen, and I. Chorkendorff, *Angewandte Chemie - International Edition* **51**, 4641 (2012).

[16] M. Shao, A. Peles, and K. Shoemaker, *Nano Letters* **11**, 3714 (2011).

[17] K. Kinoshita, *Journal of the Electrochemical Society* **137**, 845 (1990).

[18] O. Antoine, Y. Bultel, and R. Durand, *Journal of Electroanalytical Chemistry* **499**, 85 (2001).

[19] B. Hammer and J. K. Nørskov, *Surface Science* **343**, 211 (1995).

[20] J. R. Kitchin, J. K. Nørskov, M. A. Barteau, and J. G. Chen, *Journal of Chemical Physics* **120**, 10240 (2004).

[21] T. Bligaard and J. K. Nørskov, *Electrochimica Acta* **52**, 5512 (2007).

[22] I. E. L. Stephens, A. S. Bondarenko, F. J. Perez-Alonso, F. Calle-Vallejo, L. Bech, T. P. Johansson, A. K. Jepsen, R. Frydendal, B. P. Knudsen, J. Rossmeisl, and I. Chorkendorff, *Journal of the American Chemical Society* **133**, 5485 (2011).

[23] V. R. Stamenkovic, B. Fowler, B. S. Mun, G. Wang, P. N. Ross, C. A. Lucas, and N. M. Markovic, *Science* **315**, 493 (2007).

[24] H. A. Gasteiger and N. M. Marković, *Science* **324**, 48 (2009).

[25] R. M. Arán-Ais, J. Solla-Gullón, M. Gocyla, M. Heggen, R. E. Dunin-Borkowski, P. Strasser, E. Herrero, and J. M. Feliu, *Nano Energy* **27**, 390 (2016).

[26] C. Chen, Y. Kang, Z. Huo, Z. Zhu, W. Huang, H. L. Xin, J. D. Snyder, D. Li, J. A. Herron, M. Mavrikakis, M. Chi, K. L. More, Y. Li, N. M. Markovic, G. A. Somorjai, P. Yang, and V. R. Stamenkovic, *Science* **343**, 1339 (2014).

[27] D. Van Der Vliet, C. Wang, M. Debe, R. Atanasoski, N. M. Markovic, and V. R. Stamenkovic, *Electrochimica Acta* **56**, 8695 (2011).

[28] F. Calle-Vallejo, J. I. Martínez, J. M. García-Lastra, P. Sautet, and D. Loffreda, *Angewandte Chemie - International Edition* **53**, 8316 (2014).

[29] F. Calle-Vallejo, J. Tymoczko, V. Colic, Q. H. Vu, M. D. Pohl, K. Morgenstern, D. Loffreda, P. Sautet, W. Schuhmann, and A. S. Bandarenka, *Science* **350**, 185 (2015).

[30] O. Le Bacq, A. Pasturel, R. Chattot, B. Previdello, J. Nelayah, T. Asset, L. Dubau, and F. Maillard, *ChemCatChem* **9**, 2324 (2017).

[31] L. Gan, M. Heggen, R. O'Malley, B. Theobald, and P. Strasser, *Nano Letters* **13**, 1131 (2013).

[32] R. Chattot, T. Asset, P. Bordet, J. Drnec, L. Dubau, and F. Maillard, *ACS Catalysis* **7**, 398 (2017).

[33] S. Chen, H. A. Gasteiger, K. Hayakawa, T. Tada, and Y. Shao-Horn, *Journal of the Electrochemical Society* **157**, A82 (2010).

[34] Y. Yu, H. L. Xin, R. Hovden, D. Wang, E. D. Rus, J. A. Mundy, D. A. Muller, and H. D. Abruna, *Nano Letters* **12**, 4417 (2012).

[35] L. Dubau, J. Durst, F. Maillard, L. Guétaz, M. Chatenet, J. André, and E. Rossinot, *Electrochimica Acta* **56**, 10658 (2011).

[36] L. Dubau, J. Nelayah, S. Moldovan, O. Ersen, P. Bordet, J. Drnec, T. Asset, R. Chattot, and F. Maillard, *ACS Catalysis* **6**, 4673 (2016).

[37] T. Asset, R. Chattot, J. Nelayah, N. Job, L. Dubau, and F. Maillard, *ChemElectroChem* **3**, 1591 (2016).

[38] S. Koh, M. F. Toney, and P. Strasser, *Electrochimica Acta* **52**, 2765 (2007).

[39] H. R. Haas and M. T. Davis, *ECS Transactions* **25**, 1623 (2009).

[40] L. Dubau, F. Maillard, M. Chatenet, J. André, and E. Rossinot, *Electrochimica Acta* **56**, 776 (2010).

[41] F. Maillard, L. Dubau, J. Durst, M. Chatenet, J. André, and E. Rossinot, *Electrochemistry Communications* **12**, 1161 (2010).

[42] A. Schenk, C. Grimmer, M. Perchthaler, S. Weinberger, B. Pichler, C. Heinzl, C. Scheu, F. A. Mautner, B. Bitschnau, and V. Hacker, *Journal of Power Sources* **266**, 313 (2014).

[43] J. Durst, M. Chatenet, and F. Maillard, *Physical Chemistry Chemical Physics* **14**, 13000 (2012).

[44] C. M. Pedersen, M. Escudero-Escribano, A. Velázquez-Palenzuela, L. H. Christensen, I. Chorkendorff, and I. E. L. Stephens, *Electrochimica Acta* **179**, 647 (2015).

[45] B. Han, C. E. Carlton, A. Kongkanand, R. S. Kukreja, B. R. Theobald, L. Gan, R. O'Malley, P. Strasser, F. T. Wagner, and Y. Shao-Horn, *Energy & Environmental Science* **8**, 258 (2015).

[46] S. Chen, W. Sheng, N. Yabuuchi, P. J. Ferreira, L. F. Allard, and Y. Shao-Horn, *Journal of Physical Chemistry C* **113**, 1109 (2009).

[47] M. Oezaslan and P. Strasser, *Journal of Power Sources* **196**, 5240 (2011).

[48] M. Oezaslan, M. Heggen, and P. Strasser, *Journal of the American Chemical Society* **134**, 514 (2012).

[49] L. Dubau, M. Lopez-Haro, L. Castanheira, J. Durst, M. Chatenet, P. Bayle-Guillemaud, L. Guétaz, N. Caqué, E. Rossinot, and F. Maillard, *Applied Catalysis B: Environmental* **142-143**, 801 (2013).

[50] S. J. Bae, S. J. Yoo, Y. Lim, S. Kim, Y. Lim, J. Choi, K. S. Nahm, S. J. Hwang, T.-H. Lim, S.-K. Kim, and P. Kim, *Journal of Materials Chemistry* **22**, 8820 (2012).

[51] A. X. Shan, Z. C. Chen, B. Q. Li, C. P. Chen, and R. M. Wang, *Journal of Materials Chemistry A* **3**, 1031 (2015).

[52] N. Job, R. Pirard, J. Marien, and J.-P. Pirard, *Carbon* **42**, 619 (2004).

[53] N. Job, J. Marie, S. D. Lambert, S. Berthon-Fabry, and P. Achard, *Energy Conversion and Management* **49**, 2461 (2008).

[54] S. D. Lambert, N. Job, L. D'Souza, M. Pereira, R. Pirard, B. Heinrichs, J. Figueiredo, J.-P. Pirard, and J. Regalbuto, *Journal of Catalysis* **261**, 23 (2009).

[55] N. Job, B. Heinrichs, F. Ferauche, F. Noville, J. Marien, and J.-P. Pirard, *Catalysis Today* **102-103**, 234 (2005).

[56] N. Job, M. F. R. Pereira, S. D. Lambert, A. Cabiac, G. Delahay, J.-F. Colomer, J. Marien, J. L. Figueiredo, and J.-P. Pirard, *Journal of Catalysis* **240**, 160 (2006).

[57] N. Job, F. Maillard, J. Marie, S. Berthon-Fabry, J. P. Pirard, and M. Chatenet, *Journal of Materials Science* **44**, 6591 (2009).

[58] N. Job, S. D. Lambert, M. Chatenet, C. J. Gommes, F. Maillard, S. Berthon-Fabry, J. R. Regalbuto, and J.-P. Pirard, *Catalysis Today* **150**, 119 (2010).

[59] N. Job, M. Chatenet, S. Berthon-Fabry, S. Hermans, and F. Maillard, *Journal of Power Sources* **240**, 294 (2013).

[60] N. Job, S. Berthon-Fabry, M. Chatenet, J. Marie, M. Brigaudet, and J. P. Pirard, *Topics in Catalysis* **52**, 2117 (2009).

[61] A. Zubiaur, M. Chatenet, F. Maillard, S. D. Lambert, J.-P. Pirard, and N. Job, *Fuel Cells* **14**, 343 (2014).

[62] N. Job, S. D. Lambert, A. Zubiaur, C. Cao, and J.-P. Pirard, *Catalysts* **5**, 40 (2015).

Chapter 1

Using the multiple SEA method to synthesize Pt/carbon xerogel electrocatalysts for PEMFC applications

In the first chapter of this thesis, a method to synthesize Pt nanoparticles supported on carbon xerogel with high Pt loading is developed. It starts from the strong electrostatic adsorption method, which allows the deposition of 8 wt.% of Pt with high dispersion on carbon xerogel. This method was repeated several times to increase the Pt loading, while trying to streamline the synthesis method in order to diminish the Pt losses. The results of this chapter are published in *Fuel cells* **14**, 343 (2014).

1.1 Introduction

The catalytic layers used in proton exchange membrane fuel cells (PEMFCs) are classically based on Pt particles supported on carbon black (Pt/CB). The structure of these catalytic layers is however not optimal, resulting in incomplete utilization of the mass of Pt loaded onto the carbon support [1]. In order to reduce the cost of the catalytic layer without decreasing its performance, two parameters can be improved: the support and the synthesis of the Pt particles.

With respect to the support, the commonly used carbon blacks do not display optimal properties for electrocatalysis: they may contain high amount of chemical impurities, and the final structure of the electrodes is hardly tuneable [2]. A possible solution to these drawbacks is to use synthetic nanostructured materials with a controllable, reproducible texture and with a pure, known and constant chemical composition; carbon xerogels (CXs) exhibit such properties [3]. With respect to the Pt crystallites, a decrease of the particle size to nanometre dimensions allows increasing the ratio between the number of atoms on the surface to the overall number of metal atoms (the so-called dispersion), thereby heightening the mass activity (per gram of metal), and thus decreasing the cost of the catalytic layers. However, increasing the dispersion also results in a decrease in the specific activity of the Pt nanoparticles (per real cm^2 of Pt) for most of the reactions performed in PEMFCs [4]. This trend has been attributed to increased adsorption strength of oxygenated species for smaller Pt particle size, as shown from X-ray absorption spectroscopy studies [5]. As a result, the optimal mass activity is obtained for Pt nanoparticles of 3 nm in diameter [6, 7].

Highly dispersed Pt/CX catalysts can be prepared by the strong electrostatic adsorption (SEA) method [8, 9]. The SEA technique [8, 10, 11] consists in maximizing the electrostatic interactions between the metal precursor and the support by adjusting the pH of the carbon/water/Pt precursor slurry to the adequate value. The latter depends on the surface chemistry (and of the point of zero charge, PZC) of the support and on the nature of the Pt precursor. Due to the presence of various oxygen surface groups, the carbon support protonates/ deprotonates at low/high pH value, thus enhancing the adsorption of anions/cations, respectively. For instance, in the case of the impregnation of CXs with chloroplatinic acid (CPA, H_2PtCl_6) aqueous solutions (1,000 ppm_{Pt}), the final pH leading to the highest Pt uptake was found to be *ca.* 2.5, yielding electrocatalysts with Pt mass fraction close to 10 wt.% [10]. However, achieving high Pt weight percentage without sacrificying the catalytic performance requires multiple 'impregnation-drying-reduction' cycles [9]. A major hurdle with this technique is the use of large volumes of fresh 1 g_{Pt} L^{-1} solution for each impregnation step, which induces inacceptable losses of Pt. In order to improve the synthesis efficiency, efforts were targeted so as to reuse the same Pt solution for several impregnation steps (multiple SEA method).

The present chapter is focused on the synthesis and characterization of Pt/CX nanoparticles by the multiple SEA method in view of testing and using them as PEMFC catalysts.

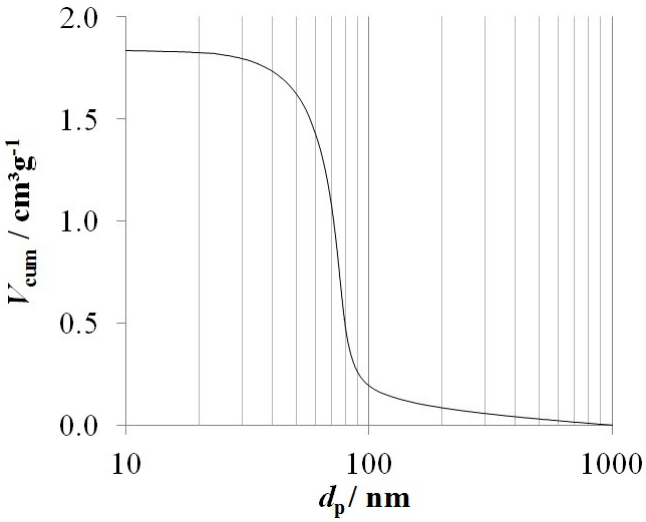

Figure 1.1: Characterization of the CX pore texture obtained from mercury porosimetry. Cumulative pore volume as a function of the pore size in the mesopores domain.

1.2 Experimental

1.2.1 Synthesis

The support used in this thesis is a CX prepared by drying and pyrolysis of a resorcinol-formaldehyde gel [12]. Briefly, the gel was obtained by polycondensation of resorcinol with formaldehyde in water. The pore size distribution of this CX was centred at 80 nm (Figure 1.1): the resorcinol/formaldehyde molar ratio, *R/F*, was fixed at 0.5, the resorcinol/sodium carbonate molar ratio, *R/C*, was chosen to be equal to 1,000 and the dilution ratio, *D*, *i.e.* the solvent/(resorcinol and formaldehyde) molar ratio, was set at 5.7. At first, 114.1 g of resorcinol and 0.11 g of sodium carbonate (Na_2CO_3) were mixed with 217.5 mL of deionized water in a 500 mL vessel under stirring. The addition of sodium carbonate fixes the pH at 5.85. After dissolution of resorcinol, 169.2 g of formaldehyde solution (37 wt.% in water, stabilized with 10-15 wt.% of methanol) were added. Then, the flask was sealed and put in an oven at 358 K for gelling and aging. After 72 h, the obtained gel was dried under vacuum: the bottle was opened and heated to 333 K; then the pressure was decreased stepwise during 8 h until it reached 1,200 Pa. At this low pressure, the flask was heated up to 423 K and left at this temperature for 12 h. When the sample was dry, it was pyrolyzed at 1,073 K under nitrogen flow following this procedure: (i) heating at 1.7 K min^{-1} up to 423 K and hold for 15 min; (ii) heating at 5 K min^{-1} up to 673 K and hold for 1 h; (iii) heating at 5 K min^{-1} up to 1,073 K and hold for 2 h; and (iv) progressively cooling down to room temperature. After pyrolysis, the xerogel was crushed and sieved between 75 and 250 μm.

To synthesize Pt/CX catalysts, the 'multiple SEA method' was used. In a previous study [9], in order to obtain high Pt weight percentage, the SEA method was performed up to three times on the same support using a new H_2PtCl_6 solution each time. In 'multiple SEA', the precursor solution is highly loaded in order to reuse it several times to increase the catalyst Pt weight percentage. Concerning the initial concentration of the H_2PtCl_6 solution, Lambert *et al.* [10] showed that the quantity of Pt adsorbed on the surface of CXs does not depend on the concentration of the H_2PtCl_6 initial solution, should it be above 5 mmol L^{-1} (*i.e.* around 1 g_{Pt} L^{-1}). As a result, one can use highly concentrated H_2PtCl_6 solution without modifying the Pt deposition.

One gram of CX powder was mixed with 567 mL of an H_2PtCl_6 solution at 8.97 mmol L^{-1} (*i.e.* 1.75 g_{Pt} L^{-1}) with an initial pH of 2.5. The surface loading (SL), *i.e.* the total area of CX surface in solution, was equal to 1,000 m^2 L^{-1} and the concentration of H_2PtCl_6 was chosen high enough to reuse the solution five times. After 1 h of stirring, the mixture was filtered and the filtrate was kept for reuse in another impregnation step. The solid was dried in an oven at 333 K during 12 h. Then, the dried CX was reduced at 473 K under H_2 flow (0.04 mmol s^{-1}) during 1 h to obtain carbon-supported Pt nanoparticles (Pt/CX). In order to synthesize several catalysts with various Pt weight percentages, the 'impregnation-drying-reduction' steps were performed from one to five times on the same support. After the last impregnation, each catalyst was reduced at 723 K under H_2 (0.04 mmol s^{-1}) during 5 h to clean the surface of the Pt particles from chlorine [9]. Hereafter, the five catalysts are labeled according to the number of 'impregnation-drying-reduction' cycles, *e.g.* Pt-1/CX for the catalyst obtained after one cycle, Pt-2/CX for the catalysts obtain after two cycles, *etc.*

1.2.2 Physicochemical Characterization

The textural properties of the CX support were determined by N_2 adsorption-desorption and mercury porosimetry. The nitrogen adsorption-desorption isotherms were measured at 77 K with a Sorptomatic CE Instruments 1990 Series. Before the measurement, the sample was outgassed at 10^{-3} Pa during 12 h at room temperature. The isotherm analysis provided the BET specific area, S_{BET}, the microporous volume calculated with the Dubinin-Radushkevich equation, V_{DUB}, and the cumulative volume of pores with width between 2 and 7.5 nm determined by the Broekhoff-de Boer theory, $V_{\mathrm{cum<7.5\ nm}}$ [13]. The mercury porosimetry measurement was performed with a Pascal Series 140 porosimeter between 0.01 and 0.4 MPa and with a Pascal Series 240 porosimeter between 0.1 and 200 MPa. This measurement provided the volume of pores with width higher than 7.5 nm, V_{Hg}. The total void volume, V_{v}, was calculated from the combination of nitrogen adsorption-desorption isotherm and mercury porosimetry measurement [14, 15]:

$$V_{\mathrm{v}} = V_{\mathrm{DUB}} + V_{\mathrm{cum<7.5\ nm}} + V_{\mathrm{Hg}} \tag{1.1}$$

The pore size distribution was determined from the mercury porosity measurement by applying Washburn's theory [16] because CXs do not crush under the mercury pressure and undergo intrusion only [3, 12, 17].

The Pt weight percentage of the catalysts was measured by inductively coupled plasma-atomic emission spectrometry (ICP-AES) using an ICAP 6500 THERMO device. The solution for the analysis was prepared as follows: a fraction of the catalyst sample was weighed and digested by 10 mL of sulphuric acid (H_2SO_4) and 5 mL of nitric acid (HNO_3), and this solution was heated at 573 K until clear. After the complete dissolution of the carbon support and evaporation, 3 mL of hydrochloric acid (HCl) and 1 mL of HNO_3 were added. The obtained solution was heated a few minutes at 393 K, and transferred into a 50 mL calibrated flask, which was finally filled by deionized water.

The Pt particles were observed by transmission electron microscopy (TEM) with a Jeol 2010 transmission electron microscope (200 kV, LaB_6 filament). A carbon-coated copper grid was cleaned in ethanol and dried before being contacted with the Pt/CX catalyst powder. Some particles of Pt/CX catalysts remained attached to the grid through electrostatic interaction. Pt nanoparticle size distribution histograms were obtained by image analysis of the TEM micrographs on at least 500 particles [9].

The catalyst powders were analyzed by X-ray diffraction (XRD) with a Siemens D5000 goniometer using the $Cu_{K\alpha}$ line (Ni filter).

1.2.3 Electrochemical Characterization

Material All the glassware was cleaned by immersion in a H_2SO_4:H_2O_2 solution overnight and thoroughly rinsed with ultrapure water (18 MΩ cm). The electrolytic solutions were prepared from ultrapure water and H_2SO_4 (98% Suprapur, Merck).

Catalytic layer preparation To measure the electrochemical properties of the catalysts, inks were first prepared. The ink composition was chosen to keep the amount of carbon constant, regardless of the metal loading [18,19]. For each sample, the amount of catalyst containing 19.8 mg of CX was crushed in a mortar then mixed with 755 mg of ultrapure water and 466 mg of 5 wt.% Nafion® solution. In order to blend it homogeneously, the mixture was then processed in an ultrasonic bath for 30 min. Once the ink was homogeneous, 10 µL of ink were deposited on a glassy carbon (GC) disk (5 mm in diameter) and sintered at 423 K during 15 min to evaporate the solvents and stick the catalyst onto the GC disk. The catalytic layer deposited on the GC disk composes the working electrode for all electrochemical measurements. This procedure yields active layers of identical thickness onto the GC disk (*i.e.* resulting in identical mass-transport limitations within the layer [18, 19]).

Electrolyte and wetting procedure During all measurements, the working electrode was immersed in an electrolyte constituted of 1 M H_2SO_4 aqueous solution, which should ensure full wetting of the metallic particles by the electrolyte [19]. In order to ensure that all the pores, *i.e.* both the extragranular and the mesoporous intergranular porosities, were fully filled, a drop of electrolyte was deposited onto the catalytic layer. Then, the electrode was put under vacuum in order to outgas the layer by bubbling air through the drop. Once no air bubbles were visible, the electrode and the drop were put back under atmospheric pressure so that the electrolyte filled the empty porosity of the layer. This wetting procedure ensures that the catalyst wetting is complete and that the Pt utilization factor is close to 100%. Indeed, previous works [9, 19] performed on similar systems showed good consistency between the Pt specific surface area measured after using this wetting procedure and the surface calculated from TEM micrographs. Finally, the electrochemical measurements were usually steady, which also hints at good wetting of the layer.

If needed, the following measurement techniques are explained with more details in the Appendix A1 at the end of this thesis.

CO stripping voltammetry The Pt specific surface area was measured by CO stripping voltammetry [20–22]. The procedure was initiated by the application of a steady potential of 0.1 V *vs.* normal hydrogen electrode (NHE) to the working electrode, while gaseous CO was bubbled in the electrolyte solution for 6 min. After an Ar purge of 39 min in order to remove the CO dissolved in the electrolyte (still at 0.1 V *vs.* NHE), the CO chemisorbed at the surface of the particles was electrooxidized into CO_2 by increasing the electrode potential from 0.05 to 1.23 V *vs.* NHE at 20 mV s^{-1}. The potential was then cycled between 0.05 and 1.23 V *vs.* NHE at the same scan speed for two more cycles. This results in three recorded cycles, *i.e.* the first cycle in which the peaks from the CO electrooxidation occur and two other cycles which are cyclic voltammetry cycles performed at 20 mV s^{-1}, as all the adsorbed CO was electrooxidized during the first cycle. As the third cycle represents the background of the CO stripping measurement, it is subtracted from the first in order to isolate the CO electrooxidation peak. The Pt specific surface area, S_{CO} (m^2 $g_{Pt}{}^{-1}$), was calculated from the CO oxidation peak current, assuming that the electrooxidation of a full monolayer of CO_{ad} requires 420×10^{-2} C $m_{Pt}{}^{-2}$ [23].

Activity for the oxygen reduction reaction The specific activity of the catalysts for the oxygen reduction reaction (ORR) was measured on a rotating disk electrode (RDE). After saturation of the electrolyte by oxygen bubbling during 15 min, the electrode potential was set at 1.09 V *vs.* NHE and then decreased at 1 mV s^{-1} to 0.25 V *vs.* NHE, while measuring the reduction current. This measurement was repeated at various rotation speeds of the electrode (400, 900, 1600, and 2500 rpm). For each rotation speed of the electrode, the kinetic current was calculated by correcting the measured current for the effect of the external mass

transfer limitations in the solution using the Koutecky-Levich equation [24]:

$$\frac{1}{i_{\mathrm{k}}} = \frac{1}{i} - \frac{1}{i_{\mathrm{l,c}}} \tag{1.2}$$

where i_{k} is the kinetic current, *i.e.* the current without any mass transfer limitations, i is the experimental current, and $i_{\mathrm{l,c}}$ is the cathodic limit current, which depends on the rotation speed of the electrode. The values of this averaged kinetic current at 0.85 V *vs.* NHE and at 0.9 V *vs.* NHE were divided by the electroactive surface of the catalysts obtained by CO stripping in order to obtain the specific activity of the catalysts at 0.85 V *vs.* NHE, SA_{85}, and at 0.9 V *vs.* NHE, SA_{90}.

1.3 Results

1.3.1 Physicochemical Characterization

The textural properties of the CX support are the following: BET specific surface area, S_{BET}, of 567 m ^{2} g^{-1}, microporous volume, V_{DUB}, of 0.23 cm^3 g^{-1}, cumulative volume of pores with width between 2 and 7.5 nm, $V_{\mathrm{cum<7.5\ nm}}$, of 0.12 cm^3 g^{-1}, pore volume of pores with width higher than 7.5 nm, V_{Hg}, of 1.72 cm^3 g^{-1}, and total void volume, V_{v}, of 2.1 cm^3 g^{-1}.

Table 1.1 shows the physicochemical properties of the catalysts. The Pt weight percentage, measured by ICP-AES, Pt_{ICP}, increases with the number of 'impregnation-drying-reduction' cycles and is equal to: 8.4, 14.7, 19.0, 22.2, and 25.3 wt.% for Pt-1/CX, Pt-2/CX, Pt-3/CX, Pt-4/CX, and Pt-5/CX, respectively. From the Pt weight percentage, Pt_{ICP}, the amount of Pt deposited at each impregnation step per mass of C support in the catalyst, m_{Pt}, can be calculated by:

$$m_{\mathrm{Pt,n}} = \frac{m_{\mathrm{Pt,tot}} - m_{\mathrm{Pt,n\text{-}1}}}{m_{\mathrm{C}}} \tag{1.3}$$

where $m_{\mathrm{Pt,n}}$ is the amount of Pt deposited at impregnation step n per mass of carbon support in the catalyst, $m_{\mathrm{Pt,tot}}$ is the total mass of Pt deposited on the catalyst, $m_{\mathrm{Pt,n\text{-}1}}$ is the mass of Pt deposited on the catalyst before impregnation step n (if no impregnation step before, $n = 0$ and $m_{\mathrm{Pt,n\text{-}1}} = 0$), and m_{C} is the mass of carbon support in the catalyst. The ICP results show that the amount of Pt deposited at each impregnation step per mass of C support in the catalysts, m_{Pt}, decreases from 0.087 and 0.090 g_{Pt} $g_{\mathrm{C}}{}^{-1}$ (Pt-1/CX and Pt-2/CX) to 0.048 and 0.051 g_{Pt} $g_{\mathrm{C}}{}^{-1}$ (Pt-4/CX and Pt-5/CX) with an intermediate value at 0.058 g_{Pt} $g_{\mathrm{C}}{}^{-1}$ (Pt-3/CX).

Figure 1.2 presents TEM micrographs of the five samples. These micrographs show that the Pt is well distributed over the support and form nanoparticles homogeneous in size and shape (spheres of *ca.* 2.2 nm in diameter). Figure 1.3 shows the particle size distributions of the catalysts obtained by image analysis of TEM micrographs. The results indicate that the maximum size of the particles of the

Table 1.1: Catalysts properties determined by physicochemical analyses.

Catalyst	ICP		TEM				XRD
	Pt_{ICP} wt.% ± 0.1	m_{Pt} $g_{\mathrm{Pt}}\ g_{\mathrm{C}}^{-1}$ ± 0.001	d_{TEM} nm	σ nm	d_{s} nm	d_{v} nm	d_{XRD} nm ± 0.5
Pt-1/CX	8.4	0.087	2.3	0.7	2.7	2.9	2.6
Pt-2/CX	14.7	0.090	2.2	0.7	2.7	3.0	2.3
Pt-3/CX	19.0	0.058	2.1	0.6	2.5	2.7	2.5
Pt-4/CX	22.2	0.048	2.2	0.7	2.6	2.8	2.4
Pt-5/CX	25.3	0.051	2.1	0.7	2.6	2.8	2.6

Pt_{ICP}: Pt weight percentage of the catalyst measured by ICP-AES; m_{Pt}: mass of Pt deposited at each impregnation step per mass of C in the catalysts; d_{TEM}: average diameter of particles estimated from TEM micrographs; σ: standard deviation associated with d_{TEM}; d_{s}: surface-weighed average diameter of particles estimated from TEM micrographs and calculated by Equation (1.4); d_{v}: volume-weighed average diameter of particles estimated from TEM micrographs and calculated by Equation (1.5); d_{XRD}: average crystallite size calculated from X-ray diffraction peaks *via* Equation (1.6).

five catalysts is 5.5 nm and no significant difference is observed between the five samples. The average diameter of the Pt particles, d_{TEM}, is between 2.1 (Pt-3/CX and Pt-5/CX) and 2.3 nm (Pt-1/CX) with a standard deviation of 0.6 (Pt-3/CX) or 0.7 nm (Pt-1/CX, Pt-2/CX, Pt-4/CX, and Pt-5/CX). The surface-weighed average diameter of particles, d_{s}, and the volume-weighed average diameter of particles, d_{v}:

$$d_{\mathrm{s}} = \Sigma \frac{n_{\mathrm{i}} d_{\mathrm{i}}^3}{n_{\mathrm{i}} d_{\mathrm{i}}^2} \tag{1.4}$$

$$d_{\mathrm{v}} = \Sigma \frac{n_{\mathrm{i}} d_{\mathrm{i}}^4}{n_{\mathrm{i}} d_{\mathrm{i}}^3} \tag{1.5}$$

where n_{i} is the number of particles with diameter d_{i} [25]. Since the Pt weight percentage increases and the particle size distribution does not change, one can conclude that the increase in Pt loading is only due to the increase in particle number and not due to the growth or the agglomeration of Pt particles.

High dispersion is also shown by the X-ray diffractograms (Figure 1.4): no narrow peak is visible. Moreover, an average crystallite diameter, d_{XRD}, can be calculated by Scherrer's equation [25]:

$$d_{\mathrm{XRD}} = \frac{k\lambda}{\beta cos\theta} \tag{1.6}$$

where k is a dimensionless shape factor and equals 0.89 in the case of spherical nanoparticles, λ is the X-ray wavelength ($Cu_{K\alpha}$: 1.5456 nm), β is the full width at

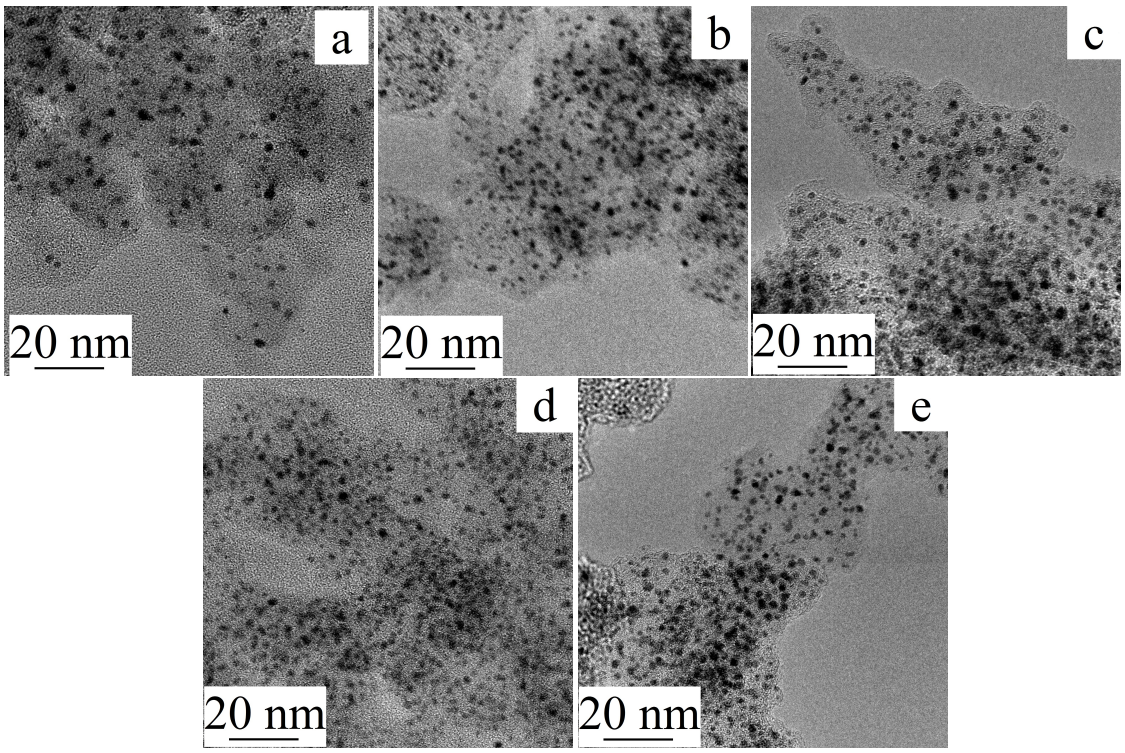

Figure 1.2: TEM micrographs of the catalysts: Pt-1/CX (a), Pt-2/CX (b), Pt-3/CX (c) Pt-4/CX (d), and Pt-5/CX (e).

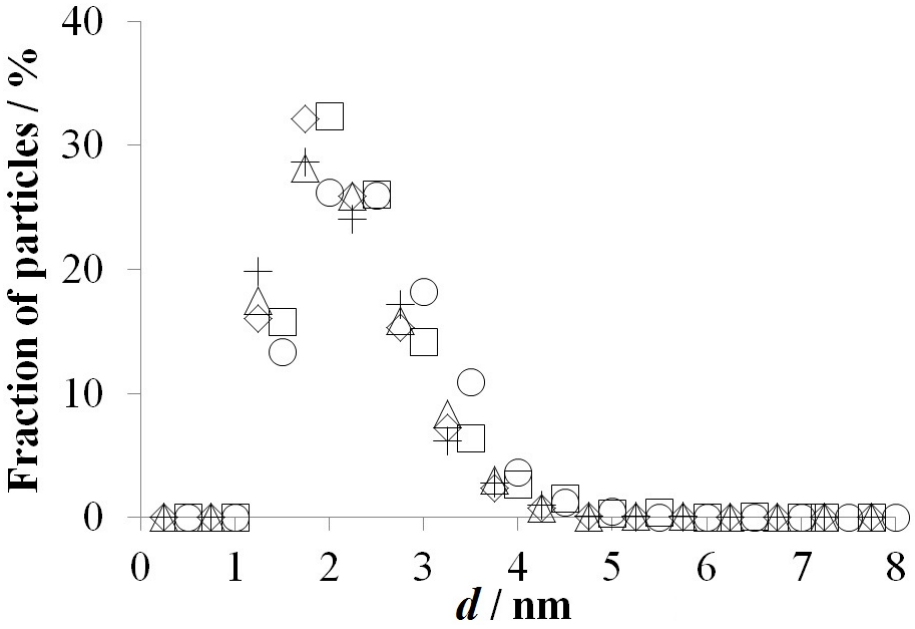

Figure 1.3: Pt particle size distribution for the five catalysts: Pt-1/CX (◯), Pt-2/CX (□), Pt-3/CX (◊), Pt-4/CX (△), and Pt-5/CX (+).

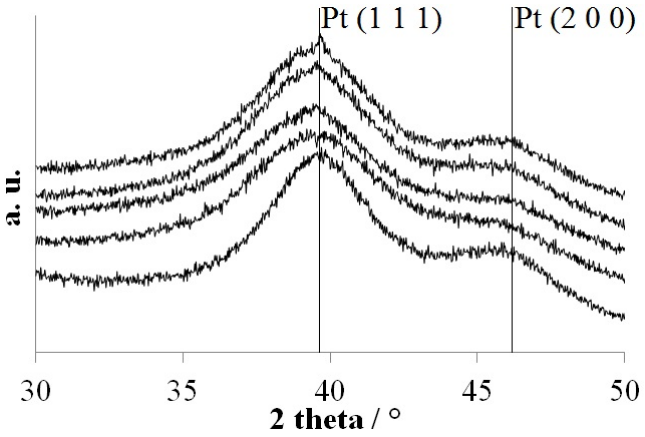

Figure 1.4: X-ray diffractograms of the five catalysts. The diffractograms are shifted vertically for better legibility. The diffraction angles of Pt are indicated by the two vertical lines.

half the maximum intensity (FWHM), and θ is the Bragg angle. The values of the average crystallite size, d_{XRD}, range from 2.3 (Pt-2/CX) to 2.6 nm (Pt-1/CX and Pt-5/CX). These crystallite sizes are similar to those of the particle sizes measured from TEM, which allows concluding that the nanoparticles are monocrystalline. As XRD is sensitive to the volume of particles, d_{XRD} corresponds to an average volume diameter and must be compared to the volume weighed average diameter, d_{v}. The values of d_{v} range from 2.7 (Pt-3/CX) to 3.0 nm (Pt-2/CX), in agreement with those of d_{XRD}.

1.3.2 Electrochemical Characterization

The Pt electroactive specific surface area, S_{CO}, and the CO equivalent diameter of Pt particles, d_{CO}, were calculated from the area under the $\mathrm{CO_{ad}}$ oxidation peak detected on the CO stripping curves (Figure 1.5). In this figure, one can see that the five curves exhibit a broad peak between 0.8 and 1.1 V *vs.* NHE, resulting from the oxidation of CO molecules on Pt nanoparticles with diameter smaller than 3.3 nm [20]. The numerical results gathered in Table 1.2 show that S_{CO} is almost constant (92-96 $\mathrm{m^2\ g_{Pt}{}^{-1}}$). The CO equivalent diameter, d_{CO}, is obtained by the following equation [26]:

$$d_{CO} = \frac{6 \times 10^{-3}}{\rho_{\mathrm{Pt}}\ S_{CO}} \tag{1.7}$$

where ρ_{Pt} is the Pt density (21.4×10^3 kg $\mathrm{m^{-3}}$) [20–22]. This diameter is almost constant (2.9-3.0 nm). Since CO stripping is sensitive to the surface of the nanoparticles, d_{CO} corresponds to a surface weighed average diameter and must be compared to d_{s}. d_{s} ranges between 2.5 and 2.7 nm (Table 1.1). d_{CO} and d_{s} are in the same range of value even though d_{CO} is slightly higher.

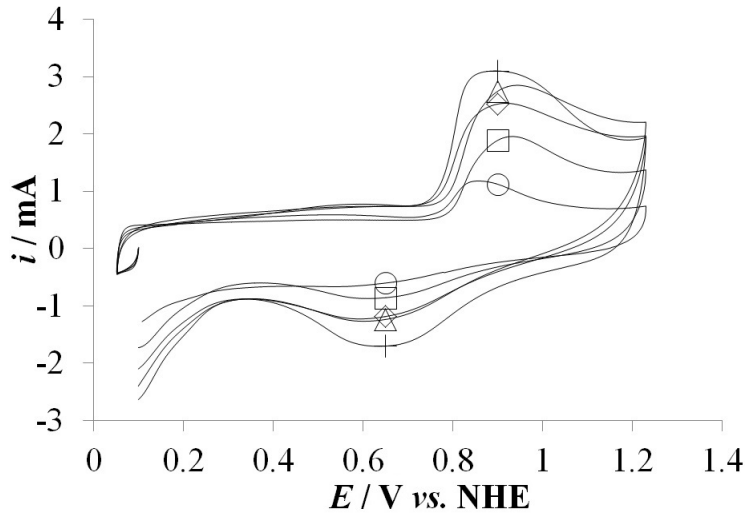

Figure 1.5: CO electrooxidation curves of the five catalysts in 1 M H_2SO_4 at a sweep rate of 20 mV s^{-1}: Pt-1/CX (◯), Pt-2/CX (□), Pt-3/CX (◊), Pt-4/CX (△), and Pt-5/CX (+).

Table 1.2: Catalysts properties determined by electrochemical analyses.

Catalyst	**CO stripping**		**ORR**		
	S_{CO} $m^2\ g_{Pt}{}^{-1}$ ± 10%[a]	d_{CO} nm ± 10%[a]	SA_{85} A $m_{Pt}{}^{-2}$ ± 10%[a]	SA_{90} A $m_{Pt}{}^{-2}$ ± 10%[a]	b mV dec^{-1} ± 10%[a]
Pt-1/CX	92	3.0	0.52	0.114	-69
Pt-2/CX	93	3.0	0.44	0.093	-72
Pt-3/CX	94	2.9	0.49	0.102	-79
Pt-4/CX	96	2.9	0.47	0.093	-78
Pt-5/CX	96	2.9	0.60	0.105	-72

S_{CO}: electroactive specific surface area of Pt particles calculated from CO stripping measurements normalized by the mass of Pt on the electrode; d_{CO}: CO equivalent diameter of the particles calculated by Equatio (1.7); SA_{85}: specific activity for the ORR measured at 0.85 V *vs.* NHE; SA_{90}: specific activity for the ORR measured at 0.90 V *vs.* NHE; b: Tafel slope calculated from the ORR measurements.
Notes: [a] The error (± 10%) is the usual standard deviation of electrochemical measurements.

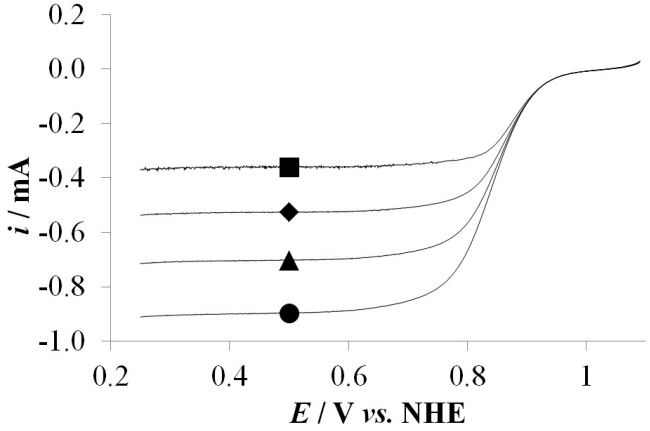

Figure 1.6: ORR curves of sample Pt-2/CX measured at a rotating speed of the electrode of: 400 rpm (■), 900 rpm (♦), 1600 rpm (▲), and 2500 rpm (●).

Figure 1.6 shows typical linear sweep voltammograms (*i.e.* the measured reduction current as a function of the potential applied at the working electrode repeated at different revolution rates) recorded on sample Pt-2/CX. In this figure, three regions can be detected. First, at potential higher than 0.9 V *vs.* NHE, the curves are superimposed. This means that the ORR is under pure kinetic control. Second, at low potential, the ORR current is limited by the mass transport (in the RDE setup, this occurs by diffusion-convection) of the O_2 molecules in solution. Third, between these two regions, the ORR is under a mixed kinetic and mass-transport control. After correction from the oxygen mass transport in the solution (Equation (1.2)), the Tafel slopes and the specific activity (SA) measured at $E = 0.90$ or 0.85 V *vs.* NHE were used to compare the ORR activity of the different samples. The SA_{85} values range from 0.44 (Pt-2/CX) to 0.60 A ${m_{Pt}}^{-2}$ (Pt-5/CX) and the SA_{90} values range from 0.093 (Pt-2/CX and Pt-4/CX) to 0.114 A ${m_{Pt}}^{-2}$ (Pt-1/CX, Table 1.2). Figure 1.7 shows the corresponding Tafel plots of the catalysts, *i.e.* the potential as a function of the logarithm of the specific activity. The slope of these curves, *i.e.* the Tafel slope, b, ranges from -69 (Pt-1/CX) to -79 mV dec^{-1} (Pt-3/CX, Table 1.2).

1.4 Discussion

The multiple SEA method leads to the synthesis of well dispersed Pt/CX catalysts with high Pt weight percentage. The latter can be adjusted *via* the number of 'impregnation-drying-reduction' cycles, and reaches 25 wt.% after five cycles (Table 1.1). However, the quantity of Pt deposited on the CX after each 'impregnation-drying-reduction' cycle, m_{Pt}, decreases after two cycles (Table 1.1). This might be due to the successive impregnations in the acidic solution, the pH of which equals 2.4-2.5, and to the successive reduction steps. Indeed, both procedures probably modify the surface chemistry of the CX, which would certainly lead to a shift of the optimal adsorption pH, the latter depending strongly on the surface chemistry of

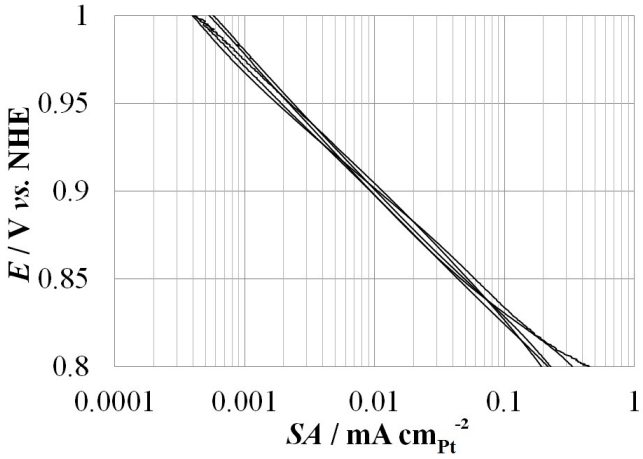

Figure 1.7: Tafel plots of the five catalysts. The plots are not labeled because of their superimposition.

the support. This pH shift would induce a decrease in the amount of Pt deposited during the next cycles. The effect of multiple 'impregnation-drying-reduction' cycles on the carbon surface chemistry should be studied in order to shed light on the phenomenon and prove this hypothesis.

Image analysis performed on TEM micrographs indicates that the five catalysts display nearly identical average Pt particle size distribution. This is corroborated by the comparison between TEM, XRD and CO stripping results. Indeed, on the one hand, the average diameter calculated from XRD, d_{XRD}, is similar to the average volume diameter, d_{v}. In fact, the values of d_{XRD} and d_{v} suffer from imprecisions due to the high width of the XRD peak in the former case (Figure 1.4) and due to the presence of some small nanoparticles (particles with a diameter lower than or equal to 1 nm), which are not distinguishable from the background by image analysis in the latter case. These errors can explain the differences between the values of d_{XRD} and d_{v} and allow concluding that d_{XRD} and d_{v} are equivalent. On the other hand, the average surface diameter, d_{s}, is almost the same to the CO equivalent diameter, d_{CO}. Moreover, in the XRD diffractograms (Figure 1.4), no narrow peak is visible, which confirms the absence of large Pt particles. Finally, CO stripping confirms that the particle size is below 3 nm (Figure 1.5): no pre-peak, characteristic of Pt particles larger than 3 nm [20–22], appears at a potential lower than the broad CO electrooxidation peak occurring at *ca.* 0.8 V, except maybe for Pt-5/CX, where a shoulder is observed at a potential lower than that of the main peak (for more details about the particle size analysis performed by CO striping, see Appendix A1.2 at the end of this thesis). These pre-peaks may be due to larger Pt particles present in the catalysts but not detected in the TEM micrographs due to sampling.

In the CO stripping curves (Figure 1.5), as no H desorption (oxidation) peak is visible at low potential, the Pt surface is supposed to be fully covered by CO. The values of the electroactive specific surface of the Pt particles calculated from CO stripping, S_{CO}, are the same for all the catalysts (92-96 $\mathrm{m^2\ g_{Pt}{}^{-1}}$).

Concerning the specific activity of the catalysts and the ORR mechanism, information is derived from the Tafel plots (Figure 1.7). The Tafel slope, b, is related to the reaction mechanism occurring on the catalyst. Two types of mechanisms may occur: (i) a four-electron per oxygen molecule mechanism, which occurs on Pt nanoparticles, with a Tafel slope of *ca.* -70 mV dec^{-1} [18] and (ii) a two-electron per oxygen molecule mechanism, which occurs on carbon, with a Tafel slope of *ca.* -120 mV dec^{-1}. The latter mechanism yields undesirable hydrogen peroxide instead of water [26]. The Tafel slope of the five catalysts ranges from -69 (Pt-1/CX) to -79 mV dec^{-1} (Pt-3/CX), as expected from theory for a four-electron mechanism.

The specific activity of the catalysts for the ORR is derived from the value of the Tafel plots and intercept (Figure 1.7). The Tafel plots are superimposed; as a result, the values of the specific activity are almost constant at a given potential, *i.e.* *ca.* 0.5 A ${m_{Pt}}^{-2}$ at 0.85 V *vs.* NHE and *ca.* 0.1 A ${m_{Pt}}^{-2}$ at 0.9 V *vs.* NHE (Table 1.2). This clearly indicates that, in the five catalysts, the Pt weight percentage has no impact on the intrinsic specific catalytic performance of the metal nanoparticles, which demonstrates that the number of Pt deposition sequences using the multiple SEA method does not promote detrimental Pt nanoparticle shape/size change from one sequence to the other.

1.5 Conclusion

The multiple SEA method allows obtaining well-dispersed Pt/CX catalysts with high weight percentage up to 25 wt.%, and particle size close to *ca.* 2.5 nm according to TEM, XRD, and CO stripping measurements. Although the highest Pt weight percentage obtained in this chapter is 25 wt.%, additional studies could be performed to determine the maximum weight percentage that can be achieved without alteration of the metal dispersion.

Moreover, the multiple SEA method requires the use of less Pt than the SEA method from which it is inspired. In fact, for the synthesis of a 25 wt.% Pt/CX, the two methods require five 'impregnation-drying-reduction' cycles. But, for the SEA method, five solutions of 1 g_{Pt} L^{-1} are used instead of one solution of 1.75 g_{Pt} L^{-1}, the latter being reused in the case of multiple SEA. This difference leads to a nearly threefold decrease in the consumption of Pt when using the multiple SEA technique.

Despite this Pt consumption decrease, using the multiple SEA method still not allows avoiding completely Pt losses. Moreover, this method requires a long time to synthesize Pt/CX catalysts with high Pt loading. This is why the next chapter focuses on the streamlining of the synthesis process of highly loaded Pt/CX catalysts with the aim to decrease as low as possible the Pt losses and the time needed to obtain Pt/CX catalysts with high Pt loading. To do so, the physico- and electrochemical properties of Pt/CX catalysts, synthesized by the multiple SEA technique, is compared to catalysts prepared from more rational synthesis processes and also to a commercial Pt/HSAC catalyst, in order to establish which synthesis method produces the best catalysts for the ORR in the most rational way.

References

[1] H. A. Gasteiger, S. S. Kocha, B. Sompalli, and F. T. Wagner, *Applied Catalysis B: Environmental* **56**, 9 (2005).

[2] F. Rodríguez-Reinoso, Porosity in Carbons: Characterization and Applications, in *Porosity in Carbons*, edited by J. W. Patrick, p. 253, John Wiley & Sons, Ltd., Chichester, United Kingdom, 1995.

[3] N. Job, B. Heinrichs, F. Ferauche, F. Noville, J. Marien, and J.-P. Pirard, *Catalysis Today* **102-103**, 234 (2005).

[4] F. Maillard, S. Pronkin, and E. R. Savinova, Influence of size on the electrocatalytic activities of supported metal nanoparticles in fuel cells related reactions, in *Handbook of Fuel Cells*, edited by W. Vielstich, H. A. Gasteiger, and H. Yokokawa, volume 5, pp. 91–111, John Wiley & Sons, Ltd, Chichester, United Kingdom, 2009.

[5] S. Mukerjee and J. McBreen, *Journal of Electroanalytical Chemistry* **448**, 163 (1998).

[6] K. Kinoshita, *Journal of the Electrochemical Society* **137**, 845 (1990).

[7] O. Antoine, Y. Bultel, and R. Durand, *Journal of Electroanalytical Chemistry* **499**, 85 (2001).

[8] J. R. Regalbuto, *Catalyst Preparation: Science and Engineering*, CRC Press/Taylor & Francis Group, Boca Raton, United States of America, 2006.

[9] N. Job, S. D. Lambert, M. Chatenet, C. J. Gommes, F. Maillard, S. Berthon-Fabry, J. R. Regalbuto, and J.-P. Pirard, *Catalysis Today* **150**, 119 (2010).

[10] S. D. Lambert, N. Job, L. D'Souza, M. Pereira, R. Pirard, B. Heinrichs, J. Figueiredo, J.-P. Pirard, and J. Regalbuto, *Journal of Catalysis* **261**, 23 (2009).

[11] J. Regalbuto, A. Navada, S. Shadid, M. Bricker, and Q. Chen, *Journal of Catalysis* **184**, 335 (1999).

[12] N. Job, R. Pirard, J. Marien, and J.-P. Pirard, *Carbon* **42**, 619 (2004).

[13] A. J. Lecloux, Texture of catalysts, in *Catalysts: Science and Technology*, edited by J. R. Anderson and M. Boudart, pp. 171–230, Springer-Verlag, Berlin, Germany, 1981.

[14] C. Alié, S. D. Lambert, B. Heinrichs, and J.-P. Pirard, *Journal of Sol-Gel Science and Technology* **26**, 827 (2003).

[15] N. Job, R. Pirard, J.-P. Pirard, and C. Alié, *Particle & Particle Systems Characterization* **23**, 72 (2006).

[16] E. W. Washburn, *Proceedings of the National Academy of Sciences of the United States of America* **7**, 115 (1921).

[17] N. Job, A. Théry, R. Pirard, J. Marien, L. Kocon, J.-N. Rouzaud, F. Béguin, and J.-P. Pirard, *Carbon* **43**, 2481 (2005).

[18] E. Guilminot, A. Corcella, M. Chatenet, and F. Maillard, *Journal of Electroanalytical Chemistry* **599**, 111 (2007).

[19] M. Chatenet, L. Dubau, N. Job, and F. Maillard, *Catalysis Today* **156**, 76 (2010).

[20] F. Maillard, M. Eikerling, O. V. Cherstiouk, S. Schreier, E. Savinova, and U. Stimming, *Faraday Discussions* **125**, 357 (2004).

[21] F. Maillard, S. Schreier, M. Hanzlik, E. R. Savinova, S. Weinkauf, and U. Stimming, *Physical Chemistry Chemical Physics* **7**, 385 (2005).

[22] F. Maillard, E. R. Savinova, and U. Stimming, *Journal of Electroanalytical Chemistry* **599**, 221 (2007).

[23] S. Trasatti and O. Petrii, *Journal of Electroanalytical Chemistry* **327**, 353 (1992).

[24] A. J. Bard and L. R. Faulkner, *Electrochemical Methods: Fundamentals and applications*, John Wiley & Sons, Inc., Weinheim, Germany, 2nd edition, 2001.

[25] G. Bergeret and P. Gallezot, Particle size and dispersion measurement, in *Handbook of Heterogeneous Catalysis*, edited by G. Ertl, H. Knözinger, and J. Weitkamp, p. 439, Wiley-VCH, Weinheim, Germany, 1997.

[26] J. Marie, S. Berthon-Fabry, P. Achard, M. Chatenet, A. Pradourat, and E. Chainet, *Journal of Non-Crystalline Solids* **350**, 88 (2004).

Chapter 2

Streamlining of the synthesis process of Pt/carbon xerogel electrocatalysts with high Pt loading for proton exchange membrane fuel cells (PEMFCs)

The second chapter of this thesis is focused on a further improvement of the Pt deposition on carbon xerogel process. The multiple strong electrostatic adsorption method developed in the previous chapter was streamlined in order to (i) avoid any Pt losses and (ii) speed up the synthesis process, while synthesizing Pt/carbon xerogel catalysts with high Pt loading. Multiple step methods (strong electrostatic adsorption, charge enhanced dry impregnation, and sodium borohydride reduction) and one-step methods (one-step sodium borohydride reduction, formic acid reduction, and Pt colloid) were then performed. The performance of the obtained catalysts were compared in a three electrode cell configuration with liquid electrolyte. Some of these results are published in *Catalysts* **5**, 40 (2015). The chapter in its entirety is under review in *Applied Catalysis B: Environmental*.

2.1 Introduction

Proton exchange membrane fuel cells (PEMFCs) are promising and eco-friendly power generators. However, they are not widely commercialized yet. This is especially because of the high cost of the device, which is partly due to one of its major component: the catalytic layer. Indeed, the catalysts used in the catalytic layer are commonly Pt or Pt-based nanoparticles supported on high surface area carbon (Pt/HSAC) [1]. These catalysts usually display high Pt loading, which increases the fuel cell price as Pt is an expensive metal with supply limitations [2, 3]. One of the fuel cell researchers' main objective is therefore to decrease the Pt loading of the catalysts while keeping high performances.

To do so, the increase of the Pt dispersion on the support was studied in order to increase the number of active sites available for reaction, *i.e.* the number of Pt atoms at the surface of the particles. The number of active sites increases when the Pt particle size decreases, *i.e.* when the Pt specific surface area increases. Indeed, the smaller the Pt particle size, the higher the Pt specific surface area. However, too small Pt nanoparticles lead to a decrease in activity of the surface Pt atoms for most of the reactions performed in PEMFCs, such as the oxygen reduction reaction (ORR). Indeed, these reactions are structure-sensitive [4]. So, the specific activity (*i.e.* current per surface unit of Pt) for the ORR increases with the particle size (up to several tens of nm). Therefore, the optimal Pt nanoparticles size, resulting in best mass activity (*i.e.* current per mass unit of Pt) is around 3-4 nm [5, 6].

Over the years, many Pt nanoparticles syntheses have been developed. Among them, the strong electrostatic adsorption (SEA) method [7–11] was developed especially on nanostructured carbon such as carbon xerogels (CXs). The main interest of such supports lies in their better electrode architecture control and enhanced mass-transport properties [8–11]. The SEA technique consists in maximizing the electrostatic interactions between the metal precursor and the support by adjusting the pH of the carbon/water/Pt precursor slurry to the adequate value. This value depends on the surface chemistry of the support and on the nature of the Pt precursor. Due to the presence of various oxygenated surface groups, the carbon support protonates/deprotonates at low/high pH value. This enhances the adsorption of anions/cations, respectively. For example, in a previous study, Lambert *et al.* [9] demonstrated that, for the impregnation of CXs by hexachloroplatinic acid (CPA, H_2PtCl_6) aqueous solutions (1000 ppm_{Pt}), the highest Pt uptake occurs at a final pH around 2.5, which yields a Pt loading *ca.* 8-10 wt.%. In order to achieve high Pt mass fraction without sacrificing the dispersion, the SEA procedure can be performed several times consecutively with fresh Pt precursor solution [10] or with the same (recycled) Pt precursor solution [11].

However, the size of the Pt particles synthesized by the SEA technique is *ca.* 2 nm [11], which is below the optimal value for PEMFC catalysts [5,6]. Another drawback of this method is the complexity of the procedure to obtain catalysts with high Pt loading. Indeed, in order to synthesize highly loaded Pt/CX catalysts ($>$ 20 wt.%), the CX undergoes several synthesis steps, *i.e.* adsorption of Pt ions, filtration,

drying, and reduction under hydrogen, which must be repeated several times since one single cycle leads to 8 wt.% in Pt. All these steps are time-consuming. As an example, three days at least are required to synthesize 20 wt.% Pt/CX catalysts *via* SEA (1 day for each impregnation-reduction cycle). This implies that some adaptations/modifications must be performed on the synthesis procedure in order to obtain easy-to-make Pt/CX catalysts with high performances.

The purpose of the first synthesis modification performed in our previous studies so far was to avoid Pt loss. To do so, the charge enhanced dry impregnation (CEDI) method was used [12]. It combines the advantages of (i) the SEA method, as the pH of the Pt precursor solution is fixed at an optimal value in order to maximize the interactions between the metallic ions and the support, which leads to a high metal dispersion, and (ii) the dry impregnation (DI) method, as the volume of the precursor solution strictly corresponds to that necessary to fill the pores of the support. This strategy avoids Pt loss during the synthesis. Cao *et al.* [12] synthesized Pt/CX catalysts with 10 wt.% Pt loading in one impregnation-reduction cycle with CPA as precursor.

Another modification of the synthesis was investigated in previous works: one-step deposition methods. These allow to deposit large Pt quantity on CX in one single impregnation-reduction step. One-step syntheses lead to highly loaded Pt/CX catalysts synthesized within a few hours, whatever the final loading.

One of these one-step syntheses, developed by Alegre *et al.* [13], uses sodium borohydride (SB) as a reductant. It consists in the impregnation of the CX support, followed by reduction with SB, in liquid phase. 20 wt.% Pt on CX catalyst was prepared by this technique [13].

Another one-step synthesis, also developed by Alegre *et al.* [13], uses formic acid (FA, HCOOH) as reductant, in liquid phase. The aim of the FA reduction is to control the reduction speed which is not possible with SB reduction. Indeed, SB-reduced catalysts usually display large Pt particle size distribution (PSD) due to the high reduction speed induced by SB [13, 14]. In the above-mentioned study, Alegre *et al.* synthesized 20 wt.% Pt on CX catalyst *via* FA reduction.

Another one-step method, the synthesis of Pt/C catalysts using a Pt colloid, was developed by Pasqualeti *et al.* [15]. The method consists in the synthesis of a Pt colloid suspension followed by the addition of a carbon support onto which adsorption of the Pt particles occurs. The aim of the colloid synthesis is to control the Pt particle size while reducing Pt ions with SB, by using tri-sodium citrate (tSC, $Na_3C_6H_5O_7$) as a surfactant. Pasqualeti *et al.* synthesized 20 wt.% Pt on carbon black (Vulcan XC-72R) catalysts [15].

All these syntheses were reproduced for this chapter. Some of them were modified in order to change the loading: (i) the CEDI method was repeated up to four times to increase the Pt loading of the catalysts; (ii) the FA reduction synthesis and the colloid synthesis were modified in order to produce 10, 30, and 40 wt.% Pt/CX catalysts in addition to the 20 wt.% Pt/CX catalyst.

Finally, another method based on SEA was performed. Contrary to SEA and CEDI synthesis (the other two method based on SEA), in which reduction step was performed under gaseous hydrogen, this method uses SB reduction in liquid phase. The purpose of this liquid-phase reduction is to fasten the synthesis of highly loaded Pt/CX catalysts obtained by multiple impregnation-reduction methods. These SB-reduced catalysts were compared to SB-reduced catalysts synthesized *via* the one-step synthesis in order to study the differences between one-step deposition and multiple impregnation-reduction steps methods.

This chapter focuses on these syntheses with the aim of simplifying at best the synthesis process while optimizing the catalyst performances.

2.2 Experimental

2.2.1 Reagents

The solid reagents used in this chapter were resorcinol $C_6H_6O_2$ (Merck, for synthesis), sodium carbonate Na_2CO_3 (Acros Organics, 99.5% extrapure, anhydrous), dihydrogen hexachloroplatinate (IV) hexahydrate $H_2PtCl_6{\cdot}6H_2O$ (Alfa Aesar, 99.9% metal basis, crystalline), sodium hydroxide NaOH (Acros Organics, extrapure, pellets), sodium borohydride $NaBH_4$ (Merck, fine granular for synthesis), and trisodium citrate dihydrate $Na_3C_6H_5O_7 \cdot 2H_2O$ (Merck, EMSURE® for analysis).

The liquid reagents used in this chapter were formaldehyde solution CH_2O (Sigma Aldrich, ACS reagent 37 wt.% in water, contains 10-15% methanol as stabilizer), hydrochloric acid HCl (Acros Organics, for analysis min. 35 wt.% solution in water), nitric acid HNO_3 (Merck, 65% for analysis), ultrapure water H_2O (18 MΩ cm), formic acid HCOOH, (Merck, 99% for synthesis), sulfuric acid H_2SO_4 (Merck, 96 wt.% Suprapur® for electrochemical measurements or Merck, 98% EMSURE®, for analysis for cleaning solution), hydrogen peroxide H_2O_2 (Merck, 30% Perhydrol®, EMSURE®, stabilized for higher storage temperature, for analysis), and Liquion™ solution (Ion Power, LQ-1105, 1100EW, 5 wt.%).

The gaseous reagents used in this chapter were nitrogen N_2 (Air Liquide, α1), hydrogen H_2 (Air Liquide, α1), carbon monoxide CO (Air Liquide, N47), argon Ar (Air Liquide, α1), and oxygen O_2 (Air Liquide, α1).

2.2.2 Syntheses

Carbon xerogel support CX used in this thesis was prepared by drying and pyrolysis of a resorcinol-formaldehyde gel [16]. This synthesis is described elsewhere [11]. Briefly, the gel was obtained by polycondensation of resorcinol with formaldehyde in water. The resorcinol/formaldehyde molar ratio, *R/F*, was set at 0.5, the resorcinol/sodium carbonate molar ratio, *R/C*, was chosen equal to 1000 and the dilution ratio, *D*, *i.e.* the solvent/(resorcinol and formaldehyde) molar ratio,

was fixed at 5.7. These values led to a CX with a meso-macropore size distribution centered at 80 nm and a BET specific surface area of 567 m^2 $g_{Pt}{}^{-1}$. After gelling and aging in an oven at 358 K, the obtained gel was dried under vacuum at 423 K, then ground with a planetary mill (PULVERISETTE 6, classical line, Fritsch) at 400 rpm during 70 min in order to obtain particles with a diameter of a few micrometers according to a procedure developed in another work [17]. After grinding, the gel was pyrolyzed at 1073 K under nitrogen flow. The resulting CX particles exhibit a mean size of 7 µm.

Strong electrostatic adsorption (SEA) The SEA method [8] was already studied and applied on CX [9–11]. The synthesis procedure is as follows [11]: (i) the pH of 0.567 L of 1.75 g_{Pt} L^{-1} hexachloroplatinic acid (CPA, $H_2PtCl_6 \cdot 6H_2O$) aqueous solution (8.97 mmol L^{-1}) was adjusted to 2.5 with 0.5 mol L^{-1} HCl and NaOH solutions; (ii) 1 g of CX was added to the solution, *i.e.* the amount of CX corresponding to a surface loading of 1000 m^2 L^{-1}; (iii) the suspension was stirred for 1 h; (iv) filtered; (v) dried at 393 K in an oven under air overnight; (vi) reduced under 0.04 mmol s^{-1} H_2 flow at 473 K for 1 h. In order to synthesize several catalysts with various Pt loadings, the Pt deposition was repeated from one to five times on the same support with the same impregnation solution, the pH of which is readjusted to the optimal value at each impregnation [11]. After the last impregnation, each catalyst underwent its last reduction step at 723 K during 5 h in order to remove the chlorine anions bound to the Pt particles. Indeed, high reduction temperature is necessary to completely clean the Pt particle surface from residual chlorine anions [18].

Charge enhanced dry impregnation (CEDI) The CEDI procedure is the following [12]: (i) 0.23 g of CPA were dissolved in 3 mL of deionized water; (ii) the initial pH was fixed at 1.8 with HNO_3; (iii) the precursor solution was added to 1 g of CX by 50 µL steps; (iv) the obtained paste was softly, manually stirred to homogenize it at best; (v) the mixture was dried at room temperature during 48 h; (vi) the sample was reduced under 0.04 mmol s^{-1} H_2 flow at 523 K for 1 h. As the CEDI method yields 10 wt.% Pt/CX catalysts, this procedure was repeated from one to four times in order to increase the amount of Pt deposited on the support. After their last impregnation, half of each catalyst was reduced as before (523 K for 1 h) but the other half underwent the last reduction step at 723 K during 5 h in order to study the effect of the temperature reduction on the CEDI synthesis.

Sodium borohydride reduction (SB) The SB synthesis proceeds as follows: (i) 1 g of CX was mixed in 200 mL of CPA solution with high concentration (4.8 g_{Pt} L^{-1}); (ii) the pH of the suspension was fixed at 2.5 with 0.5 mol L^{-1} NaOH solution; (iii) the suspension was stirred during 30 min; (iv) filtered; (v) the impregnated support was then suspended in ultrapure water with pH fixed at the optimal value for impregnation with CPA, *i.e.* 2.5; (vi) 0.25 g of sodium borohy-

dride (SB) was added to the suspension in order to reduce the Pt ions into metallic Pt; (vii) after 5 min, the suspension was filtered; (viii) the catalyst was rinsed 5 times by 125 mL of ultrapure water, then (ix) dried in an oven under air at 333 K overnight. In order to reach higher Pt loading, the deposition was repeated up to eight times by recycling the CPA solution. In this chapter, only the catalysts which underwent 2, 4, 6, and 8 Pt depositions were studied. Half of each catalyst was characterized without any post-treatment while the other half underwent another reduction step under 0.04 mmol s^{-1} H_2 flow at 723 K for 5 h in order to clean the particles surface [18] and to compare with previous catalysts.

SB reduction synthesis was also performed *via* a one-step method in order to further fasten the synthesis procedure by removing the multiple impregnation-reduction steps. The one-step SB reduction procedure to synthesize 20 wt.% Pt catalyst is as follows: (i) 0.3 g of CX were dispersed in 200 mL of ultrapure water; (ii) 130 mL of 3 mmol L^{-1} CPA solution was added to the suspension; (iii) the pH of the mixture was fixed at 5.0 with 0.5 mol L^{-1} NaOH solution; (iv) 130 mL of 25 mmol L^{-1} SB solution was slowly added in order to reduce the Pt precursor into metallic Pt; (v) after 1 h stirring, the suspension was filtered; (vi) the catalyst was rinsed 5 times with 125 mL of ultrapure water; (vii) dried at 333 K in an oven under air overnight. This procedure differs from that of Alegre *et al.* [13] in the following 5 points: (i) as they were not explicitly mentioned, the mass and volume of reagents were chosen equal to 0.3 g of CX, 200 mL of ultrapure water, 130 mL of 3 mmol L^{-1} CPA aqueous solution, and 130 mL of 25 mmol L^{-1} SB aqueous solution; (ii) the addition of CPA into the suspension was not preformed under sonication; (iii) the temperature was not maintained at 291 K but performed at room temperature; (iv) a stirring step of 1 h was performed after the addition of SB, and (v) the washing step after the filtration, not detailed in [13], was performed as explained above. The differences are mainly due to the lack of information in the original article and to the simplification of the method.

Formic acid reduction The FA method allows to synthesize Pt/CX catalysts of various Pt loading in one single Pt deposition step. For the 20 wt.% Pt/CX catalyst, the synthesis procedure is as follows: (i) 0.3 g of CX were dispersed in 200 mL of 2 mol L^{-1} FA solution; (ii) the suspension was heated to 353 K in an oil bath; (iii) 100 mL of 4 mmol L^{-1} CPA solution was added by 10 mL steps; (iv) after 1 h stirring, the suspension was filtered; (v) the catalyst was then washed 5 times with 125 mL of ultrapure water, then (vi) dried at 333 K in an oven under air overnight. The differences between the procedure from Alegre *et al.* [13] and the procedure just described are the following: (i) as they were not explicitly mentioned, the mass and volume of reagents were chosen equal to 0.3 g of CX, 200 mL of 2 mol L^{-1} FA solution, 100 mL of 4 mmol L^{-1} CPA aqueous solution, and stepwise addition of 10 mL volumes; (ii) a stirring step of 1 h was added after the addition of the CPA solution, and (iii) the washing step after the filtration, not detailed in [13], was performed as explained above. Again, the differences are mainly due to the lack of information in the original article, which does not describe all steps in details.

Colloid synthesis The Pt colloid method allows to synthesize Pt/CX catalyst of various Pt loading in one single Pt deposition step. For the 20 wt.% Pt/CX catalyst, the synthesis procedure is as follows: (i) 50 mL of 14 mmol L^{-1} tri-sodium citrate (tSC) were added to 1.6 L of 0.2 mmol L^{-1} CPA solution; (ii) after 5 min stirring, 60 mL of ultrapure water containing 60 mg of SB and 200 mg of tSC were added to the solution; (iii) 90 min after the SB addition, 0.25 g of CX were added to the colloid suspension; (iv) after 48 h stirring, the suspension was filtered; (v) the catalyst was then rinsed 5 times with 150 mL of ultrapure water, then (vi) dried in an oven under air at 333 K overnight. This synthesis procedure differs from that of Pasqualeti *et al.* [15] in the following 6 points: (i) since the quantity of CPA was not mentioned in [15], it was chosen equal to 0.32 mmol; (ii) contrary to the procedure in Reference Reference [15], tSC was added after CPA; (iii) waiting steps after tSC addition (5 min) and SB addition (90 min) were added; (iv) the quantity of carbon to add was not mentioned, so it was chosen equal to 0.25 g: (v) the carbon suspension was not sonicated; (vi) the drying step was performed as described above instead of kiln-drying at 343 K for 24 h. These differences are mainly due to the replacement of carbon black (Vulcan XC-72R) by CX, to the missing information in the article, and to some simplifications of the method.

List of samples The samples are named following their synthesis method - SEA (strong electrostatic adsorption), CEDI (charge enhanced dry impregnation), SB (sodium borohydride reduction), FA (formic acid reduction), Col (tri-sodium citrate Pt colloid) - followed by, in the case of multiple impregnations method (SEA,CEDI, and SB), the number of impregnation steps they underwent after a slash (/) or, in the case of single deposition step method (SB, FA, and Col), the targeted Pt weight percentage after a hyphen (-). If the catalyst was reduced under H_2 flow at 723 K during 5 h after the synthesis, the suffix 723 is added after the method name. For example, SB/6 is the Pt/CX catalyst reduced by SB which underwent six impregnation-reduction cycles, SB723/6 is the sample reduced by SB which underwent six impregnation-reduction cycles and, after the synthesis, was reduced at 723 K under H_2 flow for 5 h. SB-20 is the sample reduced by SB which target Pt loading is equal to 20 wt.% (single impregnation). All the sample labels are listed in Table 2.1 for catalysts synthesized *via* multiple impregnation methods (SEA, CEDI, and SB) and in Table 2.2 for catalysts synthesized *via* one-step deposition methods (SB, FA, and Col). One commercial catalyst (Pt/HSAC Tanaka 37 wt.%, provided by Paxitech) is used as reference and labeled Ref.

2.2.3 Physicochemical characterization

The metal weight percentages of the catalysts were measured by inductively coupled plasma-atomic emission spectrometry (ICP-AES) using an ICAP 6500 THERMO device. The solutions for the analyses were prepared as follows: an aliquot of the catalyst sample was weighed and digested by 10 mL of H_2SO_4 and 5 mL of HNO_3. This solution was heated at 573 K until clear. After the complete dissolution of the

Table 2.1: List of samples synthesized *via* multiple impregnation methods.

Catalyst	**Synthesis method**	n_{impr}	$T_{\text{red,f}}$ K	$t_{\text{red,f}}$ h
SEA/1	SEA	1	723	5
SEA/2	SEA	2	723	5
SEA/3	SEA	3	723	5
SEA/4	SEA	4	723	5
SEA/5	SEA	5	723	5
CEDI/1	CEDI	1	523	1
CEDI/2	CEDI	2	523	1
CEDI/3	CEDI	3	523	1
CEDI/4	CEDI	4	523	1
CEDI723/1	CEDI	1	723	5
CEDI723/2	CEDI	2	723	5
CEDI723/3	CEDI	3	723	5
CEDI723/4	CEDI	4	723	5
SB/2	SB reduction	2	–[a]	–[a]
SB/4	SB reduction	4	–[a]	–[a]
SB/6	SB reduction	6	–[a]	–[a]
SB/8	SB reduction	8	–[a]	–[a]
SB723/2	SB reduction	2	723	5
SB723/4	SB reduction	4	723	5
SB723/6	SB reduction	6	723	5
SB723/8	SB reduction	8	723	5

$n_{\text{impr.}}$: number of impregnation-reduction cycles underwent by the catalyst; $T_{\text{red,f}}$: temperature of the final reduction step under H_2; $t_{\text{red,f}}$: duration of the final reduction step under H_2.
Notes: [a] Not reduced under H_2.

Table 2.2: List of samples synthesized *via* one-step deposition methods.

Catalyst	**Synthesis method**	Pt_{target} wt.%
SB-20	SB reduction	20
FA-10	FA reduction	10
FA-20	FA reduction	20
FA-30	FA reduction	30
FA-40	FA reduction	40
Col-10	tSC Pt colloid	10
Col-20	tSC Pt colloid	20
Col-30	tSC Pt colloid	30
Col-40	tSC Pt colloid	40

Pt_{target}: Pt loading targeted by the one-step deposition synthesis.

CX support and evaporation of the solution, 3 mL of HCl and 1 mL of HNO_3 were added. The obtained solution was heated a few minutes at 393 K and transferred into a 50 mL calibrated flask, which was finally filled by deionized water.

The particles were observed by transmission electron microscopy (TEM) with a Jeol 2010 transmission electron microscope (200 kV, LaB_6 filament). An aliquot of the catalyst sample was suspended in 20 mL of ethanol. After 15 min of sonication in an ultrasonic bath, a drop of the suspension was deposited on a polymer-covered copper grid.

Image analysis was applied to the TEM micrographs (on 200 particles at least) in order to calculate the average diameter of particles, d_{TEM}, the standard deviation, σ, the surface-weighed average diameter of particles, d_{s}, and the volume-weighed average diameter of particles, d_{v}:

$$d_{\text{s}} = \frac{\Sigma n_{\text{i}} d_{\text{i}}^3}{\Sigma n_{\text{i}} d_{\text{i}}^2} \tag{2.1}$$

$$d_{\text{v}} = \frac{\Sigma n_{\text{i}} d_{\text{i}}^4}{\Sigma n_{\text{i}} d_{\text{i}}^3} \tag{2.2}$$

where n_{i} is the number of particles with diameter d_{i} [19]. d_{s} and d_{v} can be compared to the CO equivalent particle diameter obtained from CO stripping, d_{CO}, and to the average crystallite size obtained from X-ray diffraction (XRD), d_{XRD}, respectively (see below). Indeed, CO stripping (see section 2.2.4) is a surface-sensitive technique, as it is a surface measurement method, while XRD is a volume-sensitive technique as large crystallites impact more XRD diffractograms.

The catalysts powders were analyzed by X-Ray Diffraction with a Siemens D5000 goniometer using the $Cu_{K\alpha}$ line (Ni filter). Average crystallites sizes, d_{XRD}, were calculated from the diffraction peak width by Scherrer's equation [19]:

$$d_{XRD} = \frac{k\lambda}{\beta cos\theta} \tag{2.3}$$

where k is a dimensionless shape factor and equals 0.89 in the case of spherical Pt nanoparticles, λ is the X-ray wavelength ($Cu_{K\alpha}$: 1.5456 nm), β is the full width at half the maximum intensity (FWHM), and θ is the Bragg angle. Obviously, the smaller and broader the diffraction peaks, the more imprecise the measurements of FHWM and the calculations of d_{XRD}. As XRD is a volume-sensitive analysis, d_{XRD} corresponds to an average volume diameter of particles (if they are monocrystalline) and can be compared to d_v [19].

2.2.4 Electrochemical characterization

Material All the glassware was cleaned by immersion in a H_2SO_4:H_2O_2 solution overnight and thoroughly rinsed with ultrapure water (18 MΩ cm). The electrolytic solutions were prepared from ultrapure water and H_2SO_4 (98% Suprapur, Merck).

Catalytic layer preparation To measure the electrochemical properties of the catalysts, inks were first prepared. The ink composition was chosen to keep the amount of carbon constant, regardless of the metal loading [20,21]. For each sample, the amount of catalyst containing 19.8 mg of CX was crushed in a mortar then mixed with 755 mg of ultrapure water and 466 mg of 5 wt.% Nafion® solution. In order to blend it homogeneously, the mixture was then processed in an ultrasonic bath for 15 min. Once the ink was homogeneous, 10 µL of ink were deposited on a glassy carbon (GC) disk (5 mm in diameter) and sintered at 343 K during 20 min to evaporate the solvents and stick the catalyst onto the GC disk. The catalytic layer deposited on the GC disk composes the working electrode for all electrochemical measurements. In the case of CX-supported catalysts, this procedure yields active layers of identical thickness onto the GC disk (*i.e.* resulting in identical mass-transport limitations within the layer [20, 21]). It must be noted that the amount of Nafion® put in the ink and the amount of Pt put on the electrode are relatively high (Nafion® over CX mass ratio equal to 1:1; Pt amount deposited on the GC around 110 µg for the catalysts with the highest Pt loading). These high quantities were chosen for two reasons: (i) the 1:1 Nafion® over CX mass ratio was chosen in order to mimic the composition and structure of the cathode catalytic layer of a PEMFC; (ii) the high Pt content of the active layers prepared from high Pt loading catalysts results from the fact that the active layer of CX-supported catalysts were prepared in order to keep the same layer thickness whatever the Pt loading. However, these choices can induce some decrease in performance for the studied catalysts. Indeed, a high Pt loading on the electrodes introduces large uncertainties to the activity measurements [22,23]. Moreover, a large amount of Nafion® can cause problems in

O_2 diffusion through the ionomer film and towards the Pt active sites as well as a high electronic resistance [24].

Electrolyte and wetting procedure During all measurements, the working electrode was immersed in an electrolyte constituted of 1 M H_2SO_4 aqueous solution, which should ensure full wetting of the metallic particles by the electrolyte [21]. In order to ensure that all the pores, *i.e.* both the extragranular and the mesoporous intergranular porosities, were fully filled, a drop of electrolyte was deposited onto the catalytic layer. Then, the electrode was put under vacuum in order to outgas the layer by bubbling air through the drop. Once no air bubbles were visible, the electrode and the drop were put back under atmospheric pressure so that the electrolyte filled the empty porosity of the layer. This wetting procedure ensures that the catalyst wetting is complete and that the Pt utilization factor is close to 100%. Indeed, previous works [10,11,21] performed on similar systems showed good consistency between the Pt specific surface area measured after using this wetting procedure and the surface calculated from TEM micrographs. Finally, the electrochemical measurements were usually steady, which also hints at good wetting of the layer.

CO stripping voltammetry The Pt specific surface area was measured by CO stripping voltammetry [25–27]. The procedure was initiated by the application of a steady potential of 0.1 V *vs.* NHE to the working electrode, while gaseous CO was bubbled in the electrolyte solution for 6 min. After an Ar purge of 39 min in order to remove the CO dissolved in the electrolyte (still at 0.1 V *vs.* NHE), the CO chemisorbed at the surface of the particles was electrooxidized into CO_2 by increasing the electrode potential from 0.05 to 1.23 V *vs.* NHE at 20 mV s^{-1}. The potential was then cycled between 0.05 and 1.23 V *vs.* NHE at the same scan speed for two more cycles. This results in three recorded cycles, *i.e.* the first cycle in which the peaks from the CO electrooxidation occur and two other cycles which are cyclic voltammetry cycles performed at 20 mV s^{-1}, as all the adsorbed CO was electrooxidized during the first cycle. As the third cycle represents the background of the CO stripping measurement, it is subtracted from the first in order to isolate the CO electrooxidation peak. The Pt specific surface area, S_{CO} (m^2 $g_{Pt}{}^{-1}$) was calculated from the CO oxidation peak current, assuming that the electrooxidation of a full monolayer of CO_{ad} requires 420 $\times$ 10^{-2} C $m_{Pt}{}^{-2}$ [28]. The CO equivalent particle diameter, d_{CO}, was calculated from CO stripping results by [25–27]:

$$d_{CO} = \frac{6 \times 10^{-3}}{\rho_{Pt}\ S_{CO}} \tag{2.4}$$

where ρ_{Pt} is the density of Pt (21.4 $\times$ 10^3 kg m^{-3}) . As CO stripping voltammetry is a surface-sensitive method, d_{CO} corresponds to a surface weighed average diameter and can be compared to d_s.

Activity for the oxygen reduction reaction The activity of the catalysts for the oxygen reduction reaction (ORR) was measured on a rotating disk electrode (RDE). After saturation of the electrolyte by oxygen bubbling during 15 min, the electrode potential was set at 0.4 V *vs.* NHE, then increased at 2 mV s^{-1} to 1.09 V *vs.* NHE and finally decreased back to 0.4 V *vs.* NHE at the same scan rate, while measuring the reduction current. This measurement was repeated at various rotation speeds of the electrode (400, 900, 1600, and 2500 rpm). For each rotation speed of the electrode, the kinetic current was calculated by correcting the measured current for the effect of the external mass transfer limitations in the solution using the Koutecky-Levich equation [29]:

$$\frac{1}{i_{\mathrm{k}}} = \frac{1}{i} - \frac{1}{i_{\mathrm{l,c}}} \tag{2.5}$$

where i_{k} is the kinetic current, *i.e.* the current without any mass transfer limitations, i is the experimental current, and $i_{\mathrm{l,c}}$ is the cathodic limit current, which depends on the rotation speed of the electrode. The values of this averaged kinetic current at 0.9 V *vs.* NHE were divided by the electroactive surface of the catalysts in order to obtain the specific activity of the catalysts at 0.9 V *vs.* NHE, *SA* (in A $m_{\mathrm{Pt}}{}^{-2}$), or divided by the mass of Pt deposited on the electrode in order to obtain the mass activity at 0.9 V *vs.* NHE, *MA* (in A $g_{\mathrm{Pt}}{}^{-1}$).

2.3 Results

Physicochemical characterization

The physicochemical properties of the catalysts synthesized *via* multiple impregnation-reduction cycles are summarized in Table 2.3; those of the catalysts synthesized *via* one-step deposition methods are summarized in Table 2.4. In each case, the results are compared to those of the reference catalyst, Ref.

Figure 2.1 shows the TEM micrographs of the catalysts with the lowest and the highest loading for each synthesis technique (SEA, CEDI, multiple SB reduction, one-step SB reduction, *i.e.* SB-20, and the other one-step techniques *i.e.* FA and Col) and the TEM micrograph of the Ref catalyst. Pt particle size distribution (PSD) histograms of all the catalysts are shown in Figure 2.2.

X-ray diffractograms of the series of catalysts are presented in Figure 2.3. The Ref diffractogram, which is present in every XRD figure, is used for comparison. Almost every diffractogram displays two diffraction peaks: one at an angle of 39.7° and another at an angle of 46.2°, corresponding to Pt (1 1 1) and Pt (2 0 0) facets, respectively.

Electrochemical characterization

The Pt specific surface area, S_{CO}, and the CO equivalent particle diameter of Pt particles, d_{CO}, were calculated from the CO stripping voltammograms (Figure 2.4). Results are in each case compared to those obtained with the reference catalyst, Ref. The values of these parameters are gathered in Table 2.5. The catalytic activity of the catalysts were compared using the specific activity, *SA*, and the mass activity, *MA*, measured at 0.9 V *vs.* NHE (Table 2.5).

Strong electrostatic adsorption

The results obtained by SEA are in agreement with previous works [10, 11]. To sum up, the SEA method allows obtaining well-distributed Pt over the CX support with high weight percentages up to 25.3 wt.% (SEA/5, Table 2.3) and average particle size, d_{TEM}, around 2.2 nm. Nevertheless, the amount of Pt deposited decreases with the number of steps. The catalysts also display d_{CO} around 2.9 nm, which has to be compared to d_s (2.6 nm), and d_{XRD} around 2.5 nm which can be compared to d_v (2.8 nm). All the values of average particle sizes for SEA-synthesized catalysts are close to each other and the standard deviation calculated by image analysis is very low, equal to 0.6-0.7 nm. In fact, the PSD of the SEA-synthesized catalysts are the same for the five catalysts (Figure 2.2a). Moreover, the Pt specific surface area is constant (92 to 96 $m^2\ {g_{Pt}}^{-1}$, Table 2.5) as well as the specific and the mass activity (*SA* from 0.09 to 0.11 A ${m_{Pt}}^{-2}$ and *MA* ranging from 8.6 to 10.5 A ${g_{Pt}}^{-1}$). These results indicate that the Pt deposited at each impregnation-reduction step only forms new particles with the same size and the same activity as the previously deposited particles.

Charge enhanced dry impregnation

The first Pt deposition using the CEDI method allows to synthesize small, well-dispersed Pt particles (d_{TEM} equal to 1.6 nm with a standard deviation of 0.4 nm, see the PSD in Figure 2.2b) and a Pt loading of 7.7 wt.% (CEDI/1, Table 2.3). These particles are too small to induce X-ray diffraction peaks, as no peak is visible on the X-ray diffractogram (Figure 2.3b). The observed diffractogram corresponds to the background due to the CX support (very broad diffraction peak around 40°). However, the small Pt particles can be seen on the TEM micrograph (Figure 2.1c). Concerning the electrochemical properties, the CO stripping voltammogram displays a small, broad peak around 1.0 V *vs.* NHE (Figure 2.4b), representative of small particles. The S_{CO} of CEDI/1 is low (50 $m^2\ {g_{Pt}}^{-1}$) as well as the *MA* (3.6 A ${g_{Pt}}^{-1}$) and with *SA* slightly lower than that of the reference catalyst (0.072 A ${m_{Pt}}^{-2}$ compared to 0.091 A ${m_{Pt}}^{-2}$, Table 2.5). The low S_{CO} value, with regard to the size of particles (*ca.* 1-2 nm, which should correspond to a surface of at least 100 $m^2\ {g_{Pt}}^{-1}$) is certainly due to Cl anions poisoning the surface, as explained in the paragraphs below. This also explains the low *MA* value. These results are consistent with those obtained by Cao *et al.* [12].

Table 2.3: Properties determined by physicochemical analyses of catalysts synthesized *via* multiple impregnation-reduction cycles.

Catalyst	Pt_{ICP} wt.% ± 0.1	d_{TEM} nm	σ nm	d_s nm	d_v nm	d_{XRD} nm ± 0.5
SEA/1	8.4	2.3	0.7	2.7	2.9	2.6
SEA/2	14.7	2.2	0.7	2.7	3.0	2.3
SEA/3	19.0	2.1	0.6	2.5	2.7	2.5
SEA/4	22.2	2.2	0.7	2.6	2.8	2.4
SEA/5	25.3	2.1	0.7	2.6	2.8	2.6
CEDI/1	7.7	1.6	0.4	1.8	1.9	–[a]
CEDI/2	14.0	2.6	2.1	6.4	8.2	4.6
CEDI/3	19.7	2.9	2.6	7.6	9.2	4.6
CEDI/4	24.8	3.2	2.1	6.1	7.5	4.6
CEDI723/1	7.8	1.3	0.4	1.6	1.7	–[a]
CEDI723/2	13.9	1.9	1.5	5.2	7.2	6.4
CEDI723/3	19.9	2.4	1.9	6.2	8.2	7.3
CEDI723/4	24.6	2.6	1.9	5.6	6.9	7.3
SB/2	10.4	3.0	1.3	4.2	5.3	3.7
SB/4	15.6	2.8	1.8	5.1	6.1	4.1
SB/6	19.4	3.0	1.5	4.5	5.3	4.4
SB/8	23.1	4.8	4.4	14.6	20.5	4.4
SB723/2	11.0	3.8	2.5	7.3	9.2	11.0
SB723/4	16.1	4.8	4.3	15.9	24.1	12.8
SB723/6	20.3	3.8	4.9	28.4	47.1	22.0
SB723/8	23.9	4.3	4.3	13.9	18.3	22.0
Ref	37.0	3.1	0.8	3.4	3.6	2.4[b]

Pt_{ICP}: Pt weight percentage of the catalyst measured by ICP-AES; d_{TEM}: average diameter of the particles estimated from TEM micrographs; σ: standard deviation associated with d_{TEM}; d_s: surface-weighed average diameter of particles estimated from TEM micrographs and calculated by Equation (2.1); d_v: volume-weighed average diameter of particles estimated from TEM micrographs and calculated by Equation (2.2); d_{XRD}: average size of crystallites calculated from X-ray diffraction peaks *via* Equation (2.3).
Notes: [a] No Pt peak is visible; [b] Large error (± 1) due to low intensity of diffraction peaks.

Table 2.4: Properties determined by physicochemical analyses of catalysts synthesized *via* one-step deposition methods.

Catalyst	Pt_{target} wt.%	Pt_{ICP} wt.% ± 0.1	d_{TEM} nm	σ nm	d_{s} nm	d_{v} nm	d_{XRD} nm ± 0.5
SB-20	20	17.5	4.1	3.3	12.9	19.7	4.1
FA-10	10	10.2	2.8	1.0	3.8	5.2	2.6
FA-20	20	16.5	3.6	1.0	4.2	4.6	2.9
FA-30	30	22.7	3.6	1.5	5.8	9.7	2.9
FA-40	40	37.0	3.6	1.2	5.0	8.1	2.9
Col-10	10	5.2	2.8	1.9	4.8	7.3	3.7[a]
Col-20	20	15.6	2.9	1.7	6.0	8.8	2.7
Col-30	30	15.4	3.0	1.3	4.4	5.7	2.6
Col-40	40	25.2	3.7	1.7	5.4	6.4	3.1
Ref	–[b]	37.0	3.1	0.8	3.4	3.6	2.4[a]

Pt_{target}: Pt loading targeted by the one-step deposition synthesis; Pt_{ICP}: Pt weight percentage of the catalyst measured by ICP-AES; d_{TEM}: average diameter of the particles estimated from TEM micrographs; σ: standard deviation associated with d_{TEM}; d_{s}: surface-weighed average diameter of particles estimated from TEM micrographs and calculated by Equation (2.1); d_{v}: volume-weighed average diameter of particles estimated from TEM micrographs and calculated by Equation (2.2); d_{XRD}: average size of crystallites calculated from X-ray diffraction peaks *via* Equation (2.3).
Notes: [a] Large error (± 1) due to low intensity of diffraction peaks; [b] Not pertinent (commercial catalyst).

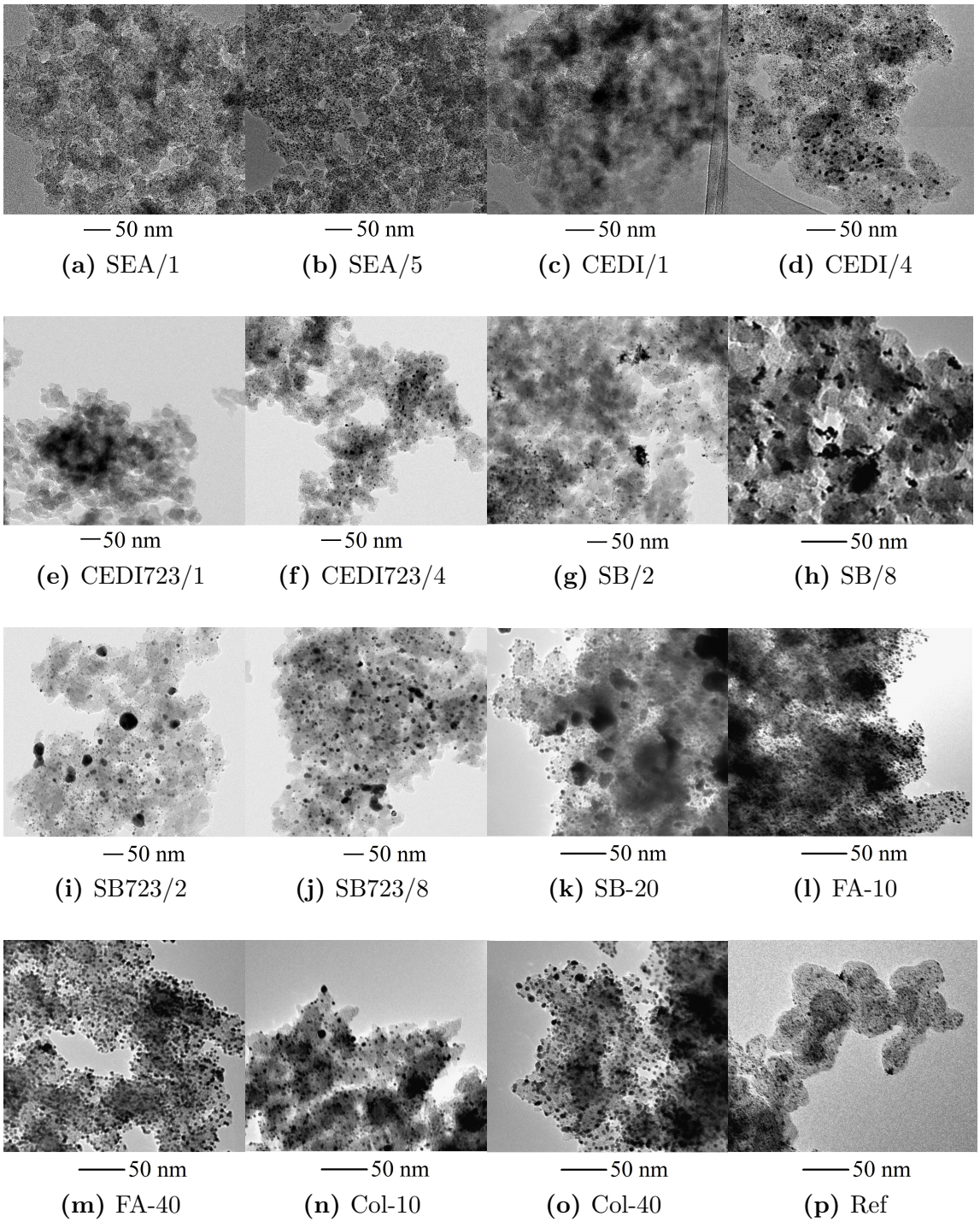

(a) SEA/1 **(b)** SEA/5 **(c)** CEDI/1 **(d)** CEDI/4

(e) CEDI723/1 **(f)** CEDI723/4 **(g)** SB/2 **(h)** SB/8

(i) SB723/2 **(j)** SB723/8 **(k)** SB-20 **(l)** FA-10

(m) FA-40 **(n)** Col-10 **(o)** Col-40 **(p)** Ref

Figure 2.1: TEM micrographs of the catalysts with the lowest and the highest loading for each synthesis and the commercial catalyst: SEA/1 (a), SEA/5 (b), CEDI/1 (c), CEDI/4 (d), CEDI723/1 (e), CEDI723/4 (f), SB/2 (g), SB/8 (h), SB723/2 (i), SB723/8 (j), SB-20 (k), FA-10 (l), FA-40 (m), Col-10 (n), Col-40 (o), and Ref (p).

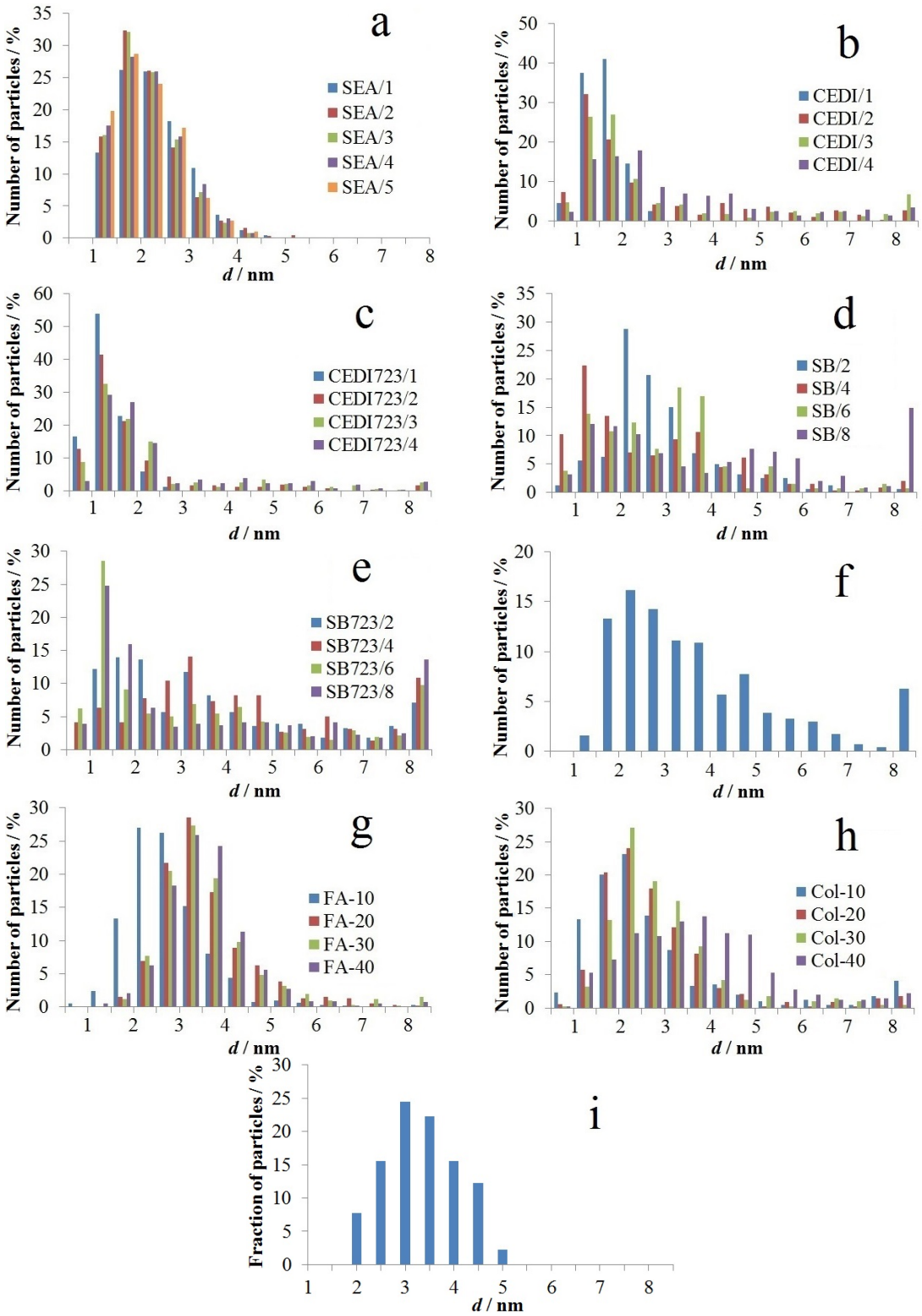

Figure 2.2: Pt particle size distribution histograms of all the catalysts obtained by image analysis: SEA/1 to SEA/5 (a); CEDI/1 to CEDI/4 (b); CEDI723/1 to CEDI723/4 (c); SB/2 to SB/8 (d); SB723/2 to SB723/8 (e); SB-20 (f); FA-10 to FA-40 (g); Col-10 to Col-40 (h); and of the reference catalyst, Ref (i). The last category of the histograms represents the fraction of Pt particles with diameter higher than 8 nm.

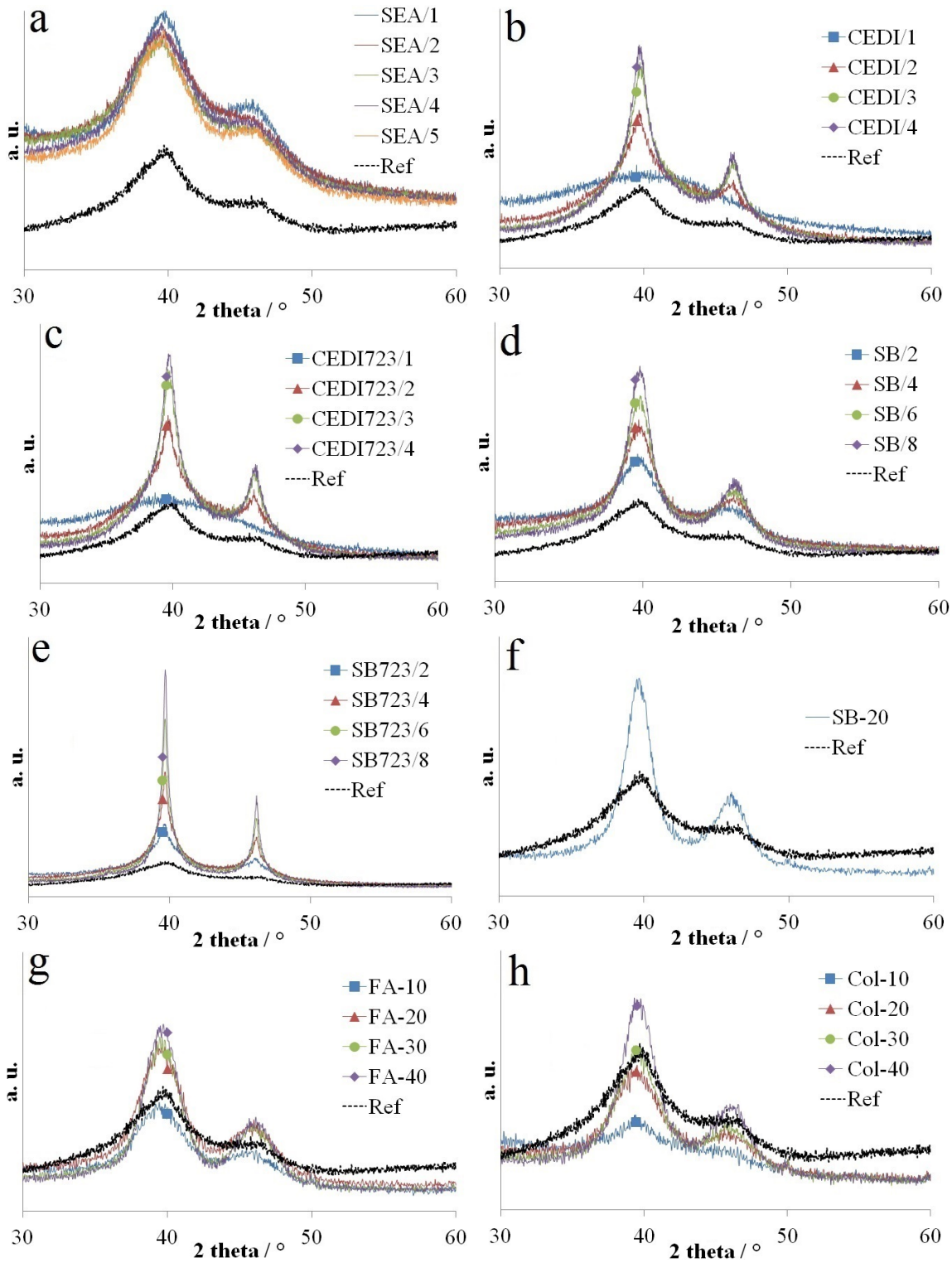

Figure 2.3: XRD diffractograms of all the catalysts: SEA/1 to SEA/5 (a); CEDI/1 to CEDI/4 (b); CEDI723/1 to CEDI723/4 (c); SB/2 to SB/8 (d); SB723/2 to SB723/8 (e); SB-20 (f); FA-10 to FA-40 (g); Col-10 to Col-40 (h). The Ref diffractogram (dotted black line) serves as a basis for comparison.

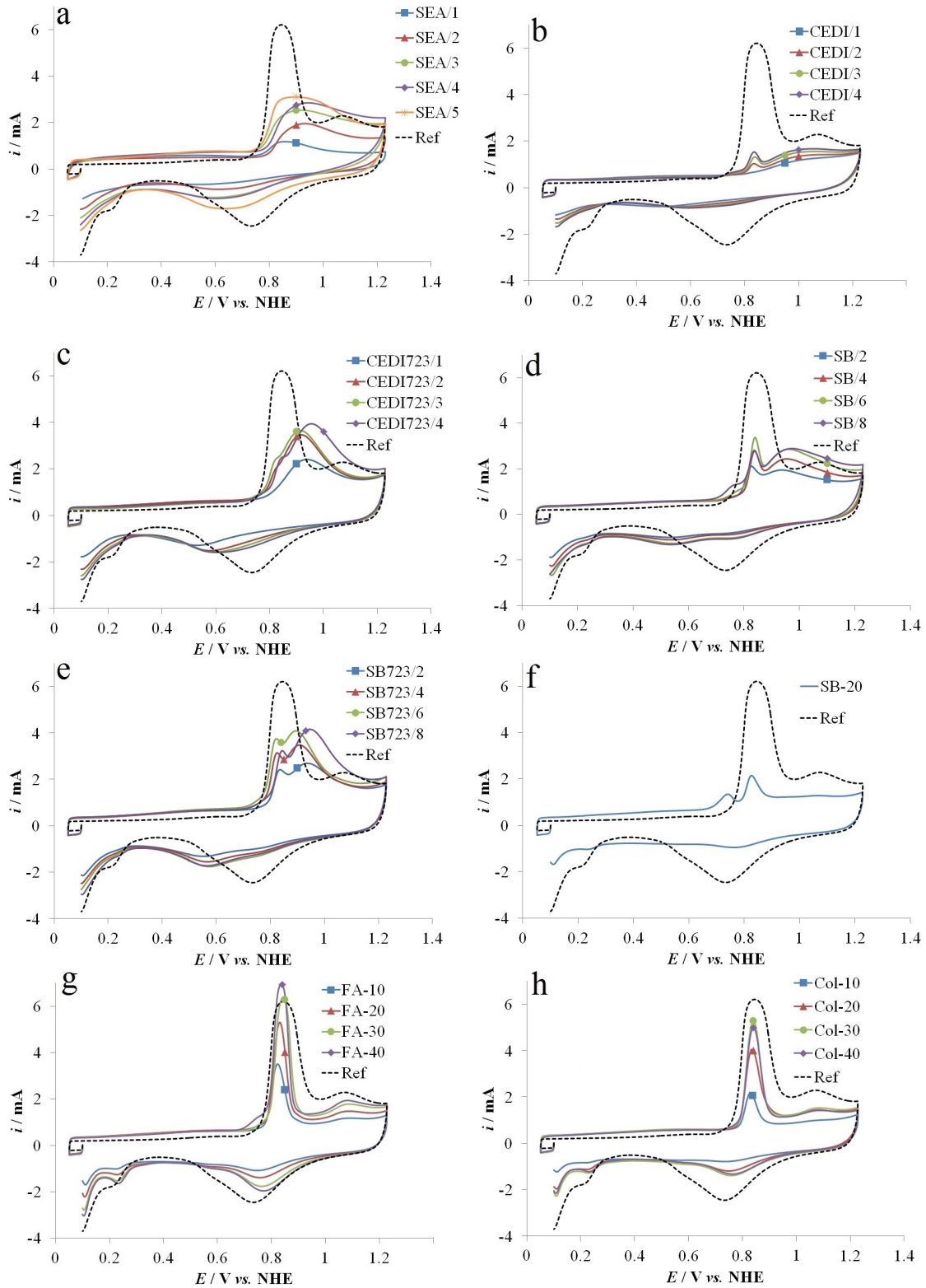

Figure 2.4: CO electrooxidation voltammograms of all the catalysts in 1 M H_2SO_4 at a sweep rate of 20 mV s^{-1} at room temperature: SEA/1 to SEA/5 (a); CEDI/1 to CEDI/4 (b); CEDI723/1 to CEDI723/4 (c); SB/2 to SB/8 (d); SB723/2 to SB723/8 (e); SB-20 (f); FA-10 to FA-40 (g); Col-10 to Col-40 (h). The voltammogram of the Ref sample (dotted line) is reported in each case for comparison.

Table 2.5: Properties determined by electrochemical analyses of all the catalysts.

Catalyst	S_{CO} $m^2\ g_{Pt}^{-1}$ ± 10%	d_{CO} nm ± 10%	SA $A\ m_{Pt}^{-2}$ ± 10%	MA $A\ g_{Pt}^{-1}$ ± 10%
SEA/1	92	3.0	0.114	10.5
SEA/2	93	3.0	0.093	8.6
SEA/3	94	2.9	0.102	9.6
SEA/4	96	2.9	0.093	8.9
SEA/5	96	2.9	0.105	10.1
CEDI/1	50	5.5	0.072	3.6
CEDI/2	38	7.2	0.147	5.6
CEDI/3	34	8.0	0.177	6.0
CEDI/4	31	8.8	0.183	5.7
CEDI723/1	247	1.1	0.030	7.4
CEDI723/2	193	1.4	0.056	10.8
CEDI723/3	145	1.9	0.065	9.4
CEDI723/4	130	2.1	0.083	10.0
SB/2	171	1.6	0.044	7.5
SB/4	133	2.1	0.050	6.7
SB/6	115	2.4	0.047	5.4
SB/8	92	3.0	0.097	8.9
SB723/2	209	1.3	0.042	8.8
SB723/4	167	1.6	0.044	8.4
SB723/6	152	1.8	0.059	9.0
SB723/8	129	2.1	0.051	6.6
SB-20	73	3.8	0.121	8.8
FA-10	131	2.1	0.086	11.3
FA-20	113	2.4	0.103	11.6
FA-30	92	3.0	0.109	10.0
FA-40	59	4.7	0.138	8.1
Col-10	137	2.0	0.069	9.5
Col-20	99	2.8	0.064	6.3
Col-30	111	2.5	0.065	7.2
Col-40	61	4.5	0.099	6.0
Ref	91	3.0	0.091	8.2

S_{CO}: Pt specific surface area calculated from CO stripping measurements normalized by the mass of Pt on the electrode; d_{CO}: CO equivalent particle diameter of the Pt particles calculated by Equation (2.4); *SA*: ORR specific activity measured at 0.9 V *vs.* NHE; *MA*: ORR mass activity measured at 0.9 V *vs.* NHE.

The second to fourth Pt deposition steps increase the loading up to 24.8 wt.% (after four impregnation-reduction cycles). However, the Pt PSD does not remain the same (Figure 2.2b), as d_{TEM} increases from 1.6 nm (CEDI/1) to 3.2 nm (CEDI/4, Table 2.3). Moreover, the standard deviation increases from 0.4 to 2.6 nm. These results indicate that, during impregnation, all the Pt ions do not adsorb on the CX support to form new particles (same mechanism as for the SEA synthesis). Indeed, particles of different sizes can be seen on the TEM micrograph (Figure 2.1d). This may be due to the fact that the CX surface chemistry is modified during the impregnation-reduction cycles. Indeed, the Pt uptake may be lowered by the modification of the CX surface chemistry. This decrease in Pt uptake with the succession of impregnation-reduction cycles has already been observed in the case of the multiple SEA method [11]. As the excess Pt ions are not withdrawn by filtration (like in SEA synthesis), Pt ions stay in the solution filling the CX pores. Therefore, during the drying step, they may adsorb on the available CX surface or agglomerate with other Pt ions, the latter producing larger nanoparticles.

X-ray diffractograms (Figure 2.3b), show sharp diffraction peaks, which results in relatively large d_{XRD} values (4.6 nm for the three multi-impregnated samples, CEDI/2, CEDI/3 and CEDI/4). However, deep analysis of the diffractograms show that they are composed of one sharp peak due to large crystallites and one broad peak due to the presence of smaller crystallites. This hints at the heterogeneity of the particle size. Regarding the electrochemical properties, the CO stripping voltammograms are composed of two very small peaks, one small, broad peak at high potential (from 0.9 to 1.1 V *vs.* NHE) due to particles with low diameters (lower than 3 nm), and one small, sharp peak at lower potential (0.85 V *vs.* NHE) due to particles with diameters higher than 3 nm [25]. Consequently, S_{CO} remains low (*ca.* 30 $\mathrm{m^2\ g_{Pt}{}^{-1}}$) leading to high d_{CO} of *ca.* 8 nm (Table 2.5) which does not match the d_{s} values (from 6.1 to 7.6 nm). The specific activities, *SA*, of CEDI/2, CEDI/3, and CEDI/4 are the highest, up to a value of 0.183 A $\mathrm{m_{Pt}{}^{-2}}$ for CEDI/4. Notwithstanding the high *SA* values, the mass activities, *MA*, of these catalysts are the lowest with a value around 6 A $\mathrm{g_{Pt}{}^{-1}}$.

These catalysts underwent a 5 h reduction at 723 K under H_2, becoming the CEDI723 catalysts. The high temperature reduction does not affect the PSD much, even though the curves are slightly narrower (Figure 2.2c), as d_{TEM}, σ, d_{s}, and d_{v} of CEDI723 catalysts are slightly lower than those of CEDI catalysts (Table 2.3). This result could be due to the sampling of the TEM micrographs (Figure 2.1c and 2.1e, and Figure 2.1d and 2.1f). However, the average crystallite size, d_{XRD} increases from 4.6 nm to 6.4 nm for CEDI723/2 or to 7.3 nm for CEDI723/3 and CEDI723/4 as the X-ray diffraction peaks gets sharper (Figure 2.3c). Nonetheless, the high temperature reduction has more significant impact on the electrochemical properties. Indeed, the CO stripping voltammograms (Figure 2.4c) exhibit one large peak at 0.95 V *vs.* NHE for CEDI723/1, one large peak at 0.9 V *vs.* NHE with a shouldering around 0.85 V *vs.* NHE for CEDI723/2 and CEDI723/3, and one large peak at 1 V *vs.* NHE with a shouldering around 0.85 V *vs.* NHE for CEDI723/4. The CO stripping peak of CEDI723/1 is representative of Pt particles with diameter

lower than 3 nm [25], which is consistent with the TEM micrograph (Figure 2.1e). Moreover, S_{CO} of CEDI723/1 is huge (247 m^2 $g_{Pt}{}^{-1}$) leading to very small d_{CO} (1.1 nm). The large CO stripping peaks of the other three CEDI723 catalysts are due to Pt particles with diameters lower than 3 nm, while the shoulderings are due to Pt particles with diameters higher than 3 nm [25]. These larger Pt particle sizes induce S_{CO} values lower than that of CEDI723/1 (from 130 to 190 m^2 $g_{Pt}{}^{-1}$ instead of 250 m^2 $g_{Pt}{}^{-1}$). Surface areas are still very high, leading to small d_{CO} values (1.4-2.1 nm).

When comparing d_{CO} and d_s of the CEDI and the CEDI723 catalysts, one can see that d_{CO} is always higher than d_s for the CEDI catalysts and always lower than d_s for the CEDI723 catalysts. The only difference between these two series of catalysts is the last reduction step, which is performed at higher temperature and for longer time (723 K for 5 h) in the case of the CEDI723 catalysts. For the CEDI catalysts, the cause of the difference between d_{CO} and d_s is the presence of Cl ions poisoning the surface. Indeed, as Cl ions can only be removed with high temperature reduction treatment [10], the small nanoparticles are still poisoned by Cl ions. These small and poisoned nanoparticles are not detected by CO stripping measurements, leading to a decrease in the Pt electroactive surface, *i.e* to an increase in d_{CO}. For the CEDI723 catalysts, the cause of the difference between d_{CO} and d_s is the presence of large nanoparticles detected by TEM. Indeed, large nanoparticles heavily impact on d_s values as the presence of a few large nanoparticles greatly increases d_s values. Concerning the electrochemical activities, the *SA* values of the CEDI catalysts are high because most of the small particles, with low activity surface atoms, are covered with Cl ions, as shown by the low S_{CO} values. Indeed, Cl ions are more strongly bonded on small Pt particles than at the surface of larger ones [18]. On the contrary, upon reduction under H_2 at high temperature (CEDI723 catalysts), the Cl ions are removed from the small particles; this leads to higher S_{CO} values, and lower *SA*, since the Pt surface atoms of small particles are much less active.

Sodium borohydride reduction

When reducing Pt ions with SB, the impregnation-reduction cycle must be repeated eight times in order to reach a Pt loading of 23.9 wt.%. Despite the higher number of impregnation-reduction steps, the SB reduction synthesis is faster than other multiple impregnation-reduction steps methods. Indeed, as both impregnation and reduction occur in liquid phase, the drying step between each cycle becomes superfluous. In that way, one impregnation-reduction cycle requires only 1.5 h.

The lower deposited Pt amount per round may be due to a desorption of Pt ions when suspending the CX in ultrapure water after the impregnation step. This step is however needed in order to proceed with the SB reduction in liquid phase. Even if the pH was fixed at the optimal pH, some ions can desorb to yield an equilibrium between the adsorbed and the desorbed Pt ions. These desorbed ions could be reduced to form Pt particles without any bonds to the CX surface. Part

of them could be washed away during rinsing, decreasing the amount of deposited Pt. The other part could deposit on the CX surface. As the size of these reduced-when-desorbed particles was not controlled, the average particle size, d_{TEM}, is higher than that of the previous catalysts (around 3 nm, Table 2.3), and the PSD wider (Figure 2.2d), as σ values are high. Large Pt particles are clearly visible on the TEM micrographs (Figures 2.1g and 2.1h: particles from 1 nm up to more than 10 nm). Moreover, some aggregates can be seen. This discrepancy in Pt particle size makes difficult the comparison between the different measurement methods (TEM, XRD, CO stripping). X-ray diffraction peaks are sharp (Figure 2.3d), which results in a relatively high d_{XRD} of *ca.* 4 nm for the four SB catalysts. The CO stripping voltammograms (Figure 2.4d) show two peaks for the four SB catalysts: one broad peak around 1 V *vs.* NHE, representative of particles with diameter lower than 3 nm, and one sharp peak around 0.85 V *vs.* NHE, representative of particles larger than 3 nm [25]. Moreover, a shouldering appears starting from the sixth Pt deposition (SB/6) at around 0.75 V *vs.* NHE, representative of Pt particles aggregates [26]. S_{CO} exhibits high values ranging from 92 to 171 $\mathrm{m^2\ g_{Pt}{}^{-1}}$, leading to small d_{CO} values ranging from 1.6 to 3.0 nm. The *SA* of these catalysts are low (around 0.050 A $\mathrm{m_{Pt}{}^{-2}}$) except for SB/8 (0.097 A $\mathrm{m_{Pt}{}^{-2}}$) but, despite the high S_{CO} values, *MA* values remain relatively low (from 5.4 to 8.9 A $\mathrm{g_{Pt}{}^{-1}}$).

The SB catalysts were also reduced at 723 K during 5 h, becoming the SB723 series. After that treatment, the Pt particle size increases and previously-formed aggregates sinter to form very large particles of several tens of nm (Table 2.3, Figures 2.1i, 2.1j and 2.2e). Figure 2.3e displays the sharpest X-ray diffraction peaks of this chapter, and so the SB723 catalysts exhibit the higher d_{XRD} with values up to 22 nm. This indicates that the high temperature reduction induces Pt particles sintering. In the CO stripping voltammograms (Figure 2.4e), two oxidation peaks are visible: one broad peak around 0.9 V *vs.* NHE representative of particles with diameter lower than 3 nm and one sharp peak around 0.85 V *vs.* NHE representative of particles with diameter higher than 3 nm. The areas under these peaks are higher than those of SB catalysts, especially for the peaks representative of small particles, most certainly because of the particle surface cleaning from Cl ions which occurs during the high temperature reduction. The third oxidation peak, appearing at around 0.75 V *vs.* NHE and attributed to aggregates, can no longer be seen. It seems that the aggregates sinter in large monocrystalline particles during the high temperature reduction. Therefore, as the contribution of large particles is integrated in the second oxidation peak around 0.85 V *vs.* NHE, the third peak tends to decrease or disappear. The S_{CO} of the SB723 catalysts are high with values ranging from 129 to 209 $\mathrm{m^2\ g_{Pt}{}^{-1}}$ for SB723/8 and SB723/2 respectively. So, d_{CO} is low, around 2 nm. Regarding catalytic activities, SB723 catalysts display low *SA* *ca.* 0.04-0.05 A $\mathrm{m_{Pt}{}^{-2}}$ and high *MA* *ca.* 8 A $\mathrm{g_{Pt}{}^{-1}}$. These results seem to indicate that the SB723 catalysts are mainly constituted of very small, clean particles (2 nm and lower, without Cl at the surface). They also contain some large particles which seem to have low impact on the properties.

Results obtained for the SB-20 catalyst are similar to those obtained for other SB-reduced catalysts. The Pt loading is close to the target of 20 wt.% (17.5 wt.%, Table 2.4) but the Pt PSD is wider (d_{TEM} equal to 4.1 nm, σ equal to 3.3 nm, see Figure 2.2f). The presence of small (around 2 nm) and huge (several tens of nm) nanoparticles can also be seen on TEM micrograph (Figure 2.1k). The X-ray diffractogram (Figure 2.3f) is similar to those of SB catalysts and the value of d_{XRD} is in the same range (equal to 4.1 nm). In the CO stripping voltammogram, no oxidation peak representative of small particles (lower than 3.3 nm), at high potential around 1 V *vs.* NHE, is visible. Again, this is probably due to the Cl poisoning. However, the curve exhibits two other peaks: one at 0.85 V *vs.* NHE, representative of particles with diameter higher than 3.3 nm, and the other at 0.75 V *vs.* NHE, representative of aggregates. SB-20 displays a small S_{CO} value (73 $\mathrm{m^2\ g_{Pt}}^{-1}$) and a high d_{CO} value (3.8 nm). However, *SA* and *MA* of SB-20 catalyst are higher than in the case of Ref (0.121 A $\mathrm{m_{Pt}}^{-2}$ and 8.8 A $\mathrm{g_{Pt}}^{-1}$, respectively, Table 2.5). These electrochemical measurements show that the Pt surface is not clean: Cl species that may be removed *via* high temperature reduction, are much probably still present on the Pt surface like in the case of previous catalysts (CEDI and SB series). The pertinence of the high temperature reduction will be debated in the section 2.4 Discussion.

Formic acid reduction

Concerning the Pt loading values, measured by ICP-AES (Table 2.4), the targeted loadings are almost reached in each case, except for sample FA-30, which displays a lower Pt loading (22.7 wt.% instead of 30 wt.%). This difference, probably a mishap as FA-40 did not suffer from the same problem, may be due to the detachment of some Pt particles with low interactions with the CX support during the filtration and/or the washing. d_{TEM} is equal to 2.8 nm for FA-10 and to 3.6 nm for the other three FA catalysts. All FA catalysts display low σ, d_{s}, and d_{v}, as the PSDs are narrow (Figure 2.2g). Moreover, in Figure 2.1l and 2.1m, it can be seen that all the Pt particles are well distributed without any large particles or aggregates. In Figure 2.3g, the X-ray diffractograms exhibit broad Pt diffraction peaks, representative of small Pt particles. Furthermore, d_{XRD} is constant for the four FA catalysts (2.6 nm for FA-10 and 2.9 nm for the others). In the CO stripping voltammograms (Figure 2.4g), the four FA catalysts display a CO oxidation peak at 0.85 V *vs.* NHE. This peak is representative of particles with diameters higher than 3.3 nm [25]. Only the FA-40 catalyst exhibits a shouldering at 0.75 V *vs.* NHE, indicating that some aggregates are present (not visible in Figure 2.1m). Both the peak area and the peak height increase with the Pt loading. S_{CO} is high for FA-10 (131 $\mathrm{m^2\ g_{Pt}}^{-1}$) and decreases to 59 $\mathrm{m^2\ g_{Pt}}^{-1}$ when increasing the loading up to 37 wt.% (FA-40). In parallel, d_{CO} increases from 2.1 nm (FA-10) to 4.7 nm (FA-40). The values of *SA* are high and increase with the Pt loading from 0.086 to 0.138 A $\mathrm{m_{Pt}}^{-2}$. The values of *MA* are high but they decrease with the Pt loading, from 11.3 to 8.1 A $\mathrm{g_{Pt}}^{-1}$.

Colloid synthesis

In Table 2.4, it can be seen that the targeted Pt loading is not reached, whatever the sample. The highest loading value equals 25.2 wt.% (Col-40). The reasons are probably that all the Pt particles in the colloid suspension did not deposit on the CX support during the mixing and that some Pt particles could be washed off. Concerning the Pt particle size, the values of d_{TEM} are quite low and increase with the targeted Pt loading, from 2.8 to 3.7 nm. The Pt PSDs are relatively wide (Figure 2.2h), which leads to large values of σ, d_{s}, and d_{v}. However, no large particles or aggregates are visible. X-ray diffraction corroborates the small particle size as detected peaks are broad. d_{XRD} values calculated from these peaks are low (*ca.* 3 nm), except for Col-10 (3.7 nm). However, this is certainly due to the accuracy, as the diffraction peaks are very small. The four CO stripping voltammograms exhibit a CO oxidation peak at 0.85 V *vs.* NHE (Figure 2.4h). The peak area and height increase with the Pt loading. This peak is representative of particles with diameter higher than 3.3 nm. S_{CO} is high (values between 99 and 137 $\mathrm{m^2\ g_{Pt}}^{-1}$ for Col-20 and Col-10 respectively) and d_{CO} is low (between 2 and 3 nm), except Col-40 (S_{CO} equal to 61 $\mathrm{m^2\ g_{Pt}}^{-1}$, d_{CO} equal to 4.5 nm). The values of *SA* are low, around 0.065 A $\mathrm{m_{Pt}}^{-2}$, except for Col-40 (0.099 A $\mathrm{m_{Pt}}^{-2}$). Furthermore, the values of *MA* are low, *ca.* 6.5 A $\mathrm{g_{Pt}}^{-1}$, except for Col-10 which displays a *MA* value equal to 9.5 A $\mathrm{g_{Pt}}^{-1}$. This high *MA* value is due to the high S_{CO} value of Col-10 (137 $\mathrm{m^2\ g_{Pt}}^{-1}$). Col-10, Col-20, and Col-30 catalysts display Pt particles around the same size, as shown by TEM results, CO stripping results, and identical *SA* values. However, Col-40 catalyst displays larger Pt particles than other Col catalysts, as proved by TEM results, CO stripping results, and higher *SA*.

2.4 Discussion

The electrochemical properties of the catalysts synthesized in this chapter were compared to those of a reference, the commercial catalyst Tanaka containing 37 wt.% of Pt, labeled hereafter Ref. The latter exhibits the following parameters: S_{CO} equal to 91 $\mathrm{m^2\ g_{Pt}}^{-1}$, d_{CO} equal to 3.0 nm, *SA* equal to 0.091 A $\mathrm{m_{Pt}}^{-2}$, and *MA* equal to 8.2 A $\mathrm{g_{Pt}}^{-1}$ (Table 2.5). Concerning the Pt loading, every synthesized catalyst displays a lower Pt loading than the reference, except FA-40 (same Pt loading: 37 wt.%).

Figure 2.5 shows the *SA* and *MA* improvement factors of the synthesized catalysts compared to the reference catalyst. The improvement factor is defined as the ratio between the *SA* (or *MA*) of the studied catalyst and the *SA* (or *MA*, respectively) of the reference catalyst. In Figure 2.5, the horizontal black line (improvement factor equal to 1) indicates the position of the reference catalyst. If the improvement factor is higher than 1, it means that the catalyst exhibits better activity than the reference. Otherwise, if the improvement factor is lower than 1, it means that the catalyst exhibits lower activity than the reference.

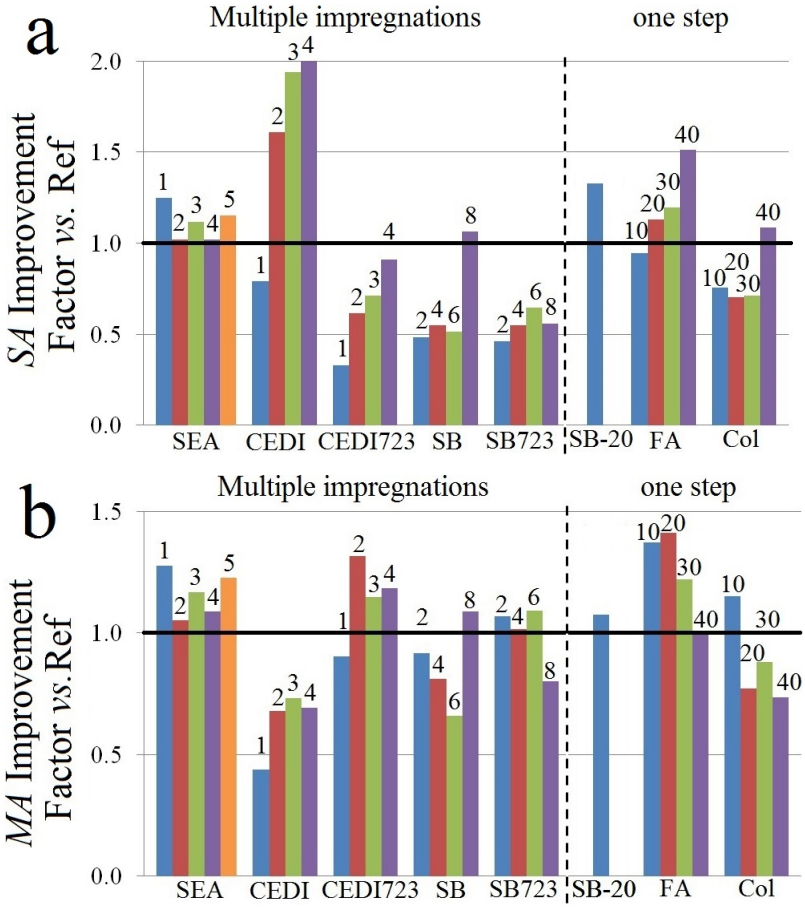

Figure 2.5: *SA* (a) and *MA* (b) improvement factor *vs.* Ref. The horizontal black line represents improvement factor of 1, *i.e.* the position of the reference (commercial catalyst). The number upon each bar represents the number of impregnations the catalyst underwent (in the case of multiple impregnations methods) or the targeted loading (in the case of one-step methods).

The first studied synthesis was the SEA method. It allows to synthesize small particle of 2 nm in diameter and each impregnation-reduction cycle adds more Pt particles without modifying the previously synthesized particles. All the catalysts were reduced under H_2 at high temperature (723 K), which ensures that Cl ions are removed from the Pt particle surface, especially for the smallest ones. The size homogeneity and cleanliness of the particles yield high *SA* and high *MA*. This is shown by the *SA* and the *MA* improvement factors (Figure 2.5). All the SEA catalysts display *SA* and *MA* improvement factor slightly higher than 1. Therefore, the SEA method allows producing catalysts with good performances compared to the commercial reference. However, its two major drawbacks are (i) the loss of Pt ions in the impregnation solution, as all the metal precursor can not adsorb on the CX support, and (ii) the complexity of the processing, *i.e.* the number of steps needed to reach high Pt loading. Thereupon, two other methods were developed in order to overcome these disadvantages: the CEDI method, which avoids any Pt losses, and the SB reduction, which renders the intermediate drying step useless, as the reduction occurs in liquid phase.

After the first Pt deposition by CEDI, the Pt particles are very small, around 1-1.5 nm. These particles are too small to be detected by XRD (Figure 2.3b), and are barely detected by CO stripping (Figure 2.4b), but they can be seen on TEM micrographs (Figure 2.1c). However, the average particle size increases when the Pt deposition is repeated and reaches a value of 3.2 nm after four cycles. Nevertheless, even if the Pt crystallites become detectable by XRD, the CO stripping voltammogram shows two very small peaks leading to small S_{CO} and high d_{CO}. This apparent contradiction can be explained when comparing the previous results with results obtained after reducing these catalysts at high temperature (723 K) during 5 h. Indeed, although no significant modification of the Pt particle size is observed between CEDI and CEDI723 catalysts (Figure 2.2b and 2.2c), the latter catalysts display higher d_{XRD} (higher crystallite size) and higher S_{CO}, leading to smaller d_{CO} (between 1 and 2 nm), than the CEDI catalysts. This proves that the high temperature reduction impacts the catalysts properties by two major effects: on the one hand, the high temperature increases the crystallite size by sintering the least stable Pt particles; on the other hand, the high temperature reduction cleans the Pt surface from the strongly-adsorbed chlorine ions, allowing to measure the actual Pt specific surface area [18].

Concerning the performance of these catalysts, the results are also dependent on the reduction. The CEDI catalysts exhibit the higher *SA* because of the covering of the small Pt particles surface by chlorine ions. Indeed, chlorine ions adsorb stronger on small Pt particles than on large Pt particles [30, 31]. This implies that only the large particles, in which the Pt surface atoms are more active, could get rid of the chlorine ions, be detected by CO stripping, and used during the oxygen reduction. This high activity over a small surface leads to very high *SA* (improvement factor up to 2) but to very low *MA* (the lowest of all catalysts, with improvement factors below 0.75). The opposite effects occur to the CEDI723 catalysts. Their *SA* are very low as they are mainly constituted of small particles which are less active but

with higher surface. Nevertheless, the high surface area values leads to high *MA*, and even to one of the best *MA* of this chapter (improvement factors *ca.* 1.2, in the same order than the SEA catalysts).

Concerning the catalysts reduced by SB, the diameter of the synthesized Pt particles ranges from *ca.* 1 nm to more than 10 nm (Figures 2.1g and 2.1h). d_{TEM} values are around 3-5 nm. It seems that two reduction mechanisms occur: (i) some Pt ions are reduced after adsorption on the CX support, leading to small particles, and (ii) some other Pt ions are reduced in liquid phase and then deposited on the CX surface, leading to larger particles [14]. The phenomenon seems to worsen with the number of Pt deposition steps (see the physicochemical properties of SB/8 in Table 2.3 and the PSD in Figure 2.2d). The SB reduction is probably too quick to control the Pt particle size. As the Pt particles are larger than those of the catalysts synthesized by the previous methods, they can be easily detected by XRD (Figure 2.3d). Concerning CO stripping results (Figure 2.4d), contrary to CEDI catalysts, all CO oxidation peaks are visible (aggregates, large particles, and small particles), even if the SB catalysts were not reduced at high temperature. The fact that the small, chlorine-poisoned Pt particles can be detected by CO stripping measurements may be due to the reductive strength of SB, which can remove a large part of the chlorine ions covering the Pt surface. This leads to high S_{CO} (over 100 $\mathrm{m^2\ g_{Pt}{}^{-1}}$), and low *SA* and *MA* with improvement factors around 0.5 and 0.75, respectively. SB/8 is an exception as its electrochemical properties are close to (and slightly higher than) those of Ref.

In order to compare with the SEA and the CEDI catalysts, SB catalysts were also reduced at high temperature (723 K) during 5 h. This results in significant sintering as suggested by TEM micrographs (Figures 2.1i and 2.1j), PSD (Figure 2.2e), and X-ray diffractograms (Figure 2.3e). The high temperature reduction treatment induces three effects on the CO stripping voltammograms: (i) the area under the CO electrooxidation peaks increases; (ii) the peak representative of small particles is shifted towards lower potential (from 1.0 to 0.9 V *vs.* NHE); (iii) the shouldering representative of aggregates at 0.75 V *vs.* NHE disappears. The first impact means that the Pt surface is cleaned from chlorine ions and the last two observations mean that the Pt particles sinter. The further cleaning of the Pt particle surface suggests that, even if the SB reduction partly cleans the Pt surface, it is not as effective as reduction under H_2 at high temperature.

Concerning the catalytic activities, the *SA* values of the SB723 catalysts are low (improvement factor *ca.* 0.5) but remain similar to those of the SB catalysts. This is due to the wide PSD (Figure 2.2e) and to the high temperature reduction treatment. Indeed, the high temperature reduction treatment sinters the Pt particles and consequently increases the *SA*. However, the high temperature reduction treatment also cleans the surface of the Pt particles, especially the smallest ones, which display low *SA*. These two opposite phenomenon compensate each other, yielding almost no evolution of the *SA*. The *MA* of the SB723 catalysts are higher than those of SB catalysts reaching a maximum improvement factor of 1.1. The good *MA* is due to the high S_{CO} values, which compensate for low *SA*. However, the *MA* improvement

factors are lower than those of the CEDI723 and SEA catalysts.

The previous methods allow to synthesize Pt/CX catalysts with good electrochemical activities. However, these multiple impregnation-reduction synthesis procedures need a lot of steps (impregnation, drying, reduction, *etc.*) and time in order to obtain highly loaded catalysts. This is why one-step deposition syntheses were also developed.

It was first attempted to deposit 20 wt.% of Pt by SB reduction in one single step. The physicochemical properties of SB-20 are similar to those of the SB and SB723 series. The PSD is wide with particle diameters ranging from 1 to 30 nm (Figure 2.1k and 2.2f). The SB-20 X-ray diffractogram (Figure 2.3f) is similar to those of the SB series, indicating that the large particles detected by TEM measurements may be aggregates as no large crystallites are detected by XRD. In Figure 2.4f, only two CO electrooxidation peaks are visible: the peak representative of particles larger than 3.3 nm at *ca.* 0.85 V *vs.* NHE and the peak representative of aggregates at *ca.* 0.75 V *vs.* NHE. No peak corresponding to small particles is detected. One can conclude that the small Pt particles detected by TEM are almost completely covered by Cl ions. So, S_{CO} is relatively small (73 m^2 $g_{Pt}{}^{-1}$) compared to that of previous catalysts. Concerning the electrochemical activities, the high *SA* of SB-20 is caused by the large particles, which are the most active towards the oxygen reduction while the small ones are probably inactive due to Cl poisoning. However, even if the *SA* value of SB-20 is higher than that of Ref (0.121 *vs.* 0.091 A $m_{Pt}{}^{-2}$), the *MA* value of SB-20 becomes similar to that of Ref, as SB-20 displays a low S_{CO}.

The high temperature reduction was not performed on SB-20 in order to keep the synthesis method simple. Nonetheless, this treatment may decrease the activities. Indeed, SB-20 can be compared to SB/8 as they display similar physicochemical and electrochemical properties. The high temperature reduction was performed on SB/8, leading to SB723/8 catalyst. The high temperature reduction performed on SB/8 cleaned the surface of the small Pt particles, but led to sintering of the aggregates to form larger particles (see, amongst others, the evolution of S_{CO}, as well as CO stripping and XRD curves between SB/8 and SB723/8 catalysts; Table 2.5, Figures 2.3d and e, Figures 2.4d and e). This treatment decreases *SA* from 0.097 to 0.051 A $m_{Pt}{}^{-2}$ (Table 2.5). Anyway, even if the high temperature reduction increases the S_{CO} value (from 92 to 129 m^2 $g_{Pt}{}^{-1}$), this does not compensate the decrease of *SA*, leading to low *MA* value of 6.6 A $g_{Pt}{}^{-1}$ (Table 2.5). So, considering the similarity between SB/8 and SB-20, one can assume that the high temperature reduction would have decreased the *SA* and *MA* of SB-20 catalyst, as it was the case for SB/8 catalyst.

The catalysts synthesized by FA reduction display narrow PSD (Figure 2.2g): all Pt particles look similar and the average diameter of the FA catalysts is equal to 3.6 nm, except for FA-10 (2.8 nm, Table 2.4 and Figures 2.1l and 2.1m). The suitable and homogeneous particle size is also demonstrated by X-ray diffractograms (Figure 2.3g) and CO stripping voltammograms (Figure 2.4g) as only one peak is visible on each curve, except the CO stripping voltammogram of FA-40 where a

small peak representative of agglomerates appears. The *SA* of the FA catalysts are high with an improvement factor up to 1.5 for FA-40. As they display high S_{CO}, *MA* values are the highest obtained in this chapter. This is due to the homogeneity and the appropriate particle size. The FA catalysts can be compared with the SEA catalysts; they both exhibit a good homogeneity in particle size, *i.e.* a narrow PSD, but the FA catalysts display slightly larger particles than SEA catalysts. These larger particles are closer to the optimum particle size, which explains the better activity of the FA catalysts.

The last method studied in this chapter was the colloid synthesis. Despite the colloidal effect of the tSC, the PSD is much wider than that of previous methods such as SEA and FA reduction (see the higher σ values in Table 2.4 and Figure 2.2h). This may be due to the presence in solution of both tSC, which is a weak reductant, and SB, a strongly active reductant. Indeed, as Pt is easily reducible, it can be reduced by both reductants, leading to more dispersed PSD, *i.e.* to small and large Pt particles. Moreover, as the Pt particles are formed before CX is put in suspension, the particle-support interactions are probably weaker, which leads to the loss of some Pt particles during filtration and washing. In spite of these drawbacks, the CO stripping voltammograms of the Col catalysts are similar to those of the FA series but with much smaller CO electrooxidation peaks. So, Col and FA catalysts display comparable S_{CO} values because (i) Col catalysts display lower Pt loading than FA catalysts and (ii) the area under the peaks of the CO stripping voltammograms of Col catalysts is lower than that of FA catalysts. However, the Col catalysts exhibit relatively low activity for the oxygen reduction (average *SA* and *MA* improvement factors equal to 0.8 and 0.9, respectively). This low activity may have three causes: (i) the Pt particle size is neither optimal nor homogeneous; (ii) some tSC may remain adsorbed on the Pt surface despite multiple washings; and (iii) the interactions between the CX support and the Pt particles may be low as the latter are synthesized in solution before contact with the CX. In any case, the Col synthesis leads to catalysts with lower catalytic activity than the best catalysts of this chapter or than the reference commercial catalyst.

2.5 Conclusion

The purpose of this chapter is to study various methods to synthesize electrocatalysts constituted of Pt nanoparticles deposited on carbon xerogel (Pt/CX catalysts) and to determine the impact of the synthesis process on the catalysts performance for the oxygen reduction reaction (ORR). The final aim is to streamline the process at best to allow easy scale-up while keeping optimal properties for PEMFC applications.

Starting from the strong electrostatic adsorption (SEA), the synthesis method of Pt/CX catalysts was streamlined in order to overcome the two major drawbacks of the SEA: the Pt loss and the long time needed to achieve a high Pt loading, as the impregnation-drying-reduction steps must be repeated (maximum 8 wt.% of Pt

deposited after the first step). To do so, two other synthesis methods were studied: (i) the charge enhanced dry impregnation (CEDI), which avoids any Pt losses as the exact amount of Pt is used during impregnation, and (ii) the reduction with sodium borohydride (SB) in liquid phase, which allows to simplify and speed up the synthesis as the drying step is avoided. However, both methods are not simple enough to scale up, as they also need several deposition steps in order to reach high Pt loadings. Therefore, three synthesis methods, which allow to deposit a chosen amount of Pt in one single step without any Pt loss, *i.e.* one-step methods, were studied. The first one-step synthesis was based on the SEA method with reduction of a high amount of Pt in liquid phase with SB. The second synthesis was the liquid-phase reduction using formic acid (FA), a weaker reductant which allows a better control of the Pt reduction. The third method was the colloid synthesis, in which tri-sodium citrate was used to synthesize a Pt colloid before mixing CX to deposit the Pt particles onto the carbon support.

The best catalysts of this chapter were those synthesized *via* the SEA, the CEDI (both after reduction at 723 K), and the FA methods. Indeed, they result in catalysts with narrow particle size distribution close to the optimal size of 3-4 nm. The very good electrochemical properties obtained are ascribed to the size homogeneity and cleanliness of the Pt particles since: (i) large Pt particles are avoided and (ii) Cl ions coming from the Pt precursor are entirely removed. Among them, only the FA synthesis allows to synthesize highly active Pt/CX catalysts with various loading (from 10 to 40 wt.% at least) in one single deposition step. As a result, this method is better suited for scale-up.

The durability and the behaviour of the best catalysts (FA catalysts) are studied in Chapter 5 and 6, in liquid electrolyte with a three-electrode setup and in PEMFCs, respectively. The adaptation of syntheses described in this chapter in order to improve the catalyst intrinsic activity by synthesizing Pt alloys with a transition metal (PtCo in this thesis) is studied in the next two chapters. In Chapter 3, the synthesis of PtCo alloys using simultaneous or successive deposition of Pt and Co by techniques based on adsorption, such as the SEA method, is discussed. Chapter 4 focuses on the adaptation of the colloid method in order to synthesize bimetallic nanoparticles on CX supports.

References

[1] H. A. Gasteiger, S. S. Kocha, B. Sompalli, and F. T. Wagner, *Applied Catalysis B: Environmental* **56**, 9 (2005).

[2] H. A. Gasteiger and M. F. Mathias, Fundamental research and development challenges in polymer electrolyte fuel cell technology, in *Proceedings of the 3rd symposium on proton conducting membrane fuel cells*, edited by M. Murthy, pp. 1–24, Salt Lake City, United States of America, 2002, Electrochemical society.

[3] C. Jaffray and G. A. Hards, Precious metal supply requirements, in *Handbook of Fuel Cells Fundamentals, Technology and Applications, vol. 3*, edited by W. Vielstich, A. Lamm, and H. A. Gasteiger, chapter 41, p. 509, Wiley, Chichester, United Kingdom, 2003.

[4] F. Maillard, S. Pronkin, and E. R. Savinova, Influence of size on the electrocatalytic activities of supported metal nanoparticles in fuel cells related reactions, in *Handbook of Fuel Cells*, edited by W. Vielstich, H. A. Gasteiger, and H. Yokokawa, volume 5, pp. 91–111, John Wiley & Sons, Ltd, Chichester, United Kingdom, 2009.

[5] K. Kinoshita, *Journal of the Electrochemical Society* **137**, 845 (1990).

[6] O. Antoine, Y. Bultel, and R. Durand, *Journal of Electroanalytical Chemistry* **499**, 85 (2001).

[7] J. Regalbuto, A. Navada, S. Shadid, M. Bricker, and Q. Chen, *Journal of Catalysis* **184**, 335 (1999).

[8] J. R. Regalbuto, *Catalyst Preparation: Science and Engineering*, CRC Press/Taylor & Francis Group, Boca Raton, United States of America, 2006.

[9] S. D. Lambert, N. Job, L. D'Souza, M. Pereira, R. Pirard, B. Heinrichs, J. Figueiredo, J.-P. Pirard, and J. Regalbuto, *Journal of Catalysis* **261**, 23 (2009).

[10] N. Job, S. D. Lambert, M. Chatenet, C. J. Gommes, F. Maillard, S. Berthon-Fabry, J. R. Regalbuto, and J.-P. Pirard, *Catalysis Today* **150**, 119 (2010).

[11] A. Zubiaur, M. Chatenet, F. Maillard, S. D. Lambert, J.-P. Pirard, and N. Job, *Fuel Cells* **14**, 343 (2014).

[12] C. Cao, G. Yang, L. Dubau, F. Maillard, S. D. Lambert, J.-P. Pirard, and N. Job, *Applied Catalysis B: Environmental* **150**, 101 (2014).

[13] C. Alegre, M. Gálvez, R. Moliner, V. Baglio, A. Aricò, and M. Lázaro, *Applied Catalysis B: Environmental* **147**, 947 (2014).

[14] N. Job, F. Maillard, J. Marie, S. Berthon-Fabry, J. P. Pirard, and M. Chatenet, *Journal of Materials Science* **44**, 6591 (2009).

[15] A. M. Pasqualeti, P.-Y. Olu, M. Chatenet, and F. H. B. Lima, *ACS Catalysis* **5**, 2778 (2015).

[16] N. Job, R. Pirard, J. Marien, and J.-P. Pirard, *Carbon* **42**, 619 (2004).

[17] M.-L. C. Piedboeuf, A. F. Léonard, K. Traina, and N. Job, *Colloids and Surfaces A: Physicochemical and Engineering Aspects* **471**, 124 (2015).

[18] N. Job, M. Chatenet, S. Berthon-Fabry, S. Hermans, and F. Maillard, *Journal of Power Sources* **240**, 294 (2013).

[19] G. Bergeret and P. Gallezot, Particle size and dispersion measurement, in *Handbook of Heterogeneous Catalysis*, edited by G. Ertl, H. Knözinger, and J. Weitkamp, p. 439, Wiley-VCH, Weinheim, Germany, 1997.

[20] E. Guilminot, A. Corcella, M. Chatenet, and F. Maillard, *Journal of Electroanalytical Chemistry* **599**, 111 (2007).

[21] M. Chatenet, L. Dubau, N. Job, and F. Maillard, *Catalysis Today* **156**, 76 (2010).

[22] K. Mayrhofer, D. Strmcnik, B. Blizanac, V. Stamenkovic, M. Arenz, and N. Markovic, *Electrochimica Acta* **53**, 3181 (2008).

[23] K. Shinozaki, J. W. Zack, R. M. Richards, B. S. Pivovar, and S. S. Kocha, *Journal of the Electrochemical Society* **162**, F1144 (2015).

[24] S. S. Kocha, J. W. Zack, S. M. Alia, K. C. Neyerlin, and B. S. Pivovar, *ECS Transactions* **50**, 1475 (2013).

[25] F. Maillard, M. Eikerling, O. V. Cherstiouk, S. Schreier, E. Savinova, and U. Stimming, *Faraday Discussions* **125**, 357 (2004).

[26] F. Maillard, S. Schreier, M. Hanzlik, E. R. Savinova, S. Weinkauf, and U. Stimming, *Physical Chemistry Chemical Physics* **7**, 385 (2005).

[27] F. Maillard, E. R. Savinova, and U. Stimming, *Journal of Electroanalytical Chemistry* **599**, 221 (2007).

[28] S. Trasatti and O. Petrii, *Journal of Electroanalytical Chemistry* **327**, 353 (1992).

[29] A. J. Bard and L. R. Faulkner, *Electrochemical Methods: Fundamentals and applications*, John Wiley & Sons, Inc., Weinheim, Germany, 2nd edition, 2001.

[30] Z. C. Zhang and B. C. Beard, *Applied Catalysis* **174**, 33 (1998).

[31] B. Coq, G. Ferrat, and F. Figueras, *Journal of Catalysis* **101**, 434 (1986).

Chapter 3

Impregnation methods to synthesize PtCo/carbon xerogel electrocatalysts for the oxygen reduction reaction

After the study of the Pt deposition on carbon xerogel in the first two chapters, the third one is focused on the synthesis of PtCo nanoparticles deposited on carbon xerogel by impregnation methods. The synthesis of PtCo nanoparticles was studied with the aim to increase the catalytic performance of the Pt catalysts for the ORR *via* Pt alloying. The strong electrostatic adsorption method studied in the first chapter was modified in order to synthesize bimetallic PtCo nanoparticles on carbon xerogel. Three synthesis processes were envisaged: (i) Pt deposition before Co; (ii) Co deposition before Pt; and (iii) Pt and Co simultaneous deposition from the same solution. The performance of the synthesized catalysts were then compared to each other in a three electrode cell configuration (liquid electrolyte).

3.1 Introduction

Commonly used catalysts for PEMFC applications are constituted of Pt nanoparticles with diameter around 2-3 nm deposited on high surface area carbon (HSAC). However, they are not optimal; their performance can be improved and their cost reduced. The previous chapter focuses on some solutions to these drawbacks: the Pt dispersion and the use of an optimized carbon support (carbon xerogel, CX). It shows that Pt nanoparticles deposited on CX (Pt/CX catalysts) with good performance for the oxygen reduction reaction (ORR) can be synthesized with various methods. These results are the starting point for the study of the synthesis of bimetallic catalysts performed in this chapter and the following one.

Among other techniques, the strong electrostatic adsorption (SEA) method allows to synthesize highly dispersed Pt on carbon xerogel with Pt particle size close to the optimal 3-4 nm [1–3]. This technique consists in maximizing the electrostatic interactions between the metal precursor and the support by adjusting the pH of the carbon/water/Pt precursor slurry to the adequate value [1, 4, 5]. The latter depends on the surface chemistry of the support and on the nature of the Pt precursor. Due to the presence of various oxygenated surface groups, the carbon support protonates/deprotonates at low/high pH value. This enhances the adsorption of anions/cations, respectively. For example, considering the impregnation of CXs by hexachloroplatinic acid (H_2PtCl_6) aqueous solutions (1000 ppm_{Pt}), the final pH yielding to the highest Pt uptake was found to be *ca.* 2.5, leading to electrocatalysts with Pt loading around 8-10 wt.% [4]. In order to achieve high Pt mass fraction without sacrificing the dispersion, the SEA procedure can be performed several times consecutively [2] and the impregnation solution can be reuse to decrease Pt losses [3].

Nevertheless, even well dispersed Pt/C catalysts may not reach the requirements for the large-scale commercialization of PEMFCs [6]. These requirements are essentially (i) a high activity for the ORR and (ii) a low Pt loading in order to decrease the quantity of Pt needed [6]. Indeed, this decrease in Pt quantity can overcome two major obstacles for the full-scale commercialization of PEMFCs: the cost of the system [7] and the Pt supply limitations [8]. A possible solution to fulfill these requirements is to use Pt-alloy catalysts instead of Pt/C. Indeed, Pt-alloy catalysts can perform better ORR activity (while containing less Pt) as the presence of the transition metal contracts the Pt lattice, leading to a widening of the *d*-band and a decrease of the average energy of the the band (*d*-band center). This phenomenon is the strain-ligand effect [9–11]. The modification of the *5d*-band of Pt impacts the adsorption properties of oxygenated species, such as hydroxyl groups ($OH^{\bullet}$) [12, 13]. The intermediates formed during the ORR, which are oxygenated species, are usually bound too strongly to the surface of Pt particles. This strong adsorption between oxygenated species and Pt atoms, which limits the kinetics of the ORR, is weakened by the strain-ligand effect, leading to binding energy closer to the optimum according to Sabatier's principle, *i.e.* the best catalyst for a chem-

ical reaction involving adsorbates must exhibit a binding energy with the reactive and intermediate species neither too strong, to allow the dissociation of the reactive species and to prevent the active sites from blocking, nor too weak, otherwise the reaction does not occur. Particularly, PtCo alloys, *e.g.* Pt_3Co, exhibit one of the best ORR activity [6, 13, 14].

In this chapter, a combination of two impregnation techniques, *i.e.* SEA and wet impregnation (WI), was used to prepare PtCo/CX catalysts: Pt was deposited by SEA, while WI was used for the Co deposition. Three synthesis pathways of Pt_3Co were investigated: (i) deposition of Pt followed by deposition of Co, (ii) deposition of Co followed by deposition of Pt, and (iii) simultaneous deposition of Pt and Co processed using the SEA conditions of Pt. In order to obtain the Pt_3Co composition, the metal loadings have to be around 20 wt.% of Pt and 2 wt.% of Co. The synthesized catalysts were characterized by physicochemical and electrochemical techniques.

3.2 Experimental

3.2.1 Reagents

The solid reagents used in this chapter were resorcinol $C_6H_6O_2$ (Merck, for synthesis), sodium carbonate Na_2CO_3 (Acros Organics, 99.5% extrapure, anhydrous), dihydrogen hexachloroplatinate (IV) hexahydrate $H_2PtCl_6{\cdot}6H_2O$ (Alfa Aesar, 99.9% metal basis, crystalline), sodium hydroxide NaOH (Acros Organics, extrapure, pellets), and cobalt (II) nitrate hexahydrate $Co(NO_3)_2 \cdot 6H_2O$ (Merck, for analysis).

The liquid reagents used in this chapter were formaldehyde solution CH_2O (Sigma Aldrich, ACS reagent 37 wt.% in water, contains 10-15% methanol as stabilizer), hydrochloric acid HCl (Acros Organics, for analysis min. 35 wt.% solution in water), sulfuric acid H_2SO_4 (Merck, 96 wt.% Suprapur® for electrochemical measurements or Merck, 98% EMSURE®, for analysis for cleaning solution), hydrogen peroxide H_2O_2 (Merck, 30% Perhydrol®, EMSURE®, stabilized for higher storage temperature, for analysis), and Liquion™ solution (Ion Power, LQ-1105, 1100EW, 5 wt.%).

The gaseous reagents used in this chapter were nitrogen N_2 (Air liquide, α1), hydrogen H_2 (Air Liquide, α1), carbon monoxide CO (Air liquide, N47), argon Ar (Air Liquide, α1), and oxygen O_2 (Air liquide, α1).

3.2.2 Syntheses

Carbon xerogel support synthesis The carbon xerogel (CX) support used in this thesis was prepared by drying and pyrolysis of a resorcinol-formaldehyde aqueous gel [15]. The procedure is fully described elsewhere [3]. Briefly, the gel was obtained by polycondensation of resorcinol with formaldehyde in water. The resorcinol/formaldehyde molar ratio, *R/F*, was set at 0.5, the resorcinol/sodium carbon-

ate molar ratio, R/C, was chosen equal to 1000 and the dilution ratio, D, *i.e.* the solvent/(resorcinol and formaldehyde) molar ratio, was fixed at 5.7. These variables were chosen in order to obtain a CX with a pore size distribution centered at 70 nm. After gelling and aging in an oven at 358 K, the obtained gel was dried under vacuum and pyrolyzed at 1073 K under nitrogen flow. After pyrolysis, the CX was ground and sieved to obtain carbon particles smaller than 125 µm. The CX, synthesized in this way, displays a BET surface area, S_{BET}, of 567 m^2 ${g_C}^{-1}$, a total pore volume, V_{p}, of 2.1 cm^3 ${g_C}^{-1}$ and an average pore size of 70 nm.

Platinum deposition The Pt deposition was performed by the strong electrostatic adsorption (SEA) method [1]. This method was already studied and applied on CX [2–4]. The synthesis procedure is the following: (i) the pH of 2.38 L of 1000 ppm hexachloroplatinic acid ($H_2PtCl_6 \cdot 6H_2O$) solution (5.1 mmol L^{-1}) was adjusted to 2.5 with 0.5 mol L^{-1} hydrochloric acid (HCl) and sodium hydroxide (NaOH) solutions; (ii) 4.2 g of ground CX were added to the solution, *i.e.* the amount of CX necessary to achieve a surface loading of 1000 m^2 L^{-1}; (iii) the suspension was stirred for 1 h; (iv) then filtered; (v) dried at 393 K in an oven for 12 h; (vi) reduced under 0.04 mmol s^{-1} H_2 flow at 473 K for 1 h. As this procedure allows to deposit *ca.* 8 wt.% of Pt, it was repeated three times in order to reach the 20 wt.% of Pt target. After the third impregnation, one half of the catalyst underwent a reduction at 473 K for 1 h (same as other reduction steps), the other half underwent the last reduction step at 723 K during 5 h in order to remove the chlorine anions bound to the Pt particles. Indeed, these anions decrease the Pt active surface area by covering the particles and a high temperature reduction is required to clean the surface [16]. The two halves of the Pt catalyst, the one reduced at 473 K for 1 h and the one reduced at 723 K for 5 h, will be used as support for the Co deposition in order to study if the particle surface cleanliness impacts the Co deposition.

Cobalt deposition The Co deposition was performed by the wet impregnation (WI) method [17]. This method was not applied on CX yet so it was adapted from the deposition on other carbons such as carbon nanofibers [18]. 1 g of CX was added to 20 mL of 0.0343 mol L^{-1} cobalt nitrate ($Co(NO_3)_2 \cdot 6H_2O$) solution in water. This suspension was stirred for 8 h, then put in an oven at 393 K during 24 h to evaporate the water, and reduced under 0.04 mmol s^{-1} H_2 flow at 623 K for 2 h.

Simultaneous deposition The simultaneous deposition of Pt and Co was performed as follows: (i) the pH of 1.13 L of 1000 ppm $H_2PtCl_6 \cdot 6H_2O$ and 100 ppm $Co(NO_3)_2 \cdot 6H_2O$ solution was fixed at 2.5 with 0.5 mol L^{-1} HCl and NaOH solutions; (ii) 2 g of ground CX was added to the solution; (iii) the suspension was stirred for 2 h; (iv) then filtered; (v) dried at 393 K in an oven for 12 h; (vi) reduced under 0.04 mmol s^{-1} H_2 flow at 623 K during 2 h. In order to reach the targeted metal loadings, this procedure was repeated three times. After each deposition, metal salt was added to the impregnation solution so as to keep constant the concentration of Pt and Co ions between each impregnation step.

Sample list Four catalysts were synthesized: (i) CX-Co-Pt, a CX on which Co was deposited by the WI method before the Pt deposition by the SEA method; (ii) CX-Pt-Co, a CX on which Pt was deposited by the SEA method before the Co deposition by the WI method; (iii) CX-Pt723-Co, a CX on which Pt was deposited by the SEA method and reduced at 723 K during 5 h in order to clean the Pt surface before the Co deposition by the WI method; (iv) CX-PtCo, a CX on which Pt and Co were deposited by the simultaneous deposition method. One commercial catalyst is used as reference. This reference catalyst is a Pt/HSAC Tanaka 37%, labeled hereafter as 'Pt/C'.

3.2.3 Physicochemical characterization

Catalyst properties The metal weight percentage of the catalysts was measured by inductively coupled plasma-atomic emission spectroscopy (ICP-AES) using an ICAP 6500 THERMO device. The solutions for the analyses were prepared as follows: an aliquot of the catalyst sample was weighed and digested by 10 mL of sulphuric acid (H_2SO_4) and 5 mL of nitric acid (HNO_3). This solution was heated at 573 K until clear. After the complete dissolution of the CX support and evaporation of the solution, 3 mL of HCl and 1 mL of HNO_3 were added. The obtained solution was heated a few minutes at 393 K and transferred into a 50 mL calibrated flask, which was finally filled by deionized water.

The Pt particles were observed by transmission electron microscopy (TEM) with a Jeol 2010 transmission electron microscope (200 kV, LaB_6 filament). An aliquot of the catalyst sample was suspended in 20 mL of ethanol. After 15 min of sonication in an ultrasonic bath, a drop of the suspension was deposited on a polymer-covered copper grid. Particle size distribution histograms (not shown) were obtained by image analysis of the TEM micrographs on at least 500 particles [2].

The atomic composition of the particles was investigated during the TEM measurements by energy dispersive X-ray spectroscopy (EDX). EDX elemental maps were acquired using a JEOL 2100F microscope operated at 200 kV and equipped with a SDD Centurio retractable detector. The EDX line scans were recorded on individual nanoparticles by scanning the beam in a square region adjusted to the particle size. The quantitative analyses were performed on Pt_L and Co_K lines using the K-factor provided by the JEOL software.

The catalysts were analyzed by X-Ray diffraction (XRD) with a Bruker D8 ADVANCE goniometer using the $Cu_{K\alpha}$ line (Ni filter).

The X-ray photoelectron spectrometry (XPS) analysis (ESCALAB250Xi, by Thermo Scientific) was performed with a monochromatic ($Al_{K\alpha}$) X-ray beam, on a 500 µm × 500 µm spot area; the spectrometer is equipped with a flood gun for charge compensation. Quantification (atomic percentages) of the atomic species (C, O, N, S, Pt, *etc.*) present at the surface (0-10 nm in depth) and chemical analysis are evaluated from peak analysis on high resolution spectra (C1s, O1s, N1s, S2p, Pt3d, *etc.*). Survey spectrum was also acquired to check for the presence of other

contaminants. Even though atomic species with surface densities down to 0.1 at.% can be detected with XPS, the error on the atomic percentage is estimated up to 1% (mostly influenced by the background and peak fitting parameters).

CX support properties The textural properties of the CX support and the catalysts were determined by nitrogen adsorption-desorption and mercury porosimetry. The adsorption-desorption isotherms were measured at 77 K with a Sorptomatic CE Instruments 1990 Series. Prior to the measurements, the samples were outgassed at 10^{-3} Pa during 12 h at room temperature. The isotherm analysis provided the BET specific area, S_{BET} [19].

The mercury porosimetry measurements were performed with a Pascal Series 140 porosimeter between 0.01 and 0.4 MPa and with a Pascal Series 240 porosimeter between 0.1 and 200 MPa. The pore size distribution was determined by applying Washburn's law to mercury porosimetry curves [20]:

$$L = \frac{-4\sigma cos\theta}{P} \tag{3.1}$$

where L is the pore diameter (nm), σ is the surface tension of mercury at 293 K (480 mN/m), θ is the contact angle of mercury (140°), and P is the mercury pressure (MPa). Washburn's law (Equation (3.1)) can be applied because CXs do not crush under the mercury pressure and undergo intrusion only [15, 21, 22].

3.2.4 Electrochemical characterization

Materials All the utilized glassware was cleaned by immersion in a H_2SO_4:H_2O_2 equivolume mixture overnight and thoroughly rinsed with ultrapure water (18 MΩ cm). The electrolytic solutions were prepared from ultrapure water and H_2SO_4 (Merck, Suprapur®).

Catalytic layer preparation To measure the electrochemical properties of the catalysts, inks were firstly prepared. The ink composition was chosen to keep the amount of carbon constant, regardless of the metal loading [23, 24]. The amount of catalyst containing 19.8 mg of carbon was crushed in a mortar then mixed with 755 mg of ultrapure water and 466 mg of 5 wt.% Liquion™ solution. In order to blend it homogeneously, the mixture was then processed in an ultrasonic bath for 15 min. Once the ink was homogeneous, 10 µL of ink were deposited on a glassy carbon (GC) disk and sintered at 343 K during 20 min to evaporate the solvents and stick the catalyst on the GC disk. The catalyst layer deposited on the GC disk composes the working electrode for all electrochemical measurements. With this procedure, the amount of catalyst deposited on the GC disk is calculated in order to obtain the same quantity of carbon composing the working electrode. This yields active layers of identical thickness onto the GC disk (*i.e.* resulting in identical mass-transport conditions within the layer [23, 24]).

Electrolyte and wetting procedure The electrolyte in which the electrode was immersed for the measurements was a 1 M H_2SO_4 liquid electrolyte, which should enable full wetting of the metallic particles [24]. However, the liquid may not penetrate in the full layer. To ensure that all the pores were fully filled, the catalytic layer was covered by a drop of electrolyte. Then, the electrode was put under vacuum in order to outgas the layer by bubbling air through the drop. Once no air bubbles were visible, the electrode and the drop were put back under atmospheric pressure. This implies that the drop filled the empty porosity of the layer, which ensures the full wetting of the catalyst. With this wetting procedure, the electrochemical measurements were usually steady. In the case of CX-supported Pt catalysts, this procedure ensures the Pt wetting and the Pt utilization factor is close to 100% [24]. Indeed, previous works [2,3,24] performed on similar systems have shown very good consistency between the electroactive surface area measured after using this wetting procedure and the surface deduced from TEM micrograph analysis. Before any electrochemical experiment, the working electrode was immersed into the electrolyte while fixing the potential at 0.4 V *vs.* NHE. This potential ensures that no Co dissolves into the electrolyte.

CO stripping voltammetry The Pt electroactive surface area of the nanoparticles was measured by CO stripping voltammetry [25–27]. The procedure was initiated by the application of a steady potential of 0.1 V *vs.* NHE to the working electrode, while gaseous CO was bubbled in the electrolyte solution for 6 min. During this time, CO molecules adsorb on Pt atoms located at the nanoparticle surface but not on Co atoms [28, 29]. After an Ar purge of 39 min in order to remove the CO dissolved in the electrolyte at this potential, the CO chemisorbed on the Pt atoms at the surface of particles was electrooxidized into CO_2 by increasing the electrode potential from 0.05 to 1.23 V *vs.* NHE at 20 mV s^{-1}. The Pt electroactive surface area was calculated from the CO oxidation peak current, assuming that the electrooxidation of a full monolayer of CO_{ads} requires 420×10^{-2} C ${m_{Pt}}^{-2}$ [30].

Activity for the oxygen reduction reaction The activity of the catalysts for the oxygen reduction reaction (ORR) was measured on a rotating disk electrode (RDE). After saturation of the electrolyte by oxygen bubbling during 15 min, the electrode potential was set at 0.4 V *vs.* NHE and then increased at 2 mV s^{-1} to 1.09 V *vs.* NHE and then decreased back to 0.4 V *vs.* NHE at the same scan rate, while measuring the reduction current. This measurement was repeated at various rotation speeds of the electrode (400, 900, 1600, and 2500 rpm). For each rotation speed of the electrode, the kinetic current was calculated by correcting the measured current for the effect of the external mass transfer limitations in the solution using the Koutecky-Levich equation [31]:

$$\frac{1}{i_{\mathrm{k}}} = \frac{1}{i} - \frac{1}{i_{\mathrm{l,c}}} \tag{3.2}$$

where i_k is the kinetic current, *i.e.* the current without any mass transfer limitations, i is the experimental current, and $i_{l,c}$ is the cathodic limit current, which depends on the rotation speed of the electrode. The values of i_k at 0.9 V *vs.* NHE were divided by the electroactive surface of the catalysts in order to obtain the specific activity of the catalysts at 0.9 V *vs.* NHE, *SA* and, then, multiplied by the electroactive surface area of the catalysts in order to obtain the mass activity at 0.9 V *vs.* NHE, *MA*.

3.3 Results

3.3.1 Physicochemical characterization

The physicochemical properties of the catalysts are summarized in Table 3.1. Two samples reach the metal loading target, CX-Pt-Co and CX-Pt723-Co: the Pt loadings are respectively 19.9 et 20.6 wt.% and the Co loading is 2.9 wt.% for both samples. For the other two catalysts, CX-Co-Pt and CX-PtCo, the targeted Pt loading is achieved (18.9 and 21.0 wt.% respectively) but the Co loading is lower than expected: it is equal to 0.4 wt.% for the CX-Co-Pt sample and below the instrument detection limit (0.008 wt.%) for the CX-PtCo sample, *i.e.* the catalyst obtained by simultaneous deposition of Pt and Co.

TEM micrographs of the CX-Co-Pt, CX-Pt-Co, CX-Pt723-Co and CX-PtCo samples are shown in Figure 3.1. It can be seen that two different families of particles are present: (i) small particles with an average diameter of 1.7 nm and (ii) large particles with diameters around 9 nm, except for CX-Co-Pt which displays small particles only. Image analysis was applied to these micrographs in order to calculate the particle size distribution histograms (not shown), the number-weighed average diameter of small particles (between 0 and 5 nm), $d_{TEM,1}$, and of large particles (higher than 5 nm), $d_{TEM,2}$:

$$d_{TEM} = \frac{\Sigma n_i d_i}{\Sigma n_i} \tag{3.3}$$

where n_i is the number of particles with diameter d_i [32], the standard deviations, σ_1 and σ_2, the surface-weighed average diameter of small particles, $d_{s,1}$, and of large particles, $d_{s,2}$:

$$d_s = \frac{\Sigma n_i d_i^3}{\Sigma n_i d_i^2} \tag{3.4}$$

where n_i is the number of particles with diameter d_i [32] and the volume-weighed average diameter of small particles, $d_{v,1}$, and of large particles, $d_{v,2}$:

$$d_v = \frac{\Sigma n_i d_i^4}{\Sigma n_i d_i^3} \tag{3.5}$$

where n_i is the number of particles with diameter d_i [32].

Table 3.1: Catalyst properties determined from physicochemical analyses.

Catalyst	ICP		TEM								XRD	
	Pt_{ICP} wt.% ± 0.1	Co_{ICP} wt.% ± 0.1	$d_{\mathrm{TEM},1}$ nm	σ_1 nm	$d_{\mathrm{s},1}$ nm	$d_{\mathrm{v},1}$ nm	$d_{\mathrm{TEM},2}$ nm	σ_2 nm	$d_{\mathrm{s},2}$ nm	$d_{\mathrm{v},2}$ nm	$d_{\mathrm{XRD},1}$ nm ± 0.5	$d_{\mathrm{XRD},2}$ nm ± 1
CX-Co-Pt	18.9	0.4	1.7	0.6	2.1	2.3	–[a]	–[a]	–[a]	–[a]	1.4	14
CX-Pt-Co	19.9	2.9	1.7	0.7	2.3	2.6	7.1	2.7	10.5	9.2	2.0	10
CX-Pt723-Co	20.6	2.9	1.7	0.7	2.3	2.6	10.5	2.7	11.9	12.8	1.5	10
CX-PtCo	21.0	< 0.008[b]	1.7	0.7	2.2	2.5	9.9	2.3	11.0	11.6	2.0	12
Pt/C	37.0	–[c]	3.1	1.1	3.4	3.6	–[a]	–[a]	–[a]	–[a]	2.4	–[d]

Pt_{ICP}: Pt weight percentage of the catalyst measured by ICP-AES; Co_{ICP}: Co weight percentage of the catalyst measured by ICP-AES; $d_{\mathrm{TEM},1}$: number-weighed average diameter of the small particles estimated from TEM micrographs and calculated by Equation (3.3); σ_1: standard deviation associated with $d_{\mathrm{TEM},1}$; $d_{\mathrm{s},1}$: surface-weighed average diameter of small particles estimated from TEM micrographs and calculated by Equation (3.4); $d_{\mathrm{v},1}$: volume-weighed average diameter of small particles estimated from TEM micrographs and calculated by Equation (3.5); $d_{\mathrm{TEM},2}$: number-weighed average diameter of the large particles estimated from TEM micrographs and calculated by Equation (3.3); σ_2: standard deviation associated with $d_{\mathrm{TEM},2}$; $d_{\mathrm{s},2}$: surface-weighed average diameter of large particles estimated from TEM micrographs and calculated by Equation (3.4); $d_{\mathrm{v},2}$: volume-weighed average diameter of large particles estimated from TEM micrographs and calculated by Equation (3.5); $d_{\mathrm{XRD},1}$: average size of small crystallites calculated from X-ray diffraction peaks *via* Equation (3.6); $d_{\mathrm{XRD},2}$: average size of large crystallites calculated from X-ray diffraction peaks *via* Equation (3.6).

Notes: [a] No large particles detected by TEM; [b] Below instrument detection limit; [c] Not measured because pure Pt catalyst; [d] No large particles detected by XRD.

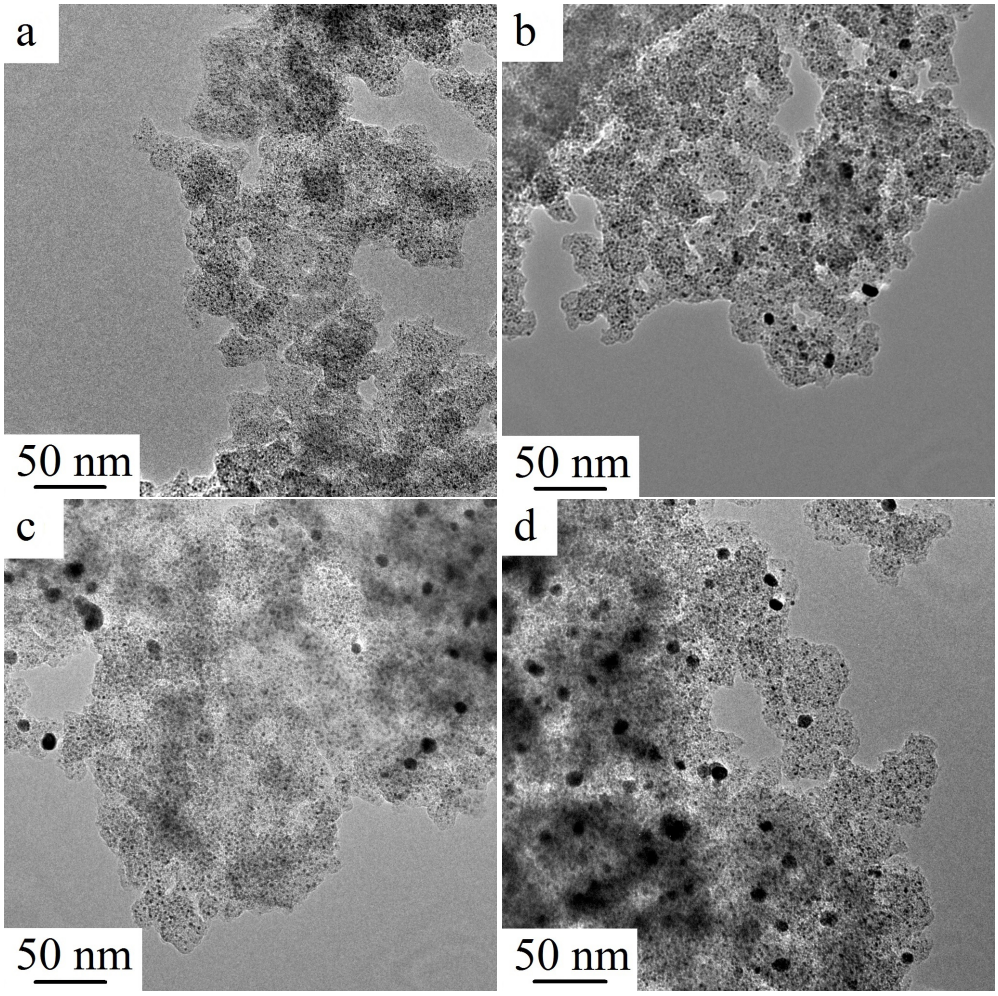

Figure 3.1: TEM micrographs of the four catalysts: CX-Co-Pt (a), CX-Pt-Co (b), CX-Pt723-Co (c), and CX-PtCo (d).

These results are shown in Table 3.1; the average diameter of the small particles, $d_{\mathrm{TEM},1}$, is equal to 1.7 nm for the four samples with a standard deviation of 0.6 nm for the CX-Co-Pt sample or 0.7 nm for the other three samples. The average diameter of the large particles, $d_{\mathrm{TEM},2}$, is equal to 7.1 nm for CX-Pt-Co, 10.5 nm for CX-Pt723-Co, and 9.9 nm for CX-PtCo with a standard deviation of 2.3 nm for the CX-PtCo sample or 2.7 nm for the other two samples. $d_{\mathrm{s},1}$ can be compared to d_{CO} as CO stripping is surface-sensitive. The other parameters, $d_{\mathrm{v},1}$ and $d_{\mathrm{v},2}$, can be compared to $d_{\mathrm{XRD},1}$ and $d_{\mathrm{XRD},2}$ respectively, because X-ray diffraction is volume-sensitive [32] (see section 3.4 Discussion). As no large particles were detected on the TEM micrographs of CX-Co-Pt, no values of $d_{\mathrm{TEM},2}$, σ_2, $d_{\mathrm{s},2}$, and $d_{\mathrm{v},2}$ could be calculated for this sample.

EDX elemental maps and line scan analysis of the two bimetallic catalysts, CX-Pt-Co and CX-Pt723-Co, are displayed in Figure 3.2 (3.2a: CX-Pt-Co; 3.2b: CX-Pt723-Co). These scans and maps were performed on large particles only because small particles (*ca.* 2 nm) do not allow obtaining representative data. EDX elemental

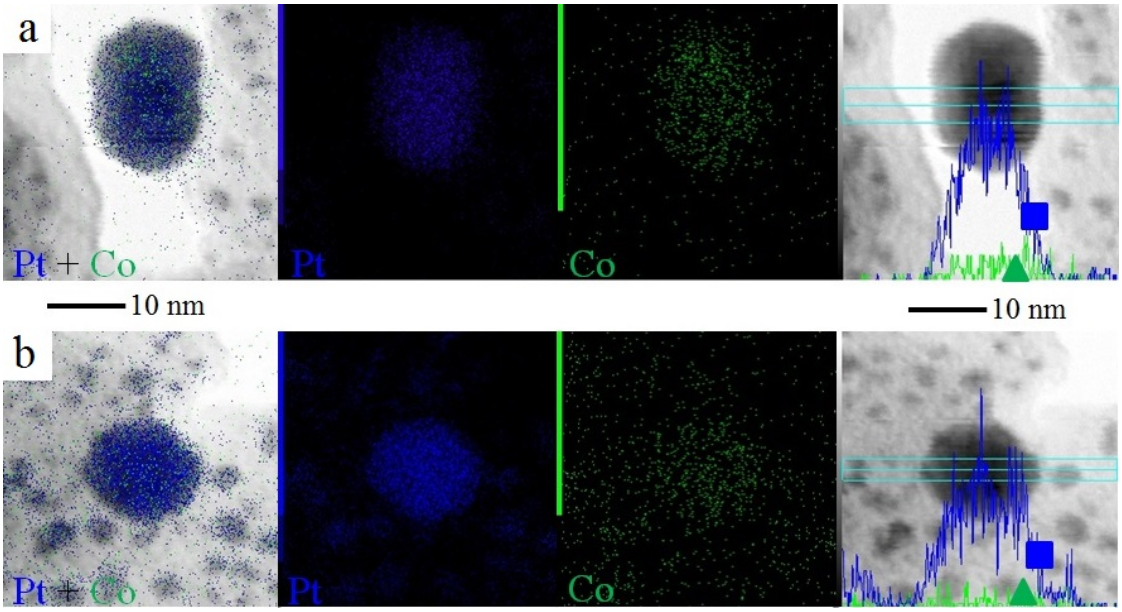

Figure 3.2: EDX elemental maps and line scan analysis of CX-Pt-Co (a) and CX-Pt723-Co (b) samples, TEM migrographs are in the background of the bi-elemental maps and the line scan analysis for better legibility (Pt: ■; Co: ▲).

maps constitute a mapping of the Pt and Co repartition over TEM micrographs. Along with Pt maps and Co maps, they indicates that the particles are composed of Pt and Co atoms. The EDX line scan analyses are the sum of three scans measured along the three horizontal lines. The particle atomic composition measured by EDX, Pt_{EDX} and Co_{EDX}, and the theoretical particle atomic composition calculated from weight loading, measured by ICP-AES, assuming all the Pt and all the Co are alloyed together, $Pt_{\mathrm{ICP,at}}$ and $Co_{\mathrm{ICP,at}}$ are presented in Table 3.2. Particles of CX-Pt-Co catalyst are composed of 76 at.% of Pt and 24 at.% of Co. Particles of CX-Pt723-Co catalyst are composed of 81 at.% of Pt and 19 at.% of Co. These results can be compared to $Pt_{\mathrm{ICP,at}}$ and $Co_{\mathrm{ICP,at}}$ which, for the two catalysts, are equal to 67-68 at.% of Pt and 32-33 at.% of Co. The values of these parameters are compared in the section 3.4 Discussion.

Figure 3.3 presents the X-ray diffractograms of the four catalysts which are vertically shifted for better legibility. The diffraction angles of Pt (1 1 1) (39.7°), Co (1 1 1) (44.8°), and Pt (2 0 0) (46.2°) are indicated by the three vertical lines. For all the catalysts, no Co, Co oxide, or PtCo alloy, represented by the shift of the Pt diffraction peaks to higher diffraction angle values, are detected. Moreover, for all catalysts, the Pt diffraction peak seems to contain two contributions: (i) one high narrow peak, corresponding to large Pt crystallites, and (ii) one less intense and broader peak, corresponding to small crystallites. Average crystallites sizes, d_{XRD}, were calculated by Scherrer's equation [32]:

$$d_{\mathrm{XRD}} = \frac{k\lambda}{\beta cos\theta} \tag{3.6}$$

Table 3.2: Particle atomic compositions measured by EDX and theoretical particle atomic compositions calculated from weight loading, measured by ICP-AES, assuming complete alloying of Pt and Co.

Catalyst	EDX		ICP	
	Pt_{EDX} at.%	Co_{EDX} at.%	$Pt_{\mathrm{ICP,at}}$ at.%	$Co_{\mathrm{ICP,at}}$ at.%
CX-Pt-Co	76	24	67	33
CX-Pt723-Co	81	19	68	32

Pt_{EDX}: Pt atomic percentage of particles measured by EDX; Co_{EDX}: Co atomic percentage of particles measured by EDX; $Pt_{\mathrm{ICP,at}}$: theoretical Pt atomic percentage of particles calculated from ICP-AES results assuming that all the Pt and all the Co are alloyed; $Co_{\mathrm{ICP,at}}$: theoretical Co atomic percentage of particles calculated from ICP-AES results assuming all the Pt and all the Co are alloyed.

where k is a dimensionless shape factor and equals 0.89, λ is the X-ray wavelength ($Cu_{K\alpha}$: 1.5456 nm), β is the full width at half the maximum intensity (FWHM), and θ is the Bragg angle. The values of the average size of small crystallites, $d_{\mathrm{XRD,1}}$, range from 1.4 (CX-Co-Pt) to 2.0 nm (CX-Pt-Co and CX-PtCo) while that of the large crystallites, $d_{\mathrm{XRD,2}}$, range from 10 (CX-Pt-Co and CX-Pt723-Co) to 14 nm (CX-Co-Pt, see Table 3.1). As XRD is a volume-sensitive analysis, d_{XRD} corresponds to an average volume diameter and can be compared to d_{v} [32]. The values of these parameters are compared in the section 3.4 Discussion.

Figure 3.4 shows the Pt4f (left) and the Co2p (right) XPS spectra of the two bimetallic catalysts, CX-Pt-Co (Figure 3.4a) and CX-Pt723-Co (Figure 3.4b). Peaks relative to metallic Pt (Pt4f met), oxidized Pt (Pt4f OH and Pt4f OO), and oxidized Co (Co2p $(OH)_2$ and Co2p CoO) are visible. No Pt-Co bound nor metallic Co peaks were detected.

The nitrogen adsorption-desorption isotherms of the raw CX support and of the CX-supported catalysts are shown in Figure 3.5. For the catalysts, the values of adsorbed volume per gram of sample are corrected by the deposited metal mass measured by ICP-AES in order to obtain the adsorbed volume per gram of support, *i.e.* per gram of carbon (g_{C}). On these isotherms, the hystereses that occur at high relative pressures indicate that all the samples are meso-macroporous. All the samples display microporosity, as shown by the abrupt volume increase at low relative pressure. BET surface areas, calculated from these isotherms, are 567 $m^2\ g_C{}^{-1}$ for the support, CX, and 395, 524, 526, and 409 $m^2\ g_C{}^{-1}$ for the catalysts CX-Co-Pt, CX-Pt-Co, CX-Pt723-Co, and CX-PtCo, respectively.

Figure 3.6 shows the cumulative pore volume as a function of the pore size in the mesoporous domain of the CX support calculated from the mercury porosimetry measurement by Washburn's equation (Equation (3.1)). This measurement was per-

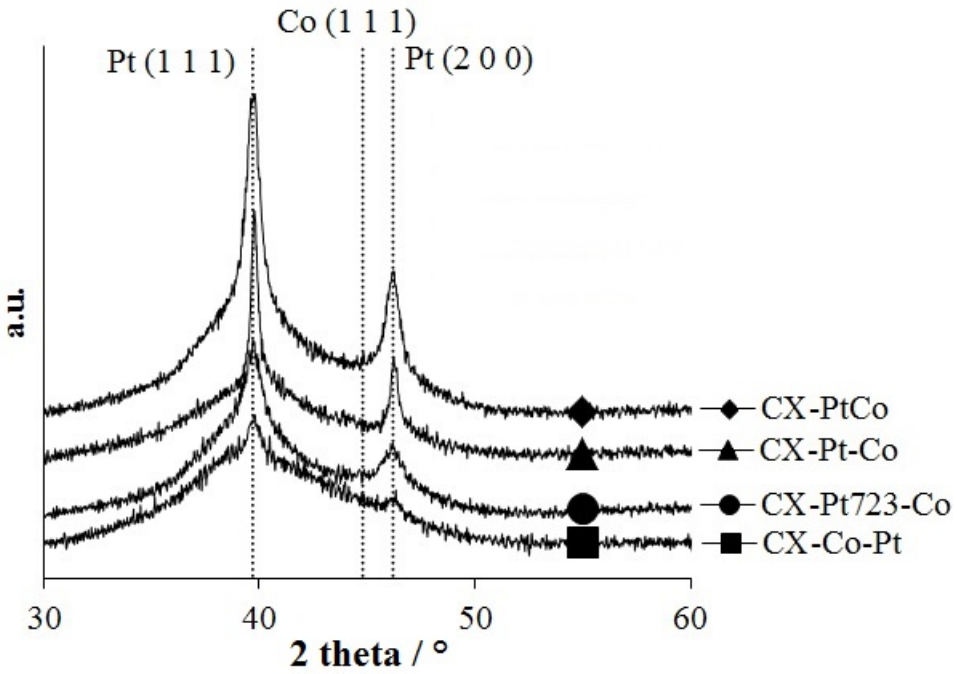

Figure 3.3: X-ray diffractograms of the four catalysts, vertically shifted for better visibility. The diffraction angles of Pt (1 1 1), Co (1 1 1), and Pt (2 0 0) are indicated respectively, from left to right, by the vertical dotted lines.

formed on a CX monolith before grinding. The porosimetry results of the catalysts are not shown because: (i) grinding does not effect the CX mesopores [33] and (ii) the deposition of nanoparticles does not block mesopores [2]. The pore size distribution of the support ranges from *ca.* 40 to 90 nm with a mean pore size around 70 nm.

3.3.2 Electrochemical characterization

The electroactive specific surface areas, S_{CO} were calculated from the CO stripping voltammograms (Figure 3.7). As the Co atoms do not participate to the CO sorption reactions [28], the CO equivalent diameter of particles, d_{CO}, was calculated from S_{CO} values for the catalysts with less than 0.5 wt.% of Co only, *i.e.* the catalysts which can be likened to pure Pt catalysts, CX-Co-Pt and CX-PtCo, and the Pt/C reference. The values of these parameters, S_{CO} and d_{CO}, are gathered in Table 3.3. Results show that S_{CO} is almost constant for all catalysts (from 105 to 110 $m^2\ g_{Pt}{}^{-1}$). The reference catalyst, Pt/C, displays an electroactive surface area of 92 $m^2\ g_{Pt}{}^{-1}$. The CO equivalent diameter, d_{CO}, is calculated by:

$$d_{CO} = \frac{6 \times 10^{-3}}{\rho_{Pt}\ S_{CO}} \tag{3.7}$$

where ρ_{Pt} is the Pt density (21.4×10^3 kg m^{-3}) [25–27]. d_{CO} was calculated for Pt catalysts only, *i.e.* for CX-Co-Pt, CX-PtCo, and the reference (Pt/C). d_{CO}

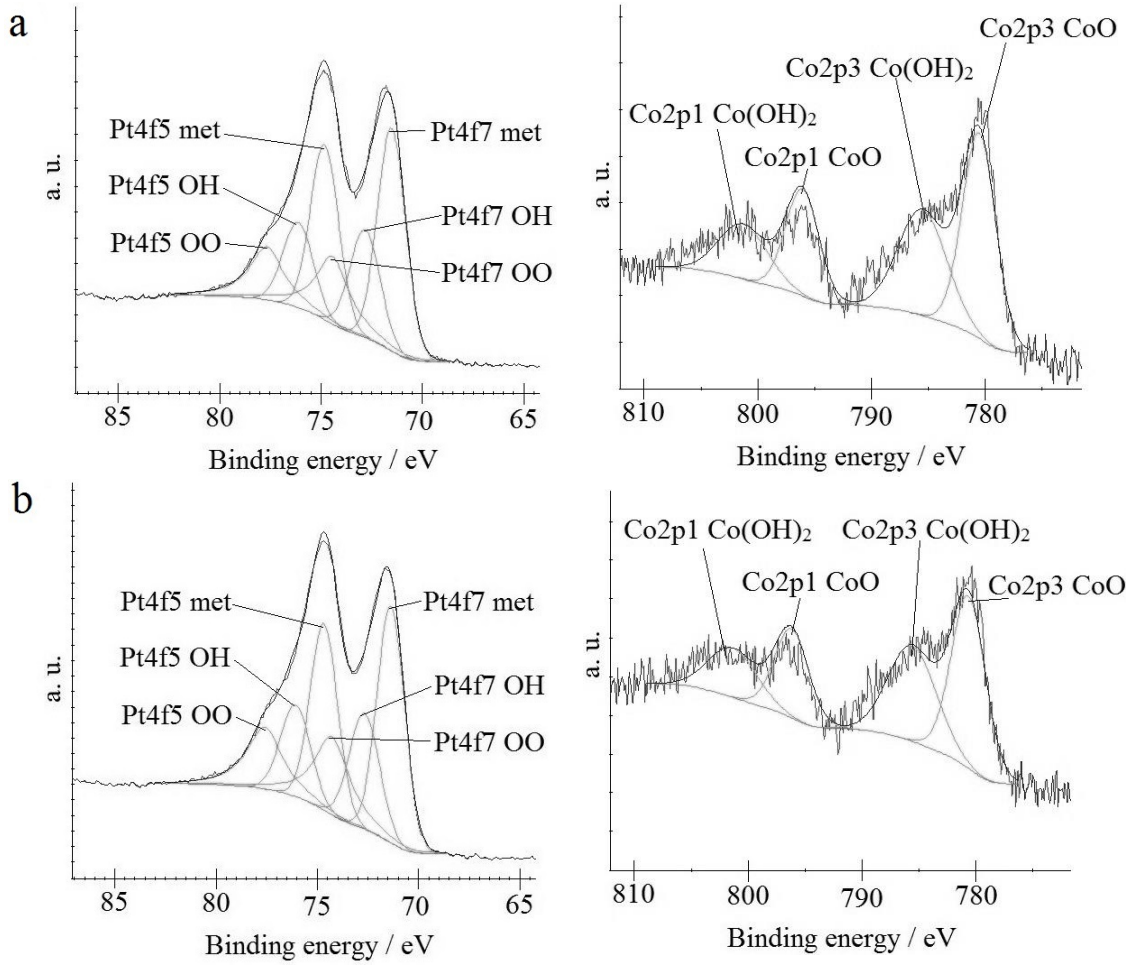

Figure 3.4: Pt 4f (left) and Co 2p (right) XPS spectra of CX-Pt-Co (a) and CX-Pt723-Co (b) catalysts.

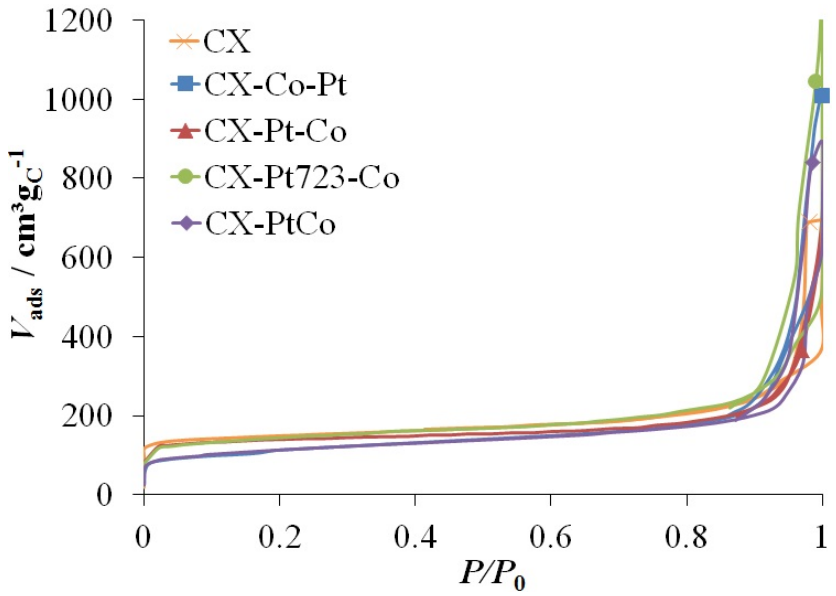

Figure 3.5: Nitrogen adsorption-desorption isotherms of the carbon xerogel support (CX, ×) and the four catalysts (CX-Co-Pt, ■; CX-Pt-Co, ▲; CX-Pt723-Co, ●; and CX-PtCo, ♦).

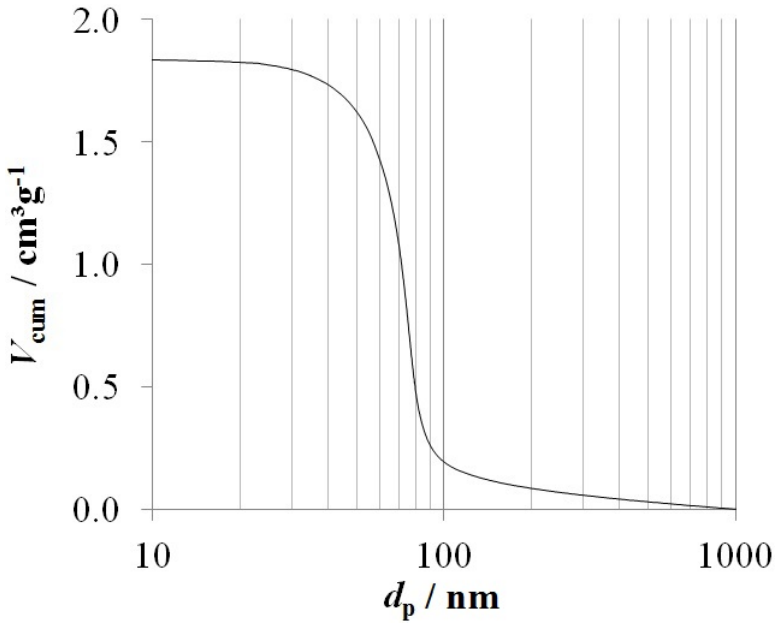

Figure 3.6: Cumulative pore volume as a function of the pore size of the CX support, calculated from the mercury porosimetry measurement by Washburn's law (Equation (3.1)).

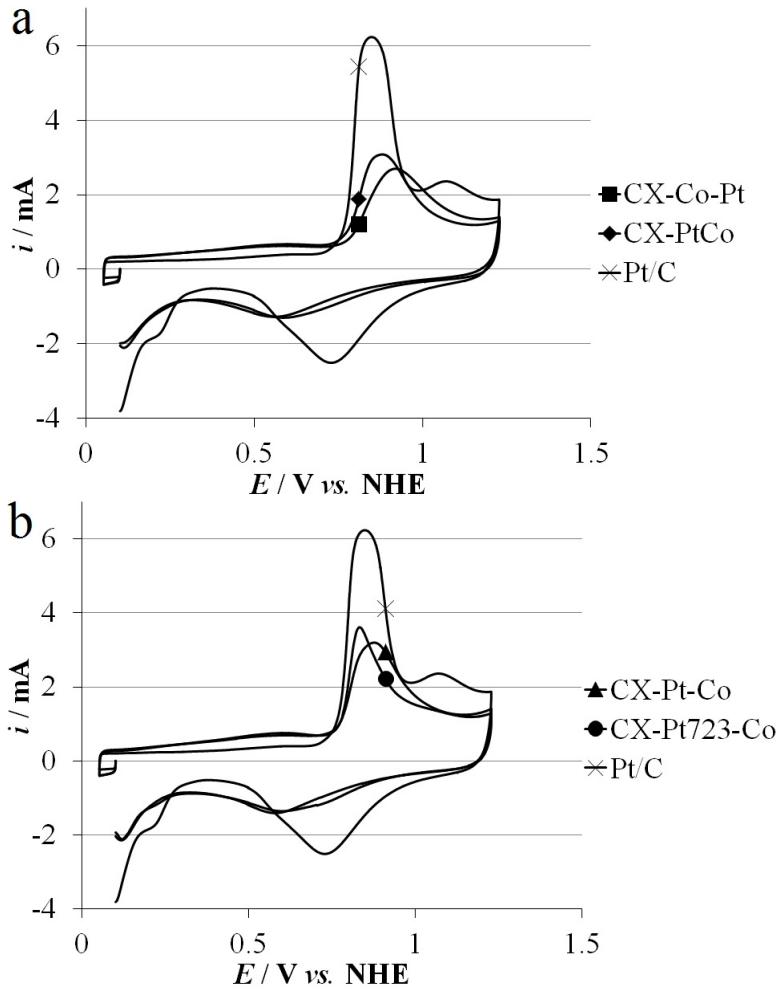

Figure 3.7: CO electrooxidation voltammograms measured in 1 M H_2SO_4 at a sweep rate of 20 mV s^{-1} at room temperature: pure Pt catalysts, CX-Co-Pt and CX-PtCo, and the reference Pt/C (a); bimetallic catalysts, CX-Pt-Co and CX-Pt723-Co, and the reference Pt/C (b). The Pt/C voltammogram can be used to compare the two sets of voltammograms.

equals 2.7 nm for CX-Co-Pt and CX-PtCo, and 3.0 nm for Pt/C. As CO stripping voltammetry is a surface-sensitive method, d_{CO} corresponds to a surface weighed average diameter and can be compared to $d_{s,1}$.

The catalytic activity of the catalysts were compared using the specific activity, *SA*, and the mass activity, *MA*, measured at 0.9 V *vs.* NHE (Table 3.3). *SA* values range from 0.031 (CX-Pt-Co) to 0.050 A $m_{Pt}{}^{-2}$ (CX-PtCo). *MA* values range from 3.4 (CX-Pt-Co) to 5.3 A $g_{Pt}{}^{-1}$ (CX-PtCo). For Pt/C, *SA* is equal to 0.091 A $m_{Pt}{}^{-2}$ and *MA* to 8.2 A $g_{Pt}{}^{-1}$.

Table 3.3: Catalysts properties determined by electrochemical analyses.

Catalyst	CO stripping		ORR	
	S_{CO} $m^2\ g_{Pt}^{-1}$ ± 10%	d_{CO} nm ± 10%	SA A m_{Pt}^{-2} ± 10%	MA A g_{Pt}^{-1} ± 10%
CX-Co-Pt	109	2.7	0.038	4.2
CX-Pt-Co	110	–[a]	0.031	3.4
CX-Pt723-Co	107	–[a]	0.049	5.2
CX-PtCo	105	2.7	0.050	5.3
Pt/C	92	3.0	0.091	8.2

S_{CO}: electroactive specific area of particles calculated from CO stripping measurements normalized by the mass of Pt on the electrode; d_{CO}: CO equivalent diameter of the particles calculated by Equation (3.7); *SA*: specific activity for the ORR measured at 0.9 V *vs.* NHE; *MA*: mass activity for the ORR measured at 0.9 V *vs.* NHE.
Notes: [a] Not calculated because Pt-Co bimetallic catalysts.

3.4 Discussion

The low Co loading of the CX-Co-Pt sample (Table 3.1), could be explained by the Co dissolution in the H_2PtCl_6 solution at a pH of 2.5. In order to prove this hypothesis, a fraction of the 260 mL of H_2PtCl_6 solution used during the first impregnation was analyzed by ICP-AES. The Co concentration of this solution was equal to 29.6 mg L^{-1}. Considering the volume of this solution, the dissolved Co amount (7.7 mg) corresponds to almost half the Co previously deposited on the catalyst (15.8 mg). As the Pt deposition was repeated three times, the Co dissolution in the acidic H_2PtCl_6 solution can explain the low Co loading at the end of the synthesis protocol.

Likewise, no Co is deposited on the CX-PtCo sample (Table 3.1). Indeed, as Co is dissolved at a pH of 2.5 (shown by the low Co loading of the CX-Co-Pt sample), which is the pH value chosen for the Pt deposition, Co atoms can not be deposited on the CX surface in presence of the acidic H_2PtCl_6 solution. Moreover, when solubilized, the Co precursor ($Co(NO_3)_2 \cdot 6H_2O$) forms Co cations, Co^{2+}. These cations can not be adsorbed on the CX surface because the surface is positively charged as the pH of the solution is set at 2.5 and the PZC of the CX is *ca.* 9. These two reasons explain why the deposition of Co cations is not possible at a pH of 2.5.

Concerning the other two catalysts, CX-Pt-Co and CX-Pt723-Co, ICP measurements (Table 3.1) show the presence of Pt and Co on the CX support. EDX measurements on large particles (Figure 3.2) indicate that these particles are composed of Pt and Co. In Figure 3.2a and 3.2b, the EDX Pt line scans are volcano-shaped. This

shape can represent the response provided by a 2D projection of a spherical particle. However, the EDX Co line scan displays so low intensities that no profile can be identified. The only deducible information of the Co line scan is that Co is present in or at the surface of the large particles. Regarding the atomic composition of the particles (Table 3.2), the theoretical composition, given by ICP-AES measurements, is *ca.* 67 at.% of Pt and 33 at.% of Co, assuming complete alloying of the metals. However, the actual composition, measured by EDX analysis, is 76 at.% of Pt and 24 at.% of Co for CX-Pt-Co and 81 at.% of Pt and 19 at.% of Co for CX-Pt723-Co. This difference implies that some particles may be constituted of pure Co or Co oxides or, at least, may be Co-enriched particles. These pure/oxidized/enriched Co particles can be part of the small particles, which can not be analyzed by EDX, or other large particles, which were not analyzed by EDX. In both cases, these results indicate that the Co distribution between small and large particles, or within the large particles, would not be homogeneous.

In order to solve the question about the possible interactions (and bounds) between Pt and Co atoms, XPS analyses were performed (Figure 3.4). Measurements show that the platinum is essentially metallic with small amounts of Pt oxides and hydroxides, supposedly present at the surface of the particles. Moreover, they indicate that Co is only present as Co oxide and hydroxide species. As no metallic Co or PtCo peaks are visible, it can be deduced that all the Co atoms are oxidized and not bound to the Pt atoms. Nevertheless, EDX measurements show that large particles are composed of Pt and Co. These two analyses seem to be contradictory but they can be explained by another hypothesis. Indeed, these results can suggest that Co, which is in the oxide or hydroxide form, is located at the surface of the Pt particles. To prove this hypothesis, the two bimetallic catalysts were characterized by EDX after acid washing. On the one hand, should Co be present as oxidized species at the surface of the Pt particles, acid washing should dissolve Co and no Co would be detected by EDX measurements. On the other hand, should Co atoms be inside the particles, they would not be removed by acid washing. Acid washing was performed as follows: (i) the catalysts were immersed in 100 mL of H_2SO_4 1 M during 23 h under stirring at room temperature, (ii) the suspensions were filtered, then (iii) thoroughly rinsed with ultrapure water, and (iv) dried at 333 K in an oven for 1 h. EDX measurements, after acid washing, are shown in Figure 3.8. The EDX elemental maps indicate that almost all the Co was washed out by the acid. In the CX-Pt-Co maps (Figure 3.8a), it seems that a few Co atoms remain on the large particles leading to a Co loading of less than 10 at.%, instead of 24 at.% before acid washing. However, in the CX-Pt723-Co maps (Figure 3.8b), the Co profile does not follow the particles location, *i.e.* the spots where Co atoms are detected and the nanoparticles location do not correspond. So, the remaining Co signal can be assimilated to noise. This seems to indicate that all the Co atoms was dissolved during the acid washing, leading to pure Pt particles. It can be concluded that Co is present on the surface of the Pt particles as Co oxides species. Unfortunately, the nature of small particles can not be measured nor deduced by EDX analysis as small particles are too small to give significant signals.

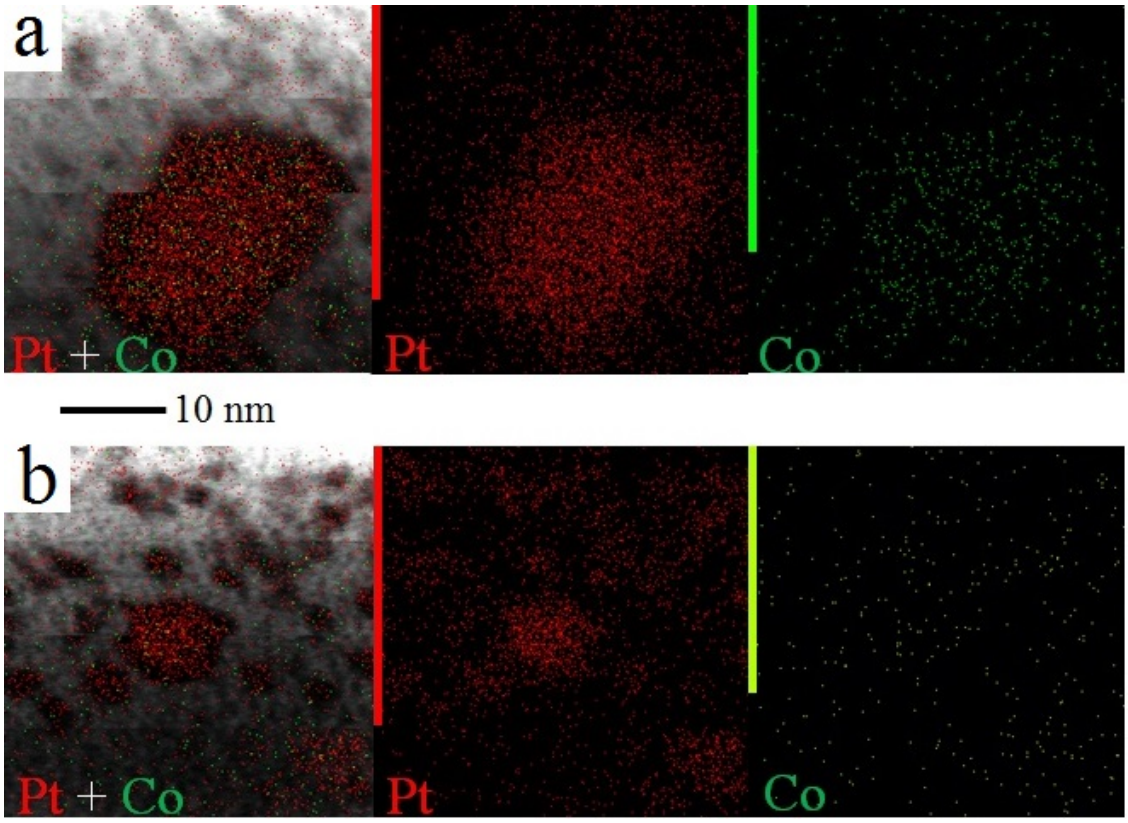

Figure 3.8: EDX elemental maps measured after acid washings of CX-Pt-Co (a) and CX-Pt723-Co samples (b), TEM micrographs are in the background of the bi-elemental maps for better legibility.

On TEM micrographs (Figure 3.1), large and small particles can be seen in each case, except for CX-Co-Pt sample where small particles only are present. CX-PtCo catalyst displays a higher amount of large particles than the other catalysts. The two bimetallic catalysts look similar: they contain a lot of small particles and some large particles.

All the XRD diffractograms show the presence of two types of crystallites (Figure 3.3). Indeed, two peaks are superimposed: (i) one broad peak due to crystallites with diameters of *ca.* 1.4-2.0 nm, $d_{\mathrm{XRD},1}$, and (ii) one narrow peak due to crystallites with diameters of *ca.* 10-14 nm, $d_{\mathrm{XRD},2}$. The presence of the two sizes of crystallites can be correlated to the two sizes of particles observed by TEM measurements. In general, the possible formation of PtCo alloys can be detected by diffraction peak shifts from the Pt diffraction angle to higher diffraction angles [34]. In Figure 3.3, the diffraction peaks are located at the Pt diffraction angles (39.7° for Pt (1 1 1) and 46.2° for Pt (2 0 0)); no peak shift is visible. Moreover, in all diffractograms, no Co nor Co oxide diffraction peaks are visible. XRD measurements were not able to detect metallic, oxidized, or alloyed Co while the presence of Co was shown by ICP-AES and EDX. This non-detection of Co peaks nor PtCo peaks could be explained by the non-presence of metallic or oxidized Co crystallites or alloyed Co. Co atoms would be present at the surface of Pt particles, as Co oxides or hydroxides, without forming crystallites or alloy.

For each sample, $d_{\mathrm{v},1}$ is higher than $d_{\mathrm{XRD},1}$ whereas $d_{\mathrm{v},2}$ is equivalent to $d_{\mathrm{XRD},2}$. This indicates that the small particles may be constituted of several small crystalline domains, as the crystallite diameter is lower than the particle diameter. On the contrary, large particles seems to be constituted of one large crystalline domain.

BET surface areas are rather constant and lower than that of the CX support. This drop could be explained by the partial blocking of micropores by the metal deposited on the support [35].

In CO stripping voltammograms (Figure 3.7), as no H desorption peak is visible at low potential, CO is assumed to fully cover the Pt surface. The values of the electroactive accessible Pt surface area, S_{CO}, are constant for the four catalysts (105-110 $\mathrm{m^2\ g_{Pt}^{-1}}$, Table 3.3). These high values of S_{CO} are a clue with regard to the composition of the small particles. Indeed, the majority of the small particles must be pure Pt particles in order to exhibit these high surface areas. Contrary to previous measurements, CO stripping analysis give some indication on the nature of the small particles: the majority of them must be pure Pt particles. Coupling CO stripping results with EDX measurements, one can suppose that some other particles are Co-enriched or Co oxides particles.

For pure Pt catalysts, the potential at which CO electrooxidation occurs can be related to the particle size [25–27]. The higher the oxidation potential, the lower the Pt particle size. Taking ICP-AES results into consideration, two catalysts can be considered as CX-supported Pt catalysts: CX-Co-Pt and CX-PtCo. They can be compared to the Pt/C reference. In Figure 3.7, the oxidation potentials of the peaks are equal to 0.83, 0.86, and 0.93 V *vs.* NHE for Pt/C, CX-PtCo,

and CX-Co-Pt respectively. No oxidation peaks representative of large particles or aggregates are detected at lower potential. CX-Co-Pt peak is the one occurring at the highest oxidation potential, followed by CX-PtCo peak and, finally, by Pt/C peak. This means that CX-Co-Pt is composed of the smallest particles amongst the Pt catalysts and Pt/C is composed of the largest particles. This result corroborates the TEM results when comparing the small particles, *i.e.* when comparing $d_{s,1}$ to d_{CO}. Indeed, for the synthesized catalysts, CX-Co-Pt and CX-PtCo, d_{CO} is equal to 2.7 nm and $d_{s,1}$ is equal to 2.1 and 2.2 nm respectively. d_{CO} is slightly higher than $d_{s,1}$ because d_{CO} is a surface average diameter including all particles, not only the small ones like $d_{s,1}$. Despite that, the two diameters are close to each other. The commercial catalyst, Pt/C, displays higher d_{CO} and $d_{s,1}$ than CX-Co-Pt and CX-PtCo. They are equal to 3.0 and 3.4 nm respectively. This result corroborates the previous discussion about the particle size of pure Pt catalysts.

For the two bimetallic catalysts, CX-Pt-Co and CX-Pt723-Co, the presence of Co prevents from drawing the same conclusions, as CO molecules do not adsorb on or are not electrooxidized by Co and as Co atoms are present at the surface of the particles (shown by EDX results). However, one can see that the CO electrooxidation peak of CX-Pt723-Co is slightly shifted towards lower potential. This shift may be caused by the cleaning of the Pt particles before the Co deposition. Indeed, a previous study shows that reduction at high temperature cleans the surface of Pt particles deposited on CX from chlorine ions [16]. This cleaning induces an improvement in the interactions between surface Pt atoms and CO and H_2O molecules which are needed for the CO electrooxidation reaction [25–27]. This improvement results in a shift of the CO electrooxidation peak to lower potential for the catalysts which was reduced at high temperature before Co deposition, *i.e.* CX-Pt723-Co.

For the CX-supported Pt catalysts (CX-Co-Pt and CX-PtCo), the catalyst with the higher *SA* and *MA* is CX-PtCo (Table 3.3). This discrepancy may be due to the Pt particle size. Indeed, CX-Co-Pt contains very small particles only, with diameter lower than 2 nm. Considering that the optimal diameter is around 3-4 nm [36, 37], this can explain why CX-PtCo displays higher activities than CX-Co-Pt as CX-PtCo is composed of small (1.7 nm) and large (9.9 nm) particles while CX-Co-Pt is composed of small particles only (1.7 nm). Indeed, small particles exhibit low activity and high surface area, while large particles exhibit high activity but low surface area. As CX-Co-Pt is composed of small particles only, it displays low activity with high surface. On the contrary, CX-PtCo is composed of a majority of small particles, leading in high surface area, and of large particles, increasing the catalytic activity.

For the bimetallic catalysts, CX-Pt-Co and CX-Pt723-Co, the catalyst with the higher *SA* and *MA* is CX-Pt723-Co (Table 3.3). The reason for this may be the cleaner surface of Pt particles in the CX-Pt723-Co catalyst. As demonstrated in Ref. [16], the high temperature reduction (723 K during 5 h) of Pt particles before Co deposition cleans the Pt particles surface as it removes the poisoning chlorine ions from this surface. As particles are freed from poisoning chlorine anions, the cleaner Pt surface may lead to better interactions between the Pt surface atoms and other

molecules, especially oxygenated species, such as hydroxyl groups (OH_{ads}). These OH_{ads} groups are inevitable steps for the oxygen reduction. Therefore, as might be expected, the cleaning of the particles surface can improve interactions between surface atoms and reactive species, and so, improve the activities. However, the cleaning of the particle surface does not affect the PtCo alloy formation, as neither CX-Pt-Co nor CX-Pt723-Co contains PtCo alloys.

The performance of the four catalysts can be compared to the performance of a commercial catalyst: the reference used in this thesis is a Tanaka Pt/HSAC catalyst with a Pt loading of 37 wt.%. This reference catalyst is composed of Pt particles with an average particle size of 3.1 nm (σ of 1.1 nm) and its performances, measured following the same procedure and in the same conditions as before, are *SA* equals to 0.091 A ${m_{Pt}}^{-2}$ and *MA* equals to 8.2 A ${g_{Pt}}^{-1}$ at 0.9 V *vs.* NHE. These activities are around twice the activities of the four catalysts studied in this chapter. It is assumed that the lack of activity of the synthesized catalysts is due to the fact that the average particle size is lower than the optimal value.

Among the four synthesized catalysts, the better are CX-Pt723-Co and CX-PtCo (Table 3.3). Contrary to what was expected, one observes no difference in activity between these bimetallic and Pt catalysts. Their activity are even below the reference activity. This low activity can be explained by the lack of interactions between Pt and Co atoms and by the particle size, which is too small to display high activity.

3.5 Conclusion

In order to synthesize bimetallic PtCo catalysts, three impregnation methods were studied, using the strong electrostatic adsorption method for Pt deposition and the wet impregnation method for Co deposition: (i) Co impregnation before Pt impregnation, (ii) Co impregnation after Pt impregnation, (iii) Co and Pt simultaneous impregnation. As Co is dissolved in the Pt impregnation solution, only the synthesis method in which Pt is deposited first leads to bimetallic catalyst, as shown by ICP-AES and EDX results. The metal loading of the bimetallic catalysts is 20 wt.% of Pt and 3 wt.% of Co. TEM micrographs shows the presence of small (less than 2 nm) and large (over 10 nm) particles for all the samples, except CX-Co-Pt, *i.e.* the catalyst obtained by Co deposition followed by Pt deposition, which contains small particles only. These results were corroborated by XRD measurements where two different peaks, broad and sharp, corresponding to small and large particles respectively, are visible. The X-ray diffractogram of CX-Co-Pt also shows a small sharp peak representative of large particles but to a lesser extent than the other catalysts. EDX results indicate that, in bimetallic catalysts, the large particles contains Pt and Co atoms. However, no Pt-Co interactions were detected by XPS analysis, no XRD diffraction peak shift is observed, and no Co was detected by EDX measurement performed after acid washing. These results indicate that the large particles are Pt particles with Co oxides clusters at their surface.

The four catalysts are constituted of a majority of small particles. This is proved by their high Pt electroactive surface area measured by CO stripping voltammetry. The high amount of particles with diameter under 2 nm leads to low activity for the ORR, as the specific activity for the ORR decreases with the particle size. Indeed, the CX-supported Pt catalyst with large particles, CX-PtCo, exhibits the best specific activity for the ORR compared with CX-Co-Pt which displays small particles only. The other catalyst with the best specific and mass activity for the ORR, CX-Pt723-Co, is the bimetallic catalyst with the cleaner Pt surface leading to better affinity with oxygenated species, as shown by CO stripping voltammograms.

However, when the activities of the synthesized catalysts are compared to the activity of a reference, commercial catalyst, the performances of the synthesized catalysts are still too low to compete with those of commercial catalysts. In order to improve the performance of the bimetallic catalysts, alloys must imperatively be formed, what the chosen strategy of this chapter did not permit. Solutions to form alloy could be the use of controlled thermal treatments, such as annealing [38] or the development of another synthesis technique, as performed in the next chapter.

References

[1] J. R. Regalbuto, *Catalyst Preparation: Science and Engineering*, CRC Press/Taylor & Francis Group, Boca Raton, United States of America, 2006.

[2] N. Job, S. D. Lambert, M. Chatenet, C. J. Gommes, F. Maillard, S. Berthon-Fabry, J. R. Regalbuto, and J.-P. Pirard, *Catalysis Today* **150**, 119 (2010).

[3] A. Zubiaur, M. Chatenet, F. Maillard, S. D. Lambert, J.-P. Pirard, and N. Job, *Fuel Cells* **14**, 343 (2014).

[4] S. D. Lambert, N. Job, L. D'Souza, M. Pereira, R. Pirard, B. Heinrichs, J. Figueiredo, J.-P. Pirard, and J. Regalbuto, *Journal of Catalysis* **261**, 23 (2009).

[5] J. Regalbuto, A. Navada, S. Shadid, M. Bricker, and Q. Chen, *Journal of Catalysis* **184**, 335 (1999).

[6] H. A. Gasteiger, S. S. Kocha, B. Sompalli, and F. T. Wagner, *Applied Catalysis B: Environmental* **56**, 9 (2005).

[7] H. A. Gasteiger and M. F. Mathias, Fundamental research and development challenges in polymer electrolyte fuel cell technology, in *Proceedings of the 3rd symposium on proton conducting membrane fuel cells*, edited by M. Murthy, pp. 1–24, Salt Lake City, United States of America, 2002, Electrochemical society.

[8] C. Jaffray and G. A. Hards, Precious metal supply requirements, in *Handbook of Fuel Cells Fundamentals, Technology and Applications, vol. 3*, edited by W. Vielstich, A. Lamm, and H. A. Gasteiger, chapter 41, p. 509, Wiley, Chichester, United Kingdom, 2003.

[9] B. Hammer and J. K. Nørskov, *Surface Science* **343**, 211 (1995).

[10] J. R. Kitchin, J. K. Nørskov, M. A. Barteau, and J. G. Chen, *Journal of Chemical Physics* **120**, 10240 (2004).

[11] T. Bligaard and J. K. Nørskov, *Electrochimica Acta* **52**, 5512 (2007).

[12] I. E. L. Stephens, A. S. Bondarenko, F. J. Perez-Alonso, F. Calle-Vallejo, L. Bech, T. P. Johansson, A. K. Jepsen, R. Frydendal, B. P. Knudsen, J. Rossmeisl, and I. Chorkendorff, *Journal of the American Chemical Society* **133**, 5485 (2011).

[13] I. E. L. Stephens, A. S. Bondarenko, U. Grønbjerg, J. Rossmeisl, and I. Chorkendorff, *Energy & Environmental Science* **5**, 6744 (2012).

[14] M. Oezaslan and P. Strasser, *Journal of Power Sources* **196**, 5240 (2011).

[15] N. Job, R. Pirard, J. Marien, and J.-P. Pirard, *Carbon* **42**, 619 (2004).

[16] N. Job, M. Chatenet, S. Berthon-Fabry, S. Hermans, and F. Maillard, *Journal of Power Sources* **240**, 294 (2013).

[17] E. Marceau, X. Carrier, and M. Che, Impregnation and Drying, in *Synthesis of Solid Catalysts*, edited by K. P. de Jong, pp. 59–82, Wiley-VCH Verlag GmbH & Co. KGaA, Weinheim, Germany, 2009.

[18] G. L. Bezemer, J. H. Bitter, H. P. C. E. Kuipers, H. Oosterbeek, J. E. Holewijn, X. Xu, F. Kapteijn, a. J. van Dillen, and K. P. de Jong, *Journal of the American Chemical Society* **128**, 3956 (2006).

[19] A. J. Lecloux, Texture of catalysts, in *Catalysts: Science and Technology*, edited by J. R. Anderson and M. Boudart, pp. 171–230, Springer-Verlag, Berlin, Germany, 1981.

[20] E. W. Washburn, *Proceedings of the National Academy of Sciences of the United States of America* **7**, 115 (1921).

[21] N. Job, A. Théry, R. Pirard, J. Marien, L. Kocon, J.-N. Rouzaud, F. Béguin, and J.-P. Pirard, *Carbon* **43**, 2481 (2005).

[22] N. Job, B. Heinrichs, F. Ferauche, F. Noville, J. Marien, and J.-P. Pirard, *Catalysis Today* **102-103**, 234 (2005).

[23] E. Guilminot, A. Corcella, M. Chatenet, and F. Maillard, *Journal of Electroanalytical Chemistry* **599**, 111 (2007).

[24] M. Chatenet, L. Dubau, N. Job, and F. Maillard, *Catalysis Today* **156**, 76 (2010).

[25] F. Maillard, M. Eikerling, O. V. Cherstiouk, S. Schreier, E. Savinova, and U. Stimming, *Faraday Discussions* **125**, 357 (2004).

[26] F. Maillard, S. Schreier, M. Hanzlik, E. R. Savinova, S. Weinkauf, and U. Stimming, *Physical Chemistry Chemical Physics* **7**, 385 (2005).

[27] F. Maillard, E. R. Savinova, and U. Stimming, *Journal of Electroanalytical Chemistry* **599**, 221 (2007).

[28] H. Schulenburg, J. Durst, E. Müller, A. Wokaun, and G. G. Scherer, *Journal of Electroanalytical Chemistry* **642**, 52 (2010).

[29] U. Paulus and A. Wokaun, *J. Phys. Chem. B.* **106**, 4181 (2002).

[30] S. Trasatti and O. Petrii, *Journal of Electroanalytical Chemistry* **327**, 353 (1992).

[31] A. J. Bard and L. R. Faulkner, *Electrochemical Methods: Fundamentals and applications*, John Wiley & Sons, Inc., Weinheim, Germany, 2nd edition, 2001.

[32] G. Bergeret and P. Gallezot, Particle size and dispersion measurement, in *Handbook of Heterogeneous Catalysis*, edited by G. Ertl, H. Knözinger, and J. Weitkamp, p. 439, Wiley-VCH, Weinheim, Germany, 1997.

[33] M.-L. C. Piedboeuf, A. F. Léonard, K. Traina, and N. Job, *Colloids and Surfaces A: Physicochemical and Engineering Aspects* **471**, 124 (2015).

[34] S. Chen, W. Sheng, N. Yabuuchi, P. J. Ferreira, L. F. Allard, and Y. Shao-Horn, *Journal of Physical Chemistry C* **113**, 1109 (2009).

[35] N. Job, M. F. R. Pereira, S. D. Lambert, A. Cabiac, G. Delahay, J.-F. Colomer, J. Marien, J. L. Figueiredo, and J.-P. Pirard, *Journal of Catalysis* **240**, 160 (2006).

[36] K. Kinoshita, *Journal of the Electrochemical Society* **137**, 845 (1990).

[37] O. Antoine, Y. Bultel, and R. Durand, *Journal of Electroanalytical Chemistry* **499**, 85 (2001).

[38] A. Schenk, C. Grimmer, M. Perchthaler, S. Weinberger, B. Pichler, C. Heinzl, C. Scheu, F. A. Mautner, B. Bitschnau, and V. Hacker, *Journal of Power Sources* **266**, 313 (2014).

Chapter 4

Synthesis and characterization of hollow PtCo nanoparticles supported on carbon xerogel as electrocatalysts for the oxygen reduction reaction

After the attempt to synthesize bimetallic PtCo catalysts performed in the third chapter, the fourth chapter describes a method to synthesize hollow PtCo nanoparticles deposited on carbon xerogel. The goal of this chapter is to synthesize highly active PtCo catalysts with a particular structure which should enhance their durability. The synthesis method developed in this chapter is based on a Pt deposition technique studied in Chapter 2: the synthesis of a Pt colloid. Despite the fact that Pt/CX catalysts obtained by the colloid method in Chapter 2 were less active than those prepared using other techniques, the colloid synthesis was here performed to obtain a particular nanoparticle structure. The obtained hollow PtCo deposited on carbon xerogel were then characterized in a three electrode cell and their properties were compared to synthesized Pt/CX catalysts and a commercial Pt/C catalyst.

4.1 Introduction

Commercial Pt on carbon (Pt/C catalysts) commonly used in proton exchange membrane fuel cell (PEMFC) cathodes exhibit several drawbacks preventing PEMFC large-scale commercialization [1, 2]. It is well known that the two major drawbacks of commercial Pt/C catalysts are the instability and the non-optimal activity for oxygen reduction reaction (ORR) [3].

In order to improve the catalytic activity, researchers from the last decades focused on alloying the Pt nanoparticles with transition metals (PtM), *e.g.* Co and Ni [1–8]. Indeed, the transition metals, when alloyed with Pt, increase the activity of the latter by strain-ligand effect, *i.e.* by contracting the Pt lattice parameter leading to a widening of the *d*-band and a decrease of the average energy of the band (the *d*-band center) [9–11]. The modification of the Pt *5d*-band impacts the adsorption properties of species, such as hydroxyl groups ($OH^{\bullet}$) and other oxygenated species [12, 13]. These oxygenated species, which are intermediates formed during the ORR, are usually bound too strongly to the Pt atoms, limiting the ORR performance. Through strain-ligand effect, these bonds are weakened, leading to binding energy closer to the optimum according to Sabatier's principle, *i.e.* the best catalyst for a chemical reaction involving adsorbates has to display a binding energy with the reactive species neither too weak, in order for the reaction to take place, nor too strong, otherwise the reactive species do not dissociate and block the catalytic sites.

In the recent years, researchers explored two different ways of improvement for PtM catalysts for ORR. On the one hand, some of them worked on increasing the activity by means of extended surfaces and well-defined facet catalysts. These improvements were based on a study of Stamenkovic *et al.* [8] which showed the huge ORR activity of the Pt_3Ni (1 1 1) facet. A lot of structures with well-defined and very active facets were then studied, *e.g.* octahedra [14, 15], nanoframes [16], nanostructured thin films [17]. On the other hand, other researchers worked on increasing the activity by increasing the density of structural defects. Indeed, the presence of structural defects leads to formation of low and high coordination active sites and contracted and dilated active sites which impact the adsorption properties of species, particularly the oxygenated species [18,19]. For example, low coordination active sites can strongly bind $OH^{\bullet}$ species promoting the oxidation reactions, such as carbon monoxide (CO) oxidation. On the contrary, high coordination active sites bind weakly $OH^{\bullet}$ species, making them active sites for reduction reactions such as ORR [20]. Nanoparticles displaying high density of structural defects have particular structures like nanoporous particles [7, 21], sponge particles [21–23], and hollow nanoparticles [21, 24–26].

All these metallic nanoparticles are commonly supported on high surface area carbons (HSACs) and carbon blacks (CBs). HSACs and CBs are not optimal for PEMFCs. Indeed, they exhibit several drawbacks: (i) the disordered graphitic domains of these carbon support are corroded during PEMFC nominal utilization [27]; (ii) the porosity of catalytic layers constituted of CB-supported catalysts is not con-

trollable, which may induce mass-transport limitations [27, 28]; (iii) they may contains impurities [28]. A solution to these two last drawbacks is to use a synthetic carbon material with reproducible and controllable texture, such as carbon xerogels (CXs) [29]. However, surface modification of the CXs is still required to avoid carbon corrosion.

The objective of the present chapter is to develop an easy-to-perform method to synthesize hollow PtCo nanoparticles deposited on CX. Hollow nanoparticles display higher activity [2,21,25,26] and are more stable than usual Pt nanoparticles [24,30]. Hollow PtCo and PtNi nanoparticle synthesis methods already exist in literature [21, 31]. However, these synthesis methods are essentially one-pot syntheses, *i.e.* methods during which all the reactive species are added and mixed at the beginning. This leads to a limited number of variables which can be used in order to modify and control the various parameters of the hollow nanoparticles, *e.g.* particle diameter, shell thickness, particle composition, *etc.* These variables are principally the amount of metallic salts and the addition speed of the reductant ($NaBH_4$). This is why another method was studied in this chapter: the synthesis of hollow nanoparticles based on a colloid technique [32–36]. The synthesis method developed in this chapter starts from on a noble metal colloid method described by Pasqualeti *et al.* [37]. This method was adapted to synthesize a Co colloid. After the Co colloid formation, Pt salt was added in order to form Co@Pt core@shell particles, as Pt is reduced by galvanic replacement of Co atoms, *i.e.* the electrons needed to reduce Pt ions are provided by the oxidation of Co atoms [31, 38]. Such core@shell nanoparticles are unstable: Co atoms migrate from the core through the Pt shell *via* the nanoscale Kirkendall effect [39–41], leading to nanoparticles with hollow structures.

The present paper is focused on the synthesis and physicochemical and electrochemical characterization of PtCo hollow nanoparticles deposited on CX by the method described above. Three hollow PtCo/CX catalysts prepared under slightly different conditions, *i.e.* various stirring speeds during synthesis, were obtained and characterized. Their catalytic activity towards the oxygen reduction reaction (ORR) was compared to those of (i) two pure Pt/CX catalysts obtained *via* a liquid phase reduction technique (see Chapter 2) and (ii) a reference, commercial Pt/C catalyst (Tanaka, 37 wt.%).

4.2 Experimental

4.2.1 Syntheses

Carbon xerogel support CX used in this thesis was prepared by drying and pyrolysis of a resorcinol-formaldehyde gel [29]. This synthesis is fully described elsewhere [42]. Briefly, the gel was obtained by polycondensation of resorcinol with formaldehyde in water. The resorcinol/formaldehyde molar ratio, *R/F*, was set at 0.5, the resorcinol/sodium carbonate molar ratio, *R/C*, was chosen to be equal to

1,000 and the dilution ratio, D, *i.e.* the solvent/(resorcinol and formaldehyde) molar ratio, was fixed at 5.7. These variables were chosen in order to obtain a CX with a pore size distribution centered at 80 nm. After gelling and aging in an oven at 358 K for 48 h, the obtained gel was dried under vacuum, then ground with a planetary mill (PULVERISETTE 6, classical line, Fritsch, agate bowl and 1-cm balls) at 400 rpm during 70 min in order to obtain particles with a diameter of a few micrometers [43]. After grinding, the gel was pyrolyzed at 1073 K under nitrogen flow. The resulting CX particles exhibit a mean size of 7 µm, as measured by laser diffraction with a Mastersizer 2000 (see Reference [43] for more details).

Hollow PtCo particles on carbon xerogel The hollow PtCo particles on CX synthesis is based on a Pt colloid synthesis [37]. This method can produce Pt/CX catalysts with various Pt loading (from 5 to 25 wt.%, see Chapter 2 for the synthesis procedure of Pt/CX catalysts). In order to synthesize bimetallic PtCo particles, this procedure was modified to form a Co colloid. To do so, a reductant, sodium borohydride ($NaBH_4$), was added to a solution containing Co ions and citrate, leading to the formation of a colloid suspension of Co nanoparticles. This colloid was formed under Ar atmosphere in order to avoid any oxidation of the Co atoms by oxygen from the air. Once the colloid was synthesized, an acidic Pt salt was added. This addition decreases the pH of the suspension, leading to the protonation of citrate molecules, which desorb from the Co nanoparticles. The Pt ions were reduced and deposited on the Co nanoparticles surface by galvanic replacement, *i.e.* the electrons needed to reduce the Pt ions are provided by the Co oxidation. This galvanic replacement leads to Co@Pt core@shell nanoparticles. Finally, in order to obtain hollow PtCo nanoparticles, an acid washing was performed: hydrochloric acid was added to the suspension to increase the Co oxidation rate and favour the Co diffusion through the Pt shell, *i.e.* the so-called nanoscale Kirkendall effect, leading to hollow PtCo nanoparticles.

The hollow PtCo particles supported on CX were synthesized as follows: (i) 45.7 mg of cobalt chlorine hexahydrate ($CoCl_2 \cdot 6H_2O$) were dissolved in 160 mL of ultrapure water; (ii) to this, 40 mL of an aqueous solution of trisodium citrate dihydrate ($Na_3C_6H_5O_7 \cdot 2H_2O$, 2.6×10^{-2} mol/L) were added; (iii) the resulting solution was sonicated for 15 min, then (iv) poured in 360 mL of ultrapure water under stirring; (v) Ar was then bubbled during 30 min. The next steps were performed under Ar bubbling: (vi) 20 mL of an aqueous solution of sodium borohydride ($NaBH_4$, 9.6×10^{-2} mol/L, degassed by Ar bubbling during a few minutes) were added dropwise in 5 min; (vii) after 10 min stirring, 20 mL of an aqueous solution of hexachloroplatinic acid hexahydrate (CPA, $H_2PtCl_6 \cdot 6H_2O$, 3.2×10^{-3} mol/L, degassed by Ar bubbling during a few minutes) were added dropwise in 5 min; (viii) 30 min after the addition of CPA, Ar bubbling was stopped; (ix) after 90 min under stirring, 136 µL of hydrochloric acid 37% (HCl) were added, then (x) 40 mL of ultrapure water containing 100 mg of CX powder were added. Finally, (xi) the suspension was left under stirring overnight, then (xii) filtered, (xiii) thoroughly washed with ultrapure water, and (xiv) dried in an oven at 353 K during 40 min.

The amounts of Pt and Co were calculated in order to synthesize a catalyst with Pt and Co loadings of 10 wt.% in each metal, *i.e.* with a Pt:Co (1:3) initial molar ratio between the precursors. Three catalysts constituted of hollow PtCo particles deposited on CX are studied in this chapter. The difference between these three catalysts is the rotation speed of the magnetic stirrer during the synthesis: 1,000, 1,250, or 1,500 rpm, remaining constant throughout the whole process in each case. It must be noted that the reproducibility of this synthesis is investigated in the Appendix 4.A1 at the end of this chapter.

Pure Pt particles on carbon xerogel The previous hollow PtCo/CX catalysts will be compared to two Pt catalysts supported on CX, synthesized by formic acid (FA, HCOOH) reduction: one with a high Pt loading, the other with a low Pt loading (respectively, 37 and 10 wt.% of Pt). The synthesis procedure was as follows (see Chapter 2): (i) 0.3 g of CX were dispersed in 200 mL of 2 mol L^{-1} FA solution; (ii) the suspension was heated to 353 K in an oil bath; (iii) once the suspension reached 353 K, the volume of 4 mmol L^{-1} CPA solution needed to obtain the target Pt loading was added by 10 mL steps; (iv) after 1 h stirring, the suspension was filtered; (v) the catalyst was then washed 5 times with 125 mL of ultrapure water, and finally (vi) dried at 333 K in an oven under air overnight.

List of samples Hereafter, the three hollow PtCo/CX catalysts are labeled PtCo/CX-1000, PtCo/CX-1250, and PtCo/CX-1500, according to the rotation speed of the magnetic stirrer. The two pure Pt/CX catalysts are labeled 37Pt/CX and 10Pt/CX for the 37 wt.% and 10 wt.% of Pt, respectively. They will also be compared to a reference commercial catalyst: a Pt/HSAC Tanaka 37%, labeled hereafter Ref.

4.2.2 Physicochemical characterization

The metal weight percentages of the catalysts were measured by inductively coupled plasma-atomic emission spectrometry (ICP-AES) using an ICAP 6500 THERMO device. The solutions for the analyses were prepared as follows: an aliquot of the catalyst sample was weighed and digested by 10 mL of sulphuric acid (H_2SO_4) and 5 mL of nitric acid (HNO_3). This solution was heated at 573 K until clear. After the complete dissolution of the CX support and evaporation of the solution, 3 mL of HCl and 1 mL of HNO_3 were added. The obtained solution was heated a few minutes at 393 K and transferred into a 50 mL calibrated flask, which was finally filled by deionized water.

The catalysts were observed by transmission electron microscopy (TEM) with a Philips CM100 transmission electron microscope (100 kV, W filament) or with a Tecnai G2 Twin FEI (200 kV) device. Lacey F/C copper TEM grids (Ted Pella, Inc.) were put in contact with the catalyst powder. The grids were then shaken in order to remove the excess of catalyst particles from the grids. The catalyst particles remaining on the grids were observed by TEM.

The hollow PtCo nanoparticles were observed by high angle annular dark field - scanning transmission electron microscopy (HAADF-STEM). The atomic composition of these particles was investigated during the HAADF-STEM measurements by energy dispersive X-ray spectroscopy (EDX). These two measurements (HAADF-STEM and EDX) were performed with a JEOL 2100F microscope operated at 200 kV and equipped with a SDD Centurio retractable detector. The EDX line scans were recorded on individual nanoparticles by scanning the beam in a square region adjusted to the particle size. The quantitative analyses were performed on Pt M line and Co K line using the K-factor provided by the JEOL software.

4.2.3 Electrochemical characterization

Setup All the utilized glassware was cleaned by immersion in a H_2SO_4:H_2O_2 solution overnight and thoroughly rinsed with ultrapure water (18 MΩ cm). The electrolytic solutions were prepared from ultrapure water and perchloric acid ($HClO_4$, 70%, 99.999% trace metals basis, Aldrich). The electrochemical properties were measured with an Autolab PGSTAT30 in a three-electrode cell at room temperature. The reference electrode used during the electrochemical characterization was a home-made reversible hydrogen electrode (RHE) constituted of a Pt wire in contact with a hydrogen bubble and the 0.1 M $HClO_4$ liquid electrolyte, and connected to the cell by a Luggin capillary. The counter-electrode was a Pt gauze soldered on a Pt wire. The working electrode was the catalytic layer deposited on the glassy carbon disk, as explained in the next paragraph.

Catalytic layer preparation To measure the electrochemical properties of the catalysts, inks were first prepared. The ink composition was chosen to keep the amount of carbon constant (*i.e.* 19.8 mg), regardless of the metal loading [44, 45]. Each catalyst was crushed in a mortar, then the right amount was mixed with 755 mg of ultrapure water and 466 mg of 5 wt.% Nafion® solution. In order to blend it homogeneously, the mixture was then processed in an ultrasonic bath for 15 min. Once the ink was homogeneous, 10 µL of ink were deposited on a glassy carbon (GC) disk and sintered at 343 K during 20 min to evaporate the solvents and stick the catalyst on the GC disk. The catalytic layer deposited on the GC disk composes the working electrode for all electrochemical measurements. In the case of CX-supported catalysts, this procedure yields active layers of identical thickness onto the GC disk (*i.e.* resulting in identical mass-transport limitations within the layer [44,45]). It must be noted that the amount of Nafion® put in the ink and the amount of Pt put on the electrode are relatively high (Nafion® over CX mass ratio equal to 1:1; Pt amount deposited on the GC around 110 µg for the catalysts with the highest Pt loading). These high quantities were chosen for two reasons: (i) the 1:1 Nafion® over CX mass ratio was chosen in order to mimic the composition and structure of the cathode catalytic layer of a PEMFC; (ii) the high Pt content of the active layers prepared from high Pt loading catalysts results from the fact that the active layer of CX-supported catalysts were prepared in order to keep the same layer

thickness whatever the Pt loading. However, these choices can induce some decrease in performance for the studied catalysts. Indeed, a high Pt loading on the electrodes introduces large uncertainties to the activity measurements [46, 47]. Moreover, a large amount of Nafion® can cause problems in O_2 diffusion through the ionomer film and towards the Pt active sites as well as a high electronic resistance [48].

Electrolyte and wetting procedure For all electrochemical measurements, the electrode was immersed in a 0.1 M $HClO_4$ aqueous solution (*i.e.* electrolyte), which should enable full wetting of the metal particles by the electrolyte [45]. To ensure that all the pores were fully filled, a drop of electrolyte was first deposited onto the catalytic layer, in such a way that all the layer was covered. Then, the electrode was put under vacuum in order to outgas the layer by bubbling air through the drop. Once no air bubbles were visible, the electrode and the drop were put back under atmospheric pressure so that the drop filled the empty porosity of the layer, which ensured the full wetting of the catalyst. With this wetting procedure, the electrochemical measurements were usually steady and reproducible. In the case of Pt/CX catalysts, this procedure ensures that the Pt particle utilization factor is close to 100%. Indeed, previous works [42, 45, 49] performed on similar systems showed good consistency between the electroactive surface area measured after using this wetting procedure and the surface calculated from TEM micrographs.

Pretreatment of catalysts Prior to any measurement, the electrolyte was deaerated by Ar bubbling. Then, the working electrode, *i.e.* the catalytic layer deposited on the glassy carbon disk, was immersed in the electrolyte at a fixed potential of 0.4 V *vs.* RHE. Three voltammetry cycles were then performed between 0.05 V *vs.* RHE and 1.23 V *vs.* RHE at 0.05 V s^{-1}. Afterwards, five additional cycles were recorded at 0.02 V s^{-1} with the same potential boundaries.

CO stripping voltammetry The electroactive surface area of the nanoparticles was measured by CO stripping voltammetry [50–52]. The procedure was initiated by the application of a steady potential of 0.1 V *vs.* RHE to the working electrode, while gaseous CO was bubbled in the electrolyte solution for 6 min. After an Ar purge of 29 min which removes the CO dissolved in the electrolyte at this potential, the CO chemisorbed at the surface of the particles was electrooxidized into CO_2 by increasing the electrode potential from 0.05 to 1.23 V *vs.* RHE at 0.02 V s^{-1}. The electroactive surface area was calculated from the CO oxidation peak current, assuming that the electrooxidation of a full monolayer of CO_{ad} requires 420×10^{-2} C ${m_{Pt}}^{-2}$ [53].

Activity for the oxygen reduction reaction The catalysts activity for the oxygen reduction reaction (ORR) was measured on a rotating disk electrode (RDE) setup. After saturation of the electrolyte by oxygen bubbling during 20 min, the electrode potential was (i) set at 0.4 V *vs.* RHE, (ii) then increased at 0.005 V s^{-1} to 1.09 V *vs.* RHE, and (iii) decreased back to 0.4 V *vs.* RHE at the same scan rate while measuring the reduction current. This measurement was repeated at various rotation speeds of the electrode (400, 900, 1,600, and 2,500 rpm). For each rotation speed of the electrode, the kinetic current was calculated by correcting the measured current for the effect of the external mass transfer limitations in the solution using the Koutecky-Levich equation [54]:

$$\frac{1}{i_{\mathrm{k}}} = \frac{1}{i} - \frac{1}{i_{\mathrm{l,c}}} \tag{4.1}$$

where i_{k} is the kinetic current, *i.e.* the current without any mass transfer limitations, i is the experimental current, and $i_{\mathrm{l,c}}$ is the cathodic limit current, which depends on the rotation speed of the electrode. These kinetic current values were then averaged in order to obtain the kinetic current of the catalysts. The values of this averaged kinetic current at 0.9 V *vs.* RHE were divided by the electroactive surface of the catalysts in order to obtain the specific activity of the catalysts at 0.9 V *vs.* RHE, *SA* (in A $m_{Pt}{}^{-2}$), or divided by the mass of Pt deposited on the electrode in order to obtain the mass activity at 0.9 V *vs.* RHE, *MA* (in A $g_{Pt}{}^{-1}$).

4.3 Results

4.3.1 Physicochemical characterization

The physicochemical properties of the catalysts are summarized in Table 4.1. The three PtCo/CX catalysts exhibit Pt loading around 10 wt.% (9.8, 9.4, and 9.3 wt.% for PtCo/CX-1000, PtCo/CX-1250, and PtCo/CX-1500, respectively) and different Co loading values (0.3, 1.8, and 4.6 wt.%, respectively). 10Pt/CX displays a Pt loading close to that of the PtCo/CX catalysts, *i.e.* around 10 wt.% (10.2 wt.%). The other two Pt catalysts display a higher Pt loading of 37.0 wt.% (37Pt/CX and Ref).

TEM micrographs of the six samples are shown in Figure 4.1. The nanoparticles of the PtCo/CX catalysts are hollow in the three micrographs. Indeed, the particle cores are bright whereas the shells are dark, *i.e.* the particle cores are less dense than the shells. In Figure 4.1b and c, the few darker particles could correspond to Co@Pt core@shell particles as the particle cores are darker than the hollow particle cores. This may be due to a denser core constituted of Co atoms which were not removed during the acid washing. In these three micrographs, one also observes small particles with an average size around 3 nm. The three pure Pt catalysts display small nanoparticles, with diameters close to 3 nm (Table 4.1). The nanoparticles of the six catalysts are homogeneously distributed on the support.

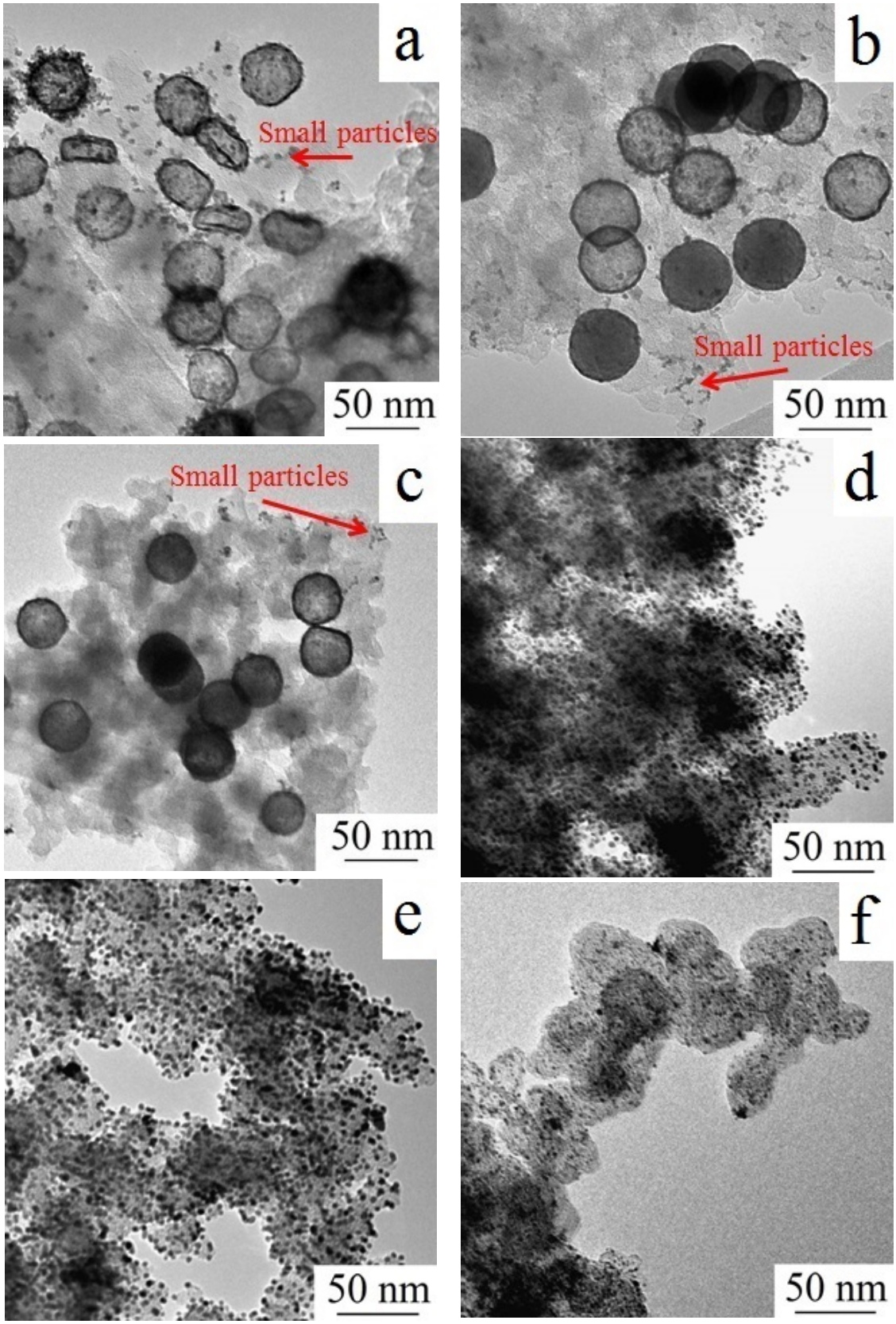

Figure 4.1: TEM micrographs of the six catalysts: PtCo/CX-1000 (a), PtCo/CX-1250 (b), PtCo/CX-1500 (c), 10Pt/CX (d), 37Pt/CX (e), and Ref (f).

Table 4.1: Catalyst properties determined from physicochemical analyses.

Catalyst	ICP		TEM							XRD
	Pt_{ICP} wt.% ± 0.1	Co_{ICP} wt.% ± 0.1	d_{TEM} nm	σ nm	d_{s} nm	d_{v} nm	t_{TEM} nm	σ_{t} nm	t_{v} nm	d_{XRD} nm ± 0.5
PtCo/CX-1000	9.8	0.3	41.0	6.2	42.7	43.3	3.3	0.7	3.7	3.6
PtCo/CX-1250	9.4	1.8	48.7	3.8	49.3	49.5	3.4	0.5	3.7	3.6
PtCo/CX-1500	9.3	4.6	45.0	3.1	45.4	45.6	3.4	0.7	3.9	3.6
10Pt/CX	10.2	–[a]	2.8	1.0	3.3	3.6	–[a]	–[a]	–[a]	2.3[b]
37Pt/CX	37.0	–[a]	3.6	1.2	4.0	4.4	–[a]	–[a]	–[a]	2.9
Ref	37.0	–[a]	3.1	0.8	3.4	3.6	–[a]	–[a]	–[a]	2.4[b]

Pt_{ICP}: Pt weight percentage of the catalyst measured by ICP-AES; Co_{ICP}: Co weight percentage of the catalyst measured by ICP-AES; d_{TEM}: average diameter of particles estimated from TEM micrographs; σ: standard deviation associated with d_{TEM}; d_{s}: surface-weighed average diameter of particles estimated from TEM micrographs and calculated by Equation (4.2); d_{v}: volume-weighed average diameter of particles estimated from TEM micrographs and calculated by Equation (4.3); t_{TEM}: average shell thickness of hollow particles estimated from TEM micrographs; σ_{t}: standard deviation associated with t_{TEM}; t_{v}: volume-weighed average shell thickness of hollow particles estimated from TEM micrographs and calculated by Equation (4.4); d_{XRD}: average crystallite size calculated from X-ray diffraction peaks *via* Equation (4.5).
Notes: [a] Not pertinent (pure Pt catalysts made of solid nanoparticles); [b] Large error due to low intensity of diffraction peaks.

Image analysis was performed on these micrographs in order to calculate the average diameter of particles, d_{TEM}, the standard deviation, σ, the surface-weighed average diameter of particles, d_{s}, and the volume-weighed average diameter of particles, d_{v}:

$$d_{\mathrm{s}} = \Sigma \frac{n_{\mathrm{i}} d_{\mathrm{i}}^3}{n_{\mathrm{i}} d_{\mathrm{i}}^2} \tag{4.2}$$

$$d_{\mathrm{v}} = \Sigma \frac{n_{\mathrm{i}} d_{\mathrm{i}}^4}{n_{\mathrm{i}} d_{\mathrm{i}}^3} \tag{4.3}$$

where n_{i} is the number of particles with diameter d_{i} [55]. For the hollow particles catalysts, other parameters were calculated such as the average shell thickness of hollow particles, t_{TEM}, the standard deviation, σ_{t}, and the volume-weighed average shell thickness of hollow particles, t_{v}, calculated by:

$$t_{\mathrm{v}} = \Sigma \frac{n_{\mathrm{i}} t_{\mathrm{i}}^4}{n_{\mathrm{i}} t_{\mathrm{i}}^3} \tag{4.4}$$

where n_{i} is the number of shells with thickness t_{i}. Results are shown in Table 4.1. The average diameter of particles, d_{TEM}, is equal to 41.0 ± 6.2, 48.7 ± 3.8, 45.0 ± 3.1, 2.8 ± 1.0, 3.6 ± 1.2, and 3.1 ± 0.8 nm for PtCo/CX-1000, PtCo/CX-1250, PtCo/CX-1500, 10Pt/CX, 37Pt/CX, and Ref, respectively. The values of the average shell thickness of hollow particles are equal to 3.3 ± 0.7, 3.4 ± 0.5, and 3.4 ± 0.7 nm for PtCo/CX-1000, PtCo/CX-1250, and PtCo/CX-1500, respectively. d_{s} of pure Pt catalysts can be compared to the CO equivalent diameter, d_{CO}, because CO stripping is surface-sensitive [56]. d_{v} of Pt catalysts and t_{v} of hollow PtCo catalysts can be compared to the average crystallite size, d_{XRD}, because X-ray diffraction is volume-sensitive [55].

HAADF micrographs, elemental distribution and line scan analysis of one PtCo hollow particle are displayed in Figure 4.2. Elemental maps consist in a mapping of the Pt and Co distribution over HAADF micrographs. For the EDX line scan analysis, the resulting scans are the sum of three scans measured along the three horizontal lines. In this figure, it can be seen that the Pt and Co atoms are located at the border of the particle, *i.e.* in the shell, and that the center of the particle contains less atoms than the shell, *i.e.* the particle core is hollow.

Figure 4.3 presents the X-ray diffractograms of the six catalysts. Scans are shifted vertically for better legibility. The theoretical values of diffraction angles of Pt (1 1 1) (39.7°), Co (1 1 1) (44.8°), Pt (2 0 0) (46.2°), and Pt (2 2 0) (67.4°) are reported as vertical lines. For all the bimetallic catalysts, no Co or Co oxide diffraction peaks are visible. The narrow peaks around 36, 50, 55, 60, and 68° are due to agate fragments coming from the wear of the grinding bowl and balls. Average crystallite sizes, d_{XRD}, were calculated by Scherrer's equation [55]:

$$d_{\mathrm{XRD}} = \frac{k\lambda}{\beta cos\theta} \tag{4.5}$$

where k is a dimensionless shape factor and equals 0.89 in the case of spherical nanoparticles, λ is the X-ray wavelength ($\mathrm{Cu_{K\alpha}}$: 1.5456 nm), β is the full width

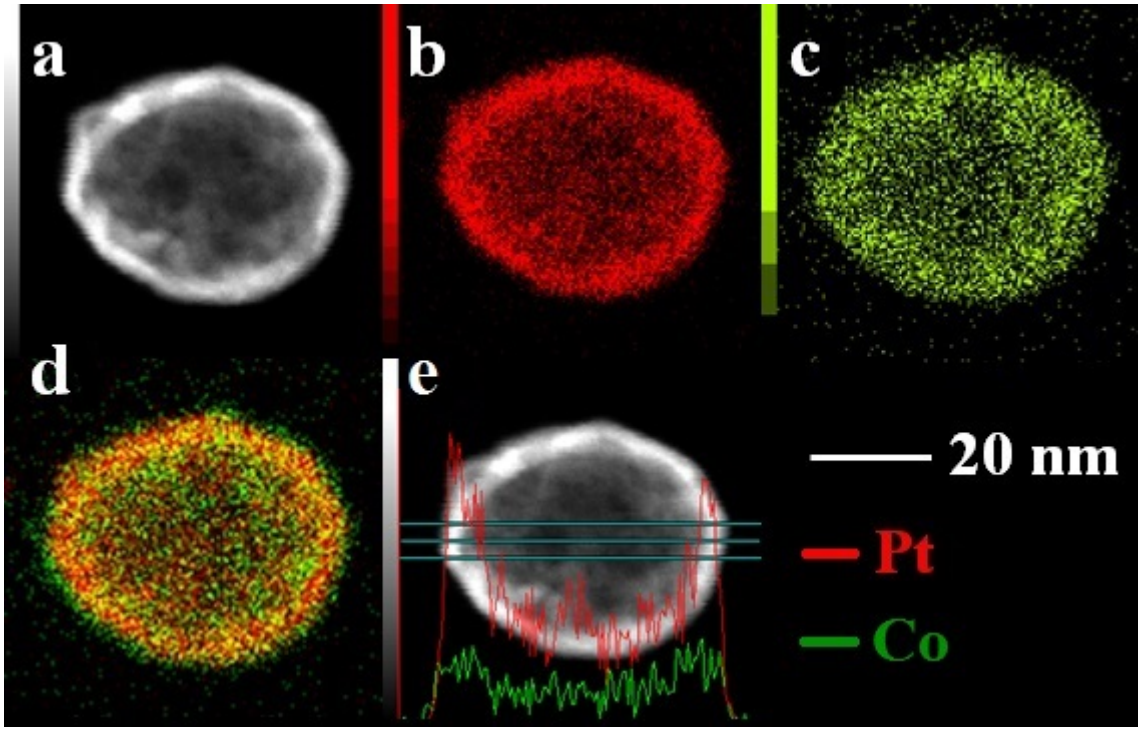

Figure 4.2: HAADF micrographs, elemental distribution and line scan analysis of a hollow nanoparticle of a PtCo/CX catalyst. From upper left corner to bottom right corner: HAADF micrograph of the particle (a), Pt elemental map (b), Co elemental map (c), Pt-Co bi-elemental map (d), EDX line scan analysis with HAADF micrograph in the background (e).

at half the maximum intensity (FWHM), and θ is the Bragg angle. The values of the average crystallite size, d_{XRD}, are equal to 3.6 nm for the three PtCo/CX catalysts and to 2.3, 2.9, and 2.4 nm for 10Pt/CX, 37Pt/CX, and Ref, respectively (see Table 4.1). As already mentioned, XRD is a volume-sensitive analysis: d_{XRD} corresponds thus to an average volume diameter and can be compared to d_{v} for the Pt catalysts and to t_{v} for the bimetallic catalysts [55].

4.3.2 Electrochemical characterization

Figure 4.4 shows the CO stripping voltammograms of the six catalysts. In this figure, the broadness of the CO electrooxidation peaks of the pure Pt catalysts can be due to the high Nafion® content in the catalytic layer (working electrode), to the nanoparticles size distribution, or to the presence of pollutants adsorbed on the Pt particle surface, *e.g.* Cl^-. However, as the larger broadening occurs for Ref catalyst which displays a narrow particle size distribution and no ion contamination (commercial catalyst), one can conclude that the broadening is mainly due to the high Nafion® content. Indeed, the formed Nafion® film probably slows the diffusion of the reactants between the electrolyte and the active sites, and therefore broadens

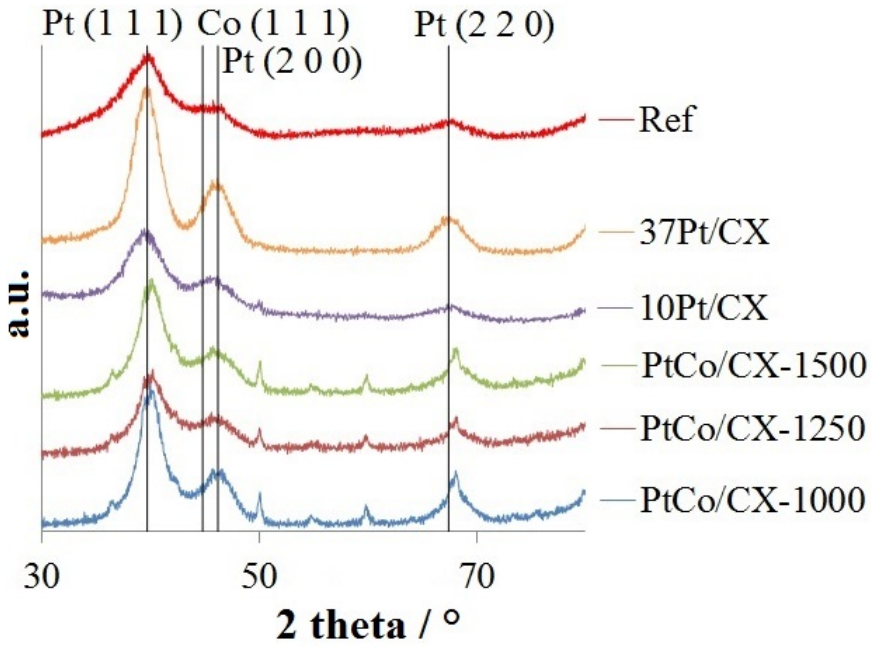

Figure 4.3: X-ray diffractograms of the six catalysts, vertically shifted for better legibility. The diffraction angles of Pt (1 1 1), Co (1 1 1), Pt (2 0 0), and Pt (2 2 0) are indicated, from left to right, by the vertical lines.

the response signal. In the case of PtCo/CX catalysts, two CO electrooxidation peaks can be seen on the Co stripping voltammograms: (i) the peak associated to structural defects around 0.7 V *vs.* RHE [21,25,26] and (ii) the small peak stemming from small Pt nanoparticles which could be present on the CX support or active sites isolated from structural defects and from which CO molecules can not diffuse, which appears around 0.8 V *vs.* RHE. The electroactive specific surface area, S_{CO}, and, in the case of pure Pt catalysts, the CO equivalent diameter of particles, d_{CO}, were calculated from the CO electrooxidation peaks. The values of these parameters are gathered in Table 4.2. The latter shows that S_{CO} is equal to 29, 22, 20, 66, 47, and 57 $m^2\ g_{Pt}{}^{-1}$ for PtCo/CX-1000, PtCo/CX-1250, PtCo/CX-1500, 10Pt/CX, 37Pt/CX, and Ref, respectively. The CO equivalent diameter, d_{CO}, is calculated by:

$$d_{CO} = \frac{6 \times 10^{-3}}{\rho_{Pt}\ S_{CO}} \tag{4.6}$$

where ρ_{Pt} is the Pt density (21.4×10^3 kg m^{-3}) [50–52]. d_{CO} was calculated for pure Pt catalysts only because, in the case of bimetallic particles, the possible presence of Co atoms at the particle surface, which do not adsorb CO molecules [57], may impact the surface measurement and because of the hollow morphology and the bimetallic composition of the shell, which prevent from using Equation (4.6). The values of d_{CO} equal 2.1, 5.6, and 3.1 nm for 10Pt/CX, 37Pt/CX, and Ref, respectively. As CO stripping voltammetry is a surface-sensitive method, d_{CO} corresponds to a surface-weighed average diameter and can be compared to d_s.

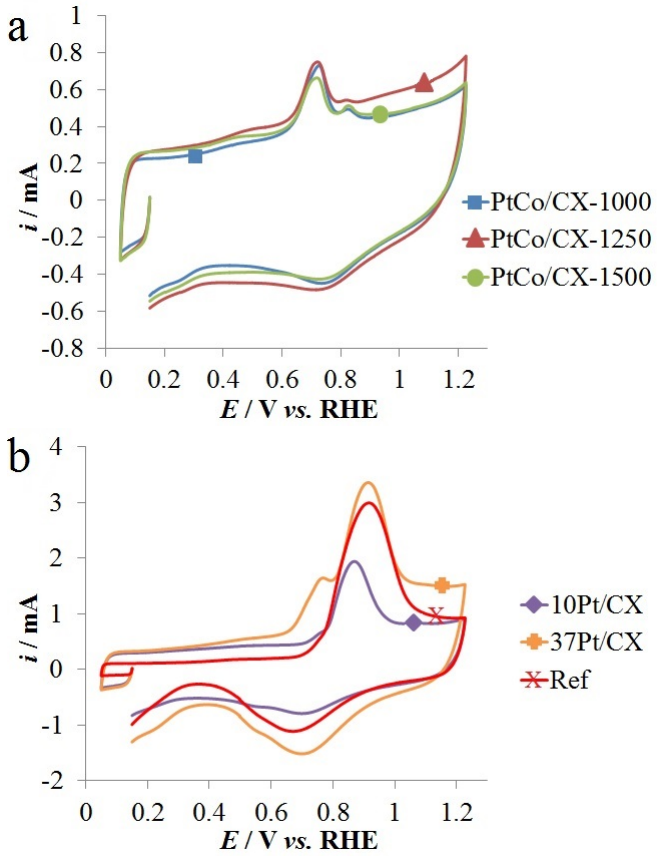

Figure 4.4: CO stripping voltammograms of the three bimetallic catalysts (a) and the three pure Pt catalysts (b) in 0.1 M $HClO_4$ at a sweep rate of 0.02 V s^{-1} at 298 K.

The catalytic activity of the catalysts were compared using the specific activity, *SA*, and the mass activity, *MA*, measured at 0.9 V *vs.* RHE (Table 4.2). *SA* values range from 0.22 (Ref) to 4.30 A $m_{Pt}{}^{-2}$ (PtCo/CX-1500). *MA* values range from 13 (Ref) to 90 A $g_{Pt}{}^{-1}$ (PtCo/CX-1000).

4.4 Discussion

The catalysts can be classified in two groups regarding their Pt loading: (i) the low Pt loading catalysts, *i.e.* the three PtCo/CX and 10Pt/CX catalysts, and (ii) the high Pt loading catalysts, *i.e.* 37Pt/CX and Ref. The former group exhibits a Pt loading around 10 wt.%, the latter group contains 37 wt.% of Pt. In the PtCo/CX catalysts, the Co quantity remaining after the acid washing increases with the stirring speed, from 0.3 to 4.6 wt.%. Assuming total alloying of Pt and Co, these loadings yield alloy compositions of 9 at.% of Co and 91 at.% of Pt for PtCo/CX-1000, 39 at.% of Co and 61 at.% of Pt for PtCo/CX-1250, 62 at.% of Co and 38 at.% of Pt for PtCo/CX-1500, *i.e.* to a Pt_9Co, Pt_3Co_2, or Pt_2Co_3 alloy

Table 4.2: Catalysts properties determined by electrochemical analyses.

Catalyst	CO stripping		ORR	
	S_{CO} $m^2\ g_{Pt}^{-1}$ ± 10%	d_{CO} nm ± 10%	*SA* A m_{Pt}^{-2} ± 10%	*MA* A g_{Pt}^{-1} ± 10%
PtCo/CX-1000	29	–[a]	3.18	90
PtCo/CX-1250	22	–[a]	4.05	87
PtCo/CX-1500	20	–[a]	4.30	88
10Pt/CX	66	2.1	0.44	29
37Pt/CX	47	5.6	0.61	29
Ref	57	3.1	0.22	13

S_{CO}: electroactive specific surface area of particles calculated from CO stripping measurements normalized by the mass of Pt on the electrode; d_{CO}: CO equivalent diameter of the particles calculated by Equation (4.6); *SA*: specific activity for the ORR measured at 0.9 V *vs.* RHE; *MA*: mass activity for the ORR measured at 0.9 V *vs.* RHE.
Notes: [a] Not pertinent (PtCo bimetallic catalysts).

composition, respectively. These values are gathered in Table 4.3 along with the theoretical values calculated assuming that all the metal added during synthesis is deposited and remains on the CX. The Pt loadings of the PtCo/CX catalysts are close to the target value of 10 wt.%. The Co loading is much lower than expected (from 0.3 to 4.6 wt.% instead of 10 wt.%). These values indicate that a significant amount of Co reduced upon $NaBH_4$ addition, *i.e.* when the Co nanoparticles are formed, is re-oxidized, dissolved, and eliminated during the next steps. It must be noted that all the added Co ions are reduced during the Co colloid formation step as the amount of $NaBH_4$ is in large excess, *i.e.* 10 times the necessary amount to reduce all the Co ions.

The PtCo/CX catalysts mainly consist of spherical hollow nanoparticles, as shown by the TEM micrographs (Figure 4.1a, b, and c), the HAADF results, and the EDX analysis (Figure 4.2). Indeed, in the TEM micrographs, the center of most particles appears brighter (*i.e.* denser) than their shells. In the HAADF micrograph (Figure 4.2a), the particle core appears darker than the shell. Moreover, the EDX analysis also shows that the particles are hollow as the Pt and Co atoms density is lower at the center of the particle compared to the shell. Furthermore, the line scan analysis shows that the atoms are concentrated at the border of the particles. In other words, the Pt and Co elemental maps of the EDX analysis correspond to the 2D projection of a hollow particle. However, all the synthesized particles are not hollow. Indeed, one can see some darker particles on the TEM micrographs of PtCo/CX-1250 and PtCo/CX-1500, *i.e.* the two PtCo/CX catalysts with the high-

est Co loading. This seems to indicate that some particles are still Co@Pt core@shell particles. So, for these two bimetallic catalysts, the assumption of complete alloying of Pt and Co is obviously not correct. The alloy compositions given by ICP-AES results are, in those case, global compositions.

The EDX analysis also shows the Pt and Co distribution in the hollow particle. The Pt and Co maps indicate that the particle shell is composed of Pt and Co atoms. XRD results agree with this interpretation. As the peak situated at the lowest diffraction angle of the PtCo/CX catalysts is slightly shifted from the Pt (1 1 1) diffraction angle (39.7°) to higher values around 40° (Figure 4.3), one can conclude that the Pt lattice is contracted due to the presence of Co atoms, forming PtCo alloys. Indeed, Table 4.3 shows the lattice parameter calculated from the diffraction angle of the Pt (1 1 1) peak for the three bimetallic catalysts and Ref. The former exhibit smaller lattice parameter than Ref (from 0.389 to 0.391 nm instead of 0.393 nm), resulting in lattice parameter contraction *ca.* 1% (0.7, 1.1, and 1.0% for PtCo/CX-1000, PtCo/CX-1250, and PtCo/CX-1500, respectively).

Starting from these lattice parameters, atomic composition of crystallites can be calculated *via* Vegard's law [58]. The Co content of crystallites is in all cases lower than the Co atomic composition of particles calculated from ICP-AES results (Table 4.3) (6.8, 10.7, and 10.2 at.% instead of 9, 39, and 62 at.% for PtCo/CX-1000, PtCo/CX-1250, and PtCo/CX-1500, respectively). This indicates again that all the Co is not alloyed to the Pt. Another information stemming from these results is that the lattice parameter contraction, and therefore the Co atomic composition in the crystallites, seem to reach maximum values around 1% and 10 at.%, respectively. Indeed, the two bimetallic catalysts with the higher Co loading, PtCo/CX-1250 and PtCo/CX-1500, exhibit the same lattice parameter. However, below a certain value of Co loading, the lattice parameter contraction seems to decrease, as indicated by the lower value of PtCo/CX-1000 lattice parameter contraction (0.7%). Moreover, the average crystallite size, d_{XRD}, which is equal to 3.6 nm for the three bimetallic catalysts, is almost equal to the volume-averaged thickness of the shell, t_{v} (3.7 nm for PtCo/CX-1000 and PtCo/CX-1250; 3.9 nm for PtCo/CX-1500). The similarity of d_{XRD} and t_{v} values suggests that the shell is composed of the crystallites detected by XRD. All these results demonstrate that the particle shells are constituted of PtCo alloy nanocrystallites, while some Co remains trapped at the center of some particles, *i.e.* forming Co@Pt core@shell nanoparticles, or inside small particles, *i.e.* forming Co-enriched alloy nanoparticles. It must be noted that, even if some core@shell particles are present, the Co cores can not be detected by XRD, as they become amorphous during the formation of the Pt shells and the acid leaching because of the galvanic replacement of Co by Pt and the interdiffusion between Co atoms and vacancies [59]. As the hollow nanoparticle shell is composed of a lot of PtCo crystallites with average diameter between 3 and 4 nm, one can assume that the particle surface present a high density of structural defects, such as grain boundaries. These structural defects play a role in ORR and increase the activity of the catalysts [21, 25, 26].

Table 4.3: ICP and XRD composition results.

Catalyst	ICP					XRD		
	Pt_{ICP}	Co_{ICP}	$Pt_{\mathrm{ICP,at}}$	$Co_{\mathrm{ICP,at}}$	**Alloy[a] composition**	**Lattice parameter**	**Lattice[b] contraction**	**Co content[c]**
	wt.% ± 0.1	wt.% ± 0.1	at.%	at.%		nm ± 0.001	%	at.% ± 10%
Theoretical[d]	10.0	10.0	25	75	$PtCo_3$	–[e]	–[e]	–[e]
PtCo/CX-1000	9.8	0.3	91	9	Pt_9Co	0.391	0.7	6.8
PtCo/CX-1250	9.4	1.8	61	39	Pt_3Co_2	0.389	1.1	10.7
PtCo/CX-1500	9.3	4.6	38	62	Pt_2Co_3	0.389	1.0	10.2
Ref	37.0	–[e]	100	–[e]	–[e]	0.393	0.0	0.0

Pt_{ICP}: Pt weight percentage of the catalyst measured by ICP-AES; Co_{ICP}: Co weight percentage of the catalyst measured by ICP-AES; $Pt_{\mathrm{ICP,at}}$: Pt atomic percentage of the catalyst calculated from ICP-AES measurements assuming total alloying of Pt and Co; $Co_{\mathrm{ICP,at}}$: Co atomic percentage of the catalyst calculated from ICP-AES measurements assuming total alloying of Pt and Co.

Notes: [a] Assuming total and homogeneous alloying of the two metals; [b] Lattice contraction *vs.* Ref; [c] Co content calculated by Vegard's law using the lattice contraction measured by XRD; [d] Theoretical values calculated from the total amount of Pt and Co added during the synthesis; [e] Not relevant.

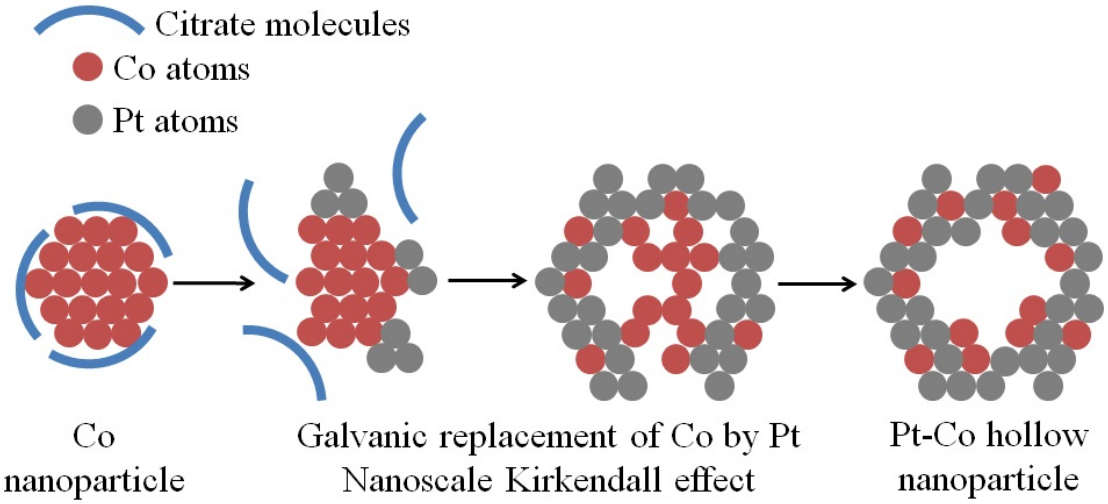

Figure 4.5: Schematic description of the formation of a PtCo hollow nanoparticle (adapted from [60]).

Figure 4.5 shows a schematic description of the formation of a hollow PtCo nanoparticle, starting from a Co nanoparticle and evolving to a hollow PtCo nanoparticle. First, a Co colloid is formed by reducing citrate-complexed Co ions with $NaBH_4$. After the formation of the Co particles colloid, acidic Pt salt is added to the colloid suspension. At the beginning of this step, as the suspension pH decreased, citrate molecules can protonate and detach from the Co particles, making them accessible to Pt ions. Then, Co atoms undergo galvanic replacement by Pt ions, *i.e.* the Co atoms oxidation produces the electrons needed for the Pt ions reduction [31, 38]. At this stage, the metallic particles of the suspension are Co@Pt core@shell particles. After Pt reduction, hydrochloric acid was added to dissolve the Co atoms located at the particle surface. Co atoms can thus be oxidized by protons as the standard electrode potential of Co^{2+}/Co is lower than the standard electrode potential of H^+/H_2 (-0.28 V *vs.* SHE and 0 V *vs.* SHE, respectively). However, no H_2 evolution was observed during synthesis but it can remain undetected because of the low amount of Co in the solution, and so the low amount of hydrogen possibly produced. After the acid addition, Co atoms from the particle core can diffuse through the Pt shell towards the particle surface *via* the nanoscale Kirkendall effect [25, 26, 39–41]. The nanoscale Kirkendall effect consists in the formation of porosity or deformations inside nanoscale bimetallic particles by interdiffusion of metal atoms and vacancies between the particle core and surface (metal atoms from core to surface and vacancies from surface to core) [39, 40], *e.g.* Co atoms diffusion through Pt in this case. The combination of all these phenomena leads to hollow PtCo nanoparticles.

In the case of pure Pt catalysts, TEM and XRD results are in agreement. The three catalysts are composed of small Pt particles *ca.* 3 nm. The catalyst with the smallest crystallite size, d_{XRD}, (2.3 nm) is one of the catalysts with the smallest

d_v, (3.6 nm), *i.e.* 10Pt/CX. 37Pt/CX displays the highest d_{XRD} and d_v values (2.9 and 4.4 nm, respectively). Ref is close to 10Pt/CX (d_{XRD} equals to 2.4 nm and d_v equals to 3.6 nm).

The Pt electroactive specific areas of Pt catalysts are in agreement with the physicochemical results. The smaller the particle size measured by TEM, the higher the Pt electroactive specific surface area. 10Pt/CX, which displays the smallest d_s (3.3 nm), exhibits the higher Pt electroactive specific area (66 m^2 $g_{Pt}{}^{-1}$), and therefore the lower CO equivalent diameter (2.1 nm). The other catalysts, in ascending order of particle size, are Ref (d_s equal to 3.4 nm, S_{CO} equal to 57 m^2 $g_{Pt}{}^{-1}$, and d_{CO} equal to 3.1 nm), then 37Pt/CX (d_s equal to 4.0 nm, S_{CO} equal to 47 m^2 $g_{Pt}{}^{-1}$, and d_{CO} equal to 5.6 nm). d_{CO} was not calculated for the bimetallic catalysts because of the possible presence of Co atoms at the particle surface, which do not adsorb CO molecules [57], and because of the hollow morphology and the bimetallic composition of the shell, which prevent from using Equation (4.6).

In Figure 4.4 showing CO stripping voltammograms of PtCo/CX catalysts (Figure 4.4a) and pure Pt catalysts (Figure 4.4b), the CO electrooxidation peaks provide information about particle morphology, *e.g.* the particle size and distribution in the case of Pt particles [50–52]. For pure Pt catalysts (Figure 4.4b), the higher the CO electrooxidation potential, the smaller the particle size. Ref displays a huge CO electrooxidation peak centered at 0.91 V *vs.* RHE. 37Pt/CX displays a CO electrooxidation peak at the same potential, *i.e.* at 0.91 V *vs.* RHE. Moreover, the CO stripping voltammogram of 37Pt/CX exhibits a second electrooxidation peak at 0.76 V *vs.* RHE, which is relative to aggregates [50,51]. 10Pt/CX displays a CO electrooxidation peak at a lower potential value, *i.e.* at 0.87 V *vs.* RHE, relative to Pt particles with diameters between 2.4 and 3.3 nm with a small shouldering around 0.76 V *vs.* RHE, corresponding again to aggregates [50–52]. The CO stripping voltammograms of the three PtCo/CX catalysts (Figure 4.4a) display two peaks: a peak at 0.71 V *vs.* RHE and a small peak around 0.80 V *vs.* RHE. The first peak (at 0.71 V *vs.* RHE) is associated to structural defects [21,25,26]. The area of this peak is proportional to the density of structural defects, *i.e.* the higher the peak area, the more defective the particle surface. Once again, structural defects are very effective for several reactions, including CO electrooxidation. This explains the low potential value at which the peak occurs. The small second peak (around 0.80 V *vs.* RHE) can stem from two types of active sites: (i) small Pt monocrystallites which can be present as nanoparticles on the CX support; (ii) active sites isolated from structural defects and from which CO molecules can not diffuse.

Regarding the ORR specific activity, the catalysts with the highest *SA* are clearly the PtCo/CX catalysts. Figure 4.6a shows the Tafel plot of the six catalysts and Figure 4.6b shows the *SA* and *MA* improvement factors calculated from the mass-transport-corrected curves at 0.9 V *vs.* RHE for all the studied catalysts. The improvement factor is defined as the ratio between the *SA* (or the *MA*) of the catalyst and the *SA* (or the *MA*) of the reference catalyst, Ref. The latter has, by definition, an improvement factor equal to 1. The improvement factors of the three PtCo/CX catalysts range from 14.4 for PtCo/CX-1000 to 19.5 for PtCo/CX-1500.

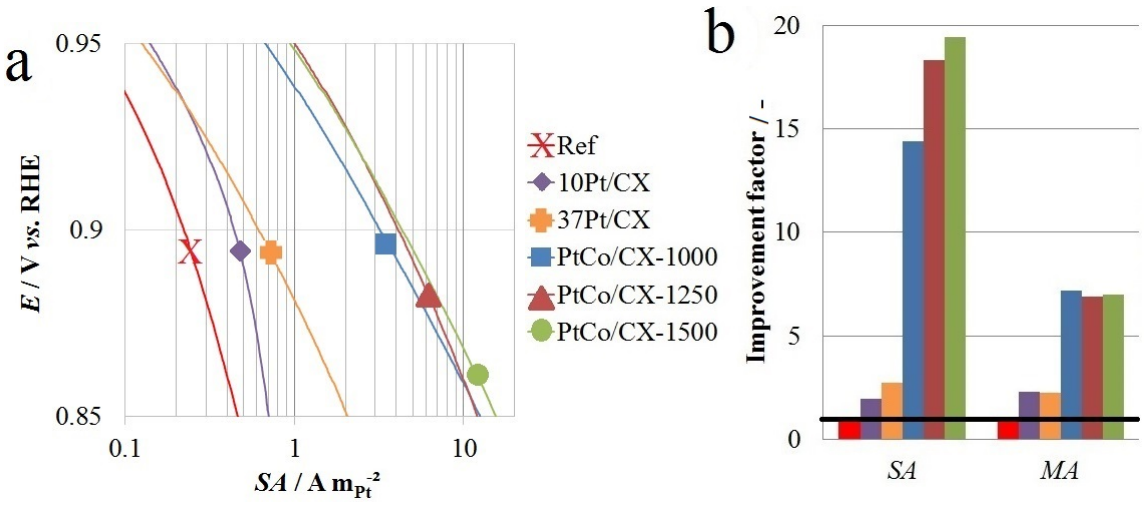

Figure 4.6: Tafel plot of the mass-transport-corrected kinetic current measured in 0.1 M $HClO_4$ electrolyte saturated with O_2 at 0.005 V s^{-1} (a). The curves are the average of four curves measured at different rotating speeds (400, 900, 1,600, and 2,500 rpm). *SA* and *MA* improvement factor of the six catalysts calculated at 0.9 V *vs.* RHE (b). By definition, the improvement factors of Ref are equal to 1 (represented by the horizontal black line).

This striking activity increase is due to the PtCo alloy, which constitute the shell of hollow particles, and to the high density of structural defects on the particle surface. Indeed, in presence of Co atoms, the Pt lattice is contracted. This contraction leads to a modification in the Pt *5d*-band, weakening the interaction between oxygenated species and Pt atoms, which increases the activity for the ORR [1–6]. Moreover, the presence of structural defects (high coordination active sites, in particular) increases the ORR performance because oxygenated species weakly bind to these active sites [18–20].

For pure Pt catalysts, as expected, the catalyst with the largest particles, 37Pt/CX, exhibits the highest specific activity, as the Pt atoms are more active at the surface of large particles than at the surface of small particles [61, 62]. Its improvement factor is equal to 2.8. Despite displaying higher d_{TEM} value than 10Pt/CX, Ref exhibits a twice lower *SA* value. The lower *SA* value of Ref may be explained by the high amount of Nafion® and Pt used to prepare the catalytic layer. Indeed, Nafion® can adsorb on Pt particles, lowering their accessibility to O_2 molecules, and therefore their activity [48]. The large amount of ionomer can also increase the electronic resistance of the working electrode. A high amount of Pt in the catalytic layer introduces large uncertainties to the results [46, 47]. For example, the O_2 diffusion limit can be reached at higher potential values or some unknown parameters (O_2 diffusion properties inside ionomer, agglomerate structure, and particle contact) can start influencing the results.

Regarding the ORR mass activity, the catalysts which display the best *MA* are again the PtCo/CX catalysts. They exhibit *MA* improvement factor of 7.2,

6.9, and 7.0 (PtCo/CX-1000, PtCo/CX-1250, and PtCo/CX-1500, respectively). The *MA* improvement factors of the bimetallic catalysts are lower than the *SA* improvement factors because the high *SA* values are counterbalanced by relatively small electroactive specific surface areas (around 20-30 $m^2\ g_{Pt}{}^{-1}$). CX-supported pure Pt catalysts, 10Pt/CX and 37Pt/CX, both display the same *MA* (29 A $g_{Pt}{}^{-1}$), and therefore the same *MA* improvement factor (2.3). Indeed, 37Pt/CX, which is composed of relatively large Pt particles (d_{TEM} equal to 3.6 nm), exhibits higher *SA* and lower S_{CO} than 10Pt/CX, which is composed of smaller Pt particles. So, when these properties are combined, they compensate each other, leading to the same *MA* for the two catalysts (29 A $g_{Pt}{}^{-1}$). 10Pt/CX and 37Pt/CX exhibit higher *MA* than Ref (13 A $g_{Pt}{}^{-1}$) because of their higher *SA* (0.44, 0.61, and 0.22 A $m_{Pt}{}^{-2}$ for 10Pt/CX, 37Pt/CX, and Ref, respectively) and because of the relatively similar S_{CO} values (66, 47, and 57 $m^2\ g_{Pt}{}^{-1}$ for 10Pt/CX, 37Pt/CX, and Ref, respectively).

When comparing the three PtCo/CX catalysts, one can see that the studied variable, *i.e.* the stirring speed, impacts the hollow particles composition and structure. In fact, the Co content in the shell increases with the stirring speed and seems to reach a limit around 10-11 at.% (Table 4.3). Moreover, the faster the stirring, the higher the global Co content. As shown in Table 4.1, the Co loading ranges from 0.3 wt.% (1,000 rpm) to 4.6 wt.% (1,500 rpm). This can be correlated with the TEM micrographs (Figure 4.1a, b, and c): core@shell particles can be seen in the micrographs of PtCo/CX-1250 and PtCo/CX-1500 only. It seems that slow stirring speed leads to the elimination of the Co core. Hypothetically, the higher Co amount of the fast stirring samples may be caused by a better homogenization of the suspension while adding reactants, especially the acidic Pt salt. Indeed, the pH drop resulting of this addition may be faster, resulting in a faster protonation of citrate. Protonated citrates may leave more quickly the Co particles which may be reached by the Pt ions in a small amount of time, leading to a faster Pt reduction, and so to a faster Pt shell formation. These Pt shells may protect the Co core leading in a higher amount of Co@Pt core@shell particles, *i.e.* in a higher Co content of the catalysts. However, further studies are necessary to confirm this hypothesis.

The stirring speed does not seem to impact the average particle size or the average shell thickness. However, the particle size distribution widens while decreasing the stirring speed (increase of σ). Moreover, in the TEM micrographs (Figure 4.1a, b, and c), the particles seem to be more spherical when the stirring speed is fast.

In all three TEM micrographs, some small particles, with an average size of 3.3 nm, can be seen on the CX. As XRD results indicate that the shell of the hollow particles are composed of PtCo alloy crystallites with an average size of 3.6 nm, one can assume that these small particles could be parts of broken hollow particles. Indeed, a few hollow particles look like aggregates of small particles (especially in Figures 4.1a and b). Furthermore, the crystallite size of the PtCo/CX catalysts determined by XRD results is the same for the three catalysts (3.6 nm) and is similar to the size of the small particles.

Concerning the electrochemical properties of the three PtCo/CX catalysts, the CO stripping curves of the three bimetallic catalysts are similar. The three catalysts display similar density of structural defects, *i.e.* the low potential peak of the CO voltammograms are similar. The electroactive specific area decreases when the stirring speed increases (from 29 to 20 m^2 $g_{Pt}{}^{-1}$). This may be due to a different amount of small particles on the CX, as the TEM micrographs seem to show. Indeed, CO stripping is more sensitive to the presence of small particles as they display a higher surface. A relatively slight decrease in the amount of small particles can be reflected by a significant decrease in S_{CO}. So, the amount of small particles seems to be inversely related to the stirring speed, as S_{CO} is inversely related to the stirring speed.

The major differences between the bimetallic catalysts is their specific activities for the ORR. Indeed, the *SA* increases with the stirring speed up to 4.30 A $m_{Pt}{}^{-2}$ (PtCo/CX-1500). As the density of structural defects seems similar for the three bimetallic cataysts, the *SA* value difference is probably due to the different Co content of the shell. In fact, PtCo/CX-1250 and PtCo/CX-1500 display high Co loading and similar Co composition of the shell, leading to comparable Pt lattice contraction and *SA* in the same range. However, it seems that, in the case of PtCo/CX-1000, the low total Co loading results in shell Co depletion, leading to lower Pt lattice contraction and a lower *SA*. The lattice contraction is related to the intrinsic Pt activity, translated into *SA*, and, in the range of Co shell compositions obtained in this chapter, the more Co atoms the shell contains, the higher the *SA*. However, the differences between the bimetallic catalysts *SA* are counterbalanced by the differences in S_{CO}, leading to similar mass activities (87 to 90 A $g_{Pt}{}^{-1}$).

4.5 Conclusion

In summary, hollow PtCo spherical nanoparticles supported on carbon xerogel were synthesized *via* a water-based method in liquid phase, at room temperature. They exhibit relatively small electroactive specific surface area, S_{CO}, (between 20 and 29 m^2 $g_{Pt}{}^{-1}$), due to the large diameter of the hollow particles (between 41.0 and 48.7 nm), but high specific and mass activities (between 3.18 and 4.30 A $m_{Pt}{}^{-2}$ and between 87 and 90 A $g_{Pt}{}^{-1}$, respectively, measured at 0.9 V *vs.* RHE in 0.1 M $HClO_4$ electrolyte). When comparing them to a commercial 37 wt.% Pt/C catalyst (from Tanaka), the specific activity (*SA*) of the bimetallic catalysts is 14.4 to 19.5 times higher than that of the commercial catalyst. The high *SA* is related to the Co content in the particle shell of the catalysts and to the high density of structural defects at the particle surface. The mass activity (*MA*) of the bimetallic catalysts is *ca.* 7 times higher than that of the commercial catalyst. This is a smaller increase than in the case of the *SA* because the high *SA* values of these catalysts are counterbalanced by their low S_{CO}.

To conclude, the hollow particles synthesis based on tri-sodium citrate yields catalysts with high performance. However, a streamlining of the synthesis process should be performed before scaling-up. To do so, several studies could be performed in order to analyze the impact of each synthesis variable. Moreover, the high performance of the hollow particles catalysts could be enhanced by an optimization of the variables of the synthesis. Indeed, further works could be performed in order to overcome the weak points of these catalysts, *e.g.* the low electroactive specific area. Solutions to improve S_{CO} may be to decrease the particle diameter or to change the shell structure, *e.g.* synthesizing porous shells. So, further studies must be conducted to investigate the impact of the structure modification (diameter, shell thickness, *etc.*) and the impact of the metal loading on the catalyst performance. The other major advantage of hollow nanoparticles, besides the high activity, is usually their better stability than that of usual Pt nanoparticles [63–65]. So, the stability and durability of such hollow nanoparticles is investigated in the next chapters: in liquid electrolyte with a three-electrode setup (Chapter 5) and in PEMFCs (Chapter 6).

References

[1] H. A. Gasteiger, S. S. Kocha, B. Sompalli, and F. T. Wagner, *Applied Catalysis B: Environmental* **56**, 9 (2005).

[2] C. M. Pedersen, M. Escudero-Escribano, A. Velázquez-Palenzuela, L. H. Christensen, I. Chorkendorff, and I. E. L. Stephens, *Electrochimica Acta* **179**, 647 (2015).

[3] B. Han, C. E. Carlton, A. Kongkanand, R. S. Kukreja, B. R. Theobald, L. Gan, R. O'Malley, P. Strasser, F. T. Wagner, and Y. Shao-Horn, *Energy & Environmental Science* **8**, 258 (2015).

[4] S. Chen, W. Sheng, N. Yabuuchi, P. J. Ferreira, L. F. Allard, and Y. Shao-Horn, *Journal of Physical Chemistry C* **113**, 1109 (2009).

[5] S. Koh, M. F. Toney, and P. Strasser, *Electrochimica Acta* **52**, 2765 (2007).

[6] M. Oezaslan and P. Strasser, *Journal of Power Sources* **196**, 5240 (2011).

[7] L. Gan, M. Heggen, R. O'Malley, B. Theobald, and P. Strasser, *Nano Letters* **13**, 1131 (2013).

[8] V. R. Stamenkovic, B. Fowler, B. S. Mun, G. Wang, P. N. Ross, C. A. Lucas, and N. M. Markovic, *Science* **315**, 493 (2007).

[9] B. Hammer and J. K. Nørskov, *Surface Science* **343**, 211 (1995).

[10] J. R. Kitchin, J. K. Nørskov, M. A. Barteau, and J. G. Chen, *Journal of Chemical Physics* **120**, 10240 (2004).

[11] T. Bligaard and J. K. Nørskov, *Electrochimica Acta* **52**, 5512 (2007).

[12] I. E. L. Stephens, A. S. Bondarenko, F. J. Perez-Alonso, F. Calle-Vallejo, L. Bech, T. P. Johansson, A. K. Jepsen, R. Frydendal, B. P. Knudsen, J. Rossmeisl, and I. Chorkendorff, *Journal of the American Chemical Society* **133**, 5485 (2011).

[13] I. E. L. Stephens, A. S. Bondarenko, U. Grønbjerg, J. Rossmeisl, and I. Chorkendorff, *Energy & Environmental Science* **5**, 6744 (2012).

[14] H. A. Gasteiger and N. M. Marković, *Science* **324**, 48 (2009).

[15] R. M. Arán-Ais, J. Solla-Gullón, M. Gocyla, M. Heggen, R. E. Dunin-Borkowski, P. Strasser, E. Herrero, and J. M. Feliu, *Nano Energy* **27**, 390 (2016).

[16] C. Chen, Y. Kang, Z. Huo, Z. Zhu, W. Huang, H. L. Xin, J. D. Snyder, D. Li, J. A. Herron, M. Mavrikakis, M. Chi, K. L. More, Y. Li, N. M. Markovic, G. A. Somorjai, P. Yang, and V. R. Stamenkovic, *Science* **343**, 1339 (2014).

[17] D. Van Der Vliet, C. Wang, M. Debe, R. Atanasoski, N. M. Markovic, and V. R. Stamenkovic, *Electrochimica Acta* **56**, 8695 (2011).

[18] F. Calle-Vallejo, J. I. Martínez, J. M. García-Lastra, P. Sautet, and D. Loffreda, *Angewandte Chemie - International Edition* **53**, 8316 (2014).

[19] F. Calle-Vallejo, J. Tymoczko, V. Colic, Q. H. Vu, M. D. Pohl, K. Morgenstern, D. Loffreda, P. Sautet, W. Schuhmann, and A. S. Bandarenka, *Science* **350**, 185 (2015).

[20] O. Le Bacq, A. Pasturel, R. Chattot, B. Previdello, J. Nelayah, T. Asset, L. Dubau, and F. Maillard, *ChemCatChem* **9**, 2324 (2017).

[21] R. Chattot, T. Asset, P. Bordet, J. Drnec, L. Dubau, and F. Maillard, *ACS Catalysis* **7**, 398 (2017).

[22] S. Chen, H. A. Gasteiger, K. Hayakawa, T. Tada, and Y. Shao-Horn, *Journal of the Electrochemical Society* **157**, A82 (2010).

[23] Y. Yu, H. L. Xin, R. Hovden, D. Wang, E. D. Rus, J. A. Mundy, D. A. Muller, and H. D. Abruna, *Nano Letters* **12**, 4417 (2012).

[24] L. Dubau, J. Durst, F. Maillard, L. Guétaz, M. Chatenet, J. André, and E. Rossinot, *Electrochimica Acta* **56**, 10658 (2011).

[25] L. Dubau, J. Nelayah, S. Moldovan, O. Ersen, P. Bordet, J. Drnec, T. Asset, R. Chattot, and F. Maillard, *ACS Catalysis* **6**, 4673 (2016).

[26] T. Asset, R. Chattot, J. Nelayah, N. Job, L. Dubau, and F. Maillard, *ChemElectroChem* **3**, 1591 (2016).

[27] L. Castanheira, *Corrosion of high surface area carbon supports used in proton- exchange membrane fuel cell electrodes*, PhD thesis, Université de Grenoble, 2014.

[28] F. Rodríguez-Reinoso, Porosity in Carbons: Characterization and Applications, in *Porosity in Carbons*, edited by J. W. Patrick, p. 253, John Wiley & Sons, Ltd., Chichester, United Kingdom, 1995.

[29] N. Job, R. Pirard, J. Marien, and J.-P. Pirard, *Carbon* **42**, 619 (2004).

[30] L. Dubau, M. Lopez-Haro, L. Castanheira, J. Durst, M. Chatenet, P. Bayle-Guillemaud, L. Guétaz, N. Caqué, E. Rossinot, and F. Maillard, *Applied Catalysis B: Environmental* **142-143**, 801 (2013).

[31] S. J. Bae, S. J. Yoo, Y. Lim, S. Kim, Y. Lim, J. Choi, K. S. Nahm, S. J. Hwang, T.-H. Lim, S.-K. Kim, and P. Kim, *Journal of Materials Chemistry* **22**, 8820 (2012).

[32] Y. Sun and Y. Xia, *Science* **298**, 2176 (2002).

[33] Y. Sun, B. Mayers, and Y. Xia, *Advanced Materials* **15**, 641 (2003).

[34] G. Chen, D. Xia, Z. Nie, Z. Wang, L. Wang, L. Zhang, and J. Zhang, *Chemistry of Materials* **19**, 1840 (2007).

[35] X. Xia, Y. Wang, A. Ruditskiy, and Y. Xia, *Advanced Materials* **25**, 6313 (2013).

[36] L. Zhang, L. T. Roling, X. Wang, M. Vara, M. Chi, J. Liu, S.-I. Choi, J. Park, J. A. Herron, Z. Xie, M. Mavrikakis, and Y. Xia, *Science* **349**, 412 (2015).

[37] A. M. Pasqualeti, P.-Y. Olu, M. Chatenet, and F. H. B. Lima, *ACS Catalysis* **5**, 2778 (2015).

[38] J. X. Wang, C. Ma, Y. Choi, D. Su, Y. Zhu, P. Liu, R. Si, M. B. Vukmirovic, Y. Zhang, and R. R. Adzic, *Journal of the American Chemical Society* **133**, 13551 (2011).

[39] Y. Yin, R. M. Rioux, C. K. Erdonmez, S. Hughes, G. A. Somorjai, and A. P. Alivisatos, *Science* **304**, 711 (2004).

[40] Y. Yin, C. K. Erdonmez, A. Cabot, S. Hughes, and A. P. Alivisatos, *Advanced Functional Materials* **16**, 1389 (2006).

[41] E. González, J. Arbiol, and V. F. Puntes, *Science* **334**, 1377 (2011).

[42] A. Zubiaur, M. Chatenet, F. Maillard, S. D. Lambert, J.-P. Pirard, and N. Job, *Fuel Cells* **14**, 343 (2014).

[43] M.-L. C. Piedboeuf, A. F. Léonard, K. Traina, and N. Job, *Colloids and Surfaces A: Physicochemical and Engineering Aspects* **471**, 124 (2015).

[44] E. Guilminot, A. Corcella, M. Chatenet, and F. Maillard, *Journal of Electroanalytical Chemistry* **599**, 111 (2007).

[45] M. Chatenet, L. Dubau, N. Job, and F. Maillard, *Catalysis Today* **156**, 76 (2010).

[46] K. Mayrhofer, D. Strmcnik, B. Blizanac, V. Stamenkovic, M. Arenz, and N. Markovic, *Electrochimica Acta* **53**, 3181 (2008).

[47] K. Shinozaki, J. W. Zack, R. M. Richards, B. S. Pivovar, and S. S. Kocha, *Journal of the Electrochemical Society* **162**, F1144 (2015).

[48] S. S. Kocha, J. W. Zack, S. M. Alia, K. C. Neyerlin, and B. S. Pivovar, *ECS Transactions* **50**, 1475 (2013).

[49] N. Job, S. D. Lambert, M. Chatenet, C. J. Gommes, F. Maillard, S. Berthon-Fabry, J. R. Regalbuto, and J.-P. Pirard, *Catalysis Today* **150**, 119 (2010).

[50] F. Maillard, M. Eikerling, O. V. Cherstiouk, S. Schreier, E. Savinova, and U. Stimming, *Faraday Discussions* **125**, 357 (2004).

[51] F. Maillard, S. Schreier, M. Hanzlik, E. R. Savinova, S. Weinkauf, and U. Stimming, *Physical Chemistry Chemical Physics* **7**, 385 (2005).

[52] F. Maillard, E. R. Savinova, and U. Stimming, *Journal of Electroanalytical Chemistry* **599**, 221 (2007).

[53] S. Trasatti and O. Petrii, *Journal of Electroanalytical Chemistry* **327**, 353 (1992).

[54] A. J. Bard and L. R. Faulkner, *Electrochemical Methods: Fundamentals and applications*, John Wiley & Sons, Inc., Weinheim, Germany, 2nd edition, 2001.

[55] G. Bergeret and P. Gallezot, Particle size and dispersion measurement, in *Handbook of Heterogeneous Catalysis*, edited by G. Ertl, H. Knözinger, and J. Weitkamp, p. 439, Wiley-VCH, Weinheim, Germany, 1997.

[56] F. Maillard, S. Pronkin, and E. R. Savinova, Influence of size on the electrocatalytic activities of supported metal nanoparticles in fuel cells related reactions, in *Handbook of Fuel Cells*, edited by W. Vielstich, H. A. Gasteiger, and H. Yokokawa, volume 5, pp. 91–111, John Wiley & Sons, Ltd, Chichester, United Kingdom, 2009.

[57] H. Schulenburg, J. Durst, E. Müller, A. Wokaun, and G. G. Scherer, *Journal of Electroanalytical Chemistry* **642**, 52 (2010).

[58] A. R. Denton and N. W. Ashcroft, *Physical Review A* **43**, 3161 (1991).

[59] R. Chattot, T. Asset, J. Drnec, P. Bordet, J. Nelayah, L. Dubau, and F. Maillard, *Nano Letters* **17**, 2447 (2017).

[60] L. Dubau, T. Asset, R. Chattot, C. Bonnaud, V. Vanpeene, J. Nelayah, and F. Maillard, *ACS Catalysis* **5**, 5333 (2015).

[61] K. Kinoshita, *Journal of the Electrochemical Society* **137**, 845 (1990).

[62] O. Antoine, Y. Bultel, and R. Durand, *Journal of Electroanalytical Chemistry* **499**, 85 (2001).

[63] L. Dubau, M. Lopez-Haro, J. Durst, L. Guetaz, P. Bayle-Guillemaud, M. Chatenet, and F. Maillard, *Journal of Materials Chemistry A* **2**, 18497 (2014).

[64] L. Dubau, M. Lopez-Haro, J. Durst, and F. Maillard, *Catalysis Today* **262**, 146 (2016).

[65] L. Dubau, J. Nelayah, T. Asset, R. Chattot, and F. Maillard, *ACS Catalysis* **7**, 3072 (2017).

Appendix

4.A1 Reproducibility

In order to study the reproducibility of the synthesis and the impact of the aging of the reagents, the hollow PtCo nanoparticles synthesis was repeated after 10 months with the same reagents and after 15 months (i) with the same reagents and (ii) with fresh reagents. The two batches of reagents used for the syntheses were labeled hereafter A or B; the latter was provided several months after the reagents A. As an example, Citrate-A is the tri-sodium citrate used for the syntheses at various times (initial, after 10 months, and after 15 months) while Citrate-B is the tri-sodium citrate used as 'fresh reagents' after 15 months only. These catalysts were characterized by TEM and by the same electrochemical techniques as explained in the section 4.2 Experimental of the present chapter.

Figure 4.A1.1 shows the micrographs of catalysts synthesized at different times using the reagents A and the exact same synthesis method and the micrograph of a catalyst synthesized with reagents B and the exact same synthesis method. It can be clearly seen that the size of the hollow nanoparticles decreases with time. The TEM micrographs were used to calculate the average hollow particle size for each catalysts. The evolution of the average particle size with time is illustrated in Figure 4.A1.2. Once again, the decrease in average particle size with time can be clearly seen. The reason for these variations in size was suspected to be the hydration of the tri-sodium citrate used in order to form the Co colloid, which is the starting point of the hollow particle synthesis. However, the humidity content, measured in a moisture analyzer (Precisa 330XM XM60, maintained at 483 K during 10 min), was equal to 12.69 and 12.63% for the Citrate-A and the Citrate-B, respectively. It must be noted that the tri-sodium citrate theoretically contains 12.24% of water, as it was already hydrated (tri-sodium citrate dihydrate). The humidity content seems to correspond to the theoretical amount of water.

Thermogravimetric analysis - differential scanning calorimetry (TGA-DSC, Setaram Sensys evo) was performed in order to highlight possible differences between Citrate-A and Citrate-B. The two samples were heated at 5 K/min up to 1073 K while measuring the mass of the sample and the heat flow emitted or absorbed by the sample. Results are displayed in Figure 4.A1.3. The curves are superimposed until 600 K. Indeed, the only phenomenon happening at temperature lower than 600 K is the evaporation of the water (between 440 and 460 K), which is the same for all the samples (*ca.* 12.75% of water content). This corroborates the previous results obtained by the moisture analyzer. The differences start to occur from 600 K; in particular, a peak is present at 670 K in the Citrate-A curve but not in the Citrate-B curve, while peaks appear between 770 and 880 K in the Citrate-B curve and not in the Citrate-A curve. These peaks show a variation in the citrate quality which could be linked to the modification of the nanoparticles size. It must be noted that other characterization techniques were used (UV-visible spectroscopy, pH mea-

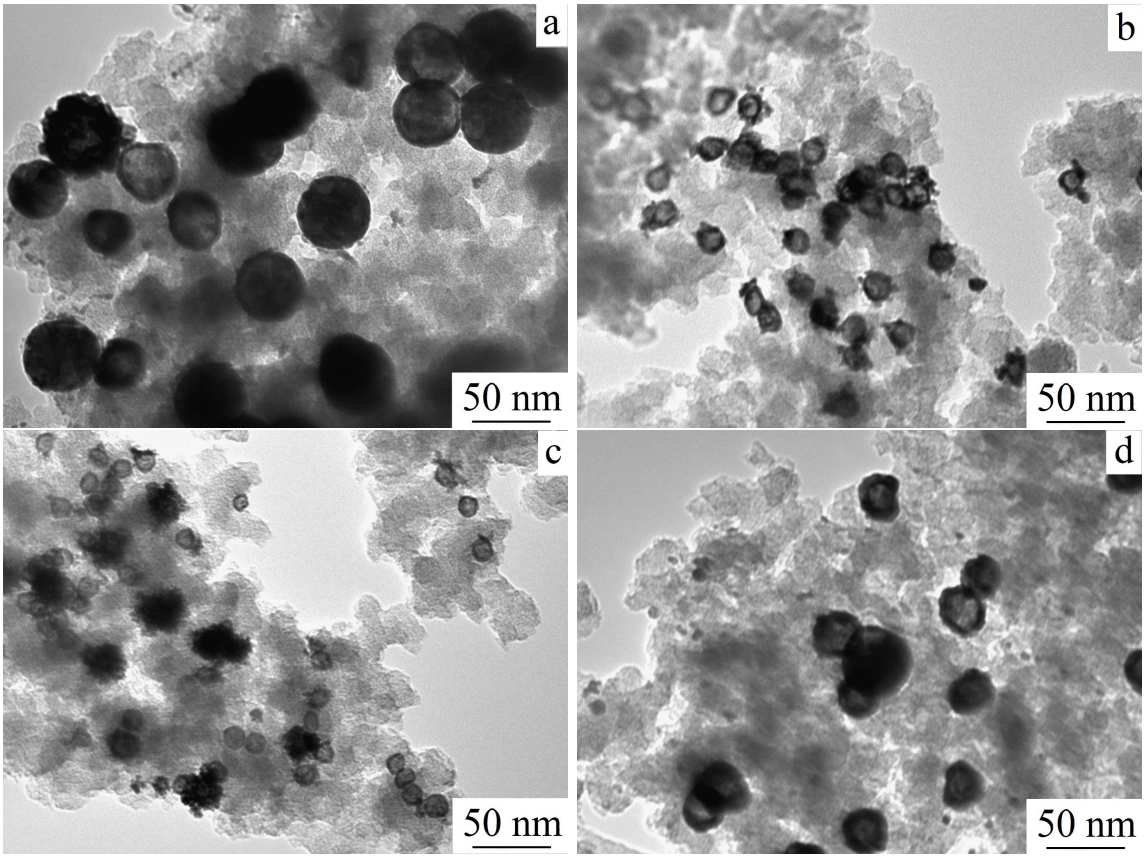

Figure 4.A1.1: TEM micrographs of four catalysts synthesized at different times: initial synthesis (reagents A, a), synthesized after 10 months with the reagents A (b), synthesized after 15 months with the reagents A (c), and synthesized after 15 months with reagents B (d).

surements of tri-sodium citrate solutions, and XRD) but none of them could point differences between Citrate-A and Citrate-B. Therefore, although TGA-DSC measurements clearly shows different behaviour, the exact nature of difference between the two citrate samples remains unclear. Further analysis are needed to monitor the possible evolution of these peaks and to conclude if they are due to a potential degradation of the tri-sodium citrate.

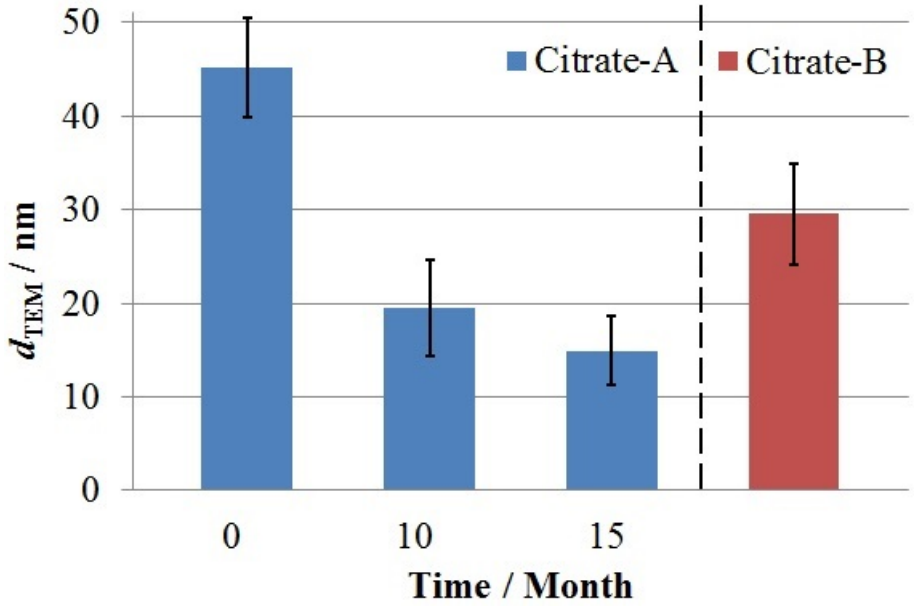

Figure 4.A1.2: Evolution of the average particle size of the hollow nanoparticles with time for synthesis using Citrate-A and comparison with nanoparticles prepared using Citrate-B.

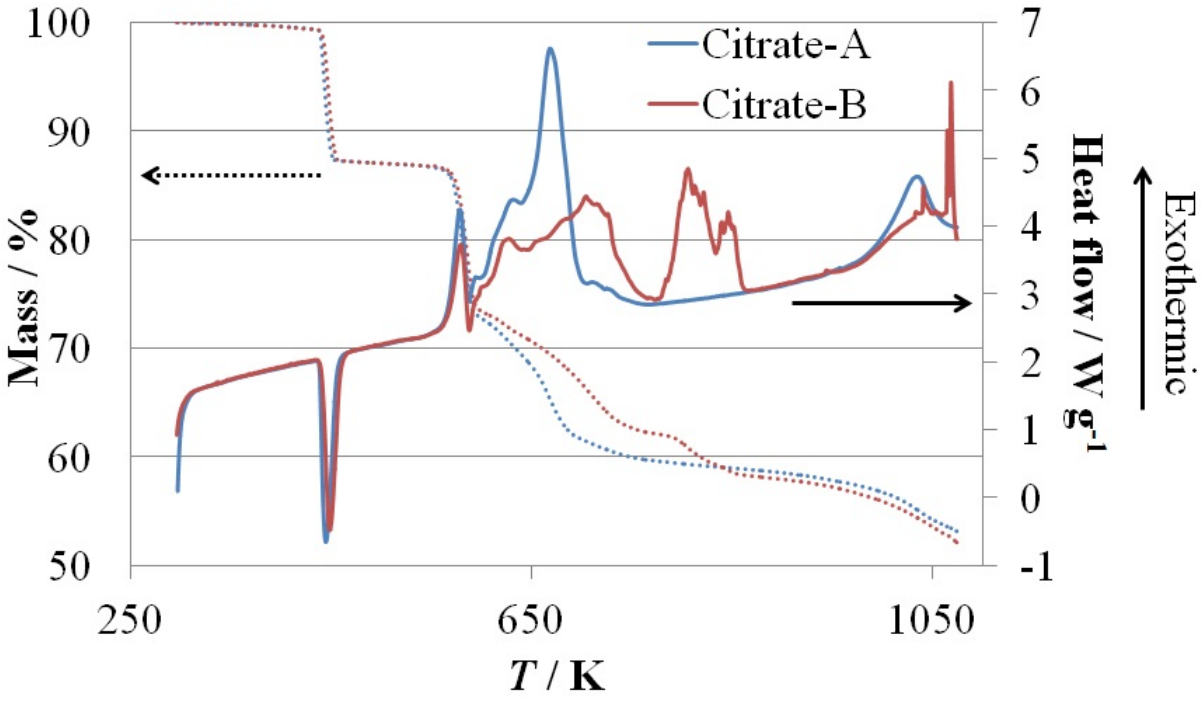

Figure 4.A1.3: TGA-DSC results of Citrate-A and the Citrate-B: mass (dotted lines) and heat flow (full lines) as a function of the temperature (heating rate of 5 K/min).

Chapter 5

Durability of Pt and hollow PtCo nanoparticles supported on carbon xerogel designed as electrocatalysts for the oxygen reduction reaction

After studying the synthesis and the characterization of Pt and PtCo nanoparticles supported on carbon xerogel in the previous chapters, the penultimate chapter consists in the study of the durability of the best catalysts synthesized and characterized in Chapter 2 and 4, in a three electrode cell. The durability of formic acid-reduced Pt nanoparticles deposited on carbon xerogel and that of hollow PtCo nanoparticles deposited on carbon xerogel were compared to that of a commercial Pt/HSAC catalyst.

5.1 Introduction

Commercial PEMFC cathode catalysts often consist of Pt nanoparticles supported on a high surface area carbon (Pt/HSAC). The high cost of PEMFCs is mainly due to the large amount of Pt needed to accelerate the sluggish oxygen reduction reaction (ORR) at the cathode of PEMFCs. In order to decrease the PEMFC cost, researchers try to decrease the quantity of Pt while keeping a high catalytic activity for the ORR. To do so, many works were performed on the alloying of the Pt nanoparticles with a transition metal (PtM), *e.g.* Ni, Cu, Co, *etc.*, which increases the catalyst activity for the ORR while decreasing the Pt quantity [1–8]. Indeed, the activity of PtM alloys is increased because the transition metals widen the *d*-band and decrease the average energy of the *d*-band center of Pt, *i.e.* the strain-ligand effect [9–11]. This effect decreases the bond strength between Pt atoms and oxygenated species by modifying the Pt *5d*-band [12, 13]. The weakening of this bond increases the performance of the catalyst because oxygenated species, which are intermediates formed during the ORR, usually bind too strongly on Pt atoms, limiting the catalysts performance. These observations follow the Sabatier's principle which states that the best catalyst for a chemical reaction has to exhibit an optimal binding energy with the reactive species, *i.e.* not too high to allow the adsorbed species to dissociate but not too low, otherwise the reaction can not take place.

Concerning the other major issue, the catalyst durability, Pt/C catalysts are not stable enough during PEMFCs operation. Indeed, Pt/C catalysts can undergo four degradation phenomena impacting the Pt nanoparticles under PEMFC-operating conditions [14–17]: (i) Pt nanoparticles can detach from the carbon support when the latter deteriorates; (ii) Pt crystallites can migrate on the carbon support towards other Pt crystallites and coalesce; (iii) Pt atoms can dissolve, especially those from the less stable small particles, and be redeposited on larger particles, *i.e.* Pt atoms can undergo electrochemical Ostwald ripening; (iv) Pt atoms can dissolve and be redeposited elsewhere, *e.g.* in the polymer membrane of PEMFCs, resulting in nanoparticles isolated from the conductive carbon. All these phenomena lead to a decrease in catalysts ORR mass activity, *i.e.* the amount of electricity produced per mass unit of Pt [14–17].

Durability studies performed on PtM/C catalysts show that alloying Pt with transition metal allows to mitigate Pt particle growth and migration as they lower the amount of dissolved Pt [16]. However, these PtM nanoparticles catalysts may suffer from other stability issues, such as the transition metal dissolution, which can lead to new kind of particle morphology or structure [2–4, 6, 7, 18–24]. Among these, one morphology seems to be worthy of interest: hollow nanoparticles [20, 22, 23]. This particular structure can be obtained after aging of Co@Pt core@shell nanoparticles, *i.e.* constituted of a Co core surrounded by a Pt shell, in PEMFC-operating conditions [25, 26]. The fact that the hollow structures are formed after thousands of hours of operation indicates that these particles are stable under such conditions [27–29]. Therefore, synthesis methods were developed in order to form these

hollow nanoparticles directly [20, 22, 23, 30, 31]. The formation of hollow nanoparticles proceeds as follows: (i) a suspension/colloid of transition metal nanoparticles is synthesized; (ii) Pt ions (added at this step or at the beginning of the synthesis) reduce using the electrons produced by the transition metal atoms oxidation, *i.e.* galvanic replacement of transition metal atoms by Pt, leading to M@Pt core@shell nanoparticles; (iii) transition metal atoms diffuses from the core towards the Pt shell *via* the nanoscale Kirkendall effect, forming the hollow core; and (iv) transition metal atoms at the particle surface are oxidized by acid leaching.

One of these methods producing hollow PtCo nanoparticles was developed and described in the previous chapter. This method consists in controlling the Co nanoparticle size by chelation of the Co ions with tri-sodium citrate before their reduction with sodium borohydride ($NaBH_4$). Once the Co colloid is synthesized, an acidic Pt salt is added. This addition provokes two phenomena: (i) the citrate molecules protonate, as the acid decreases the pH of the solution, and leave the Co particles; (ii) as the Co particles are freed from citrate molecules, the galvanic replacement of Co by Pt can occur, *i.e.* the oxidation of Co atoms produces the electrons needed to reduce the Pt ions. After the Pt reduction, the hollow nanoparticle formation can occur *via* nanoscale Kirkendall effect, *i.e.* the interdiffusion of Co atoms and vacancies between the particle core and surface. Finally, acid leaching oxidizes the Co atoms located at the surface of the particles. Several hollow PtCo nanoparticles catalysts were synthesized and characterized in the previous chapter: their performance for the ORR, measured in $HClO_4$ electrolyte, was far better than the other Pt catalysts studied, including a commercial catalyst. Indeed, the specific activity of hollow PtCo nanoparticles catalysts (in A ${m_{Pt}}^{-2}$) was 14 to 20 times higher than that of the commercial reference catalyst and their mass activity (in A ${g_{Pt}}^{-1}$) was 7 times higher.

This chapter focuses on the evolution in performance and structure of hollow PtCo nanoparticles supported on carbon xerogel (PtCo/CX catalysts) under accelerated stress tests (ASTs) in 0.1 M sulfuric acid (H_2SO_4) electrolyte. The ASTs allow the acceleration of the catalyst degradation by reproducing the start/stop conditions of a PEMFC [15]. H_2SO_4 was used during ASTs and electrochemical measurements in order to mimic at best the environment of the catalysts inside the PEMFC. The behaviour of the PtCo/CX catalyst was compared to that of Pt nanoparticles supported on carbon xerogel (Pt/CX catalysts) and to that of a commercial Pt catalyst supported on high surface area carbon (Pt/HSAC, Tanaka, 37 wt.%).

A carbon xerogel (CX) was used as support for the synthesized nanoparticles (Pt and PtCo) because its properties make it suitable for PEMFC catalyst support. Indeed, CXs are pure carbons with controllable and reproducible pore texture [32]. This feature leads to catalytic layers with high porosity, inducing better performance in PEMFCs as it mitigates the mass-transport limitations [33]. In addition, these materials proved to be excellent supports to deposit metals with high dispersion, as demonstrated in previous works [33–38]. Stability of Pt and PtCo nanoparticles are thus compared on the same carbon support and with Pt/HSAC as reference.

5.2 Experimental

5.2.1 Syntheses

Carbon xerogel support Carbon xerogel (CX) used in this thesis was prepared by drying and pyrolysis of a resorcinol-formaldehyde gel [32]. This synthesis is described elsewhere [34]. Briefly, the gel was obtained by polycondensation of resorcinol with formaldehyde in water. The resorcinol/formaldehyde molar ratio, *R/F*, was set at 0.5, the resorcinol/sodium carbonate molar ratio, *R/C*, was chosen to be equal to 1,000 and the dilution ratio, *D*, *i.e.* the solvent/(resorcinol and formaldehyde) molar ratio, was fixed at 5.7. These variables were chosen in order to obtain a CX with a pore size distribution centered at 80 nm. After gelling and aging in an oven at 358 K, the obtained gel was dried under vacuum, then ground with a planetary mill (PULVERISETTE 6, classical line, Fritsch) at 400 rpm during 70 min in order to obtain particles with a diameter of a few micrometers [39]. After grinding, the gel was pyrolyzed at 1073 K under nitrogen flow. The resulting CX particles exhibit a mean size of 7 µm, as measured by laser diffraction with a Mastersizer 2000 (see Reference [39] for more details).

Hollow PtCo nanoparticles on carbon xerogel The synthesis of hollow PtCo particles supported on CX was developed in the previous chapter. Briefly, the catalyst was synthesized as follows: (i) 45.7 mg of cobalt chlorine hexahydrate ($CoCl_2 \cdot 6H_2O$) were dissolved in 160 mL of ultrapure water; (ii) to this, 40 mL of an aqueous solution of trisodium citrate dihydrate ($Na_3C_6H_5O_7 \cdot 2H_2O$, 2.6×10^{-2} mol/L) were added; (iii) the resulting solution was sonicated for 15 min, then (iv) poured in 360 mL of ultrapure water under stirring; (v) Ar was then bubbled during 30 min. The next steps were performed under Ar bubbling: (vi) 20 mL of an aqueous solution of sodium borohydride ($NaBH_4$, 9.6×10^{-2} mol/L, degassed by Ar bubbling during a few minutes) were added dropwise in 5 min; (vii) after 10 min, 20 mL of an aqueous solution of hexachloroplatinic acid hexahydrate (CPA, $H_2PtCl_6 \cdot 6H_2O$, 3.2×10^{-3} mol/L, degassed by Ar bubbling during a few minutes) was added dropwise in 5 min; (viii) 30 min after the addition of CPA, Ar bubbling was stopped; (ix) after 90 min under stirring, 136 µL of hydrochloric acid 37% (HCl) were added, then (x) 40 mL of ultrapure water containing 100 mg of CX powder were added; (xi) the suspension was left under stirring overnight, then (xii) filtered, (xiii) thoroughly washed with ultrapure water, and (xiv) dried in an oven at 353 K during 40 min. The added amounts of Pt and Co correspond to a catalyst composition of 10 wt.% in each metal.

Pure Pt particles on carbon xerogel The previous hollow PtCo/CX catalyst will be compared to two Pt catalysts supported on CX, synthesized by formic acid (FA, HCOOH) reduction of a Pt salt: one with a low Pt loading, the other with a high Pt loading (10 and 37 wt.% of Pt, respectively). The synthesis procedure was

as follows (see Chapter 2): (i) 0.3 g of CX were dispersed in 200 mL of 2 mol L^{-1} FA solution; (ii) the suspension was heated to 353 K in an oil bath; (iii) once the suspension reached 353 K, the volume of 4 mmol L^{-1} CPA solution needed to obtain the target Pt loading (in this case, 10 or 37 wt.%) was added by 10 mL steps; (iv) after 1 h stirring, the suspension was filtered; (v) the catalyst was then washed 5 times with 125 mL of ultrapure water, and finally (vi) dried at 333 K in an oven under air overnight.

List of samples Hereafter, the hollow PtCo/CX catalyst is labeled PtCo/CX. The two Pt/CX catalysts are labeled 10Pt/CX and 37Pt/CX for the 10 wt.% and 37 wt.% of Pt, respectively. These samples will be compared to a commercial catalyst, a Pt/HSAC Tanaka 37 wt.%, labeled hereafter Ref.

5.2.2 Physicochemical characterization

The metal weight percentages of the catalysts were measured by inductively coupled plasma-atomic emission spectrometry (ICP-AES) using an ICAP 6500 THERMO device. The solutions for the analyses were prepared as follows: an aliquot of the catalyst sample was weighed and digested by 10 mL of sulphuric acid (H_2SO_4) and 5 mL of HNO_3. This solution was heated at 573 K until clear. After the complete dissolution of the CX support and evaporation of the solution, 3 mL of HCl and 1 mL of HNO_3 were added. The obtained solution was heated a few minutes at 393 K and transferred into a 50 mL calibrated flask, which was finally filled by deionized water.

The nanoparticles were observed by transmission electron microscopy (TEM) with a Philips CM100 transmission electron microscope (100 kV, W filament). Lacey F/C copper TEM grids (Ted Pella, Inc.) were put in contact with the catalyst powder.

The catalysts powders were analyzed by X-Ray diffraction (XRD) with a Bruker D8 ADVANCE (TWIN/TWIN) goniometer using the $Cu_{K\alpha}$ line (Ni filter).

5.2.3 Electrochemical characterization

Setup All the utilized glassware was cleaned by immersion in a H_2SO_4:H_2O_2 solution (molar ratio 2:1) overnight and thoroughly rinsed with ultrapure water (18 MΩ cm). The electrolytic solutions were prepared from ultrapure water and H_2SO_4 (98% Suprapur, Merck). The electrochemical properties were measured with an Autolab PGSTAT204 in a three-electrode cell thermostated at 298 K. The reference electrode used during electrochemical characterization was a home-made reversible hydrogen electrode (RHE) constituted of a Pt wire in contact with a hydrogen bubble and the H_2SO_4 liquid electrolyte, and connected to the cell by a Luggin capillary. The reference electrode used during the ASTs was a commercial RHE

(Hydroflex®, Gaskatel GmbH) connected to the cell by a Luggin capillary. The counter-electrode was a Pt gauze soldered on a Pt wire. The working electrode was the catalytic layer deposited on the glassy carbon disk, as explained in the next paragraph.

Catalytic layer preparation To obtain catalytic layers on glassy carbon (GC) electrode, inks were first prepared. The ink composition was chosen to keep the amount of carbon constant (*i.e.* 19.8 mg), regardless of the metal loading [40, 41]. Each catalyst was crushed in a mortar, then the right amount was mixed with 755 mg of ultrapure water and 466 mg of 5 wt.% Nafion® solution. In order to blend it homogeneously, the mixture was then processed in an ultrasonic bath for 15 min. Once the ink was homogeneous, 10 µL of ink were deposited on a GC disk and sintered at 343 K during 20 min to evaporate the solvents and stick the catalyst to the GC disk. The catalytic layer deposited on the GC disk composes the working electrode for all electrochemical measurements. In the case of CX-supported catalysts, this procedure yields active layers of identical thickness onto the GC disk (*i.e.* resulting in identical mass-transport limitations within the layer [40, 41]). It must be noted that the amount of Nafion® in the ink and the amount of Pt on the electrode are relatively high (Nafion® over CX mass ratio equal to 1:1; Pt amount deposited on the GC around 110 µg for the catalysts with the highest Pt loading). These high quantities were chosen for two reasons: (i) the 1:1 Nafion® over CX mass ratio was chosen in order to mimic the composition and structure of the cathode catalytic layer of a PEMFC; (ii) the high Pt content of the active layers prepared from high Pt loading catalysts results from the fact that the active layer of Pt/CX catalysts were prepared in order to keep the same layer thickness whatever the Pt loading. However, these choices may induce some decrease in performance for the studied catalysts [42–44].

Electrolyte and wetting procedure For all electrochemical measurements, the electrode was immersed in a 0.1 M H_2SO_4 aqueous solution (*i.e.* electrolyte), which should enable full wetting of the metallic particles by the electrolyte [41]. In order to ensure that all the pores were fully filled, a drop of electrolyte was deposited onto the catalytic layer, in such a way that all the layer was covered. Then, the electrode was put under vacuum in order to outgas the layer by bubbling air through the drop. Once no air bubbles were visible, the electrode and the drop were put back under atmospheric pressure so the drop filled the empty porosity of the layer, which ensured the full wetting of the catalyst. With this wetting procedure, the electrochemical measurements were usually steady and reproducible. In the case of Pt/CX catalysts, this procedure ensures the Pt wetting and the Pt utilization factor is close to 100% [41]. Indeed, previous works [33, 34, 41] performed on similar systems showed good consistency between the electroactive surface area measured after using this wetting procedure and the surface measured from TEM micrographs.

CO stripping voltammetry The electroactive surface area of the nanoparticles was measured by CO stripping voltammetry [45–47]. The procedure was initiated by the application of a steady potential of 0.1 V *vs.* RHE to the working electrode, while gaseous CO was bubbled in the electrolyte solution for 6 min. After an Ar purge of 39 min in order to remove the CO dissolved in the electrolyte at this potential, the CO chemisorbed at the surface of the particles was electrooxidized into CO_2 by increasing the electrode potential from 0.05 to 1.23 V *vs.* RHE at 0.02 V s^{-1}. The electroactive surface area was calculated from the CO oxidation peak current, assuming the electrooxidation of a full monolayer of CO_{ad} requires 420×10^{-2} C ${m_{Pt}}^{-2}$ [48].

Activity for the oxygen reduction reaction The catalysts activity for the oxygen reduction reaction (ORR) was measured on a rotating disk electrode (RDE). After saturation of the electrolyte by oxygen bubbling during 15 min, the electrode potential was (i) set at 0.4 V *vs.* RHE, (ii) then increased at 0.002 V s^{-1} to 1.09 V *vs.* RHE, and (iii) decreased back to 0.4 V *vs.* RHE at the same scan rate while measuring the reduction current. This measurement was repeated at various rotation speeds of the electrode (400, 900, 1,600, and 2,500 rpm). For each rotation speed of the electrode, the kinetic current was calculated by correcting the measured current for the effect of the external mass transfer limitations in the solution using the Koutecky-Levich equation [49]:

$$\frac{1}{i_k} = \frac{1}{i} - \frac{1}{i_{l,c}} \tag{5.1}$$

where i_k is the kinetic current, *i.e.* the current without any mass transfer limitations, i is the experimental current, and $i_{l,c}$ is the cathodic limit current, which depends on the rotation speed of the electrode. These kinetic current values were then averaged in order to obtain the kinetic current of the catalyst. The values of this averaged kinetic current at 0.9 V *vs.* RHE were either divided by the electroactive surface of the catalysts in order to obtain the specific activity of the catalysts at 0.9 V *vs.* RHE, *SA* (in A ${m_{Pt}}^{-2}$) or divided by the mass of Pt present on the working electrode in order to obtain the mass activity at 0.9 V *vs.* RHE, *MA* (in A ${g_{Pt}}^{-1}$).

5.2.4 Measurement procedure and accelerated stress tests

Prior to any measurement, the electrolyte was deaerated by Ar bubbling. Then the working electrode was immersed in the electrolyte at a fixed potential of 0.4 V *vs.* RHE. Thirteen voltammetry cycles were then performed between 0.05 V *vs.* RHE and 1.23 V *vs.* RHE at 0.05 V s^{-1}. After the cyclic voltammetry (CV) measurement, the CO stripping voltammetry was carried out. Next, three cyclic voltammograms were recorded in the same conditions as previously. Then, the measurement of the activity for the ORR was performed. After the ORR measurement, the resistance of the electrolyte was measured by potential electrochemical impedance spectroscopy (PEIS, all the measured resistance values were around 17 Ω). Finally, three cyclic voltammograms were recorded in the same conditions than the previous CV measurements.

After this electrochemical characterization sequence, corresponding to the beginning of life (BoL), the catalytic layer underwent 5,000 voltammetry cycles between 0.6 and 1.0 V *vs.* RHE at 0.05 V s^{-1} while heated to 353 K and with a low Ar bubbling. After the 5,000 cycles, the electrolyte was replaced by a fresh H_2SO_4 solution and the cell was cooled down to 298 K. The catalytic layer was again electrochemically characterized following the same procedure as before (CV, CO stripping measurement, CV, ORR activity measurement, PEIS, and CV). This electrical characterization correspond to the middle of life (MoL) status. After that, the cell was heated again to 353 K and the catalytic layer underwent 15,000 voltammetry cycles between 0.6 and 1.0 V *vs.* RHE at 0.05 V s^{-1} with a low Ar bubbling. After the 15,000 cycles, the electrolyte was replaced again and the cell was cooled down to 298 K. Finally, the catalytic layer was electrochemically characterized following the same procedure as before (CV, CO stripping measurement, CV, ORR activity measurement, PEIS, and CV), corresponding to the end of life (EoL) status.

5.3 Results

5.3.1 Physicochemical characterization

The physicochemical properties of the catalysts are summarized in Table 5.1. As expected, two catalysts exhibit Pt loading around 10 wt.%, PtCo/CX (9.4 wt.%) and 10Pt/CX (10.2 wt.%). The other two display a higher Pt loading of 37.0 wt.% (37Pt/CX and Ref). The Co loading of PtCo/CX is 1.8 wt.%, which is much lower than the targeted value (10 wt.%).

TEM micrographs of the four samples are shown in Figure 5.1. The nanoparticles of PtCo/CX seems to be hollow in the micrograph. Indeed, the particle cores are bright whereas the shells are dark., *i.e.* the particle cores are less dense that their shells. Some smaller nanoparticles with diameter around 3-4 nm can be seen in several micrographs. The three other samples show much smaller nanoparticles; the smallest are displayed by 10Pt/CX and Ref. In all cases, the metal is well distributed over the carbon. Image analysis was applied to these micrographs in order to calculate the average diameter of particles, d_{TEM}, the standard deviation, σ, the surface-weighed average diameter of particles, d_{s}, and the volume-weighed average diameter of particles, d_{v}:

$$d_{\mathrm{s}} = \Sigma \frac{n_{\mathrm{i}} d_{\mathrm{i}}^3}{n_{\mathrm{i}} d_{\mathrm{i}}^2} \tag{5.2}$$

$$d_{\mathrm{v}} = \Sigma \frac{n_{\mathrm{i}} d_{\mathrm{i}}^4}{n_{\mathrm{i}} d_{\mathrm{i}}^3} \tag{5.3}$$

where n_{i} is the number of particles with diameter d_{i} [50].

Table 5.1: Catalyst properties determined from physicochemical analyses.

Catalyst	ICP		TEM							XRD
	Pt_{ICP} wt.% ± 0.1	Co_{ICP} wt.% ± 0.1	d_{TEM} nm	σ nm	d_{s} nm	d_{v} nm	t_{TEM} nm	σ_{t} nm	t_{v} nm	d_{XRD} nm ± 0.5
PtCo/CX	9.4	1.8	48.7	3.8	49.3	49.5	3.4	0.5	3.7	3.6
10Pt/CX	10.2	–[a]	2.8	1.0	3.3	3.6	–[a]	–[a]	–[a]	2.3[b]
37Pt/CX	37.0	–[a]	3.6	1.2	4.0	4.4	–[a]	–[a]	–[a]	2.9
Ref	37.0	–[a]	3.1	0.8	3.4	3.6	–[a]	–[a]	–[a]	2.4[b]

Pt_{ICP}: Pt weight percentage of the catalyst measured by ICP-AES; Co_{ICP}: Co weight percentage of the catalyst measured by ICP-AES; d_{TEM}: average diameter of particles estimated from TEM micrographs; σ: standard deviation associated with d_{TEM}; d_{s}: surface-weighed average diameter of particles estimated from TEM micrographs and calculated by Equation (5.2); d_{v}: volume-weighed average diameter of particles estimated from TEM micrographs, calculated by Equation (5.3); t_{TEM}: average shell thickness of particles estimated from TEM micrographs; σ_{t}: standard deviation associated with t_{TEM}; t_{v}: volume-weighed average shell thickness of particles estimated from TEM micrographs, calculated by Equation (5.4); d_{XRD}: average size of crystallites calculated from X-ray diffraction peaks *via* Equation (5.5).
Notes: [a] Not relevant (pure Pt catalysts made of solid nanoparticles); [b] Large error (± 1) due to low intensity of diffraction peaks.

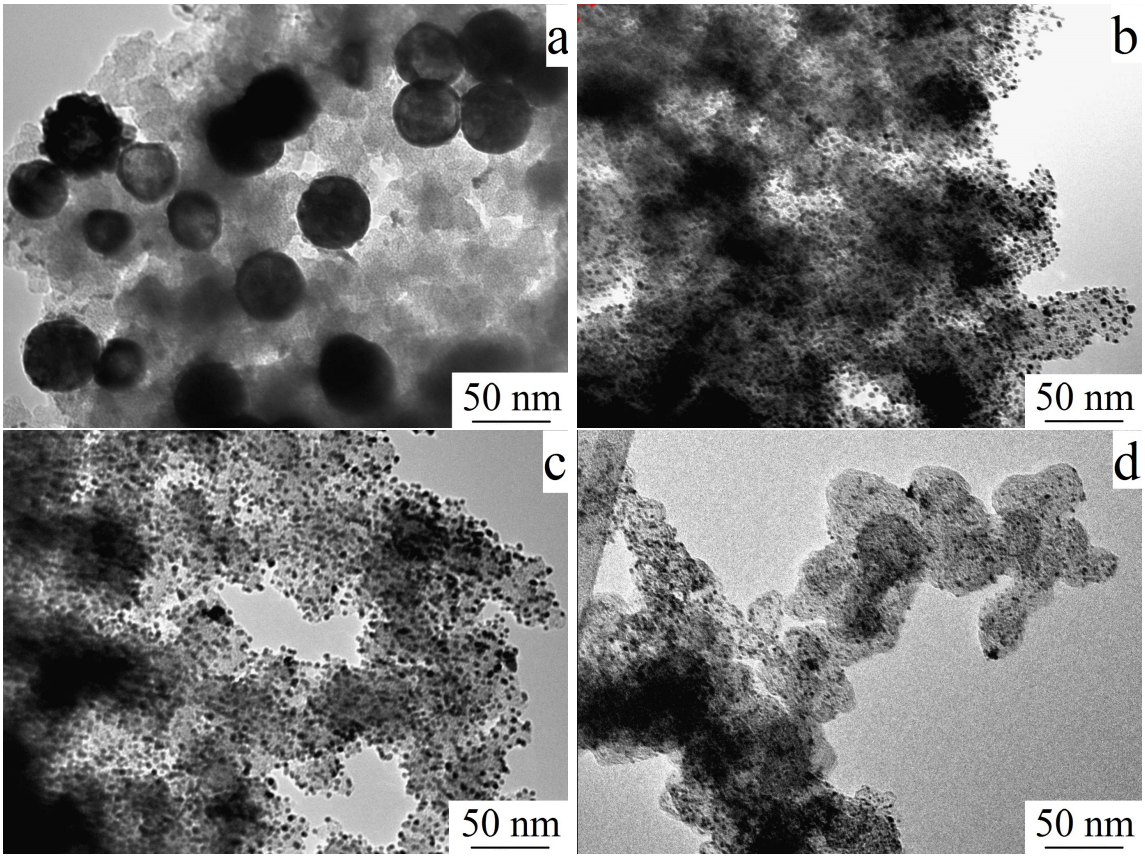

Figure 5.1: TEM micrographs of the four catalysts: PtCo/CX (a), 10Pt/CX (b), 37Pt/CX (c), and Ref (d).

For PtCo/CX, other parameters were calculated: the average shell thickness of particles, t_{TEM}, the standard deviation, σ_{t}, and the volume-weighed average shell thickness of particles, t_{v}, calculated by:

$$t_{\mathrm{v}} = \Sigma \frac{n_{\mathrm{i}} t_{\mathrm{i}}^4}{n_{\mathrm{i}} t_{\mathrm{i}}^3} \tag{5.4}$$

where n_{i} is the number of shells with thickness t_{i}. These results are shown in Table 5.1. The average diameter of particles, d_{TEM}, is equal to 48.7, 2.8, 3.6, and 3.1 nm for PtCo/CX, 10Pt/CX, 37Pt/CX, and Ref, respectively, with a standard deviation of 3.8, 1.0, 1.2, and 0.8 nm, respectively. The average shell thickness of PtCo/CX particles is equal to 3.4 nm, with a standard deviation of 0.5 nm. d_{s} of pure Pt catalysts can be compared to the CO equivalent diameter, d_{CO}, because CO stripping is surface-sensitive [51]; d_{v} of Pt catalysts and t_{v} of the hollow PtCo catalyst can be compared to the average crystallite size, d_{XRD}, because X-ray diffraction is volume-sensitive [50] (see below).

Figure 5.2 shows the X-ray diffractograms of the four catalysts which are shifted vertically for better legibility. The diffraction angles of Pt (1 1 1) (39.7°), Co (1 1 1) (44.8°), and Pt (2 0 0) (46.2°) are indicated by the three vertical lines. All the peaks shown by the diffractograms of Pt catalysts correspond to Pt peaks. For

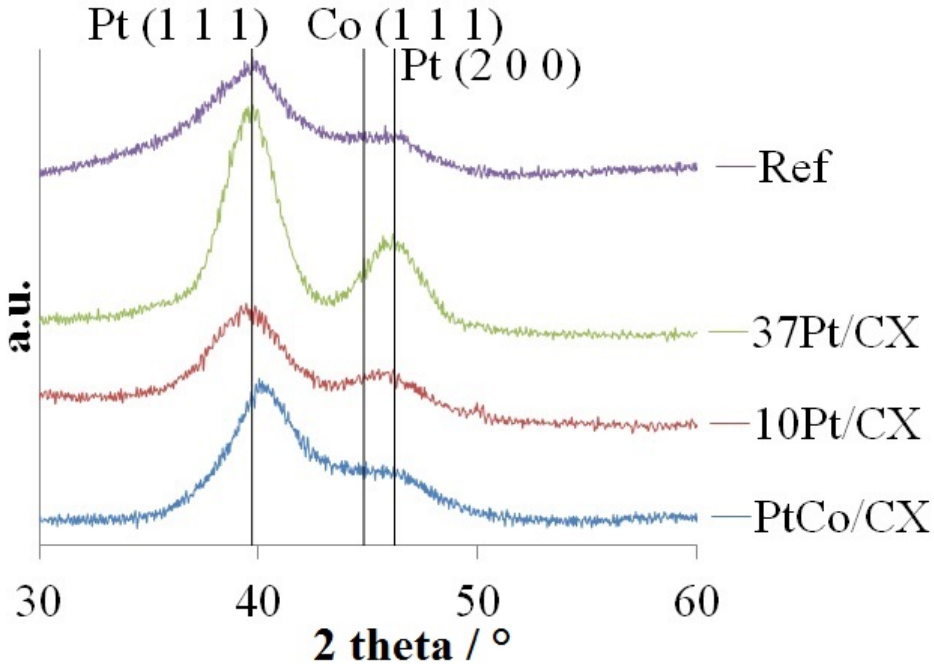

Figure 5.2: X-ray diffractograms of the four catalysts, vertically shifted for better legibility. The diffraction angles of Pt (1 1 1), Co (1 1 1), and Pt (2 0 0) are indicated respectively, from left to right, by the vertical lines.

the bimetallic catalyst, neither Co nor Co oxide diffraction peaks are visible. For PtCo/CX catalyst, a shift of the Pt (1 1 1) peak to a higher diffraction angle is clearly visible. This peak shift is due to the presence of Co atoms inside the Pt lattice leading to its contraction, *i.e.* the alloying of Pt and Co. Average crystallites sizes, d_{XRD}, were calculated by Scherrer's equation [50]:

$$d_{\mathrm{XRD}} = \frac{k\lambda}{\beta cos\theta} \tag{5.5}$$

where k is a dimensionless shape factor and equals 0.89 if spherical nanoparticles are considered, λ is the X-ray wavelength ($Cu_{K\alpha}$: 1.5456 nm), β is the full width at half the maximum intensity (FWHM), and θ is the Bragg angle. The values of the average size of crystallites, d_{XRD}, are equal to 3.6, 2.3, 2.9, and 2.4 nm for PtCo/CX, 10Pt/CX, 37Pt/CX, and Ref, respectively (see Table 5.1). As XRD is a volume-sensitive analysis, d_{XRD} corresponds to an average volume diameter and can be compared to d_{v} for the Pt catalysts and to t_{v} for the bimetallic catalyst [50].

5.3.2 Electrochemical characterization

In the CO stripping voltammograms (Figure 5.3), each catalyst exhibits a peak representative of the CO electrooxidation. For the three Pt catalysts, and especially for the commercial catalyst, the peaks are relatively high and broad. This broadness is due to the high Nafion® content in the catalytic layer (Nafion® over carbon

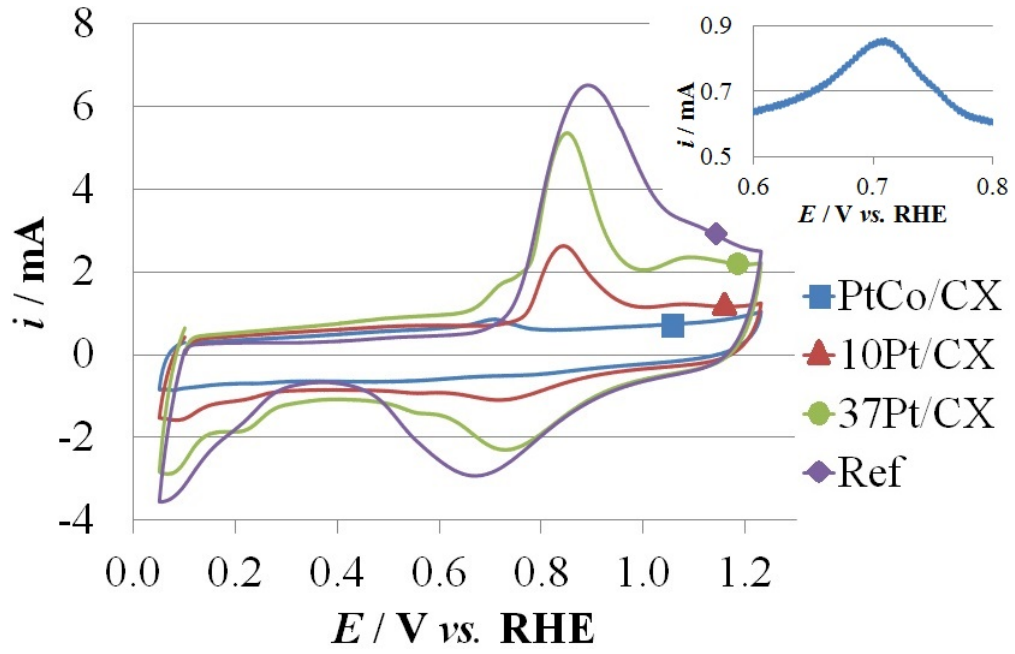

Figure 5.3: CO stripping voltammograms of the four catalysts in 0.1 M H_2SO_4 at a sweep rate of 0.02 V s^{-1} at 298 K. The insert is an enlargement of the CO electrooxidation peak of PtCo/CX catalyst.

mass ratio equal to 1:1). For PtCo/CX, the insert of Figure 5.3, representing an enlargement of the CO electrooxidation peak, shows that this peak is the sum of two peaks (shouldering around 0.75 V *vs.* RHE): (i) the peak at 0.71 V *vs.* RHE associated to structural defects and (ii) the shouldering stemming from either small Pt monocrystallites or active sites, isolated from structural defects, where adsorbed CO molecules can not diffuse. The electroactive specific surface areas, S_{CO}, and, in the case of pure Pt catalysts, the CO equivalent diameter of particles, d_{CO}, were calculated from the CO electrooxidation peaks measured before the accelerated stress tests, *i.e.* at BoL. The values of these parameters are gathered in Table 5.2. The latter shows that S_{CO} is equal to 31, 109, 50, and 90 m^2 $g_{Pt}{}^{-1}$ for PtCo/CX, 10Pt/CX, 37Pt/CX, and Ref, respectively. The CO equivalent diameter, d_{CO}, expressed in meter, is calculated by:

$$d_{CO} = \frac{6 \times 10^{-3}}{\rho_{Pt}\ S_{CO}} \tag{5.6}$$

where ρ_{Pt} is the Pt density (21.4×10^3 kg m^{-3}) [45–47]. d_{CO} was calculated for pure Pt catalysts only, *i.e.* for 10Pt/CX, 37Pt/CX, and Ref. Indeed, in bimetallic catalysts, (i) the possible presence of Co atoms at the surface of particles, which do not adsorb CO molecules [52], and (ii) the presence of hollow particles prevent the calculation of the average particle diameter from Equation (5.6). The values of d_{CO} equal 2.6, 5.6, and 3.1 nm for 10Pt/CX, 37Pt/CX, and Ref, respectively. As CO stripping voltammetry is a surface-sensitive method, d_{CO} corresponds to a surface weighed average diameter and can be compared to d_s.

Table 5.2: Catalysts properties determined by electrochemical analyses at beginning of life (BoL), after 5,000 AST cycles (middle of life, MoL), and after 20,000 AST cycles (end of life, EoL).

Catalyst		**CO stripping**		**ORR**	
		S_{CO} $m^2\ g_{Pt}^{-1}$ ± 10%	d_{CO} nm ± 10%	SA A m_{Pt}^{-2} ± 10%	MA A g_{Pt}^{-1} ± 10%
	BoL	31	–[a]	1.17	35.7
PtCo/CX	MoL	31	–[a]	0.76	23.2
	EoL	27	–[a]	0.58	15.3
	BoL	109	2.6	0.44	47.3
10Pt/CX	MoL	63	4.5	0.43	27.4
	EoL	43	6.5	0.55	23.6
	BoL	50	5.6	0.34	16.7
37Pt/CX	MoL	34	8.3	0.25	8.4
	EoL	25	11.2	0.33	8.3
	BoL	90	3.1	0.16	14.0
Ref	MoL	66	4.2	0.19	12.3
	EoL	44	6.4	0.23	10.2

S_{CO}: electroactive specific area of particles calculated from CO stripping measurements normalized by the mass of Pt on the electrode; d_{CO}: CO equivalent diameter of the Pt particles calculated by Equation (5.6); *SA*: specific activity for the ORR measured at 0.9 V *vs.* RHE; *MA*: mass activity for the ORR measured at 0.9 V *vs.* RHE.
Notes: [a] Not relevant (bimetallic catalyst).

The catalytic activity of the catalysts at BoL were compared using the ORR specific activity, *SA*, and the ORR mass activity, *MA*, measured at 0.9 V *vs.* RHE (Table 5.2). *SA* values range from 0.16 (Ref) to 1.17 A $m_{Pt}{}^{-2}$ (PtCo/CX). *MA* values range from 14.0 (Ref) to 47.3 A $g_{Pt}{}^{-1}$ (10Pt/CX).

5.3.3 Accelerated stress tests at 353 K

ASTs were performed at 353 K (temperature representative of the real PEMFC working conditions) in order to check the stability of hollow particles and to compare it to those of a commercial Pt/C and synthesized Pt/CX catalysts. Figure 5.4 shows the evolution of the catalysts during the ASTs monitored by cyclic and CO stripping voltammograms: at BoL, after 5,000 AST cycles (at MoL), and after 20,000 AST cycles (at EoL). The values of the surface area, the values of *SA*, and the values of *MA*, all measured at BoL, MoL, and EoL, are collected in Table 5.2 and are represented in the bar graphs of Figure 5.5. Concerning the S_{CO} (Figure 5.5a), the bar graph shows the evolution of the electroactive surface area normalized by the initial S_{CO} of each catalyst. S_{CO} is stable for PtCo/CX (31, 31, and 27 m^2 $g_{Pt}{}^{-1}$) but, for the pure Pt catalysts, it decreases drastically, to 40-50 % of the initial values (109, 63, and 43 m^2 $g_{Pt}{}^{-1}$ for 10Pt/CX; 50, 34, and 25 m^2 $g_{Pt}{}^{-1}$ for 37Pt/CX; 90, 66, and 44 m^2 $g_{Pt}{}^{-1}$ for Ref). *SA* slightly increases for 10Pt/CX and Ref (0.44, 0.43, and 0.55 A $m_{Pt}{}^{-2}$; 0.16, 0.19, and 0.23 A $m_{Pt}{}^{-2}$, respectively) while it remains almost constant for 37Pt/CX (0.34, 0.25, and 0.33 A $m_{Pt}{}^{-2}$) and decreases for PtCo/CX (1.17, 0.76, and 0.58 A $m_{Pt}{}^{-2}$). However, *MA* decreases for all the catalysts (35.7, 23.2, and 15.3 A $g_{Pt}{}^{-1}$ for PtCo/CX; 47.3, 27.4, and 23.6 A $g_{Pt}{}^{-1}$ for 10Pt/CX; 16.7, 8.4, 8.3 A $g_{Pt}{}^{-1}$ for 37Pt/CX; 14.0, 12.3, and 10.2 A $g_{Pt}{}^{-1}$ for Ref).

Figure 5.6 shows the TEM micrographs of PtCo/CX, 10Pt/CX, and Ref after the ASTs and the particle size distribution (PSD) of these catalysts before and after the ASTs. In Figure 5.6a, hollow particles can be seen. The associated d_{TEM} slightly decreases (from 48.7 to 39.1 nm), but the average shell thickness slightly increases (t_{TEM} values from 3.4 to 4.1 nm). Moreover, some small particles, with an average particle size of 6.0 nm, are detected in the micrographs (but not shown in the PSD of PtCo/CX). In the TEM micrograph of 10Pt/CX after the ASTs (Figure 5.6c), the Pt particles are larger than initially, with presence of aggregates. The average diameter of these particles is equal to 5.2 nm (*vs.* 2.8 nm initially). The Pt particles growth can also be observed for the commercial Ref (Figure 5.6e), as its average particles size increases from 3.1 to 7.7 nm.

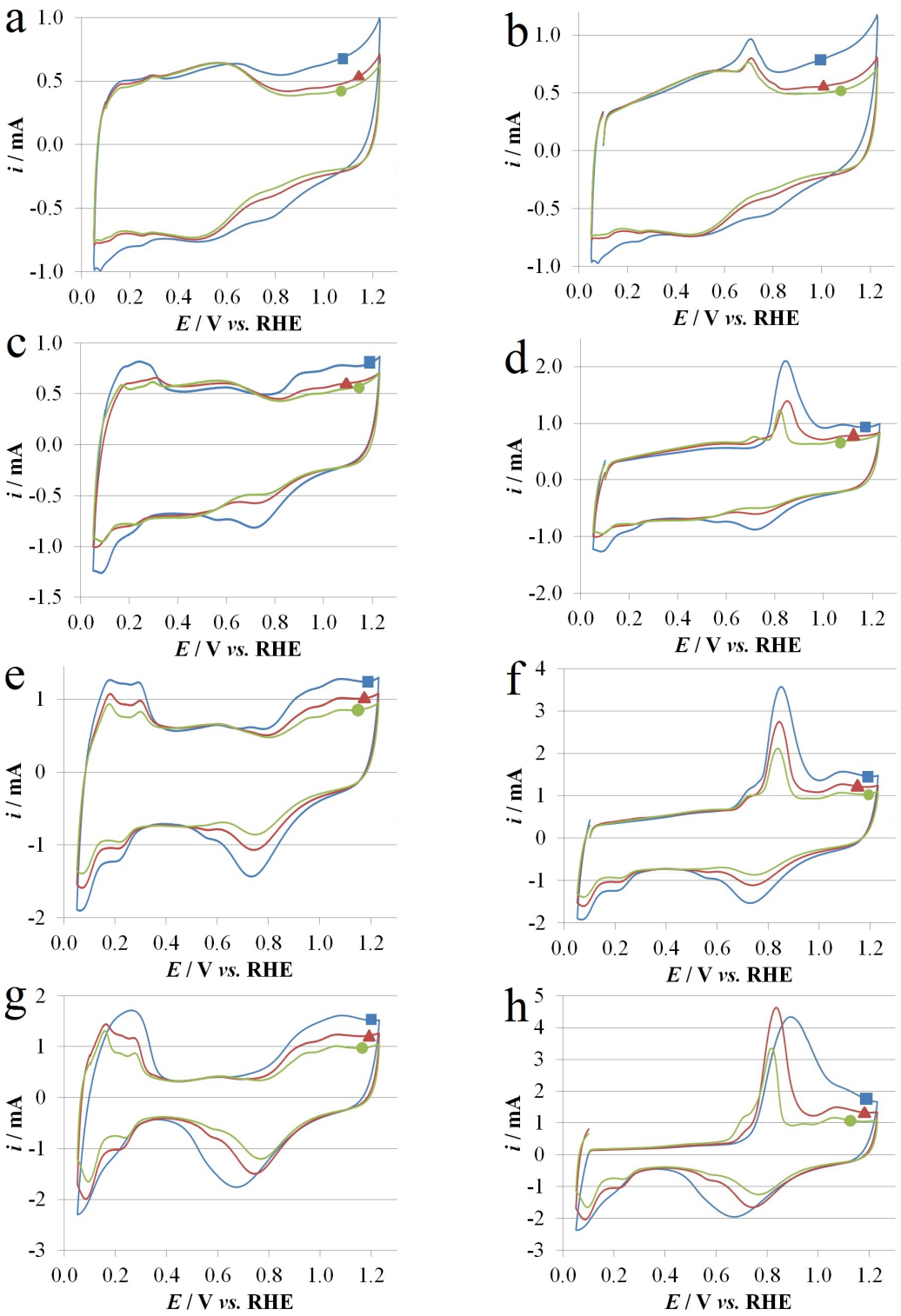

Figure 5.4: Cyclic and CO electrooxidation voltammograms of: PtCo/CX (a and b, respectively); 10Pt/CX (c and d, respectively); 37Pt/CX (e and f, respectively); Ref (g and h, respectively). The measurements were performed in 0.1 M H_2SO_4 at a sweep rate of 0.02 V s^{-1} at 298 K during accelerated stress tests at beginning of life (BoL, ■), middle of life (MoL, ▲), and end of life (EoL, ●).

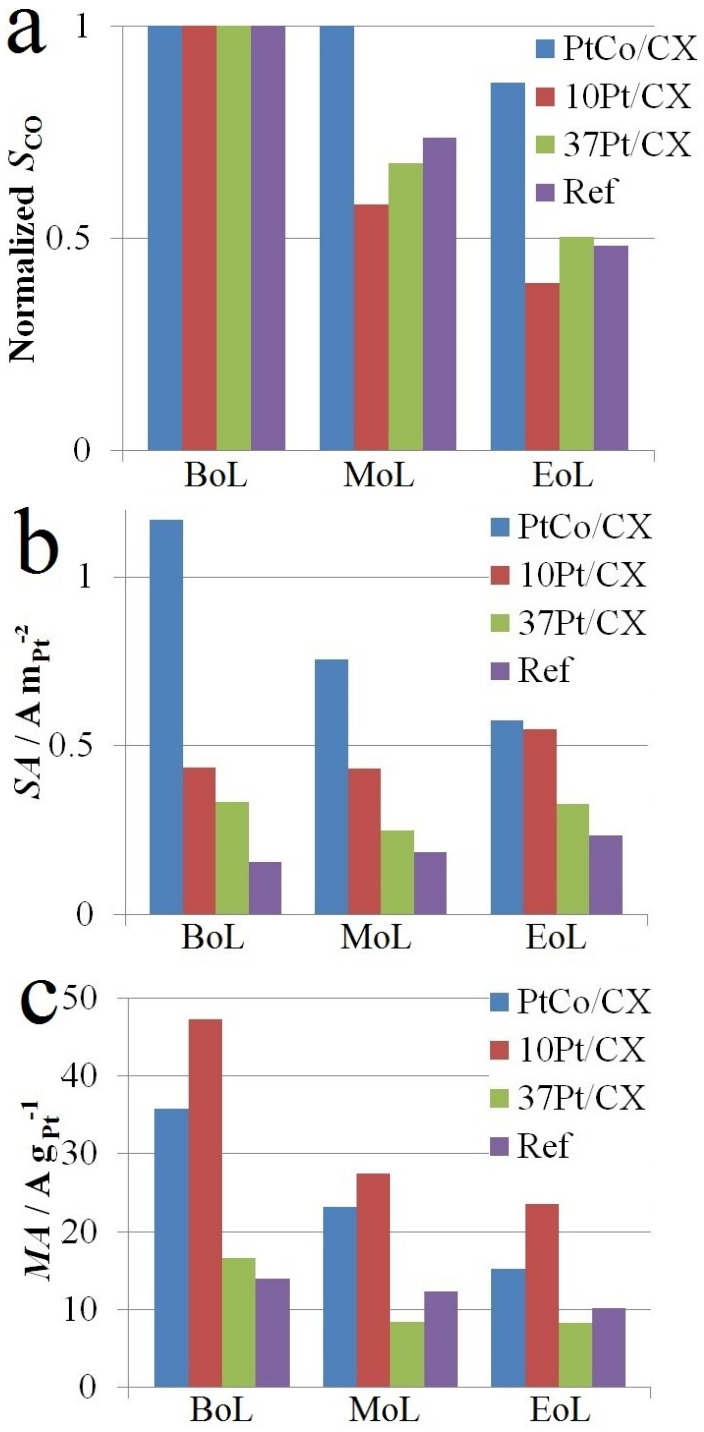

Figure 5.5: Evolution of the normalized electroactive specific area measured by CO stripping analysis (S_{CO}, a), the ORR specific activity measured at 0.9 V *vs.* RHE (SA, b), and the ORR mass activity measured at 0.9 V *vs.* RHE (MA, c) during the accelerated stress tests consisting of potential cycles between 0.6 and 1.0 V *vs.* RHE at 353 K. The values of S_{CO}, SA, and MA were measured at beginning of life (BoL), middle of life (MoL, 5,000 cycles) and end of life (EoL, 20,000 cycles), at 298 K. The electroactive specific areas are normalized by the values at BoL.

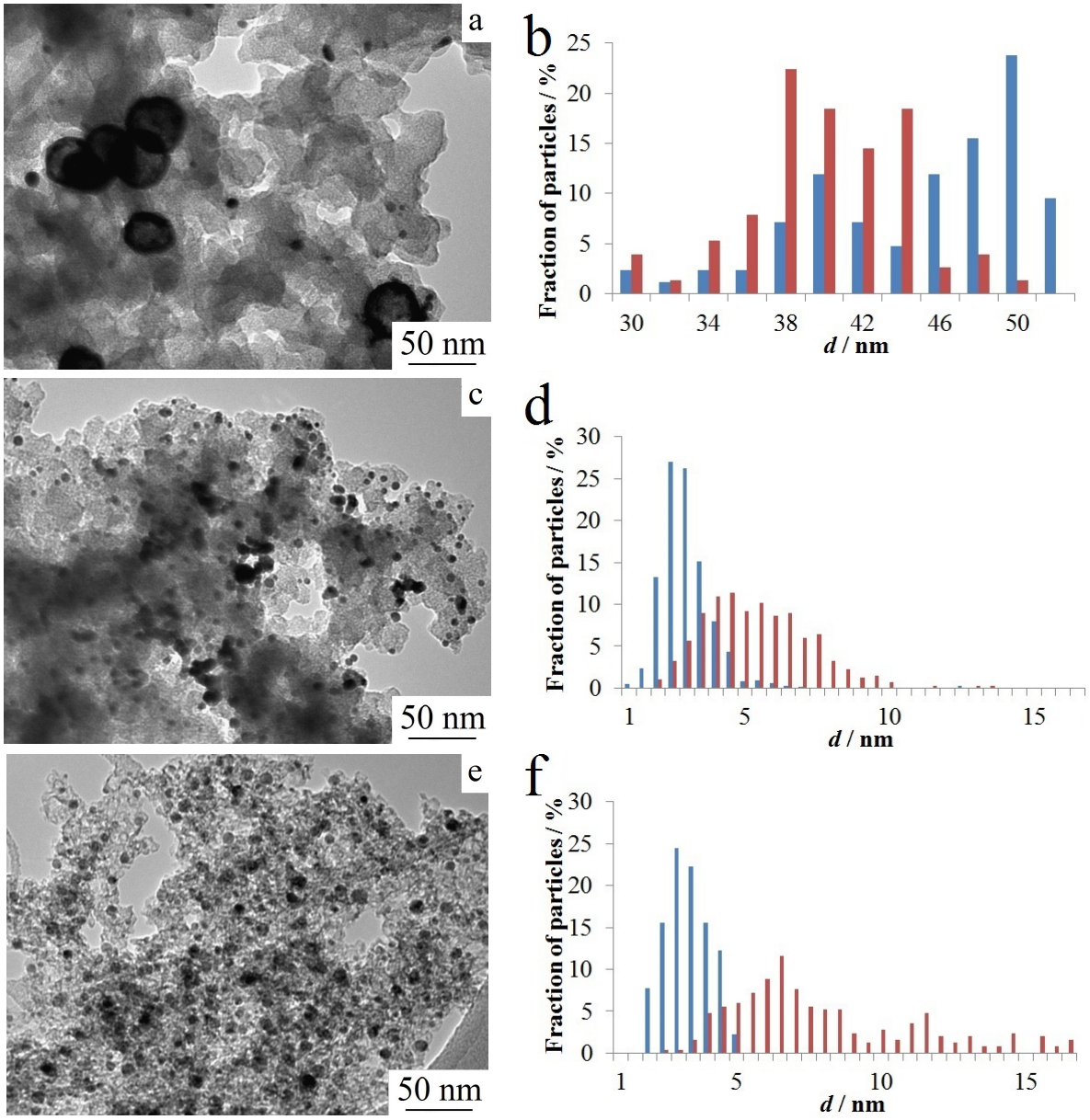

Figure 5.6: TEM micrographs and corresponding particle size distribution of: PtCo/CX (a and b, respectively), 10Pt/CX (c and d, respectively), and Ref (e and f, respectively) after the accelerated stress tests (at end of life, EoL), *i.e.* after 20,000 potential cycles between 0.6 and 1.0 V *vs.* RHE at 353 K. The particle size distribution at beginning of life (BoL) are presented for comparison.

5.4 Discussion

The catalysts can be classified in two groups with regard to their Pt loading: the low Pt loading catalysts (10 wt.%), PtCo/CX and 10Pt/CX, and the high Pt loading catalysts (37 wt.%), 37Pt/CX and Ref. The Pt loading of PtCo/CX is close to the target value (9.4 wt.% *vs.* 10 wt.%). The difference may be due to particles

which could detach from the support and be washed out during the washing steps. The Co loading is much lower than expected (1.8 wt.% instead of 10 wt.%). This value indicates that the majority of Co, reduced by $NaBH_4$ to form the Co colloid, is re-oxidized, dissolved, and eliminated during the next steps of the synthesis.

The nanoparticles of the PtCo/CX catalysts are hollow, as proved by the TEM micrograph (Figure 5.1a) and previous results (see previous chapter). The hollow nanoparticles formation mechanism can be summarized as follows: (i) a Co colloid was synthesized from a mixture of Co chloride and tri-sodium citrate solutions to which $NaBH_4$ was added; (ii) an acidic Pt salt was added to this Co colloid, leading to the protonation of citrates which leave the Co particle surface; (iii) as Co particles are accessible to Pt ions, galvanic replacement of Co atoms by Pt occurs, *i.e.* the oxidation of Co atoms provided the electrons needed to reduce Pt ions [30, 53]; (iv) Co atoms from the particle core and vacancies from the particle surface interdiffused through the Pt shells *via* the nanoscale Kirkendall effect [22, 23, 54–56]; (v) the acid washing performed at the end of the synthesis caused the dissolution of Co atoms located at the particles surface. These phenomena are the causes of the Co depletion of particles (Co loading of 1.8 wt.% instead of 10 wt.%).

XRD results show that the shell of the hollow particles is composed of Pt and Co atoms. As the diffraction angle of the low angle peak of PtCo/CX is slightly shifted from the Pt (1 1 1) diffraction angle (39.7°) to a higher value (40.1°, Figure 5.2), one can conclude that the Pt lattice is contracted due to the presence of Co atoms inside the Pt lattice, forming a PtCo alloy. Moreover, the average crystallite size, d_{XRD} (3.6 nm), is similar to the volume averaged thickness of the shell, t_v (3.7 nm). All these results demonstrate that the particle shells are constituted of small PtCo alloy crystalline domains.

For the Pt catalysts, TEM and XRD results are in agreement. The three catalysts are composed of small Pt particles between 3 and 4 nm. The catalysts with the smallest d_v (3.6 nm) exhibit the smallest crystallite sizes, d_{XRD} (2.3 and 2.4 nm for 10Pt/CX and Ref, respectively). 37Pt/CX displays the highest d_v and d_{XRD} (4.4 and 2.9 nm, respectively). The small difference between these average diameter values may be due to the large error of the XRD results, stemming from the low peak intensity.

The Pt electroactive specific areas are in agreement with the physicochemical results. The smaller the particle size measured by TEM, the higher the Pt electroactive specific area. For example, 10Pt/CX, which displays the smallest particle size and the smallest d_s (2.8 and 3.3 nm, respectively), exhibits the highest Pt electroactive specific area (109 $m^2\ g_{Pt}{}^{-1}$), and so, the lowest CO equivalent diameter (2.6 nm). For the Pt catalysts, d_s (Table 5.2) and d_{CO} (Table 5.1) are in good agreement. This result suggests that the synthesized Pt particles are cleaned from Cl present in the Pt precursor by formic acid reduction. Indeed, if the Pt particles were poisoned by Cl ions, the S_{CO} values would be lower, *i.e.* d_s would be significantly higher (see Chapter 2) [38]. d_{CO} was not calculated for the bimetallic catalyst because (i) the possible presence of Co atoms at the surface of the particle may impacts the d_{CO}

value, as Co atoms do not adsorb CO molecules [52], and (ii) the presence of hollow nanoparticles prevents from calculating d_{CO} from Equation (5.6).

In Figure 5.3, the CO electrooxidation peaks can provide information about the particle size and distribution for pure Pt catalysts [45–47]. The higher the CO electrooxidation potential, the smaller the particle size. Ref displays a huge and wide CO electrooxidation peak centered at 0.89 V *vs.* RHE. The width of the peak is due to the high Nafion® content in the catalytic layer. Indeed, Nafion® film formed around the Pt particles probably slows the diffusion of the reactants between the liquid electrolyte and the particles, leading to a broadening of the signal. 10Pt/CX and 37Pt/CX display a CO electrooxidation peak at the same potential, *i.e.* at 0.84 V *vs.* RHE, representative of Pt particle with diameter higher than 2 nm. Moreover, the CO stripping voltammogram of 37Pt/CX exhibits a shouldering at 0.73 V *vs.* RHE, which is relative to Pt particles aggregates. Concerning the bimetallic catalyst, PtCo/CX displays a small peak at 0.71 V *vs.* RHE with a small shouldering around 0.75 V *vs.* RHE. The peak at 0.71 V *vs.* RHE stems from structural defects [20, 22, 23]. The higher the peak area, the higher the density of structural defects. These defects are very effective for several reactions, including CO electrooxidation, leading to a peak shift towards lower potential values. The shouldering can be associated to two types of active sites: (i) small Pt crystallites present on the CX support and (ii) active sites isolated from structural defects and from which CO molecules can not diffuse to sites with higher activity.

Regarding the ORR specific activity, the catalyst with the highest *SA* is PtCo/CX. It displays a specific activity around three to seven times higher than the other catalysts of this chapter due to the PtCo alloy present in the hollow particle shell and to the high density of structural defects. Indeed, PtCo alloys are well known to display better specific activity for the ORR than pure Pt catalysts as the Co atoms contract the Pt lattice, leading to a modification of the Pt *5d*-band and a weakening of the interaction between oxygenated species and Pt atoms [1–6]. As for structural defects, the high coordination active sites adsorb oxygenated species more weakly than low-coordinated catalytic sites found in small nanoparticles, leading in an increase of the ORR performance [57–59]. For pure Pt catalysts, 10Pt/CX exhibits the higher specific activity (0.44 A $m_{Pt}{}^{-2}$), followed by 37Pt/CX (0.34 A $m_{Pt}{}^{-2}$). The *SA* value of Ref is twice lower than that of the other Pt catalysts (0.16 A $m_{Pt}{}^{-2}$). The difference between the *SA* values of 10Pt/CX and Ref may be due to the high quantity of Pt in the catalytic layer of Ref contrary to that of 10Pt/CX. Indeed, the high amount of Pt in the catalytic layer introduces larger uncertainties to the results, *e.g.* more diffusion limitations or more parameters influencing the results (such as O_2 diffusion inside ionomer, agglomerate structure, particle contact, *etc.*) [42–44]. The difference between the *SA* values of 37Pt/CX and Ref may be due to the presence of agglomerates, structural defects, and/or grain boundaries in 37Pt/CX sample, proved by the pre-peak around 0.73 V *vs.* RHE in CO voltammograms. Indeed, these defective structures exhibit higher *SA*.

For the ORR mass activity, the catalyst which displays the best *MA* is 10Pt/CX (47.3 A $g_{Pt}{}^{-1}$). This is due to its huge Pt specific area and its good *SA*. The

second best catalyst is PtCo/CX (35.7 A $g_{Pt}{}^{-1}$). In this case, the huge *SA* is counterbalanced by a small Pt specific area, leading to a good *MA* right below that of 10Pt/CX. The other two catalysts, 37Pt/CX and Ref, display similar mass activity for the ORR (16.7 and 14.0 A $g_{Pt}{}^{-1}$). Indeed, 37Pt/CX, which is composed of relatively large Pt particles, exhibits higher *SA* and lower S_{CO} than Ref, which is composed of smaller Pt particles. So, when these properties are combined, the advantages of each catalyst compensate their drawbacks, leading to similar *MA* values for the two catalysts. It must be noted that the PtCo/CX activities are underestimated because of the adsorption of the SO_4^{2-} ions from the electrolyte on the particles surface. These ions, indeed, adsorb on the particle surface stronger than the oxygenated intermediates of the ORR, leading to a decrease in activity for the ORR [60, 61]. The activities of the pure Pt catalysts are also underestimate but it seems that the impacts of the adsorption of SO_4^{2-} is lower in the case of Pt particles than in the case of hollow nanoparticles with a high density of structural defects. For more details, see the Appendix 5.A1 at the end of this chapter where the activities measured in H_2SO_4 or $HClO_4$ electrolyte are compared.

5.4.1 Accelerated stress tests at 353 K

The hollow particles catalyst, PtCo/CX, displays a very different behaviour than the pure Pt catalysts. Indeed, in Figure 5.4, one can see that the cyclic and CO stripping voltammograms of PtCo/CX are nearly unchanged during the ASTs, except for a small variation of the double layer capacitance and ohmic resistance during the 5,000 first AST cycles probably due to carbon corrosion. This leads to stable values of the electroactive surface area, from 31 to 27 m^2 $g_{Pt}{}^{-1}$, *i.e.* a S_{CO} decrease of 13% (Figure 5.5a). Moreover, the TEM micrograph registered after 20,000 AST cycles shows that the hollow structure of the particles remains, even if the particles dimensions change slightly (d_{TEM} decreases from 48.7 to 39.1 nm, t_{TEM} increases from 3.4 to 4.1 nm). On the contrary, the pure Pt catalysts underwent huge changes during the ASTs. Indeed, for each Pt catalyst, the area under the different peaks (H^+ (ad/de)sorption, Pt oxidation, reduction of Pt oxides, and CO electrooxidation) decreases during the ASTs, resulting in a S_{CO} decrease of 50% for 37Pt/CX, 51% for Ref, and 61% for 10Pt/CX after 20,000 cycles (Figure 5.5a). Moreover, the position of the peaks of the Pt catalysts are shifted to lower potential for the oxidation peaks and to higher potential for the reduction peaks. These shifts indicate that the Pt particles grew during the AST cycles, as can be seen in Figures 5.6c and e. Indeed, the average particle size increases from 2.8 to 5.2 nm and from 3.1 to 7.7 nm for 10Pt/CX and Ref, respectively. The particle growth is due to the dissolution and redeposition of Pt atoms from small particles to larger particles, *i.e. via* the Ostwald ripening mechanism, and to the migration and coalescence of Pt crystallites [14–17]. Another phenomenon which can be observed is the formation of Pt particle agglomerates in samples 10Pt/CX and Ref, proved by the appearance of the CO electrooxidation peak around 0.75 V *vs.* RHE (representative of Pt aggregates) and of the aggregates on the TEM micrographs (Figure 5.6c). This phenomenon is

caused by the migration of Pt crystallites over the carbon support [14–17]. Moreover, some Pt particles can detach from the support, migrate to the ionomer, or be dissolved and may be redeposited in a place without any contact with the carbon support, *e.g.* in the ionomer [14–17]. All these results show that the hollow particles display better morphology stability than the usual solid Pt nanoparticles.

Despite the structural stability of PtCo/CX particles, the specific activity of PtCo/CX decreases from 1.17 to 0.58 A $m_{Pt}{}^{-2}$, *i.e.* the *SA* value suffers a 51% decrease. This may be due to a further Co depletion, leading to Pt lattice relaxation, and to a decrease of the density of structural defects of the hollow PtCo nanoparticles during the AST cycles. On the contrary, 10Pt/CX and Ref show a significant rise in *SA*, 26% and 50% increase, respectively. This increase in specific activity is due to the higher particle size and the appearance of agglomerates, as shown by the appearance of a CO electrooxidation pre-peak in 10Pt/CX and Ref CO voltammograms. Indeed, the formation of agglomerates induces the formation of grain boundaries. The grain boundaries correspond to sites where the Pt lattice is dilated. Because of the presence of these dilated sites, the Pt lattice around the grain boundaries is contracted. These contracted sites, which weakly adsorb the oxygenated intermediates of the ORR, exhibit higher specific activity for the ORR. So, the larger and more defective the particles, the higher the *SA* value [57–59,62,63]. For 37Pt/CX, the *SA* value remains almost constant (only 2% decrease after 20,000 cycles). This steadiness is due to the combination of two opposite phenomena. On the one hand, the size of the particles slightly increases, as shown by the slight shift of the peaks in Figures 5.4e and f, rising the *SA* value. On the other hand, one can see in Figure 5.4f that the pre-peak at 0.73 V *vs.* RHE, representative of agglomerates and structural defects, decreases during ASTs. This decrease leads to a drop in *SA*, as the density of very active and defective sites tends to decrease. These phenomena counterbalance each other, leading to almost constant *SA* value. When comparing the four catalysts, PtCo/CX exhibits the best *SA* all along the ASTs. However, at the end of the 20,000 cycles, the *SA* value of PtCo/CX becomes similar to that of 10Pt/CX (0.58 *vs.* 0.55 A $m_{Pt}{}^{-2}$) but remains more than twice higher than that of Ref.

Concerning the mass activity, the four samples exhibit a decrease in *MA* value, which drops by 57% for PtCo/CX, 50% for 10Pt/CX, 50% for 37Pt/CX, and 27% for Ref. In the case of PtCo/CX, even if the electroactive surface area is almost constant, the fall in specific activity leads to the decrease in mass activity. This drop is due to a further Co depletion, leading to a Pt lattice relaxation, and to a diminution of the density of structural defects. For 10Pt/CX and Ref, the large drop of S_{CO} is counterbalanced by the *SA* increase, leading to smaller decrease of *MA*, especially in the case of Ref. The *MA* decrease of 37Pt/CX mostly results from the drop in S_{CO}, as the initial and final *SA* values are almost the same. When comparing the activities of the four catalysts, one can notice that 10Pt/CX is each time the best catalyst, closely followed by PtCo/CX. After 20,000 AST cycles, these two catalysts still display a *MA* value twice higher than Ref. The high final *MA* value of PtCo/CX is due to its high *SA* value, even if it decreased of *ca.* 50%, and

to the good morphological stability of the hollow nanoparticles. The high final *MA* value of 10Pt/CX is due to the high *SA* value, which increased during the ASTs, and to its S_{CO} value (43 m^2 $g_{Pt}{}^{-1}$ after 20,000 AST cycles) which remains high despite the huge decrease it suffered during the ASTs. It must be reminded that the activity measurements are performed in H_2SO_4, which impacts the performance by producing SO_4^{2-} ions blocking the active sites [60, 61]. For more details, see the Appendix 5.A1 at the end of this chapter where the activities measured in H_2SO_4 or $HClO_4$ electrolyte are compared.

5.5 Conclusion

The goal of this chapter was to study the behaviour of hollow PtCo nanoparticles supported on carbon xerogel (CX) during accelerated stress tests (ASTs) and to compare it with those of pure Pt nanoparticles deposited on CX and a commercial reference (Pt/HSAC catalyst, Tanaka 37 wt.%). Concerning the physicochemical properties, the hollow PtCo nanoparticles remain hollow after the ASTs with a small decrease in the average particle diameter and a slight increase in the average shell thickness. In the case of pure Pt catalysts, the average diameter of particles increases significantly and some Pt particles aggregates are formed.

Concerning the electrochemical properties, the electroactive surface area of the hollow PtCo particles catalyst remains almost constant (only 13% decrease after 20,000 AST cycles), as the morphology and the size of the hollow nanoparticles remain nearly unchanged after the ASTs. However, the specific activity decreases a lot. This drop may stem from two causes: (i) the depletion of the shell Co atoms, leading to the relaxation of the Pt lattice which has been contracted due to the Co presence; (ii) the decrease of the density of structural defects, due to the reorganization of crystalline domains under operation. These phenomena result in a 57% decrease in mass activity (*i.e.* per mass unit of Pt). In spite of this, the mass activity of the hollow particles catalyst remains *ca.* twice higher than that of the commercial reference catalyst. As for the pure Pt catalysts, their electroactive surface area decreases to 40-50% of the initial values, the specific activity increases or, at least, remains constant, and the mass activity decreases. The Pt catalyst with low Pt loading displays the best mass activity, slightly higher than that of the hollow PtCo particles catalyst. However, it is known that the strong interaction between the SO_4^{2-} ions from the H_2SO_4 electrolyte and the hollow particles decreases the hollow particles catalyst activities (for more details, see the Appendix 5.A1 at the end of this chapter). It must be noted that the higher activity of the Pt catalyst with low Pt loading may be mitigated during operation in fuel cell. Indeed, in order to produce the same amount of current in fuel cells with the catalyst with low Pt loading and with the catalysts with high Pt loading, the amount of Pt in the catalytic layer needs to be the same. However, as the catalysts does not display the same Pt loading, the thickness of the catalytic layer will be larger with catalysts with low Pt loading. This increased thickness may impact the diffusion of O_2 molecules, leading to more diffusion limitations.

The next step is to study the behaviour of the hollow particles in PEMFC to check for the morphological stability of the hollow nanoparticles in a complete membrane-electrodes assembly. This is the subject of the next chapter. Moreover, in order to improve the performance of hollow PtCo particles catalysts, the synthesis of hollow nanoparticles have to be thoroughly studied and optimized. For example, the synthesis variables, such as the quantity of reactants, the adding time, *etc.*, have to be optimized in order to increase the electroactive surface area of the catalysts, *e.g.* by decreasing the hollow particle size. A first insight into the effect of hollow nanoparticle size on the ASTs can be read in the Appendix 5.A2 at the end of this chapter. Another way to increase the electroactive specific area, and so the mass activity of hollow PtCo particles catalysts, may be to synthesize hollow and porous nanoparticles in order for the reactants to have access to the internal surface of the hollow nanoparticles. These ways of improvement should lead to increase further the mass activity and the durability of the hollow PtCo nanoparticles catalysts, which already exhibit a good morphological stability.

References

[1] H. A. Gasteiger, S. S. Kocha, B. Sompalli, and F. T. Wagner, *Applied Catalysis B: Environmental* **56**, 9 (2005).

[2] C. M. Pedersen, M. Escudero-Escribano, A. Velázquez-Palenzuela, L. H. Christensen, I. Chorkendorff, and I. E. L. Stephens, *Electrochimica Acta* **179**, 647 (2015).

[3] B. Han, C. E. Carlton, A. Kongkanand, R. S. Kukreja, B. R. Theobald, L. Gan, R. O'Malley, P. Strasser, F. T. Wagner, and Y. Shao-Horn, *Energy & Environmental Science* **8**, 258 (2015).

[4] S. Chen, W. Sheng, N. Yabuuchi, P. J. Ferreira, L. F. Allard, and Y. Shao-Horn, *Journal of Physical Chemistry C* **113**, 1109 (2009).

[5] S. Koh, M. F. Toney, and P. Strasser, *Electrochimica Acta* **52**, 2765 (2007).

[6] M. Oezaslan and P. Strasser, *Journal of Power Sources* **196**, 5240 (2011).

[7] L. Gan, M. Heggen, R. O'Malley, B. Theobald, and P. Strasser, *Nano Letters* **13**, 1131 (2013).

[8] V. R. Stamenkovic, B. Fowler, B. S. Mun, G. Wang, P. N. Ross, C. A. Lucas, and N. M. Markovic, *Science* **315**, 493 (2007).

[9] B. Hammer and J. K. Nørskov, *Surface Science* **343**, 211 (1995).

[10] J. R. Kitchin, J. K. Nørskov, M. A. Barteau, and J. G. Chen, *Journal of Chemical Physics* **120**, 10240 (2004).

[11] T. Bligaard and J. K. Nørskov, *Electrochimica Acta* **52**, 5512 (2007).

[12] I. E. L. Stephens, A. S. Bondarenko, F. J. Perez-Alonso, F. Calle-Vallejo, L. Bech, T. P. Johansson, A. K. Jepsen, R. Frydendal, B. P. Knudsen, J. Rossmeisl, and I. Chorkendorff, *Journal of the American Chemical Society* **133**, 5485 (2011).

[13] I. E. L. Stephens, A. S. Bondarenko, U. Grønbjerg, J. Rossmeisl, and I. Chorkendorff, *Energy & Environmental Science* **5**, 6744 (2012).

[14] Y. Shao-Horn, W. C. Sheng, S. Chen, P. J. Ferreira, E. F. Holby, and D. Morgan, *Topics in Catalysis* **46**, 285 (2007).

[15] X. Z. Yuan, H. Li, S. Zhang, J. Martin, and H. Wang, *Journal of Power Sources* **196**, 9107 (2011).

[16] S. Zhang, X. Z. Yuan, J. N. C. Hin, H. Wang, J. Wu, K. A. Friedrich, and M. Schulze, *Journal of Power Sources* **195**, 1142 (2010).

[17] L. Dubau, L. Castanheira, F. Maillard, M. Chatenet, O. Lottin, G. Maranzana, J. Dillet, A. Lamibrac, J. C. Perrin, E. Moukheiber, A. Elkaddouri, G. De Moor, C. Bas, L. Flandin, and N. Caqué, *Wiley Interdisciplinary Reviews: Energy and Environment* **3**, 540 (2014).

[18] S. Chen, H. A. Gasteiger, K. Hayakawa, T. Tada, and Y. Shao-Horn, *Journal of the Electrochemical Society* **157**, A82 (2010).

[19] M. Oezaslan, M. Heggen, and P. Strasser, *Journal of the American Chemical Society* **134**, 514 (2012).

[20] R. Chattot, T. Asset, P. Bordet, J. Drnec, L. Dubau, and F. Maillard, *ACS Catalysis* **7**, 398 (2017).

[21] Y. Yu, H. L. Xin, R. Hovden, D. Wang, E. D. Rus, J. A. Mundy, D. A. Muller, and H. D. Abruna, *Nano Letters* **12**, 4417 (2012).

[22] L. Dubau, J. Nelayah, S. Moldovan, O. Ersen, P. Bordet, J. Drnec, T. Asset, R. Chattot, and F. Maillard, *ACS Catalysis* **6**, 4673 (2016).

[23] T. Asset, R. Chattot, J. Nelayah, N. Job, L. Dubau, and F. Maillard, *ChemElectroChem* **3**, 1591 (2016).

[24] C. Chen, Y. Kang, Z. Huo, Z. Zhu, W. Huang, H. L. Xin, J. D. Snyder, D. Li, J. A. Herron, M. Mavrikakis, M. Chi, K. L. More, Y. Li, N. M. Markovic, G. A. Somorjai, P. Yang, and V. R. Stamenkovic, *Science* **343**, 1339 (2014).

[25] L. Dubau, J. Durst, F. Maillard, L. Guétaz, M. Chatenet, J. André, and E. Rossinot, *Electrochimica Acta* **56**, 10658 (2011).

[26] L. Dubau, M. Lopez-Haro, L. Castanheira, J. Durst, M. Chatenet, P. Bayle-Guillemaud, L. Guétaz, N. Caqué, E. Rossinot, and F. Maillard, *Applied Catalysis B: Environmental* **142-143**, 801 (2013).

[27] L. Dubau, M. Lopez-Haro, J. Durst, L. Guetaz, P. Bayle-Guillemaud, M. Chatenet, and F. Maillard, *Journal of Materials Chemistry A* **2**, 18497 (2014).

[28] L. Dubau, M. Lopez-Haro, J. Durst, and F. Maillard, *Catalysis Today* **262**, 146 (2016).

[29] L. Dubau, J. Nelayah, T. Asset, R. Chattot, and F. Maillard, *ACS Catalysis* **7**, 3072 (2017).

[30] S. J. Bae, S. J. Yoo, Y. Lim, S. Kim, Y. Lim, J. Choi, K. S. Nahm, S. J. Hwang, T.-H. Lim, S.-K. Kim, and P. Kim, *Journal of Materials Chemistry* **22**, 8820 (2012).

[31] A. X. Shan, Z. C. Chen, B. Q. Li, C. P. Chen, and R. M. Wang, *Journal of Materials Chemistry A* **3**, 1031 (2015).

[32] N. Job, R. Pirard, J. Marien, and J.-P. Pirard, *Carbon* **42**, 619 (2004).

[33] N. Job, S. D. Lambert, M. Chatenet, C. J. Gommes, F. Maillard, S. Berthon-Fabry, J. R. Regalbuto, and J.-P. Pirard, *Catalysis Today* **150**, 119 (2010).

[34] A. Zubiaur, M. Chatenet, F. Maillard, S. D. Lambert, J.-P. Pirard, and N. Job, *Fuel Cells* **14**, 343 (2014).

[35] S. D. Lambert, N. Job, L. D'Souza, M. Pereira, R. Pirard, B. Heinrichs, J. Figueiredo, J.-P. Pirard, and J. Regalbuto, *Journal of Catalysis* **261**, 23 (2009).

[36] N. Job, M. F. R. Pereira, S. D. Lambert, A. Cabiac, G. Delahay, J.-F. Colomer, J. Marien, J. L. Figueiredo, and J.-P. Pirard, *Journal of Catalysis* **240**, 160 (2006).

[37] N. Job, F. Maillard, J. Marie, S. Berthon-Fabry, J. P. Pirard, and M. Chatenet, *Journal of Materials Science* **44**, 6591 (2009).

[38] N. Job, M. Chatenet, S. Berthon-Fabry, S. Hermans, and F. Maillard, *Journal of Power Sources* **240**, 294 (2013).

[39] M.-L. C. Piedboeuf, A. F. Léonard, K. Traina, and N. Job, *Colloids and Surfaces A: Physicochemical and Engineering Aspects* **471**, 124 (2015).

[40] E. Guilminot, A. Corcella, M. Chatenet, and F. Maillard, *Journal of Electroanalytical Chemistry* **599**, 111 (2007).

[41] M. Chatenet, L. Dubau, N. Job, and F. Maillard, *Catalysis Today* **156**, 76 (2010).

[42] K. Mayrhofer, D. Strmcnik, B. Blizanac, V. Stamenkovic, M. Arenz, and N. Markovic, *Electrochimica Acta* **53**, 3181 (2008).

[43] S. S. Kocha, J. W. Zack, S. M. Alia, K. C. Neyerlin, and B. S. Pivovar, *ECS Transactions* **50**, 1475 (2013).

[44] K. Shinozaki, J. W. Zack, R. M. Richards, B. S. Pivovar, and S. S. Kocha, *Journal of the Electrochemical Society* **162**, F1144 (2015).

[45] F. Maillard, M. Eikerling, O. V. Cherstiouk, S. Schreier, E. Savinova, and U. Stimming, *Faraday Discussions* **125**, 357 (2004).

[46] F. Maillard, S. Schreier, M. Hanzlik, E. R. Savinova, S. Weinkauf, and U. Stimming, *Physical Chemistry Chemical Physics* **7**, 385 (2005).

[47] F. Maillard, E. R. Savinova, and U. Stimming, *Journal of Electroanalytical Chemistry* **599**, 221 (2007).

[48] S. Trasatti and O. Petrii, *Journal of Electroanalytical Chemistry* **327**, 353 (1992).

[49] A. J. Bard and L. R. Faulkner, *Electrochemical Methods: Fundamentals and applications*, John Wiley & Sons, Inc., Weinheim, Germany, 2nd edition, 2001.

[50] G. Bergeret and P. Gallezot, Particle size and dispersion measurement, in *Handbook of Heterogeneous Catalysis*, edited by G. Ertl, H. Knözinger, and J. Weitkamp, p. 439, Wiley-VCH, Weinheim, Germany, 1997.

[51] F. Maillard, S. Pronkin, and E. R. Savinova, Influence of size on the electrocatalytic activities of supported metal nanoparticles in fuel cells related reactions, in *Handbook of Fuel Cells*, edited by W. Vielstich, H. A. Gasteiger, and H. Yokokawa, volume 5, pp. 91–111, John Wiley & Sons, Ltd, Chichester, United Kingdom, 2009.

[52] H. Schulenburg, J. Durst, E. Müller, A. Wokaun, and G. G. Scherer, *Journal of Electroanalytical Chemistry* **642**, 52 (2010).

[53] J. X. Wang, C. Ma, Y. Choi, D. Su, Y. Zhu, P. Liu, R. Si, M. B. Vukmirovic, Y. Zhang, and R. R. Adzic, *Journal of the American Chemical Society* **133**, 13551 (2011).

[54] Y. Yin, R. M. Rioux, C. K. Erdonmez, S. Hughes, G. A. Somorjai, and A. P. Alivisatos, *Science* **304**, 711 (2004).

[55] Y. Yin, C. K. Erdonmez, A. Cabot, S. Hughes, and A. P. Alivisatos, *Advanced Functional Materials* **16**, 1389 (2006).

[56] E. González, J. Arbiol, and V. F. Puntes, *Science* **334**, 1377 (2011).

[57] F. Calle-Vallejo, J. I. Martínez, J. M. García-Lastra, P. Sautet, and D. Loffreda, *Angewandte Chemie - International Edition* **53**, 8316 (2014).

[58] F. Calle-Vallejo, J. Tymoczko, V. Colic, Q. H. Vu, M. D. Pohl, K. Morgenstern, D. Loffreda, P. Sautet, W. Schuhmann, and A. S. Bandarenka, *Science* **350**, 185 (2015).

[59] O. Le Bacq, A. Pasturel, R. Chattot, B. Previdello, J. Nelayah, T. Asset, L. Dubau, and F. Maillard, *ChemCatChem* **9**, 2324 (2017).

[60] J. Tymoczko, F. Calle-Vallejo, V. Colic, M. T. M. Koper, W. Schuhmann, and A. S. Bandarenka, *ACS Catalysis* **4**, 3772 (2014).

[61] J. Tymoczko, W. Schuhmann, and A. S. Bandarenka, *ChemElectroChem* **1**, 213 (2014).

[62] K. Kinoshita, *Journal of the Electrochemical Society* **137**, 845 (1990).

[63] O. Antoine, Y. Bultel, and R. Durand, *Journal of Electroanalytical Chemistry* **499**, 85 (2001).

Appendix

5.A1 Effect of the electrolyte

This Appendix section focuses on the electrochemical properties of all the above-mentioned hollow particles catalysts, especially on the difference caused by the use of two different electrolytes ($HClO_4$ and H_2SO_4, both at concentration of 0.1 M) and the variation of these properties with the electroactive specific area (S_{CO}). Figure 5.A1.1 shows the evolution of the average diameter of the particles (d_{TEM}), of the ORR specific activity (SA), and of the ORR mass activity (MA) as a function of S_{CO}. The first observation which can be made is that no clear relationship between S_{CO} and d_{TEM} can be drawn from Figure 5.A1.1a, whatever the electrolyte. Indeed, S_{CO} seems to be independent of d_{TEM} as S_{CO} values are relatively constant (between 15 and 30 $m^2\ {g_{Pt}}^{-1}$). This can be explained by the hollow morphology of the particles. If one compares two hollow nanoparticles catalysts with different average diameter of particles, *e.g.* 20 and 50 nm, considering the same shell thickness and the same Pt loading, the ratio of the total surface area of the two catalysts is equal to 1.3. This ratio close to unity and the error due to the small peak intensity of the CO stripping measurement lead to an apparent independence between d_{TEM} and S_{CO}.

Regarding the SA and MA, values measured in H_2SO_4 electrolyte seem almost constant and always lower than the values measured in $HClO_4$ electrolyte. Activity is in fact limited by the nature of the electrolyte. Indeed, for all the samples, SA values measured in H_2SO_4 range from 1 to 2 A ${m_{Pt}}^{-2}$ while MA values, also measured in H_2SO_4, are between 30 and 50 A ${g_{Pt}}^{-1}$. These can be compared to the values measured in $HClO_4$: SA values between 3 and 6 A ${m_{Pt}}^{-2}$ and MA values between 70 and 100 A ${g_{Pt}}^{-1}$. It is well-known that sulfate ions SO_4^{2-} adsorb much more strongly on the Pt surface atoms than perchlorate ions ClO_4^- [60,61]. These adsorbed sulfate ions block the Pt catalytic active sites, preventing the adsorption of reactants (oxygen molecules). This blocking leads to a decrease in the ORR activities (MA and SA) of the catalysts compared to values observed in $HClO_4$. When comparing the activities measured in $HClO_4$ in Chapter 4 with the activity measured in H_2SO_4 in the present chapter, one can see that the impact of the electrolyte on the ORR activity of the pure Pt catalysts is between a factor 1 and 2. However, considering the hollow PtCo catalysts, the activities measured in $HClO_4$ are three to four times higher thant those measured in H_2SO_4. So, the effect of the electrolyte seems to worsen in the case of hollow PtCo nanoparticles. Furthermore, the activities of hollow particles catalysts seem to reach an upper limit (*ca.* 2 A ${m_{Pt}}^{-2}$ and 50 A ${g_{Pt}}^{-1}$ for SA and MA value, respectively) and do not depend on S_{CO}.

By opposition, the specific and mass activities measured in $HClO_4$ seem to increase while decreasing the electroactive specific area, S_{CO} (Figures 5.A1.1b and c). However, the S_{CO} range studied in the present chapter is relatively narrow (between 15 and 30 $m^2\ {g_{Pt}}^{-1}$). It will be interesting to study catalysts with lower or higher electroactive specific area in order to analyze further these parameters.

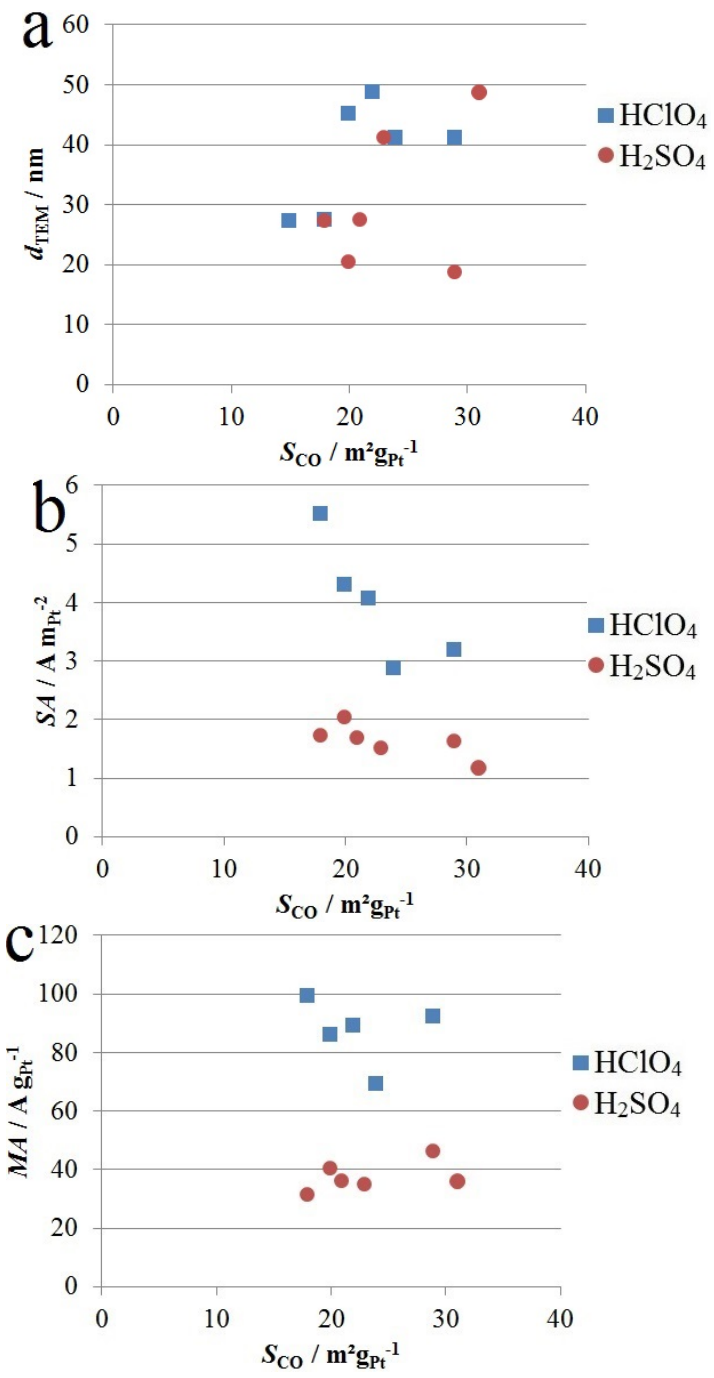

Figure 5.A1.1: Evolution of the average hollow particle diameter (a), of the ORR specific activity measured at 0.9 V *vs.* RHE (b), and the ORR mass activity measured at 0.9 V *vs.* RHE (c) as a function of the electroactive specific area. The measurements were performed either in 0.1 M $HClO_4$ (■) or 0.1 M H_2SO_4 (●) electrolyte.

5.A2 Effect of hollow particle size on ASTs

The durability of a hollow PtCo particles catalyst with lower average particle size, labeled hereafter PtCo/CX-B, was studied. PtCo/CX-B was synthesized following the same procedure as PtCo/CX and using Citrate-A (see Appendix 4.A1 at the end of Chapter 4 for more details). As PtCo/CX-B was synthesized after PtCo/CX, the hollow particles of PtCo/CX-B are smaller than those of PtCo/CX (average particle size of 18.6 nm with a standard deviation of 2.9 nm, instead of 48.7 ± 3.8 nm). The electrochemical properties of PtCo/CX-B were compared to those of the four catalysts described in the present chapter, *i.e.* PtCo/CX, 10Pt/CX and 37Pt/CX (two catalysts constituted of Pt particles deposited on carbon xerogel with 10 or 37 wt.% of Pt, respectively) and Ref (commercial Pt catalyst, 37 wt.% from Tanaka). Figure 5.A2.1 compares the electrochemical results of these five catalysts.

Initially, the electrochemical properties of PtCo/CX-B were the following: (i) an electroactive specific area, S_{CO}, of 29 m^2 $g_{Pt}{}^{-1}$, similar to PtCo/CX (31 m^2 $g_{Pt}{}^{-1}$), (ii) an ORR specific activity, *SA*, of 1.610 A $m_{Pt}{}^{-2}$, the highest of all the catalysts studied in the present chapter, and (iii) an ORR mass activity, *MA*, of 46.2 A $g_{Pt}{}^{-1}$, higher than PtCo/CX (35.7 A $g_{Pt}{}^{-1}$) but similar to the best catalyst of the present chapter (10Pt/CX, 47.3 A $g_{Pt}{}^{-1}$).

For the electrochemical properties after the accelerated stress tests, S_{CO} of PtCo/CX-B was even more stable than PtCo/CX with only 5% decrease after 20,000 AST cycles. The *SA* value remains the highest of all the catalysts, even if it drops by 59% after 20,000 AST cycles. The *MA* value (46.2 A $g_{Pt}{}^{-1}$) starts close to that of 10Pt/CX, the studied catalyst with the higher *MA* value (47.3 A $g_{Pt}{}^{-1}$), but it decreases by 60% after 20,000 AST cycles, getting closer to the *MA* value of PtCo/CX (18.3 *vs.* 15.3 A $g_{Pt}{}^{-1}$, respectively).

With these results, one can conclude that both hollow particles catalysts behave the same way while undergoing the accelerated stress tests. Indeed, the electroactive specific area remains almost constant during the ASTs, proving that the hollow particle morphology is stable. However, the ORR specific activity of both hollow particles catalysts decreases by 50-60%. Despite that drop, the ORR specific activity of both hollow nanoparticles catalysts remains higher than those of the Pt catalysts studied in thie present chapter. The decrease in ORR specific activity leads to a similar ORR mass activity drop as the eletroactive specific area remains constant. As no morphological changes occur, these decreases may be due to Co depletion, Pt lattice relaxation, and decrease in the density of structural defects.

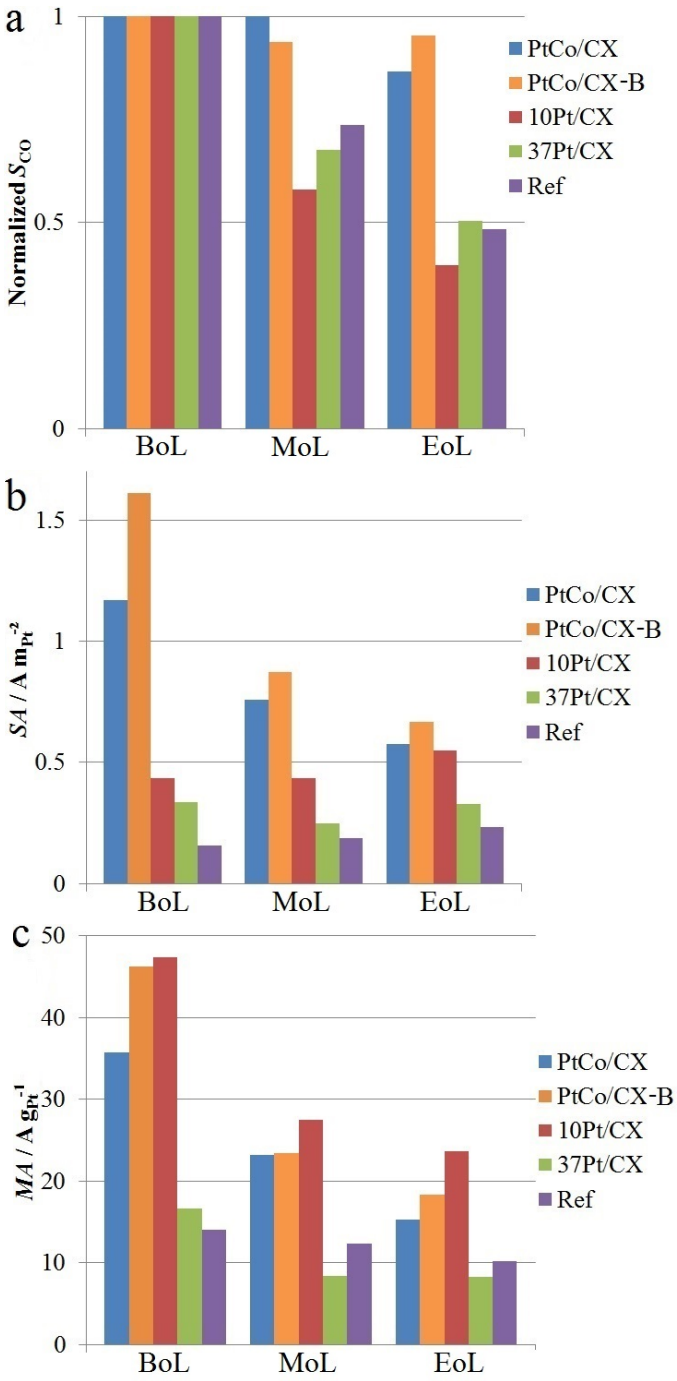

Figure 5.A2.1: Evolution of the normalized electroactive specific area measured by CO stripping analysis, S_{CO} (a), the ORR specific activity measured at 0.9 V *vs.* RHE, *SA* (b), and the ORR mass activity measured at 0.9 V *vs.* RHE, *MA* (c) during the accelerated stress tests consisting of potential cycles between 0.6 and 1.0 V *vs.* RHE at 353 K. The values of S_{CO}, *SA*, and *MA* were measured at beginning of life (BoL), after 5,000 cycles (middle of life, MoL), and after 20,000 cycles (end of life, EoL), at 298 K. The electroactive specific areas are normalized by the initial values.

Chapter 6

Durability of Pt and hollow PtCo nanoparticles supported on carbon xerogel during accelerated stress tests performed in proton exchange membrane fuel cell (PEMFC)

The final chapter of this thesis consists in a first insight into the performance and the durability of the best catalysts synthesized and characterized in Chapters 2 and 4, in proton exchange membrane fuel cell (PEMFC). Fuel cell membrane electrode assemblies were prepared from (i) a Pt/carbon xerogel catalyst prepared *via* the formic acid reduction of a Pt precursor and (ii) a hollow PtCo/carbon xerogel catalyst. They were characterized at the cathode side of a membrane electrode assembly in monocell configuration. Their performance and durability were compared to those of membrane electrode assemblies prepared from a commercial Pt/HSAC catalyst with a high Pt loading and from a commercial active carbon-supported Pt catalyst with a low Pt loading.

6.1 Introduction

During the last decades, many studies about proton exchange membrane fuel cells (PEMFCs) were conducted in order to improve their properties towards their large-scale commercialization. Nowadays, after huge developments, some drawbacks still remain. One of the most important drawbacks is the stability and durability of the PEMFC components. Among these PEMFC components, the cathode electrocatalyst suffers from aging, which induces significant performance losses with time.

Commonly used cathode catalysts are Pt nanoparticles deposited on high surface area carbon (Pt/HSAC catalysts). However, these catalysts are not stable enough under PEMFC-operating conditions. Indeed, the Pt nanoparticles of the catalysts can undergo four degradation phenomena during PEMFC operations [1–3]: (i) Pt nanoparticles can detach from the carbon support when the latter deteriorates (as carbon is oxidized into CO_2); (ii) Pt particles can suffer from electrochemical Ostwald ripening, *i.e.* Pt atoms can dissolve, especially those from the less stable small particles, and be redeposited on larger particles; (iii) dissolved Pt atoms can also be redeposited elsewhere, *e.g.* inside the PEMFC polymer membrane, resulting in inactive Pt nanoparticle isolated from the conductive carbon support; and (iv) Pt crystallites can migrate on the carbon support towards other Pt crystallites and coalesce. These phenomena lead to the decrease in performance of Pt/HSAC catalysts, lowering the amount of produced current.

The next generation of cathode catalysts is constituted of Pt nanoparticles alloyed with transition metals (PtM) such as Ni, Cu, Co, *etc.* Alloying serves several purposes: (i) the presence of the transition metal leads to the contraction of the Pt lattice, increasing the catalytic activity for the oxygen reduction reaction by decreasing the binding energy of the reaction intermediates [4–11]; (ii) the alloying of Pt to transition metal allows to lower the amount of dissolved Pt atoms, leading to the mitigation of the Pt particle growth and migration [2]. However, PtM catalysts may suffer from different stability issues, such as the transition metal dissolution, which can lead to new kind of particle morphology or structure [7–18]. Among these, one structure raises interest: hollow nanoparticles [16–18]. Indeed, hollow structures can be obtained after aging of Co@Pt core@shell nanoparticles, *i.e.* a Co core surrounded by a Pt shell, in PEMFC-operating conditions [19,20]. These works pointed out that the hollow structures are formed after thousands of hour of operation, indicating that the hollow structures must be stable under PEMFC-operating conditions [21–23]. This is why several synthesis methods were developed in order to form directly hollow nanoparticles [16–18,24,25]. Hollow particles formation usually proceeds *via* the following steps: (i) the reduction of a transition metal salt in aqueous solution, usually with sodium borohydride ($NaBH_4$), in order to form metal nanoparticles; (ii) the reduction of Pt ions (added during this step or in solution since the beginning) using the electrons provided by the transition metal oxidation, *i.e.* galvanic replacement of transition metal atoms by Pt, resulting in a Pt shell

formation around the transition metal core; (iii) the transition metal atoms diffusion from the core towards the Pt shell *via* the nanoscale Kirkendall effect, forming the hollow core; and (iv) the oxidation of the transition metal atoms at the surface by acid leaching.

A synthesis method to obtain hollow PtCo nanoparticles supported on carbon xerogel was developed in Chapter 4. It consists in using tri-sodium citrate as a chelating agent for the Co ions in order to control the reduction by $NaBH_4$ and then, better control the size and morphology of the nanoparticles. Afterwards, Pt salts can be added to the Co colloid. In that way, the formation of hollow PtCo nanoparticles occurs (galvanic replacement of Co by Pt, diffusion of Co atoms from the core through the Pt shell, and nanoscale Kirkendall effect). Several hollow PtCo nanoparticles catalysts synthesized *via* this method were characterized in a three-electrodes cell. In $HClO_4$ electrolyte, they display far better activity than pure Pt catalysts, including commercial ones: the specific activity (*i.e.* per electroactive Pt surface) of hollow PtCo nanoparticles catalysts was 14 to 20 times higher than that of the commercial reference while their mass activity (*i.e.* expressed by mass unit of Pt) was *ca.* 7 times higher than that of the commercial reference. A first glimpse of the good durability of hollow nanoparticles was observed during accelerated stress tests (ASTs) performed in three-electrode cell (Chapter 5). Indeed, the hollow structure remains after 20,000 cycles between 0.6 and 1.0 V *vs.* RHE at 0.05 V s^{-1}.

The next step is the study of the durability of hollow PtCo nanoparticles *in situ*, *i.e.* in PEMFC. This is the purpose of the present chapter. The evolution in performance and structure of hollow PtCo nanoparticles supported on carbon xerogel (PtCo/CX catalyst) was compared to that of a carbon xerogel-supported Pt catalyst made of metal nanoparticles with diameter of *ca.* 3-4 nm (Pt/CX catalyst) and two commercial Pt catalysts: one supported on high surface area carbon (Pt/HSAC, Tanaka, 37 wt.%) and one supported on activated carbon (Pt/AC, Alfa Aesar, 10 wt.%).

The support used to synthesized the Pt and PtCo catalysts was a carbon xerogel (CX) because it exhibits properties suitable for a PEMFC catalyst support. Indeed, CXs are pure porous carbons with controllable and reproducible pore texture [26]. This particular property leads to highly porous catalytic layers with better performance in PEMFCs as it mitigates the mass-transport limitations [27]. Moreover, previous works [27–32] proved that these materials are excellent support to deposit metals with high dispersion. The stability of Pt and hollow PtCo nanoparticles are thus compared on the same CX support and with two commercial references using different supports (HSAC and AC).

In order to investigate the stability and durability of PEMFC components within a relatively short time, ASTs must be performed on membrane electrode assemblies [1]. Some organizations try to establish standard ASTs measurement procedures to enable comparisons between results obtained by various research groups. Two major organizations in the field of PEMFC, the US Department of Energy, DoE [33], and the Fuel cell Commercialization Conference of Japan, FCCJ [34, 35],

published similar ASTs measurement procedures. The procedure they defined for the durability of the catalyst metal nanoparticles was used in the present chapter.

6.2 Experimental

6.2.1 Syntheses

Carbon xerogel support Carbon xerogel (CX) used in this thesis was prepared by drying and pyrolysis of a resorcinol-formaldehyde gel [26]. This synthesis is described elsewhere [28]. Briefly, the gel was obtained by polycondensation of resorcinol with formaldehyde in water. The resorcinol/formaldehyde molar ratio, *R/F*, was set at 0.5, the resorcinol/sodium carbonate molar ratio, *R/C*, was chosen equal to 1,000 and the dilution ratio, *D*, *i.e.* the solvent/(resorcinol and formaldehyde) molar ratio, was fixed at 5.7. These variables were chosen in order to obtain a CX with a pore size distribution centered at 80 nm. After gelling and aging in an oven at 358 K, the obtained gel was dried under vacuum, then ground with a planetary mill (PULVERISETTE 6, classical line, Fritsch) at 400 rpm during 70 min in order to obtain particles with a diameter of a few micrometers [36]. After grinding, the gel was pyrolyzed at 1073 K under nitrogen flow. The resulting CX particles exhibit a mean size of 7 µm, as measured by laser diffraction with a Mastersizer 2000 (see Reference [36] for more details).

Hollow PtCo particles on carbon xerogel The synthesis of hollow PtCo particles supported on CX was developed in Chapter 4. Briefly, the catalyst was synthesized as follows: (i) 45.7 mg of cobalt chlorine hexahydrate ($CoCl_2 \cdot 6H_2O$) were dissolved in 160 mL of ultrapure water; (ii) to this, 40 mL of an aqueous solution of trisodium citrate dihydrate ($Na_3C_6H_5O_7 \cdot 2H_2O$, 2.6×10^{-2} mol/L) were added; (iii) the resulting solution was sonicated for 15 min, then (iv) poured in 360 mL of ultrapure water under stirring; (v) Ar was then bubbled during 30 min. The next steps were performed under Ar bubbling: (vi) 20 mL of an aqueous solution of sodium borohydride ($NaBH_4$, 9.6×10^{-2} mol/L, degassed by Ar bubbling during a few minutes) were added dropwise in 5 min; (vii) after 10 min, 20 mL of an aqueous solution of hexachloroplatinic acid hexahydrate (CPA, $H_2PtCl_6 \cdot 6H_2O$, 3.2×10^{-3} mol/L, degassed by Ar bubbling during a few minutes) were added dropwise in 5 min; (viii) 30 min after the addition of CPA, Ar bubbling was stopped; (ix) after 90 min under stirring, 136 µL of hydrochloric acid 37% (HCl) were added, then (x) 40 mL of ultrapure water containing 100 mg of CX powder were added; (xi) the suspension was left under stirring overnight and, then (xii) filtered, (xiii) thoroughly washed with ultrapure water, and (xiv) dried in an oven at 353 K during 40 min. The added amounts of Pt and Co correspond to a catalyst composition of 10 wt.% in each metal.

Pure Pt particles on carbon xerogel The previous hollow PtCo particles deposited on CX will be compared to a pure Pt/CX catalyst, synthesized by formic acid (FA, HCOOH) reduction, with a Pt loading of 37 wt.%. The synthesis procedure was as follows (see Chapter 2): (i) 0.3 g of CX were dispersed in 200 mL of 2 mol L^{-1} FA solution; (ii) the suspension was heated to 353 K in an oil bath; (iii) once the suspension reached 353 K, the volume of 4 mmol L^{-1} CPA solution needed to obtain the target Pt loading was added by 10 mL steps; (iv) after 1 h stirring, the suspension was filtered; (v) the catalyst was then washed 5 times with 125 mL of ultrapure water, and finally (vi) dried at 333 K under air overnight.

List of samples Hereafter, the catalyst constituted of hollow PtCo particles deposited on CX is labeled PtCo/CX. The pure Pt catalyst supported on CX is labeled Pt/CX. These home-made catalysts will be compared to two commercial ones, an active carbon-supported Pt catalyst (Pt/AC, Alfa Aesar, 10 wt.%) and a Pt catalyst supported on high surface area carbon (Pt/HSAC, Tanaka, 37 wt.%), labeled hereafter Ref10 and Ref37, respectively.

6.2.2 Physicochemical characterization

The metal weight percentages of the catalysts were measured by inductively coupled plasma-atomic emission spectrometry (ICP-AES) using an ICAP 6500 THERMO device. The solutions for the analyses were prepared as follows: an aliquot of the catalyst sample was weighed and digested by 10 mL of sulphuric acid (H_2SO_4) and 5 mL of HNO_3. This solution was heated at 573 K until clear. After the complete dissolution of the CX support and evaporation of the solution, 3 mL of HCl and 1 mL of HNO_3 were added. The obtained solution was heated a few minutes at 393 K and transfered into a 50 mL calibrated flask, which was finally filled by deionized water.

The nanoparticles were observed by scanning transmission electron microscopy (STEM) with a JEOL 2100F microscope operated at 200 kV. The atomic composition of the alloy particles was investigated during STEM measurements by energy dispersive X-ray spectroscopy (EDX). EDX elemental maps were acquired by the same microscope, equipped with a SDD Centurio retractable detector. The EDX line scans were recorded on individual nanoparticle by scanning the beam in a square region adjusted to the particle size. The quantitative analyses were performed on Pt M and Co K lines using the K-factor provided by the JEOL software.

The catalysts powders were analyzed by X-Ray diffraction (XRD) with a Bruker D8 ADVANCE (TWIN/TWIN) goniometer using the $Cu_{K\alpha}$ line (Ni filter).

6.2.3 Fuel cell characterization

Setup The membrane electrode assemblies (MEAs) were studied in individual fuel cells at 343 K with a Biologic HCP-803 potentiostat. The utilized gases were, at the anode, H_2 (Air Liquide, α1) or N_2 (Air Liquide, α1) and, at the cathode, air (Air Liquide, α1), O_2 (Air Liquide, α1), or N_2, depending on the measurement. Before entering the cell, the gases were preheated at 343 K and humidified with ultrapure water (18 MΩ cm) in controlled evaporator mixer (CEM) from Bronkhorst. The gases and water flows were controlled by mini CORI-FLOW (digital mass flow meter/controller) from Bronkhorst. A back pressure of 0.5 bar was applied during all the measurements. All the voltage values of this chapter are expressed *vs.* the anode potential, which is considered as the reference potential, owing to the low overvoltage induced by the anode.

Ink preparation The composition of the inks was: (i) a carbon support/Nafion® mass ratio of 1/1; (ii) an isopropanol/ultrapure water volume ratio of 1/1, and (iii) a carbon support concentration of 1.5 g_C L^{-1}. Once the right amount of catalyst, 15 wt.% Nafion® solution (LIQUION solution, LQ-1115, 1100 EW), ultrapure water, and isopropanol were mixed together, the ink was stirred 5 min with a magnetic stirrer, then put in an ultrasound bath for 15 min, and finally magnetically stirred overnight before spraying.

MEA preparation and fuel cell assembly The MEAs were prepared by spraying catalyst inks on membranes with a home-made robotic spray. The membranes were made of Nafion® N117 (175 µm thick) with an anode catalytic layer already sprayed on it (purchased from Paxitech, catalyst from Tanaka, 0.5 mg_{Pt} cm^{-2}, 25 cm^2). The MEA preparation procedure is as follows: (i) the anode catalytic layer and membrane assembly was deposited on a heated vacuum plate (363 K, anode side down) and covered by a mask with a 25 cm^2 square-shaped aperture; (ii) the ink was sprayed on a 49 cm^2 square-shaped surface centered on the 25 cm^2 hole at a flow rate of 0.714 mL min^{-1} until the cathode catalytic layer reached a thickness of *ca.* 8 µm (passing 60 times, covering each time 49 cm^2 in order to obtain a good homogeneity of the 25 cm^2 layer, *i.e.* to avoid edge effect, and for a total duration of 31 min); (iii) the obtained membrane, with the anode and cathode catalytic layers on each side, was then sandwiched between two gas diffusion layer (GDL), covered by a microporous layer on one side (Freudenberg H23C6), and two gaskets (Sil-Pad® 400) to ensure the gas impermeability of the fuel cell; (iv) the gaskets, GDLs, catalytic layers and membrane assembly was then pressed at 20,000 N for 3 min with a hydraulic press heated at 393 K; then, (v) the obtained MEA was placed between two bipolar plates in graphite on which zigzag gas channels were engraved in order to distribute the gases all over the catalytic layers; (vi) the overall assembly (MEA + bipolar plates) were maintained together by two flanges tightened up together with eight screws tightened at 8 Nm; finally, (vii) the fuel cell was connected to the gas tubes, the heating rods and the potentiostat.

With these ink composition and spraying procedure, the mass of deposited carbon was the same whatever the Pt loading of the catalysts and the obtained Pt cathode loadings were equal to 0.034 and 0.171 mg_{Pt} cm^{-2} for the catalysts with a low Pt loading (10 wt.%, PtCo/CX and Ref10) and for the catalysts with a high Pt loading (37 wt.%, Pt/CX and Ref37), respectively.

Fuel cell conditioning Prior to any measurements, the fuel cells were conditioned by stoichiometric functioning for 1 h at 0.6 V and 343 K (H_2 in the anode side, air in the cathode side). This working mode is based on the stoichiometric gas flows, *i.e.* the theoretical gas flows which should be sent inside the cell in order to produce the current actually produced by the cell (as measured by the potentiostat), considering the complete reaction of all the reactants (H_2 and O_2) injected inside the cell. So, the gas flows used during the stoichiometric functioning were these stoichiometric gas flows multiplied by a factor chosen to be equal to 1.2 or 2 for the anode or cathode side, respectively. In other words, the gas flows were 1.2 (or 2) times higher than the stoichiometric gas flows in the anode (or cathode) side. These factors were chosen in order to maintain a sufficient flow at the exhaust of the cell, *i.e.* a sufficient purge of water and gases. The value of the multiplying factor for the cathode gas is higher in order to improve the problematic O_2 diffusion inside the electrode. Moreover, minimum gas flows were used at the beginning of the conditioning to start the cell before it reaches the stoichiometric conditions. The minimum gas flows were equal to 100 mL min^{-1} for the anode and 200 mL min^{-1} for the cathode. The other variables were fixed: 65% inlet relative humidity in the anode; 85% inlet relative humidity in the cathode; a back pressure equal to 0.5 bar in both electrode.

Fuel cell stabilization This step consists in waiting for the stabilization of the measured current produced by the fuel cell working under fixed conditions. These conditions were: for the anode, H_2 flow equal to 420 mL min^{-1} with 65% inlet relative humidity; for the cathode, air flow equal to 1,000 mL min^{-1} with 85% inlet relative humidity and cell voltage fixed at 0.6 V; for both, the temperature and the back pressure were fixed at 343 K and 0.5 bar, respectively. The fuel cell stabilization was also performed when switching cathode gas from air to pure O_2. In this case, all the variables were set as previously, except the cathode gas flow which was fixed at 500 mL min^{-1}. Usually, the produced current was stable after *ca.* 30 min. However, in order to ensure the complete stabilization of the fuel cell, the stabilization step was performed for 1 h.

If needed, the following measurement techniques are explained with more details in the Appendix A2 at the end of this thesis.

Dynamic voltage-current (E-I) curve In order to measure and monitor the fuel cells performances, dynamic E-I curves were performed. They consists in measuring the current produced by the fuel cell while decreasing the cell voltage from the open circuit voltage (OCV) to 0.3 V and, then, increasing the cell voltage from 0.3 V to

the OCV, both at 0.05 V s^{-1}. Only the voltage-increasing part was studied as it is more stable and reproducible. The other variables were kept equal to those fixed during the fuel cell stabilization.

Potential electrochemical impedance spectroscopy - PEIS The fuel cell resistance was measured by potential electrochemical impedance spectroscopy (PEIS). This technique consists in applying several sinusoidal variations to the voltage, each with a different frequency, around a fixed voltage value and measuring the current response. For each frequency value, knowing the voltage and the current at any time, one can calculate the magnitude of the impedance, Z, by dividing the amplitude of the voltage sine wave by the amplitude of the current sine wave, and measure the phase difference ϕ between these two sine waves. The combination of Z and ϕ results in a complex number, the impedance $\mathbf{Z}$. As the impedance is composed of a real part, Z_{Re}, and an imaginary part, Z_{Im}, one can draw a Nyquist plot ($-Z_{\mathrm{Im}}$ as a function of Z_{Re}), where the intersection of the drawn curve and the abscissa axis at high frequencies gives the value of the fuel cell resistance [37]. The frequencies of the variations ranges from 10 Hz to 20 kHz. The voltage variations were performed around the stabilized voltage measured right before the beginning of the PEIS measurement (*e.g.* at 0.6 V, if the PEIS is performed during the fuel cell stabilization, or at OCV, if the PEIS is performed during the dynamic E-I curve measurement) with a sinus amplitude equal to 0.01 V. The temperature, pressure and gas flows were the same as during the fuel cell stabilization and the dynamic E-I measurement.

Cyclic voltammetry - CV Cyclic voltammetry (CV) was performed in order to measure the electrochemical surface area, *ECSA*, of the cathode, *i.e.* the actually active Pt surface in the MEAs. The variables concerning the gases were: for the anode, H_2 flow equal to 80 mL min^{-1} with 0% inlet relative humidity; for the cathode, N_2 flow equal to 200 mL min^{-1} with 100% inlet relative humidity; for both, the temperature and the back pressure were fixed at 343 K and 0.5 bar, respectively. Prior to the CV measurement, a N_2 purge was performed on the cathode side: the cell voltage was put at the OCV which was monitored until stabilization (usually, around 0.12 V). Once the cell voltage was stabilized, the CV measurement was started. It consists in measuring the cell current while sweeping the voltage between 0.05 and 1.2 V at 0.02 V s^{-1}. Four complete voltammetry cycles were recorded but only the last cycle was used for calculation. This calculation consists in measuring the area under the current peak produced by the proton desorption, *i.e.* between *ca.* 0.05 and 0.4 V, and calculating the *ECSA* assuming the desorption of a full monolayer of H_{ad} requires 210×10^{-6} C $cm_{Pt}{}^{-2}$ [38].

Crossover measurement This technique is used to measure the crossover current, *i.e.* the current loss due to H_2 molecules crossing from the anode, through the membrane, and towards the catalytic cathode layer where they react with O_2 molecules. It consists in measuring the current produced when increasing the volt-

age from the OCV to 0.6 V at 0.0005 V s^{-1}, when flowing H_2 at the anode and N_2 at the cathode. This results in a linear relationship between the voltage and the current. In the plot representing the evolution of current as a function of the cell voltage, the curve between 0.4 and 0.6 V is a straight line. The intersection between the extrapolation of this line and the current axis is the H_2 crossover current. All the other variables (gas flows, temperature, *etc.*) were the same as during the CV measurement.

Amperometry The cathode catalytic activity was measured by amperometry. This consists in measuring the current produced by the cell while fixing the cell voltage in a range where there are no diffusion limitations, *i.e.* at high voltage. This current measurement was repeated several times at different voltage values: from 0.93 to 0.84 V with 0.01 V step. The duration of the measurement was 1 min for the 0.93 and the 0.94 V steps and 2 min for the other voltage steps. For each voltage step, the current was averaged over the last 10 seconds and corrected by subtracting the crossover baseline. It was also divided by the geometric surface of the catalytic layer (25 cm^2) or by the mass of Pt in the catalytic layer in order to calculate the activity of the catalytic layer (in A $cm_{geo}{}^{-2}$) or the mass activity (in A $g_{Pt}{}^{-1}$), respectively. The voltage values were corrected from the resistance of the cell by adding the product of the averaged current and the cell resistance measured by PEIS. Finally, a plot of the corrected voltage as a function of the logarithm of the current can be drawn. The amperometry measurement was performed under air or under O_2. The other variables were fixed as during the fuel cell stabilization, the dynamic E-I measurement, and the PEIS measurement.

6.2.4 Measurement procedure and accelerated stress tests

The measurement procedure can be divided into four parts: (i) the fuel cell stabilization, (ii) the initial performance measurement (beginning of life, BoL), (iii) the performance measurement after 10,000 AST cycles (middle of life, MoL), and (iv) the performance measurement after 30,000 AST cycles (end of life, EoL). The fuel cell stabilization proceeds as follows: (i) fuel cell conditioning for 1 h (cathode under air); (ii) fuel cell stabilization for 5 h (cathode under air); (iii) PEIS; (iv) dynamic E-I curve (cathode under air); (v) CV; and (vi) crossover measurement. The initial performance (BoL) measurements proceeds as follows: (i) fuel cell conditioning for 1 h (cathode under air); (ii) fuel cell stabilization for 1 h (cathode under air); (iii) PEIS, (iv) dynamic E-I curve (cathode under air); (v) amperometry (cathode under air); (vi) fuel cell stabilization for 1 h (cathode under O_2); (vii) PEIS; (viii) dynamic E-I curve (cathode under O_2); (ix) amperometry (cathode under O_2); (x) fuel cell stabilization for 1 h (cathode under air); (xi) PEIS, (xii) dynamic E-I curve (cathode under air); (xiii) CV; and (xiv) crossover measurement. After the initial performance measurement, the anode and cathode relative humidity were both fixed at 100% (the other variables remained unchanged from the crossover measurement) for the ASTs.

The ASTs consist in fixing the cell voltage at 1.0 V for 3 s, then at 0.6 V for 3 s. These two voltage steps were repeated 10,000 times. After the 10,000 cycles, another performance measurement can be operated (MoL). The procedure was the same as the initial performance measurement (BoL), except that no conditioning step was carried out. After that second performance measurement, the anode and cathode relative humidity were both fixed again at 100% (the other variables still remained unchanged from the crossover measurement) for the ASTs. 20,000 more AST cycles were operated for a total of 30,000 AST cycles underwent by the cathode catalytic layer of the fuel cell. The procedure of the final performance (EoL) measurement was exactly the same that the procedure of the second performance (MoL) measurement. It must be noted that the measurements with air at the cathode were performed twice (before and after the measurements with O_2) in order to compare each other and check that the measurements under O_2 did not affect the cathode properties. As a reminder, all the measurements and the ASTs were performed at 343 K and with a back pressure equal to 0.5 bar.

6.3 Results

6.3.1 Physicochemical characterization

The catalysts were fully characterized in the previous chapters, except Ref10 which is used as a low Pt loading commercial reference (10 wt.%, for comparison with PtCo/CX). Table 6.1 summarizes the physicochemical properties of the four catalysts studied in this chapter. Briefly, PtCo/CX catalyst exhibits a Pt loading equal to 9.4 wt.% and a Co loading equal to 0.3 wt.%. For the pure Pt catalysts, the Pt loading is equal to 10.0 wt.% (Ref10) or 37.0 wt.% (Pt/CX and Ref37). Average crystallites sizes, d_{XRD}, were calculated by Scherrer's equation [39]:

$$d_{\mathrm{XRD}} = \frac{k\lambda}{\beta cos\theta} \tag{6.1}$$

where k is a dimensionless shape factor and equals 0.89 for spherical nanoparticles, λ is the X-ray wavelength ($Cu_{K\alpha}$: 1.5456 nm), β is the full width at half the maximum intensity (FWHM), and θ is the Bragg angle. The values of the average size of crystallites, d_{XRD}, are equal to 3.6, 20.2, 2.9, and 2.4 nm for PtCo/CX, Ref10, Pt/CX, and Ref37, respectively. The X-ray diffractograms of the four catalysts are shown in Figure 6.1, where they are shifted vertically for better legibility. Each Pt catalyst displays the two Pt diffraction peaks present in that range of angles (at 39.7° and 46.2°). The diffraction peaks of PtCo/CX catalyst are slightly shifted towards higher angle values because of the presence of Co atoms, which contracts the Pt lattice. It must be noted that, for Ref10, XRD also detects small Pt crystallites but the average size of small crystallites can not be calculated because the small crystallites broad peak is eclipsed by the high intensity of the large crystallites peak.

Table 6.1: Summary of the catalyst properties determined from physicochemical analyses.

Catalyst	ICP		TEM				XRD
	Pt_{ICP} wt.% ± 0.1	Co_{ICP} wt.% ± 0.1	d_{TEM} nm	σ nm	t_{TEM} nm	σ_{t} nm	d_{XRD} nm ± 0.5
PtCo/CX	9.4	0.3	33.0	5.8	4.3	0.9	3.6
Ref10	10.0	–[a]	2.5	1.2	–[a]	–[a]	20.2[b]
Pt/CX	37.0	–[a]	3.6	1.2	–[a]	–[a]	2.9
Ref37	37.0	–[a]	3.1	0.8	–[a]	–[a]	2.4

Pt_{ICP}: Pt weight percentage of the catalyst measured by ICP-AES; Co_{ICP}: Co weight percentage of the catalyst measured by ICP-AES; d_{TEM}: average diameter of particles estimated from TEM micrographs; σ: standard deviation associated with d_{TEM}; t_{TEM}: average shell thickness of particles estimated from TEM micrographs; σ_{t}: standard deviation associated with t_{TEM}; d_{XRD}: average size of crystallites calculated from X-ray diffraction peaks *via* Equation (6.1).
Notes: [a] Not pertinent (pure Pt catalysts made of solid nanoparticles); [b] Small crystallites peak eclipsed by large crystallites peak.

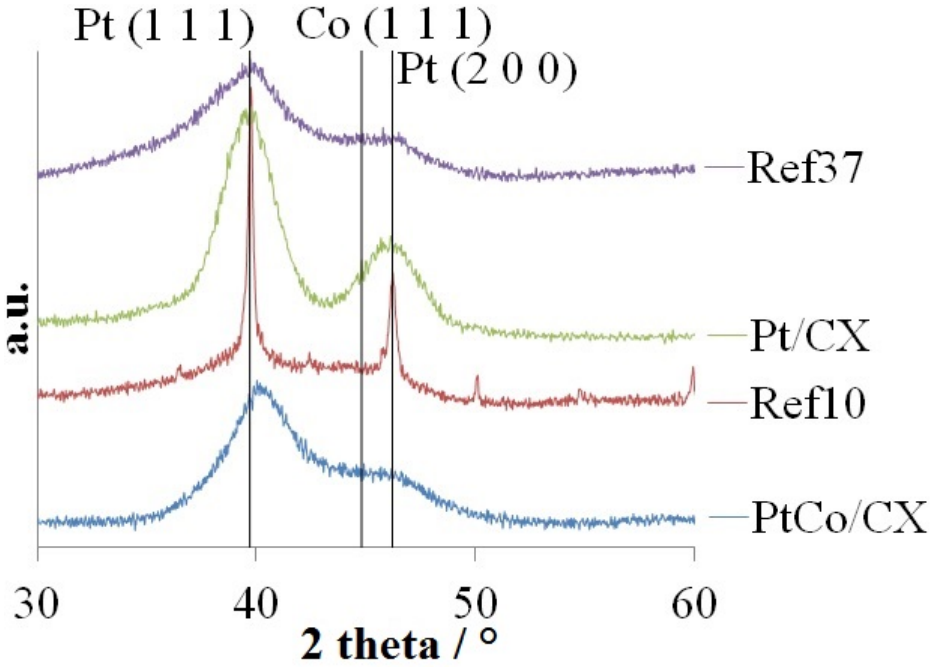

Figure 6.1: X-ray diffractograms of the four catalysts, vertically shifted for better legibility. The diffraction angles of Pt (1 1 1), Co (1 1 1), and Pt (2 0 0) are indicated respectively, from left to right, by the vertical lines.

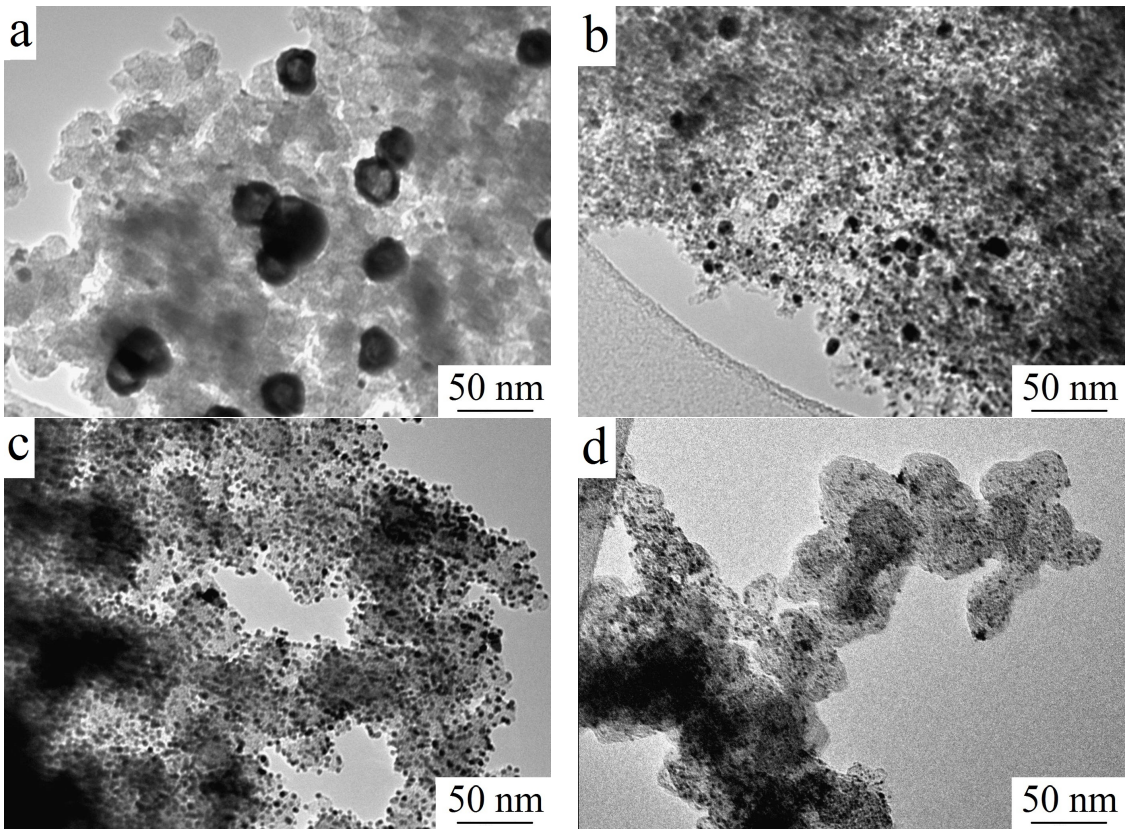

Figure 6.2: TEM micrographs of the four catalysts: PtCo/CX (a), Ref10 (b), Pt/CX (c), and Ref37 (d).

TEM micrographs of the four catalysts are shown in Figure 6.2. The nanoparticles of PtCo/CX catalyst are hollow as the particle cores are brighter than the shells, *i.e.* the particle cores are less dense than the shells. The pure Pt catalysts exhibit much smaller particles, the smaller particles are displayed by the two Ref catalysts (around 2-3 nm). The micrograph of Ref10 also exhibits large particles (around 20 nm). Image analysis was applied to these micrographs (on hundreds of nanoparticles) in order to calculate the average diameter of particles, d_{TEM}, and the standard deviation, σ. For PtCo/CX catalyst, other parameters were calculated: the average shell thickness of particles, t_{TEM}, and the standard deviation, σ_{t}. These results are shown in Table 6.1. The average particle diameters, d_{TEM}, are equal to 33.0, 2.5, 3.6, and 3.1 nm, with standard deviations equal to 5.8, 1.2, 1.2, and 0.8 nm, for PtCo/CX, Ref10, Pt/CX, and Ref37, respectively. The average shell thickness of PtCo/CX particles is equal to 4.3 nm, with a standard deviation of 0.9 nm.

STEM micrographs and elemental distributions of two particles of PtCo/CX catalyst are displayed in Figure 6.3. Elemental maps constitute a mapping of the Pt and Co repartition over STEM micrographs. They show that the particles are composed of Pt and Co. The average composition of particles (measured on *ca.* 50 particles) is 91.7 at.% of Pt and 8.3 at.% of Co.

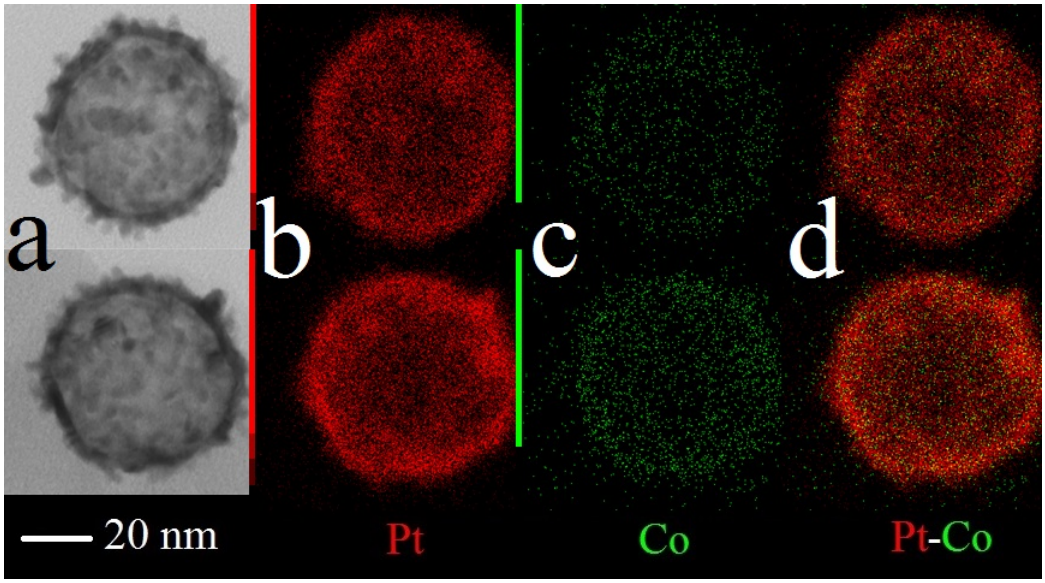

Figure 6.3: STEM micrographs and elemental distributions of two hollow nanoparticles of PtCo/CX. From left to right: STEM micrographs of particles (a), Pt elemental maps (b), Co elemental maps (c), and Pt-Co bi-elemental maps (d).

6.3.2 Fuel cell characterization

Figure 6.4 shows the dynamic E-I curves of the four catalytic layers under air flow (Figure 6.4a) or under O_2 flow (Figure 6.4b). Three regions can be delimited on these curves: (i) at high cell voltage values, the current is essentially limited by the low kinetics of the oxygen reduction reaction; (ii) at intermediate cell voltage values, where the curves are linear, the resistance of the cell starts impacting the current by Joule effect; and (iii) at low cell voltage values and under air, the current is essentially limited by the diffusion of O_2 molecules. On both graphs, one can see that the catalytic layers can be split into two groups: the MEAs with low Pt loading (PtCo/CX and Ref10, 0.034 mg_{Pt} cm^{-2}) and the MEAs with high Pt loading (Pt/CX and Ref37, 0.171 mg_{Pt} cm^{-2}). Indeed, low Pt loading means low active Pt surface, which results in high kinetic overvoltage. The catalytic layer with the higher performance is the one prepared from Ref37, closely followed by the one constituted of Pt/CX. The performance of the catalytic layer prepared from PtCo/CX is lower than the previous two and that of the catalytic layer constituted of Ref10 is the lowest.

The initial cyclic voltammograms of the four catalytic layers can be seen in Figure 6.5. The graph can be divided in four areas: (i) the low voltage and positive current area, where adsorbed hydrogen atoms (H_{ad}) desorb from the Pt surface, as they are oxidized into H^+; (ii) the high voltage and positive current area, where the Pt surface oxidizes; (iii) the high voltage and negative current area, where the oxidized Pt surface reduces; and (iv) the low voltage and negative current area, where protons adsorb on the Pt surface and reduce into H_2. The *ECSA* values,

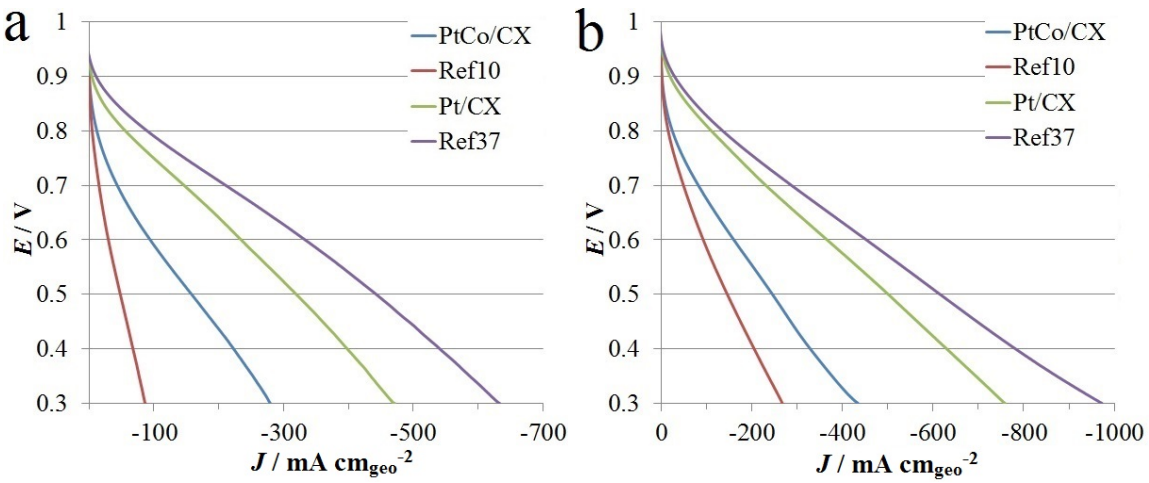

Figure 6.4: Initial dynamic E-I curves of the four catalytic layers under air (a) or under O_2 (b), recorded at 0.05 V s^{-1}. The measurement conditions were: for the anode, H_2 flow equal to 420 mL min^{-1} with 65% inlet relative humidity; for the cathode, air flow equal to 1,000 mL min^{-1} or O_2 flow equal to 500 mL min^{-1} with 85% inlet relative humidity; for both, the temperature and the back pressure were fixed at 343 K and 0.5 bar, respectively.

calculated from the proton desorption peak, are shown in Table 6.2 (values at BoL). They were equal to 21, 31, 42, and 79 m^2 $g_{Pt}{}^{-1}$ for PtCo/CX, Ref10, Pt/CX, and Ref37, respectively. Note however that the signal corresponding to H_{ad} oxidation is very low for Ref10 and PtCo/CX. The values obtained for these two catalysts must be taken with much caution.

Figure 6.6 shows the results of the amperometry measurement. The voltage values were corrected by adding the drop due to the cell resistance (see Table 6.A1.1 in Appendix 6.A1 at the end of this chapter for resistance values). The current values (in A) were corrected by subtracting the crossover current (see Table 6.A1.1 in Appendix 6.A1 at the end of this chapter for crossover current values) and divided by the electrode surface area (25 cm^2). Whether it be under air (Figure 6.6a) or under O_2 (Figure 6.6b), the MEA constituted of Ref37 produces the highest current. It is closely followed by the one made of Pt/CX. The MEAs with low Pt loading, PtCo/CX and Ref10 MEAs, follow. The MEA constituted of Ref10 is the MEA with the lowest activity. One can see in Figure 6.6a (measurement under air) that, for high voltage values ($E \geq 0.87$ V), a large error measurement occurs for the MEAs with low Pt loading, *i.e.* the measured values are a little bit erratic and do not result in a straight line as it should be (Tafel plot). This is certainly due to the high kinetic overpotential of the MEAs with low Pt loading. This is why, for the next amperometry results, only those performed under O_2 will be shown and discussed.

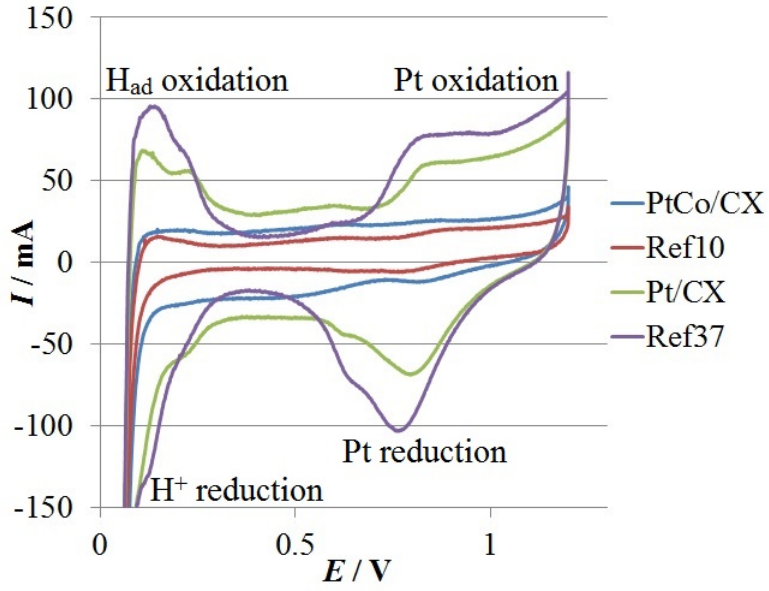

Figure 6.5: Initial cyclic voltammograms of the four catalytic layers recorded at 0.02 V s^{-1}. The measurement conditions were: for the anode, H_2 flow equal to 80 mL min^{-1} with 0% inlet relative humidity; for the cathode, N_2 flow equal to 200 mL min^{-1} with 100% inlet relative humidity; for both, the temperature and the back pressure were fixed at 343 K and 0.5 bar, respectively.

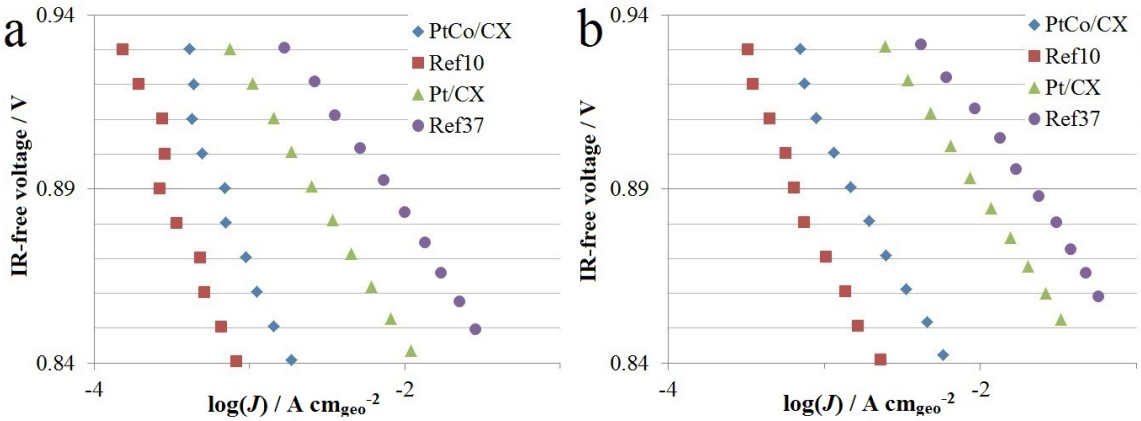

Figure 6.6: Initial amperometry results of the four catalytic layers under air (a) or under O_2 (b). The voltage values were corrected from the resistance measured by PEIS and the measured current values (in A) were divided by the electrode surface area (25 cm^2). The measurement conditions were: for the anode, H_2 flow equal to 420 mL min^{-1} with 65% inlet relative humidity; for the cathode, air flow equal to 1,000 mL min^{-1} or O_2 flow equal to 500 mL min^{-1} with 85% inlet relative humidity; for both, the temperature and the back pressure were fixed at 343 K and 0.5 bar, respectively.

Table 6.2: Evolution of the electrochemical surface area (*ECSA*) measured by integration of the proton desorption peak of the cyclic voltammograms for the four MEAs, at the beginning of life (BoL), after 10,000 AST cycles (middle of life, MoL), and after 30,000 AST cycles (end of life, EoL).

Catalyst		*ECSA* $m^2\ g_{Pt}{}^{-1}$ $\pm$ 10%
PtCo/CX	BoL	21[a]
	MoL	6[a]
	EoL	0.5[a]
Ref10	BoL	31[a]
	MoL	3[a]
	EoL	0.1[a]
Pt/CX	BoL	42
	MoL	17
	EoL	7
Ref37	BoL	79
	MoL	26
	EoL	15

Notes: [a] High error due to low peak intensity ($\leq$ 300 $cm_{Pt}{}^2$, corresponding to 35 $m^2\ g_{Pt}{}^{-1}$ in the case of the two MEAs with low Pt loading).

6.3.3 Accelerated stress tests

Figure 6.7 shows TEM micrographs of the four catalysts after the 30,000 AST cycles, *i.e.* at EoL. In Figure 6.7a, one can see that the hollow nanoparticles remain hollow after ASTs. Image analysis was performed on these micrographs and the results were compared to the values obtained before the ASTs. For the hollow particles of PtCo/CX, d_{TEM} is equal to 35.6 nm with σ equal to 7.2 nm (initially, d_{TEM} equals 33.0 $\pm$ 5.8 nm), t_{TEM} is equal to 5.4 nm with σ_t equal to 1.1 nm (initialy, t_{TEM} equals 4.3 $\pm$ 0.9 nm). The average size of the small particles of PtCo/CX is equal to 6.4 nm with a standard deviation equal to 1.8 nm (initially, 5.0 $\pm$ 1.5 nm). This shows that the hollow particles grew slightly and that the shell thickened. Concerning the Pt catalysts, the particles grew and aggregates were formed during ASTs (Figures 6.7b, c, and d). The average size of Ref10 increased from 2.5 $\pm$ 1.2 nm to 7.9 $\pm$ 3.0 nm; that of Pt/CX increased from 3.6 $\pm$ 1.2 nm to 6.3 $\pm$ 3.0 nm; and that of Ref37 increased from 3.1 $\pm$ 0.8 nm to 9.0 $\pm$ 5.5 nm.

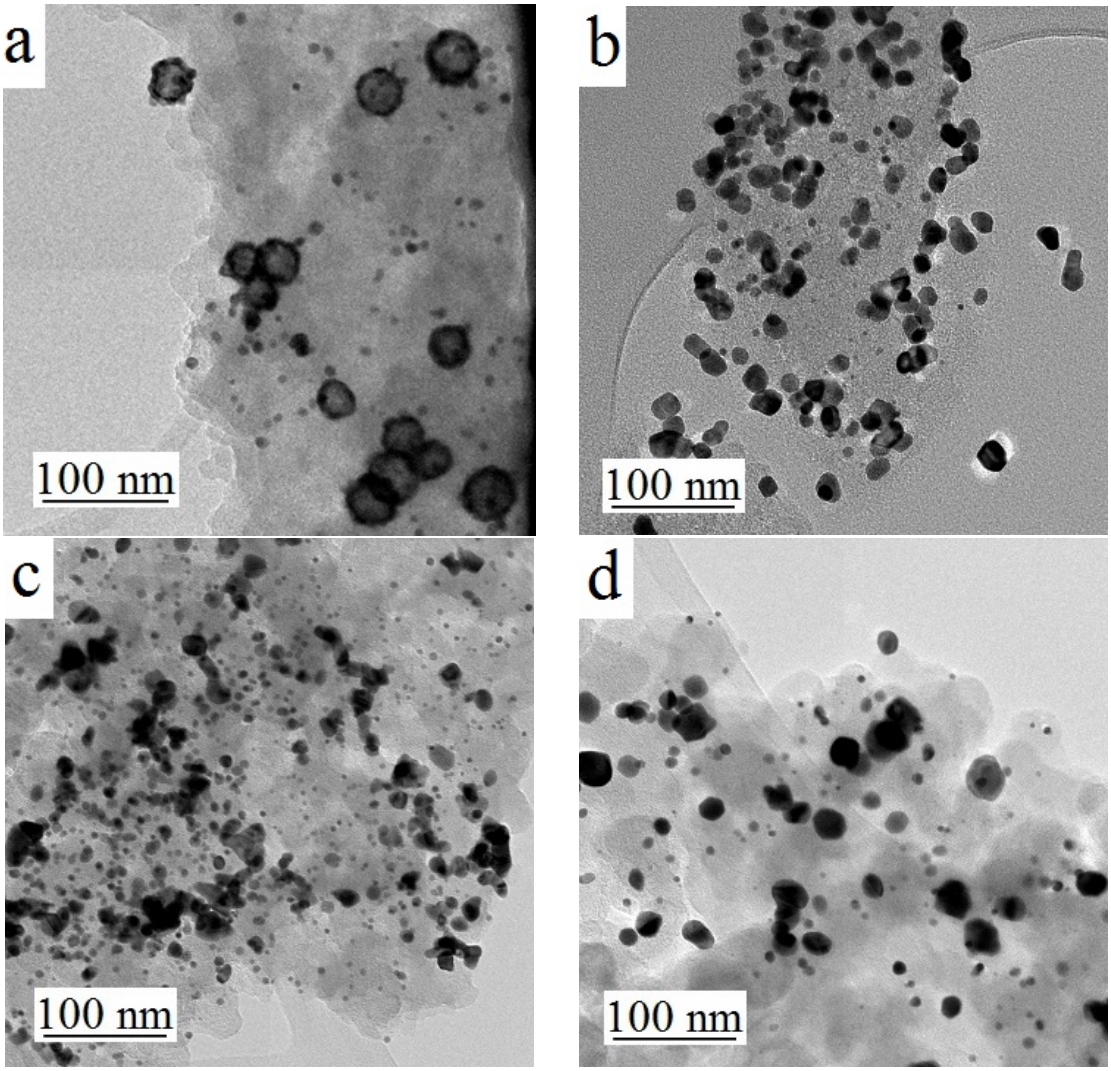

Figure 6.7: TEM micrographs of the four catalysts after ASTs: PtCo/CX (a), Ref10 (b), Pt/CX (c), and Ref37 (d).

STEM micrographs and elemental distributions of three PtCo/CX particles after 30,000 AST cycles (EoL) are displayed in Figure 6.8. STEM micrographs show that the particles remain hollow after the ASTs. Elemental maps show the Pt and Co repartition in the particles: in aged PtCo/CX catalyst, the particles are still constituted of Pt and Co, but their composition evolved towards a Co depletion. Indeed, the hollow particles composition after ASTs is between 96 and 99 at.% of Pt and between 1 and 4 at.% of Co (*vs.* 92 at.% of Pt and 8 at.% of Co at the BoL).

The evolution of the dynamic E-I curves during the ASTs (initial - BoL, after 10,000 AST cycles - MoL, and after 30,000 AST cycles - EoL) are shown in Figure 6.9. The catalytic layers were grouped with regard to the Pt loading: the MEAs with low Pt loading, PtCo/CX and Ref10 (0.034 mg_{Pt} $cm_{geo}{}^{-2}$, Figures 6.9a and b) and the MEAs with high loading, Pt/CX and Ref37 (0.171 mg_{Pt} $cm_{geo}{}^{-2}$, Figures 6.9c

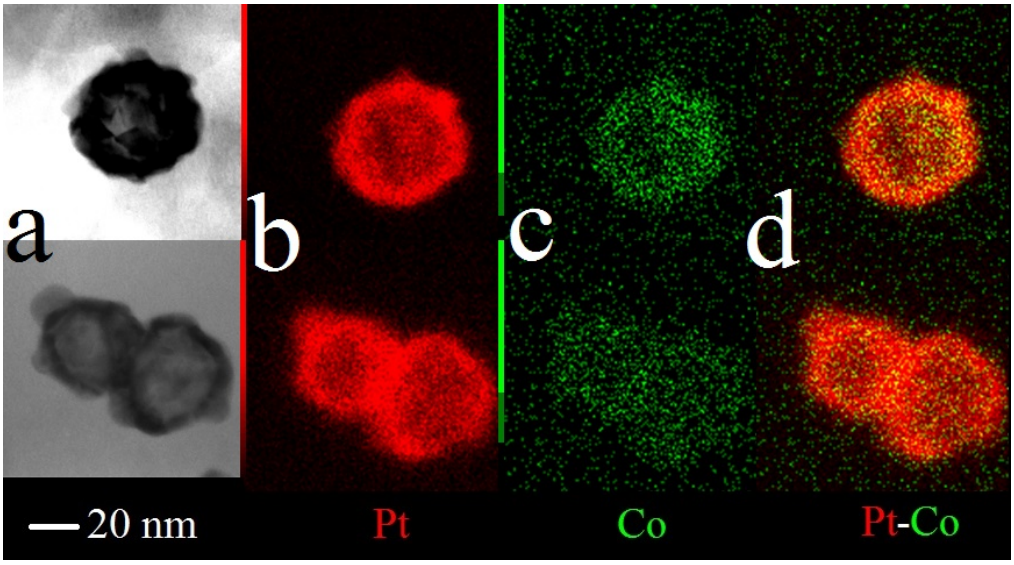

Figure 6.8: STEM micrographs and elemental distributions of hollow nanoparticles of PtCo/CX after 30,000 AST cycles. From left to right: STEM micrographs of particles (a), Pt elemental maps (b), Co elemental maps (c), and Pt-Co bi-elemental maps (d).

and d). All the dynamic E-I curves were performed either under air (Figures 6.9a and c) or under O_2 (Figures 6.9b and d). The current produced by all the MEAs decreases after 10,000 AST cycles and decreases further after 30,000 AST cycles, except for the catalytic layer constituted of PtCo/CX for which no drop is observed between 10,000 and 30,000 AST cycles.

Figure 6.10 displays the cyclic voltammograms recorded initially (BoL), after 10,000 AST cycles (MoL), and after 30,000 AST cycles (EoL), of the catalytic layers constituted of PtCo/CX (Figure 6.10a), of Ref10 (Figure 6.10b), of Pt/CX (Figure 6.10c), and of Ref37 (Figure 6.10d). For the MEAs with low Pt loading, PtCo/CX and Ref10 (Figure 6.10a and b), an enlargement of the proton desorption peak was added for better legibility. For the catalytic layers with high Pt loading, the area under the peaks decreases after 10,000 AST cycles and decreases further after 30,000 AST cycles. For PtCo/CX and Ref10, one notes that the signal corresponding to H_{ad} oxidation is very low at BoL and seems to decrease with cycling. It is however difficult to calculate *ECSA* values and confirm the drop, especially for PtCo/CX, since the H_{ad} oxidation peak is superimposed on the quinone/hydroquinone peak of the carbon support (peak starting around 0.2 V and up to *ca.* 0.75 V). The *ECSA* values, calculated from the proton desorption peak at BoL, at MoL, and at EoL, are shown in Table 6.2. The *ECSA* seems to decrease for all the catalytic layers and are equal to 21, 6, and 0.5 $m^2\ {g_{Pt}}^{-1}$ for PtCo/CX; to 31, 3, and 0.1 $m^2\ {g_{Pt}}^{-1}$ for Ref10; to 42, 17, and 7 $m^2\ {g_{Pt}}^{-1}$ for Pt/CX; and to 79, 26, and 15 $m^2\ {g_{Pt}}^{-1}$ for Ref37. It must be noted that the low *ECSA* values of MEAs with low Pt loading exhibit large imprecision due to the low peak intensity ($\leq$ 300 ${cm_{Pt}}^2$) and therefore these values should be treated cautiously.

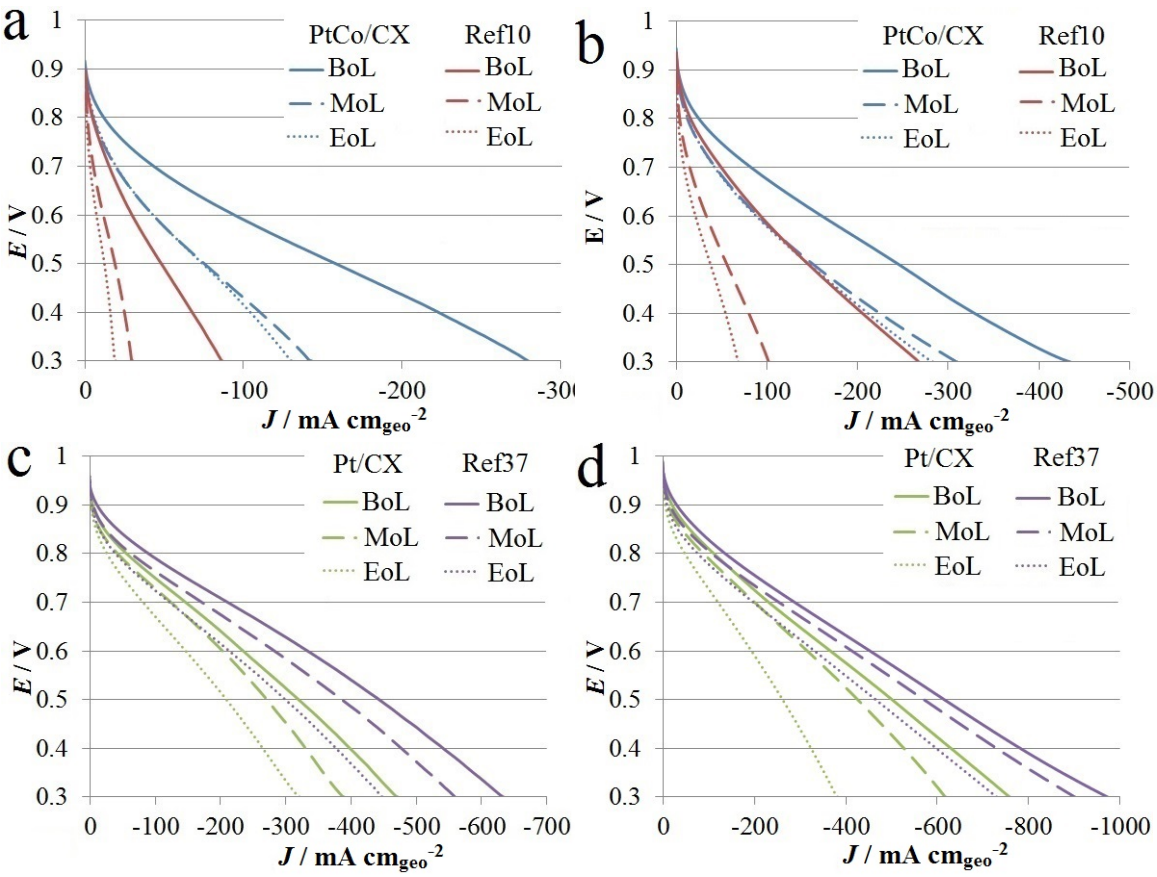

Figure 6.9: Dynamic E-I curves at beginning of life (BoL), at middle of life (MoL), and at end of life (EoL) of the four catalytic layers: the MEAs with low Pt loading, PtCo/CX and Ref10, under air (a) or under O_2 (b) and the MEAs with high Pt loading, Pt/CX and Ref37, under air (c) or under O_2 (d), recorded at 0.05 V s^{-1}. The measurement conditions were: for the anode, H_2 flow equal to 420 mL min^{-1} with 65% inlet relative humidity; for the cathode, air flow equal to 1,000 mL min^{-1} or O_2 flow equal to 500 mL min^{-1} with 85% inlet relative humidity; for both, the temperature and the back pressure were fixed at 343 K and 0.5 bar, respectively.

Figure 6.11 shows the evolution of the amperometry results measured under O_2 during the ASTs, initially (BoL), after 10,000 AST cycles (MoL), and after 30,000 AST cycles (EoL). The voltage values were corrected from the resistance measured by PEIS (see Table 6.A1.1 in Appendix 6.A1 at the end of this chapter for the resistance values) and the measured current values (in A) were divided by the mass of Pt in the cathode catalytic layer (j_{Pt}, in A g_{Pt}^{-1}). One can see that the current expressed per mass unit of Pt decreases after 10,000 AST cycles and decreases further after 30,000 AST cycles, except for the catalytic layer constituted of PtCo/CX for which they stabilized after 10,000 AST cycles, reaching the values of the MEAs with high Pt loading, Pt/CX and Ref37.

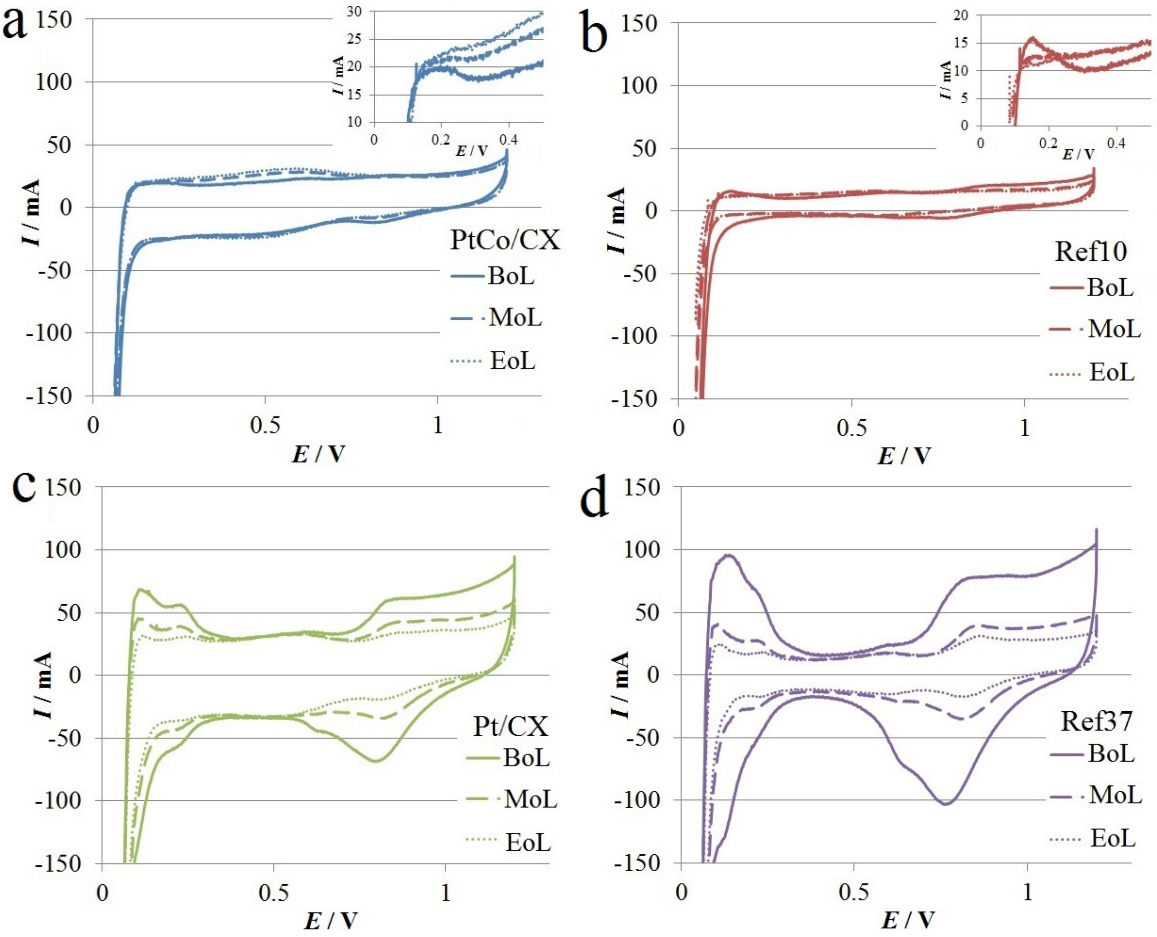

Figure 6.10: Cyclic voltammograms at beginning of life (BoL), at middle of life (MoL) and at end of life (EoL) of the four catalytic layers: PtCo/CX (a), Ref10 (b), Pt/CX (c), and Ref37 (d), recorded at 0.02 V s^{-1}. The measurement conditions were: for the anode, H_2 flow equal to 80 mL min^{-1} with 0% inlet relative humidity; for the cathode, N_2 flow equal to 200 mL min^{-1} with 100% inlet relative humidity; for both, the temperature and the back pressure were fixed at 343 K and 0.5 bar, respectively.

6.4 Discussion

The physicochemical analysis results show that PtCo/CX catalyst is composed of large, hollow PtCo nanoparticles (*ca.* 33 nm) and a few small PtCo nanoparticles with an average size around 5 nm (the small particles are visible in Figure 6.2a). Even if the *ECSA* detected at BoL is low, these small particles may contribute to a large part of it. The shell of the hollow particles is composed of PtCo crystallites with average size equal to 3.6 nm, as indicated by the XRD and TEM results. The pure Pt catalysts display much smaller particles (between 2 and 4 nm) as well as smaller average crystallite size (between 2 and 3 nm), except for Ref10 for which d_{XRD} is equal to 20.2 nm. However, the large average Pt crystallite size of Ref10 obtained

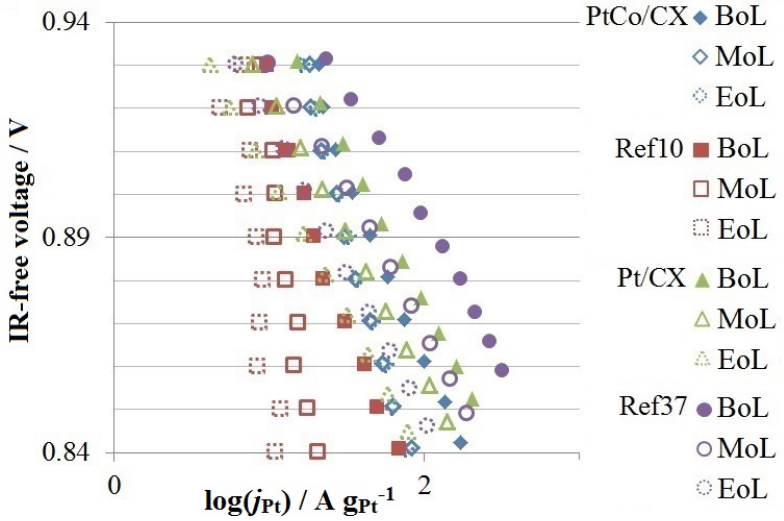

Figure 6.11: Amperometry results at beginning of life (BoL), at middle of life (MoL), and at end of life (EoL) of the four catalytic layers under O_2. The voltage values were corrected from the resistance measured by PEIS and the measured current values (in A) were divided by the mass of Pt in the cathode catalytic layer. The measurement conditions were: for the anode, H_2 flow equal to 420 mL min^{-1} with 65% inlet relative humidity; for the cathode, O_2 flow equal to 500 mL min^{-1} with 85% inlet relative humidity; for both, the temperature and the back pressure were fixed at 343 K and 0.5 bar, respectively.

by XRD can be caused by a few large crystallites. As XRD measurements are very sensitive to large crystallites, their presence masks the peak corresponding to small ones, which is also detected. The size of the small particles of pure Pt catalysts is close to the optimal particle size for the oxygen reduction reaction (3-4 nm) [40,41].

Concerning characterization in fuel cell, the catalytic layer prepared from Ref37 exhibits the highest produced current (dynamic E-I curve, Figure 6.4, and amperometry results, Figure 6.6) and the highest *ECSA* (79 m^2 $g_{Pt}{}^{-1}$). The second catalytic layer, the one prepared from Pt/CX, is very close to that constituted of Ref37, especially in the kinetics-limited part of the dynamic E-I curves measured under O_2 (Figure 6.4b, at high voltage), despite the twice lower *ECSA* (42 m^2 $g_{Pt}{}^{-1}$) for the same Pt loading. The third one, slightly lower than the first two, is that prepared from PtCo/CX, despite the Pt loading five times lower and the *ECSA* almost four times lower than Ref37 (21 m^2 $g_{Pt}{}^{-1}$). The catalytic layer with the lowest produced current, that prepared from Ref10, exhibits the same Pt loading than the catalytic layer constituted of PtCo/CX and an *ECSA* 2.5 times lower than the one constituted of Ref37 (31 m^2 $g_{Pt}{}^{-1}$). It must be reminded that the *ECSA* values of the catalytic layers with low Pt loading suffer from high imprecision because of the low peak intensity. All these results suggests that Ref37 and Pt/CX are catalysts with similar performance and that PtCo/CX displays higher performance than Ref10. However, it is difficult to compare the performance of the MEAs with high Pt loading, Ref37 and Pt/CX, with that of the MEAs with low Pt loading, PtCo/CX and

Ref10, because of the discrepancies between the metal loading and *ECSA*. Ideally, the Pt loading of the PtCo/CX catalyst should be increased to *ca.* 37 wt.% to be compared with Ref37. The difference between PtCo/CX and Ref10 is however striking and very encouraging. At this stage, it must also be noted that the values of the variables used to prepare the MEAs from CX-supported catalysts (carbon/Nafion® ratio, amount of carbon deposited on the membrane, *etc.*) may not be optimal. Indeed, these values were optimized in the case of commercial catalysts, which display properties different from CX-supported catalysts. This is why the performance of the MEAs prepared from CX-supported catalysts may not be the best performance they can achieve.

6.4.1 Accelerated stress tests

The TEM micrograph of PtCo/CX catalyst after ASTs shows that the hollow particles remain hollow all along the experiment. It also shows that the particles slightly grow and the shells slightly thicken during ASTs. This result proves that the hollow structure is stable under PEMFC-operating conditions and mitigates the Pt aging by partly preventing the Ostwald ripening, the Pt crystallites migration, and the Pt atoms dissolution. Concerning the Pt catalysts, TEM micrographs show that the Pt particles are not stable under PEMFC-operating conditions. Indeed, the average particle size of the three catalysts increases dramatically and aggregates of particles are formed during ASTs. The increase in particle size is due to the Ostwald ripening and the coalescence of Pt particles, while the formation of aggregates is due to the Pt crystallites migration.

EDX performed on the PtCo/CX catalyst shows that Co depletion occurs and that some Co atoms still remain within the particle shells. Therefore, one can consider the hollow structure stable under PEMFC operations even if the majority of the Co atoms were dissolved and oxidized (from 8.3 at.% of Co at BoL to between 1 and 4 at.% of Co at EoL).

The modifications in particles morphology lead to modifications of the CV peaks and the *ECSA* (Table 6.2 and Figure 6.10). Indeed, for the catalytic layers prepared from high Pt loading catalysts, the peaks intensity decreases, indicating a decrease in electroactive surface. The Pt oxides reduction peaks are shifted towards higher voltage value during the ASTs. This shift is due to the growth of the Pt particles. Indeed, during PEMFC operations, the Pt particles are submitted to Ostwald ripening [1–3] (dissolution of the small Pt particles followed by the redeposition of these Pt atoms on larger particles). For the MEAs with low Pt loading, the peaks intensity is too low to be analyzed easily. However, one can see that the peaks of the catalytic layer constituted of Ref10 disappear almost completely after 10,000 AST cycles only, which is in agreement with the Pt particle growth observed in Figure 6.7b. The *ECSA* values of the MEA prepared from PtCo/CX are too low to obtain accurate measurements but the peak corresponding to H_{ad} oxidation seems to decrease too. The decrease in *ECSA* of PtCo/CX seems to be contradictory to

the structure stability of hollow nanoparticles. However, as the hollow particles are very large (*ca.* 33 nm), their contribution to the *ECSA* is limited. Therefore, the *ECSA* decrease could be due to the dissolution or growing of the small particles observed on Figure 6.2a [1–3]. Another possibility is the masking of the H_{ad} oxidation peak by the quinone/hydroquinone peak resulting from the carbon support oxidation. Since the H_{ad} oxidation peak is very low, it is difficult to conclude

Considering the dynamic E-I curves (Figure 6.9), one catalytic layer exhibits a remarkable behaviour. The catalytic layer constituted of PtCo/CX is the only one which displays a stabilization of the performance during the ASTs. Indeed, the PtCo/CX dynamic E-I curves at MoL and at EoL are superimposed. This result is another evidence of the good stability of hollow nanoparticles during PEMFC operations. The decrease before stabilization is explained by the Co depletion and the Pt lattice relaxation which happens during the first 10,000 AST cycles. The stabilization is due to the morphological stability of hollow nanoparticles.

When comparing the MEAs with low Pt loading with the MEAs with high Pt loading (Figures 6.9a and b with Figures 6.9c and d), one can notice that the O_2-diffusion-limited part of the dynamic E-I curves of the MEAs with low Pt loading starts at much lower produced current than in the case of MEAs with high Pt loading. This phenomenon seems to be caused by a huge O_2 local transfer resistance occurring in low Pt loading PEMFC [42]. On the contrary, the dynamic E-I curves of the MEAs with high Pt loading after 10,000 and 30,000 AST cycles are parallel to the initial curves. This means that the degradation mainly impacts the kinetics-limited part of the results, *i.e.* the performance decrease is mainly due to the Pt surface loss.

Concerning the amperometry results (expressed in A $g_{Pt}{}^{-1}$, Figure 6.11), the two catalytic layers with the highest mass activity are Ref37 and Pt/CX. Their activity decreases during the ASTs and get closer to each other, with Ref37 remaining the highest. This decrease in mass activity stems from two major phenomena: the Pt particle growth and the active Pt loss. The Pt particle growth decreases the performance by reducing the available active Pt surface (Ostwald ripening). The active Pt loss can be due to several phenomena: (i) some Pt particles can detach from the carbon support; (ii) some Pt particles can migrate until they leave the carbon support, *i.e.* they move inside membrane or ionomer; and (iii) some Pt particles can be dissolved and redeposited within the membrane or the ionomer, *i.e.* in some place where they are not in contact with the carbon support anymore [1–3].

The initial mass activity of PtCo/CX is slightly below the initial mass activity of Pt/CX (Figure 6.11. Here again, after the first 10,000 AST cycles, the mass activity of PtCo/CX stabilized and did not decrease during the last 20,000 AST cycles, contrary to the case of catalytic layers prepared from Pt catalysts. This results from the good stability of the hollow nanoparticles after Co depletion and Pt lattice relaxation which happened during the first AST cycles. Moreover, the mass activity of PtCo/CX after 30,000 AST cycles is equivalent to that of Pt/CX and Ref37 after the ASTs, even if their Pt loading are very different. The last catalytic

layer, Ref10, exhibits very poor mass activity which decreases during the ASTs for the same reason than the pure Pt catalysts.

6.5 Conclusion

The durability of catalysts constituted of Pt nanoparticles and hollow PtCo nanoparticles deposited on carbon xerogel, Pt/CX and PtCo/CX catalysts, was studied and compared to the durability of two commercial Pt catalysts with different Pt loadings, 10 wt.%. and 37 wt.%, deposited on activated carbon and high surface area carbon, respectively, and labeled Ref10 and Ref37, respectively.

After the 30,000 accelerated stress test (AST) cycles, the electrochemical surface area (*ECSA*) of the MEAs with high Pt loading, Ref37 and Pt/CX, decreases of *ca.* 80%. This *ECSA* decrease is due to the growing and detachment from the carbon support of the Pt particles. Concerning the MEAs with low Pt loading, PtCo/CX and Ref10, the measurements of the *ECSA* suffer from high imprecision because of the low intensity of the H_{ad} oxidation peak. However, the same *ECSA* decrease seems to hold true for Ref10. For the PtCo/CX sample, the decrease is supposed to be due to either the growing of the small nanoparticles, which are probably responsible of the major part of the initial *ECSA* of the catalytic layer constituted of PtCo/CX, or the masking of the H_{ad} oxidation peak by the quinone/hydroquinone peak resulting from the carbon support oxidation.

During the ASTs, the performance of all the catalysts decreased. For the Pt catalytic layers, the cause of that drop is essentially the *ECSA* fall. All along the degradation, the MEA prepared from Ref37 produced the highest amount of current, closely followed by that constituted of Pt/CX. The catalytic layer prepared from Ref10 produced the lower amount of current. However, PtCo/CX catalyst behave differently than the pure Pt catalysts. Indeed, although a significant drop is recorded after 10,000 cycles, no performance decrease is observed between 10,000 and 30,000 AST cycles. Moreover, PtCo/CX micrographs recorded after the ASTs showed that the hollow structure remained even after 30,000 AST cycles at 353 K. This structure stability is the cause of the observed performance stability. This result, combined with the EDX observations, suggests that the performance drop of the PtCo/CX catalytic layer is due to the Co depletion and the Pt lattice relaxation of the hollow particles.

Future works should take advantage of the high stability of the hollow PtCo nanoparticles. The major drawback to overcome is the low performance compared to the commercial catalyst with 37 wt.% of Pt. One solution could be to increase the metal loading of the PtCo MEA in order to get rid of the huge overpotentials and resistances which decrease the performance of the MEAs with low Pt loading. To do so, one can either increase the catalyst Pt loading and the catalytic layer thickness, which can be performed using CXs as supports without impacting too much the mass-transport properties of the cathode. Finally, the values of the variables used

for the preparation of the MEAs from CX-supported catalysts must be optimized in order to maximize the performance of MEAs prepared from CX-supported catalysts.

References

[1] X. Z. Yuan, H. Li, S. Zhang, J. Martin, and H. Wang, *Journal of Power Sources* **196**, 9107 (2011).

[2] S. Zhang, X. Z. Yuan, J. N. C. Hin, H. Wang, J. Wu, K. A. Friedrich, and M. Schulze, *Journal of Power Sources* **195**, 1142 (2010).

[3] L. Dubau, L. Castanheira, F. Maillard, M. Chatenet, O. Lottin, G. Maranzana, J. Dillet, A. Lamibrac, J. C. Perrin, E. Moukheiber, A. Elkaddouri, G. De Moor, C. Bas, L. Flandin, and N. Caqué, *Wiley Interdisciplinary Reviews: Energy and Environment* **3**, 540 (2014).

[4] H. A. Gasteiger, S. S. Kocha, B. Sompalli, and F. T. Wagner, *Applied Catalysis B: Environmental* **56**, 9 (2005).

[5] S. Koh, M. F. Toney, and P. Strasser, *Electrochimica Acta* **52**, 2765 (2007).

[6] V. R. Stamenkovic, B. Fowler, B. S. Mun, G. Wang, P. N. Ross, C. A. Lucas, and N. M. Markovic, *Science* **315**, 493 (2007).

[7] C. M. Pedersen, M. Escudero-Escribano, A. Velázquez-Palenzuela, L. H. Christensen, I. Chorkendorff, and I. E. L. Stephens, *Electrochimica Acta* **179**, 647 (2015).

[8] B. Han, C. E. Carlton, A. Kongkanand, R. S. Kukreja, B. R. Theobald, L. Gan, R. O'Malley, P. Strasser, F. T. Wagner, and Y. Shao-Horn, *Energy & Environmental Science* **8**, 258 (2015).

[9] S. Chen, W. Sheng, N. Yabuuchi, P. J. Ferreira, L. F. Allard, and Y. Shao-Horn, *Journal of Physical Chemistry C* **113**, 1109 (2009).

[10] M. Oezaslan and P. Strasser, *Journal of Power Sources* **196**, 5240 (2011).

[11] L. Gan, M. Heggen, R. O'Malley, B. Theobald, and P. Strasser, *Nano Letters* **13**, 1131 (2013).

[12] S. Chen, H. A. Gasteiger, K. Hayakawa, T. Tada, and Y. Shao-Horn, *Journal of the Electrochemical Society* **157**, A82 (2010).

[13] M. Oezaslan, M. Heggen, and P. Strasser, *Journal of the American Chemical Society* **134**, 514 (2012).

[14] Y. Yu, H. L. Xin, R. Hovden, D. Wang, E. D. Rus, J. A. Mundy, D. A. Muller, and H. D. Abruna, *Nano Letters* **12**, 4417 (2012).

[15] C. Chen, Y. Kang, Z. Huo, Z. Zhu, W. Huang, H. L. Xin, J. D. Snyder, D. Li, J. A. Herron, M. Mavrikakis, M. Chi, K. L. More, Y. Li, N. M. Markovic, G. A. Somorjai, P. Yang, and V. R. Stamenkovic, *Science* **343**, 1339 (2014).

[16] R. Chattot, T. Asset, P. Bordet, J. Drnec, L. Dubau, and F. Maillard, *ACS Catalysis* **7**, 398 (2017).

[17] L. Dubau, J. Nelayah, S. Moldovan, O. Ersen, P. Bordet, J. Drnec, T. Asset, R. Chattot, and F. Maillard, *ACS Catalysis* **6**, 4673 (2016).

[18] T. Asset, R. Chattot, J. Nelayah, N. Job, L. Dubau, and F. Maillard, *ChemElectroChem* **3**, 1591 (2016).

[19] L. Dubau, J. Durst, F. Maillard, L. Guétaz, M. Chatenet, J. André, and E. Rossinot, *Electrochimica Acta* **56**, 10658 (2011).

[20] L. Dubau, M. Lopez-Haro, L. Castanheira, J. Durst, M. Chatenet, P. Bayle-Guillemaud, L. Guétaz, N. Caqué, E. Rossinot, and F. Maillard, *Applied Catalysis B: Environmental* **142-143**, 801 (2013).

[21] L. Dubau, M. Lopez-Haro, J. Durst, L. Guetaz, P. Bayle-Guillemaud, M. Chatenet, and F. Maillard, *Journal of Materials Chemistry A* **2**, 18497 (2014).

[22] L. Dubau, M. Lopez-Haro, J. Durst, and F. Maillard, *Catalysis Today* **262**, 146 (2016).

[23] L. Dubau, J. Nelayah, T. Asset, R. Chattot, and F. Maillard, *ACS Catalysis* **7**, 3072 (2017).

[24] S. J. Bae, S. J. Yoo, Y. Lim, S. Kim, Y. Lim, J. Choi, K. S. Nahm, S. J. Hwang, T.-H. Lim, S.-K. Kim, and P. Kim, *Journal of Materials Chemistry* **22**, 8820 (2012).

[25] A. X. Shan, Z. C. Chen, B. Q. Li, C. P. Chen, and R. M. Wang, *Journal of Materials Chemistry A* **3**, 1031 (2015).

[26] N. Job, R. Pirard, J. Marien, and J.-P. Pirard, *Carbon* **42**, 619 (2004).

[27] N. Job, S. D. Lambert, M. Chatenet, C. J. Gommes, F. Maillard, S. Berthon-Fabry, J. R. Regalbuto, and J.-P. Pirard, *Catalysis Today* **150**, 119 (2010).

[28] A. Zubiaur, M. Chatenet, F. Maillard, S. D. Lambert, J.-P. Pirard, and N. Job, *Fuel Cells* **14**, 343 (2014).

[29] S. D. Lambert, N. Job, L. D'Souza, M. Pereira, R. Pirard, B. Heinrichs, J. Figueiredo, J.-P. Pirard, and J. Regalbuto, *Journal of Catalysis* **261**, 23 (2009).

[30] N. Job, M. F. R. Pereira, S. D. Lambert, A. Cabiac, G. Delahay, J.-F. Colomer, J. Marien, J. L. Figueiredo, and J.-P. Pirard, *Journal of Catalysis* **240**, 160 (2006).

[31] N. Job, F. Maillard, J. Marie, S. Berthon-Fabry, J. P. Pirard, and M. Chatenet, *Journal of Materials Science* **44**, 6591 (2009).

[32] N. Job, M. Chatenet, S. Berthon-Fabry, S. Hermans, and F. Maillard, *Journal of Power Sources* **240**, 294 (2013).

[33] The US Department of Energy, Multi-year research, development, and demonstration plan, Technical report, 2016.

[34] A. Iiyama, K. Shinohara, S. Iguchi, and A. Daimaru, Membrane and catalyst performance targets for automotive fuel cells, in *Handbook of Fuel Cells Fundamentals, Technology and Applications, vol. 6*, chapter 61, Wiley, New York, United States of America, 2009.

[35] A. Ohma, K. Shinohara, A. Iiyama, T. Yoshida, and A. Daimaru, *ECS Transactions* **41**, 775 (2011).

[36] M.-L. C. Piedboeuf, A. F. Léonard, K. Traina, and N. Job, *Colloids and Surfaces A: Physicochemical and Engineering Aspects* **471**, 124 (2015).

[37] A. J. Bard and L. R. Faulkner, *Electrochemical Methods: Fundamentals and applications*, John Wiley & Sons, Inc., Weinheim, Germany, 2nd edition, 2001.

[38] S. Trasatti and O. Petrii, *Journal of Electroanalytical Chemistry* **327**, 353 (1992).

[39] G. Bergeret and P. Gallezot, Particle size and dispersion measurement, in *Handbook of Heterogeneous Catalysis*, edited by G. Ertl, H. Knözinger, and J. Weitkamp, p. 439, Wiley-VCH, Weinheim, Germany, 1997.

[40] K. Kinoshita, *Journal of the Electrochemical Society* **137**, 845 (1990).

[41] O. Antoine, Y. Bultel, and R. Durand, *Journal of Electroanalytical Chemistry* **499**, 85 (2001).

[42] A. Kongkanand and M. F. Mathias, *Journal of Physical Chemistry Letters* **7**, 1127 (2016).

Appendix

6.A1 PEIS and crossover results

Table 6.A1.1 shows the evolution during ASTs of some properties of the four studied MEAs: the fuel cell resistance measured by PEIS under air or O_2, R_{air} and R_{O_2}, respectively, and the crossover current, i_{cross}. These parameters depend directly on the chosen Nafion® membrane (N117 electrolyte membrane, 175 µm thick). This thick membrane was chosen in order to prevent short circuits and H_2 crossover. Indeed, some previous results with carbon xerogel (CX) and thin membranes (NRE212 membrane, 50 µm thick, not shown) brought to light that the relatively large CX particles (mean size: 7 µm) could penetrate the membrane during hot pressing, provoking large short circuits and H_2 crossover. The low values of i_{cross} presented in this table show that thick membranes fulfill their role.

However, thick membranes have a significant drawback: their thickness induces high cell resistance (Table 6.A1.1). These high resistance values directly impact the fuel cell performance as they contribute to the performance decrease in the central and linear part of the dynamic E-I curves, *i.e.* where the cell resistance is not negligible anymore. In addition, these results highlight the problem of the performance dependence on the utilized materials which are not optimized for the different studied catalysts, as it was the case with the MEAs with low Pt loading of the present chapter.

Table 6.A1.1: Evolution of the MEA properties at beginning of life (BoL), at middle of life (MoL), and at end of life (EoL).

Catalyst		**PEIS**		**Crossover**
		R_{air}	R_{O_2}	i_{cross}
		Ω	Ω	mA
		$\pm$ 10%	$\pm$ 10%	$\pm$ 10%
PtCo/CX	BoL	0.0175	0.0159	-6.5[a]
	MoL	0.0160	0.0153	-3.4[a]
	EoL	0.0154	0.0131	-0.4[a]
Ref10	BoL	0.0155	0.0155	5.1
	MoL	0.0150	0.0153	7.0
	EoL	0.0141	0.0128	7.4
Pt/CX	BoL	0.0133	0.0153	0.6
	MoL	0.0150	0.0128	0.4
	EoL	0.0155	0.0162	-0.7[a]
Ref37	BoL	0.0135	0.0133	1.1
	MoL	0.0123	0.0109	0.4
	EoL	0.0132	0.0135	-0.1[a]

R_{air}: Fuel cell resistance measured by PEIS while flowing air in the cathode; R_{O_2}: Fuel cell resistance measured by PEIS while flowing O_2 in the cathode; i_{cross}: H_2 crossover current.
Notes: [a] Negative value due to the imprecision of the measurement and to the low crossover current.

Conclusion and outlook

Conclusion

The present thesis aimed at investigating possible solutions to overcome the limitations of catalysts currently used in cathodes of proton exchange membrane fuel cells (PEMFCs). As a reminder, these limitations are (i) the low catalytic activity for the oxygen reduction reaction (ORR); (ii) the low stability of the catalysts; and (iii) the not optimal architecture of the catalytic layer, leading to O_2 diffusion limitations. To do so, several methods for the synthesis of Pt and PtCo nanoparticles deposited on carbon xerogel (Pt/CX and PtCo/CX catalysts) were studied. The activity for the ORR of all the synthesized catalysts was measured in a three-electrode cell (liquid electrolyte) and compared to that of a commercial catalyst (Tanaka, 37 wt.% of Pt deposited on high surface area carbon, Pt/HSAC). The durability of the catalysts with the best performance was then examined and compared to that of the same commercial catalyst. This thesis swept from the synthesis of the catalysts (carbon support and metallic nanoparticles) to the operation in PEMFCs (activity and durability studies). The thesis was structured around three axes, each composed of two consecutive chapters: (i) the synthesis of Pt/CX catalysts for the ORR and its streamlining; (ii) the synthesis of (solid and hollow) PtCo/CX catalysts for the ORR; and (iii) the study of the durability of the best catalysts synthesized in the two previous parts.

Study and streamlining of the synthesis of Pt/CX catalysts

In the first chapter, the strong electrostatic adsorption (SEA) method, previously developed at the laboratory, was adapted in order to synthesize Pt/CX catalysts with various Pt loading (from 8 to 25 wt.%) and with as low Pt losses as possible. The obtained Pt/CX catalysts are all constituted of Pt particles with a narrow particle size distribution centered around 2-3 nm. They also exhibit the same specific and mass activities for the ORR, whatever the Pt loading. However, the synthesis process exhibits two major drawbacks: it needs (i) a huge quantity of Pt, which mainly remains in the impregnation solution, and so, can be considered as wasted, and (ii) a long time to reach high Pt loading, because of the multiple impregnation-drying-

reduction steps. This is why the second chapter focused on the streamlining of the synthesis process while struggling to maintain high electrochemical performance of the catalysts. The first improvement was to avoid completely the Pt losses. This can be achieved by using the charge enhanced dry impregnation (CEDI) technique, which is a combination of SEA and dry impregnation. The CEDI method yields good catalysts, similar to SEA-synthesized catalysts, when reduced at high temperature. However, the time needed to achieve high Pt loading is just as long as for the SEA method. A first attempt in order to speed up the synthesis process was to substitute the reduction under hydrogen with a reduction in liquid phase after each impregnation step, *e.g.* reduction with sodium borohydride, in order to avoid the intermediate drying steps.

Even if the last synthesis process was quicker, the catalysts obtained by Pt reduction using sodium borohydride display poor Pt dispersion, thus a low activity towards ORR. So, other synthesis methods where envisaged. In particular, techniques combining the two approaches, *i.e.* (i) avoid the Pt loss and (ii) speed up the synthesis (one-step methods) were developed. These one-step processes allow to synthesize Pt/CX catalysts with various Pt loading, without any Pt loss, and in a relatively short time. Three one-step methods were investigated in order to synthesize Pt/CX catalysts with a high Pt loading: (i) a method including a single reduction step using sodium borohydride as a reductant; (ii) a method including a single reduction step using formic acid as a reductant; and (iii) a method starting from a colloid of Pt nanoparticles. Among these three one-step syntheses, only the one based on the reduction with formic acid (FA) yields highly loaded Pt/CX catalysts (40 wt.%) with excellent dispersion and good performance for the ORR. Among all the above-mentioned catalysts, the ones which exhibit the best activities for the ORR were the SEA, the CEDI (both when reduced at high temperature to get rid of the Cl poisoning the Pt surface and coming from the Pt precursor), and the FA catalysts. They display better ORR activities than the commercial Pt/HSAC catalyst owing to their very homogeneous nanoparticle size.

Synthesis of PtCo/CX catalysts

The first bimetallic synthesis approach was based on the SEA method. It was attempted to deposit Pt and Co consecutively (Pt then Co or Co then Pt) or simultaneously. However, only the deposition of Pt followed by that of Co yields bimetallic catalysts. Indeed, the low pH needed for the impregnation of the CX support with Pt anions is sufficient to oxidize the already deposited Co and to prevent its (re)deposition. Nevertheless, even if the deposition of Pt followed by that of Co yields bimetallic catalysts, the activities for the ORR of such catalysts were relatively low. It was established that the low performance was due to the lack of interaction between the two metals, as the catalysts were constituted of Co oxide clusters deposited on the surface of Pt particles, *i.e.* the two metals were not alloyed. The second bimetallic synthesis method allows to synthesize hollow PtCo/CX catalysts *via* a water-based method in liquid phase, using tri-sodium citrate, at room

temperature. The hollow PtCo nanoparticles catalysts display the best activities for the ORR among all the studied catalysts. In particular, when compared to the activities of the commercial Pt/HSAC catalyst, hollow PtCo/CX catalysts exhibit a specific activity 14 to 20 times higher and a mass activity 7 times higher. When compared to Pt/CX catalysts, hollow PtCo/CX catalysts display a specific activity 5 to 10 times higher and a mass activity 3 times higher.

Durability study

The last two chapters focused on the durability of the best catalysts synthesized in the previous chapters (Pt/CX catalysts synthesized *via* formic acid reduction and hollow PtCo/CX catalysts), first in a three-electrode setup using liquid electrolyte and, finally, in operating PEMFCs. In both cases, the durability of the synthesized catalysts was compared to that of the commercial Pt/HSAC catalyst. In the three-electrode setup, after 20,000 cycles of accelerated stress tests (ASTs), the Pt nanoparticles size of the synthesized Pt/CX and commercial Pt/HSAC catalysts increases significantly and Pt particles aggregates appear. This increase in particle size, *i.e.* decrease in electroactive surface area, leads to a decrease in the mass activity of the Pt catalysts. On the contrary, the structure of the hollow PtCo nanoparticles remains nearly unchanged, *i.e.* the size of the particles slightly decreases, the thickness of the shells slightly increases, and the particles remain hollow. Despite the good structural stability of hollow nanoparticles, the activity for the ORR of hollow PtCo/CX catalysts decreases. The decrease is due to the depletion of the shell Co atoms, leading to the relaxation of the Pt lattice, and to the decrease of the density of structural defects, as the structural domains reorganized during operation. However, the hollow PtCo/CX catalysts still display a mass activity twice higher than the commercial Pt/HSAC after 20,000 AST cycles. Regarding the durability in operating PEMFCs, the particle size of the synthesized Pt/CX and commercial Pt/HSAC catalysts increases significantly during all the 30,000 AST cycles, leading to a huge and continuous decrease of performance. On the contrary, the hollow structure of the PtCo nanoparticles remains, like in the case of ASTs performed in liquid electrolyte. Moreover, after a decrease occurring in the first 10,000 AST cycles, the performance of the hollow PtCo/CX catalysts stabilizes and no performance decrease is observed during the last 20,000 AST cycles.

Outlook

As this thesis browses the whole life of ORR catalysts for PEMFCs, from the synthesis to the durability in PEMFC, it shows that there is still room for improvement in each link of the chain. However, these improvements must be performed while thinking of the overall process and the final application.

This thesis focused on two major properties of the electrocatalysts: the activity for the ORR and the durability. Concerning the activity, next works must be focused on simple syntheses of highly active bimetallic catalysts. In particular, the synthesis of hollow PtCo nanoparticles catalysts described in this thesis can be optimized. Indeed, several synthesis variables can be studied, such as the ratio between the reactants (Pt:Co:citrate:$NaBH_4$), the concentration of the reactants, the stirring speed, the atmosphere during the synthesis (oxidative, reductive, or inert), or the waiting time between the addition of reactants. This will lead to a better control of the hollow particles parameters, *e.g.* the particle size, the shell thickness, the composition, *etc.* and maybe to a streamlining of the synthesis process. Indeed, the streamlining of the synthesis process could be performed after identifying the mandatory steps and suppressing the low-impact ones. The activity for the ORR of these catalysts can then be compared in order to find the values of the variables yielding the catalyst with the best performance and stability. Another improvement is to increase the metal loading of the catalytic layers constituted of hollow PtCo/CX catalysts. Indeed, the low metal loading of these catalytic layers causes problems during the utilization in PEMFC, as shown in the last chapter of this thesis.

Concerning the durability, hollow particles synthesized in this thesis exhibit very interesting behaviour, especially during ASTs performed in PEMFC. This property needs to be thoroughly investigated. For instance, the potential impact of the hollow particles structure (size, shell thickness, composition, *etc.*) on the durability must be determined, as well as the potential impact of other parameters, such as the metal loading. In addition to the durability of the metal nanoparticles, the durability of the support also has to be investigated in order to obtain entirely durable catalysts. For example, the surface of carbon xerogel can be modified by chemical vapor deposition (CVD), which allows the coverage of the inner CX surface by a layer of graphitized carbon [1]. This graphitization can increase the durability of the support. Indeed, graphitized carbons exhibit better durability than amorphous carbons such as carbon xerogels [2]. So, the next objective will be to investigate the activity and durability of hollow PtCo nanoparticles deposited on a CVD-modified CX with at least 20 wt.% of Pt.

Other future works could concern the major interest of the CXs: the architecture of the catalytic layer. Indeed, the optimization of the texture of membrane electrode assemblies (MEAs) constituted of PtCo/CX was not performed yet. It could be interesting to study how the architecture of the catalytic layer impacts the performance and durability of catalysts composed of hollow PtCo nanoparticles. In this context, CVD-modified CXs could play another role. Indeed, the surface modi-

fication produced by CVD also leads to a texture modification. It decreases the CX microporosity by blocking the micropores [1], which could impact the formation of the Nafion® network within the CX particles. In addition, several variables used for the preparation of the MEAs can be optimized, *e.g.* the ink composition, the loading of catalyst on the electrode, the quantity of Nafion®, the manufacturing (such as the pressing conditions), *etc.*

In the end, the study methodology developed in this thesis can be adapted for any type of applications implying catalysts with high loading of (noble) metal.

References

[1] M.-L. Piedboeuf, *Xérogels de carbone comme matériaux modèles pour l'étude du comportement électrochimique en tant qu'anodes de batteries Li-ion*, PhD thesis, Université de Liège, 2016.

[2] L. Castanheira, *Corrosion of high surface area carbon supports used in proton-exchange membrane fuel cell electrodes*, PhD thesis, Université de Grenoble, 2014.

Appendix

A1 Introduction to electrochemical measurements in three-electrode cell [1]

Electrochemical measurements in three-electrode cell were performed in order to investigate and compare the electrochemical properties of catalysts. This allows obtaining a rapid, first insight into the electrochemical properties of the catalysts with no need to experiment each one in a complete PEMFC assembly. The particularity of this measurement is that, in principle, every catalytic particle is in contact with the liquid electrolyte. In other words, the liquid electrolyte penetrates the pores of the catalyst to contact every catalytic site present on the support, allowing the catalysts to be fully utilized, *i.e.* to exhibit a catalyst utilization ratio of 100%.

Figure A1.1 shows a picture and a scheme of a three electrode cell setup. The setup is constituted of a glass cell containing a liquid electrolyte, usually H_2SO_4 or $HClO_4$ aqueous solution, with an immersed gas inlet. The three electrodes are (i) a reference electrode (RE); (ii) a counter electrode (CE); and (iii) a working electrode (WE). The RE is an electrode with a fixed potential, which is the potential reference. During this thesis, two REs were used: (i) a homemade RE constituted of a Pt wire in contact with both a H_2 bubble and the electrolyte solution; and (ii) a commercial RE, which continuously flows a small quantity of H_2 through a Pt-Pd electrode, in contact with the electrolyte solution. Both REs exhibit the same fixed potential as they are based on the H^+/H_2 reaction:

$$2H^+ + 2e^- \rightleftharpoons H_2 \tag{A1.1}$$

which conventionally displays a standard potential of 0 V. The RE potential depends on the H^+ concentration of the electrolyte and is equal to 0 + 0.06*pH, *e.g.* if the H^+ concentration is equal to 1 M (pH = 0), the RE potential is equal to 0 V, the so-called normal hydrogen electrode (NHE), and if the H^+ concentration is equal to 0.1 M (pH = 1), the RE potential is equal to 0.06 V, the so-called reversible hydrogen electrode (RHE). The liquid electrolyte in contact with the RE is separated from the electrolyte solution in contact with the two others electrodes by a Luggin capillary in order to prevent the contamination of the RE. The tip of the Luggin capillary is as close as possible to the WE in order to measure the potential difference with the highest accuracy.

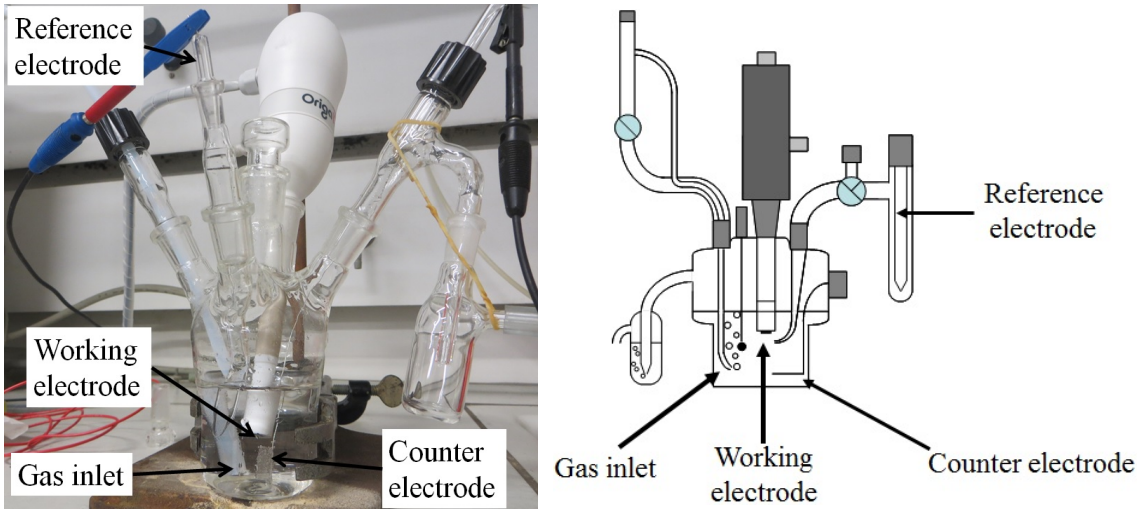

Figure A1.1: Picture and scheme of a three electrode setup.

The CE consists of a Pt gauze soldered to a Pt wire and immersed in the electrolyte solution. On the CE, half reactions, which are complementary to those happening on the WE, occur.

The WE is constituted of a layer of the analyzed catalyst deposited on a glassy carbon disk, which is connected to a rotating disk electrode (RDE). The catalytic layer is immersed in the electrolyte solution. The RDE allows the rotation of the glassy carbon disk, and so the catalytic layer, around an axis perpendicular to the planar surface of the disk and passing by the center of the disk. This rotation forces the convection of reactive species in the electrolyte solution, especially near the catalytic layer, where a stable, steady-state laminar flow is produced. This forced convection homogenized the diffusion of reactive species over all the catalytic layer. Through this homogeneity, the diffusion of the reactants towards the catalytic active sites is fully controlled by two variables: (i) the kinetics of the reaction and (ii) the rotating speed of the RDE. In other words, the reaction kinetics can be easily studied knowing the rotating speed of the electrode.

The other components of the three-electrode cell are the electrolyte, which enable the transfer of ions between the three electrodes, and a PTFE tube partially immersed in the electrolyte solution and connected to gas bottles in order to bubble these gases in the solution. In function of the chosen gas, this bubbling allows to deaerate the solution by bubbling inert gas, such as Ar, or to provide the reactive species, *e.g.* O_2 or CO molecules.

For the electrochemical measurements, the three electrodes are connected to a potentiostat which measures the current produced or consumed by the WE while fixing or sweeping its potential *vs.* the RE potential. The electrochemical measurements used in this thesis are (i) the cyclic voltammetry, (ii) the CO stripping voltammetry and (iii) the measurement of the activity for the ORR. The next paragraphs briefly explain these electrochemical measurements.

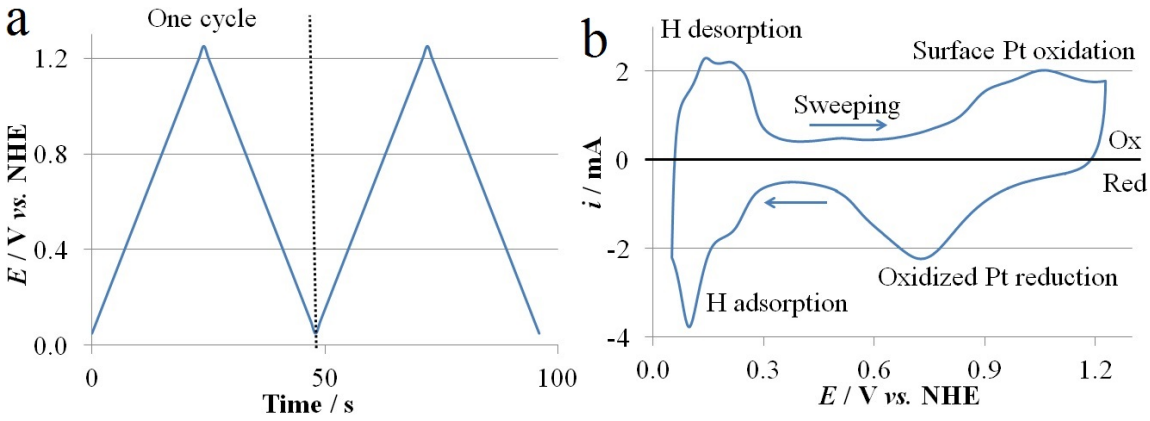

Figure A1.2: Cyclic potential sweep (a) and cyclic voltammogram of a commercial catalyst (b).

A1.1 Cyclic voltammetry

The cyclic voltammetry (CV) consists in recording the current while sweeping the potential of the WE linearly between two boundaries (Figure A1.2a). Increasing the WE potential allows the oxidation reactions to occur, while decreasing the WE potential permits the reduction reactions to happen. By convention, the current resulting from oxidation reactions is considered positive, while the current produces by reduction reactions is considered negative. The CV technique provides voltammograms (current in function of potential cycles, see Figure A1.2b) where reversible phenomena occurring on the WE are shown by the current peaks, *e.g* the reductive adsorption/oxidative desorption of hydrogen on the Pt nanoparticles occurring at low potential or the surface oxidation/reduction of the Pt nanoparticles occurring at high potential. Several results stem from cyclic voltammograms: (i) the Pt electroactive surface area by measuring the area under the proton desorption peak, knowing that the desorption of one monolayer of H_{ad} produces 210×10^{-2} C ${m_{Pt}}^{-2}$ [2]; and (ii) the potential at which the peaks occur provides information about the nature of the surface, the size of the particles, the type of active sites, *etc.* As cyclic voltammetry is a quick and easy measurement to perform, it can also be used for monitoring the catalytic layer between each electrochemical measurement.

A1.2 CO stripping voltammetry

The CO stripping voltammetry is based on the same principle than the cyclic voltammetry but with the addition of a non-reversible reaction: the CO electrooxidation. In a few words, carbon monoxide is bubbled in the electrolyte solution while fixing the potential of the WE. Under these conditions, CO molecules chemisorb on the Pt atoms. Once the Pt surface is fully covered by CO, Ar is bubbled in the solution in order to remove all the dissolved CO molecules which are not adsorbed on Pt atoms. After this step, the potential of the WE is linearly increased to electrooxidize the adsorbed carbon monoxide according to the following reaction:

$$CO + H_2O \longrightarrow CO_2 + 2H^+ + 2e^- \tag{A1.2}$$

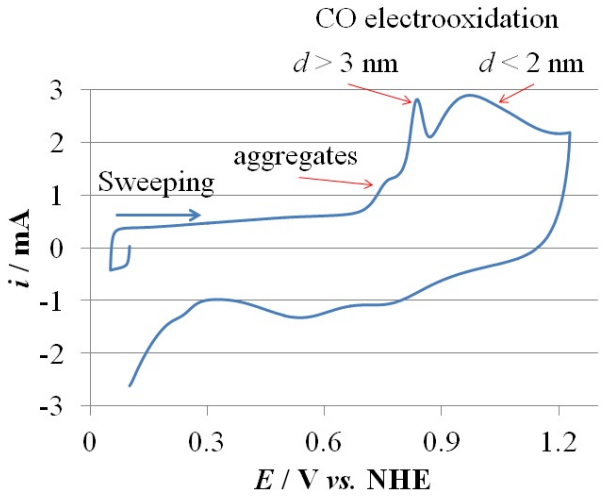

Figure A1.3: CO stripping voltammogram of a Pt/CX catalyst with a polydisperse Pt particle size distribution (SB/8 from Chapter 2).

which produces electrons, *i.e.* induces a current peak. The recording of the current in function of the potential yields a CO_{ad} stripping voltammogram (Figure A1.3). If the Pt nanoparticles are fully covered by CO molecules, no H oxidative desorption peak can occur at low potential (as in the part below 0.3 V *vs.* NHE of the CO stripping voltammogram of Figure A1.3). As the CO electrooxidation happens at the surface of the Pt particles, the area under the current peak of this oxidation is proportional to the electrochemically active surface area of the Pt nanoparticles, *i.e.* the oxidation of one monolayer of CO_{ad} produces 420×10^{-2} C $m_{Pt}{}^{-2}$. The measurement of the Pt electroactive surface area from CO stripping volatmmetry is more precise than that from cyclic voltammetry because (i) the produced current is twice as high as for cyclic voltammetry (420×10^{-2} instead of 210×10^{-2} C $m_{Pt}{}^{-2}$), *i.e.* the CO_{ad} oxidation produces twice as many electrons as the H_{ad} desorption; (ii) the oxidation of H_2, which can be produced at low potential, in parallel with the reductive adsorption of H^+, can interfere with the H oxidative desorption, leading to imprecision in the measurement; and (iii) a baseline can be subtracted from the CO stripping voltammogram in order to remove the impact of side reactions, such as the double layer capacitance or the surface Pt oxidation. In addition to the Pt electroactive specific area, the position and the width of the peak can inform about the structure of the catalytic particles (size, density of defects, *etc.*) or the poisoning of the particle surface by anions such as Cl^- [3–7]. For example, concerning the Pt particle size, Figure A1.3 exhibits three CO electrooxidation peaks: (i) a peak stemming from the electrooxidation of CO molecules chemisorbed on Pt particle aggregates at low potential (around 0.75 V *vs.* NHE); (ii) a peak caused by the electrooxidation of CO molecules chemisorbed on Pt particles with diameter larger than 3 nm (at *ca.* 0.85 V *vs.* NHE); and (iii) a peak due to the electrooxidation of CO molecules chemisorbed on Pt particles with diameter below 2 nm (around 1 V *vs.* NHE). It must be noted that the lower the potential of the peak, the higher the activity for the CO electrooxidation of corresponding catalytic sites.

A1.3 Measurement of the activity for the ORR

The activity for the ORR is measured in an O_2-saturated electrolyte solution, while rotating the WE. For this measurement, the potential of the WE is linearly decreased from the equilibrium potential (obtained from Nernst equation), where the O_2 molecules are not reduced, to lower potential, where O_2 molecules start reducing. In fact, the O_2 reduction is supposed to start at potential right below the equilibrium potential. However, because of the high activation energy of the oxygen reduction, a lower potential must be applied in order to overcome the energy barrier. This difference of potential needed for the oxygen reduction to start is called the kinetic overpotential. Once this overpotential has been overcome, the O_2 molecules can be reduced. When reducing further the potential, the oxygen reduction current increases until it reaches a plateau. This plateau is due to O_2 transport limitations. Indeed, at this potential, the O_2 consumption inside the catalytic layer is not compensated anymore by the O_2 transport through the diffusion film, the thickness of which is dependent of the rotating speed of the RDE. By performing the measurement of the reduction current at different rotation speed of the electrode, one can obtain several ORR voltammograms (one for each rotating speed) which are superimposed at high potential and form parallel plateaus at low potential (Figure A1.4a). In fact, the ORR voltammograms can be divided in three parts: (i) the part at high potential and low current, where the produced current is limited by the kinetics of the ORR; (ii) the part at low potential where the current reaches a plateau as it is limited by the mass transport of O_2 molecules, *i.e.* by the thickness of the diffusion film, which is dependent of the rotation speed of the RDE; and (iii) the intermediate part where the system is in transition between the kinetics-limited region and the diffusion-limited region. The catalytic activity for the ORR can be calculated in the kinetics-limited region after correction of the mass-transport limitations, while knowing the current value of the plateau, *i.e.* the limit current, using the Koutecky-Levich equation:

$$\frac{1}{i_{\mathrm{k}}} = \frac{1}{i} - \frac{1}{i_{\mathrm{l,c}}} \tag{A1.3}$$

where i_{k} is the kinetic current, *i.e.* the current without any mass transfer limitations, i is the experimental current, and $i_{\mathrm{l,c}}$ is the cathodic limit current, which depends on the rotation speed of the electrode. Once these mass-transport-corrected currents have been calculated, one can draw the so-called Tafel plot (Figure A1.4b), *i.e.* the potential as a function of the logarithm of the kinetic current. In the Tafel plot, the kinetics-limited region are represented by straight lines. These lines can be used to compare the ORR activity of several catalysts. Indeed, for a fixed potential, the best catalyst is the one which produces the higher current.

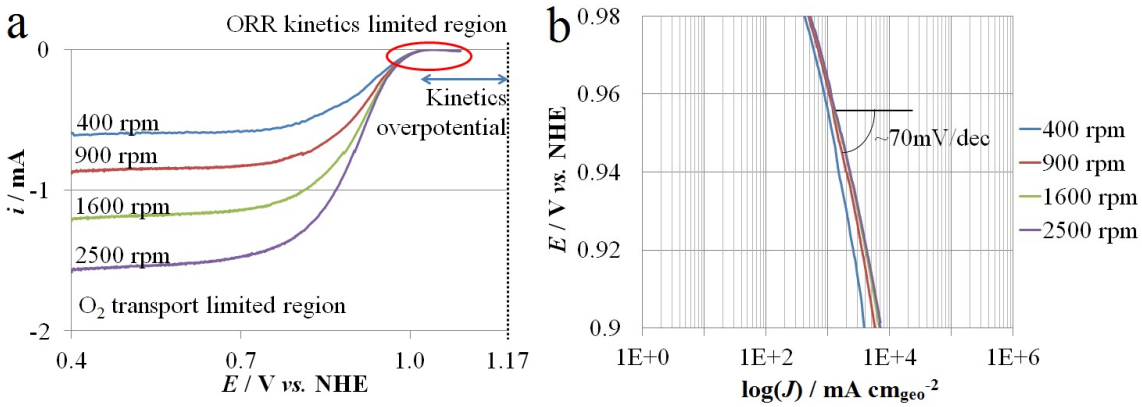

Figure A1.4: ORR voltammograms measured at various rotating speed of the electrode (a) and resulting Tafel plot (b) of a commercial catalyst.

A2 Introduction to electrochemical measurements in proton exchange membrane fuel cell

The measurements in three electrode cell described in the previous section can be considered as ideal measurements as the system is simplified compared to the PEMFC applications. This simplification impacts several measurement conditions, *e.g.* the electrolyte and the reference. The liquid electrolyte used in the three electrode setup allows (i) the electrical contact between the electrolyte and every catalytic particle present on the WE and (ii) the transport of the O_2 molecules to all the particles by diffusion through the liquid solution. As for the solid electrolyte used in PEMFCs, only a fraction of particles are effectively active as they have to be accessible by protons from the electrolyte and O_2 molecules from the gas flow (see the section 'Proton exchange membrane fuel cells' in the Introduction). For the measurement in PEMFCs, no classic reference electrode can be used. The potential reference is conventionally the potential of the anode, where the H_2 molecules are oxidized, because of the negligible overvoltage induced by the anode.

Despite all the differences, the principles of some measurement methods are the same in both setups. For example, cyclic voltammetry of MEAs is performed the same way and give information about the same properties as cyclic voltammetry in liquid electrolyte, but in real conditions, *i.e.* the Pt surface measured in PEMFC is the Pt surface which is really active, contrary to the Pt surface measured in liquid electrolyte for which every Pt particle is supposed to be active.

A2.1 Dynamic voltage-current (E-I) curve

The dynamic E-I curves are obtained by measuring the current produced when sweeping the cell voltage, while flowing H_2 in the anode and air or O_2 in the cathode. The obtained curve (Figure A2.1) is similar to the ORR voltammograms measured

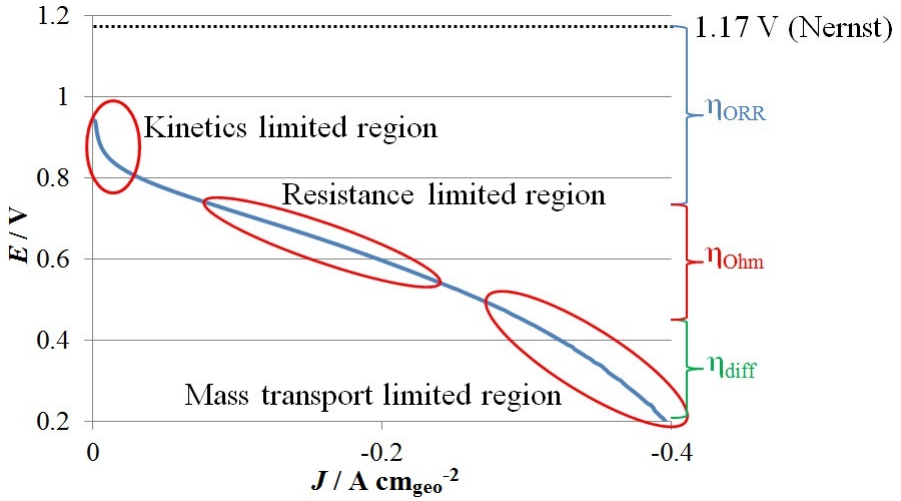

Figure A2.1: Voltage-current (E-I) curve of a commercial PEMFC measured under air.

in three electrode setup (Figure A1.4a). E-I curves can be divided into three regions (as already explained in the section 'Drawbacks of PEMFCs' in the Introduction and as shown by Figure 7 of the Introduction): (i) the kinetics-limited region, (ii) the region where the cell resistance is not negligible anymore, and (iii) the mass-transport-limited region. From E-I curves, one can draw several results, such as the kinetic overpotential (η_{ORR}), the cell resistance, the diffusion overpotential (η_{diff}), *etc.*

A2.2 Potential electrochemical impedance spectroscopy - PEIS

In this thesis, the potential electrochemical impedance spectroscopy (PEIS) measurement is used to measure the resistance of fuel cells. This measurement consists in measuring the current, while applying sinusoidal variations of the voltage around an operating point of a fuel cell. Each sinusoidal variation is performed with different frequencies. By comparing the voltage sinusoidal input with the current sinusoidal response for each frequency, one can calculate the magnitude of the impedance, Z, by dividing the amplitude of the voltage sine wave by the one of the current sine wave, and also measure the phase difference, ϕ, between the two sine waves. The combination of the magnitude of the impedance and the phase difference results in a complex number, the impedance **Z**:

$$\mathbf{Z} = Ze^{j\phi} = Z_{\mathrm{Re}} + jZ_{\mathrm{Im}} \tag{A2.1}$$

When plotting the opposite of the imaginary part of this complex number, $-Z_{\mathrm{Im}}$, as a function of its real part, Z_{Re} for each frequency, one can draw the Nyquist plot (Figure A2.2a). At high frequencies, it is assumed that the mass-transport limitations can be neglected. In these conditions, the equivalent circuit of the PEMFC system

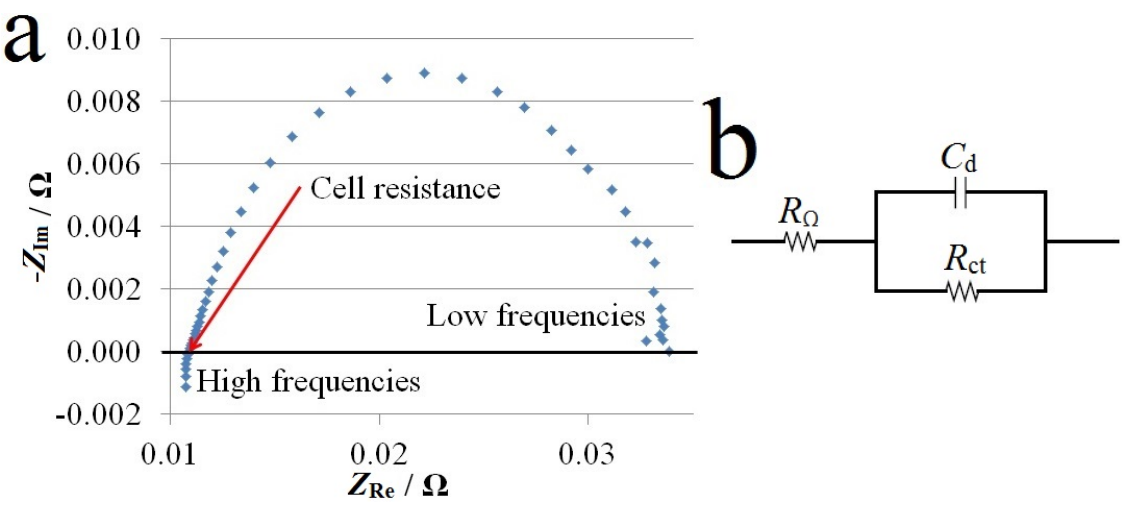

Figure A2.2: Nyquist plot of a commercial PEMFC (a) and equivalent circuit for a PEMFC system at high frequencies, *i.e.* considering no diffusion limitations (b, equivalent circuit adapted from Reference [1]).

can be simplified as shown in Figure A2.2b where R_Ω includes the electronic resistance, the contact resistance of the cell, and the resistance of the membrane (the last one being predominant), C_d is the double-layer capacitance of the carbon support, and R_ct is the charge-transfer resistance. At very high frequencies, the contribution of the capacitance, C_d, falls to zero. R_Ω is then the only resistance influencing the impedance. This is why the intersection of the Nyquist plot with the abscissa axis at high frequencies represents the resistance of the cell. Of course, information concerning other properties, such as the kinetic and mass-transport limitations, can also be withdrawn from the Nyquist plot. For example, at low frequencies, the phenomena dominating the impedance are the mass-transfer limitations. However, such investigations are not performed in this thesis.

A2.3 Crossover measurement

In PEMFCs, the polymer membrane must be as impermeable as possible in order to isolate H_2 from O_2. However, some H_2 molecules can cross through the membrane, *i.e.* from the anode to the cathode, and react with O_2 molecules, resulting in current loss, as the reaction occurs at the same electrode. This current loss, *i.e.* the crossover current, i_cross, can be measured while flowing H_2 at the anode and N_2 at the cathode. This measurement consists in determining the current produced when sweeping the voltage (usually between 0.1 and 0.6 V) at very slow scan speed (*ca.* 0.0005 V s^{-1}). This slow scan speed induces very low capacitive and peak current, *e.g.* very low hydrogen desorption current, as shown by Figure A2.3. Through the slow scan speed, the current of side reactions become negligible when compared to i_cross. In particular, the part of the resulting voltammogram recorded between 0.4 and 0.6 V becomes a straight line. The intersection between the extrapolation of this straight line and the ordinate axis, *i.e.* at 0 V, gives the value of i_cross.

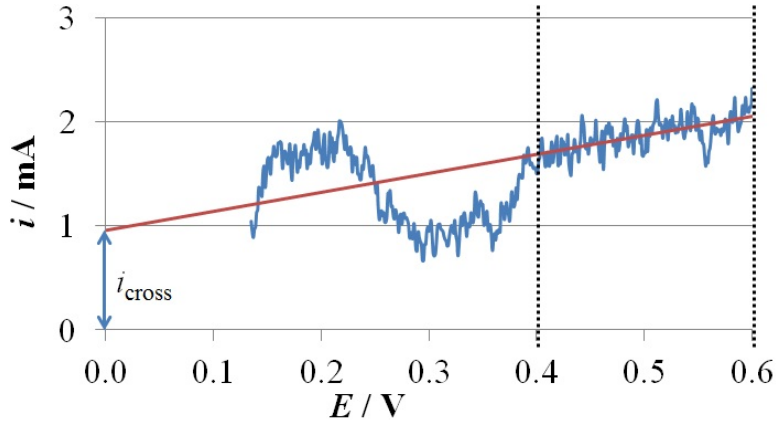

Figure A2.3: Crossover voltammogram of a commercial PEMFC.

A2.4 Amperometry

Amperometry is used to measure the cathode catalytic activity. As a consequence, amperometry is focused on the kinetics-limited region of the E-I curve. The measurement consists in a chronoamperometry measurement, *i.e.* in measuring the current for one or two minutes, while fixing the voltage. The chronoamperometry measurement is repeated at several voltage values comprised in the kinetics-limited region, *i.e.* where no diffusion limitations occur. This allows obtaining steady values of the current for each voltage, contrary to E-I curves, for which the voltage is swept. The resulting graph is shown in Figure A2.4a. For each voltage value, the corresponding current is measured at the end of the voltage step, *i.e.* the current is averaged over the last seconds of each measurement. The obtained E-I pairs can be plotted (voltage as a function of current, Figure A2.4b). This graph is similar to an enlargement on the kinetics-limited region of the E-I curve. Then, several corrections can be applied on these E-I pairs: (i) the voltage can be corrected from the resistance overvoltage, knowing the cell resistance from PEIS measurements, leading to the IR-free voltage and (ii) the current can be corrected from the crossover by subtracting the crossover current baseline, *i.e.* the straight line obtained from crossover measurement. Finally, these corrected E-I pairs can be plotted (IR-free voltage as a function of the logarithm of the current, Figure A2.4c). This graph is similar to the Tafel plot obtained from the ORR activity measurement performed in a three electrode cell: it provides information about the kinetic activity of the cathode catalytic layer. It must be noted that the obtained current can also be expressed by electroactive Pt surface or by mass of Pt, in order to obtain the specific or the mass activity of the catalytic layer, respectively.

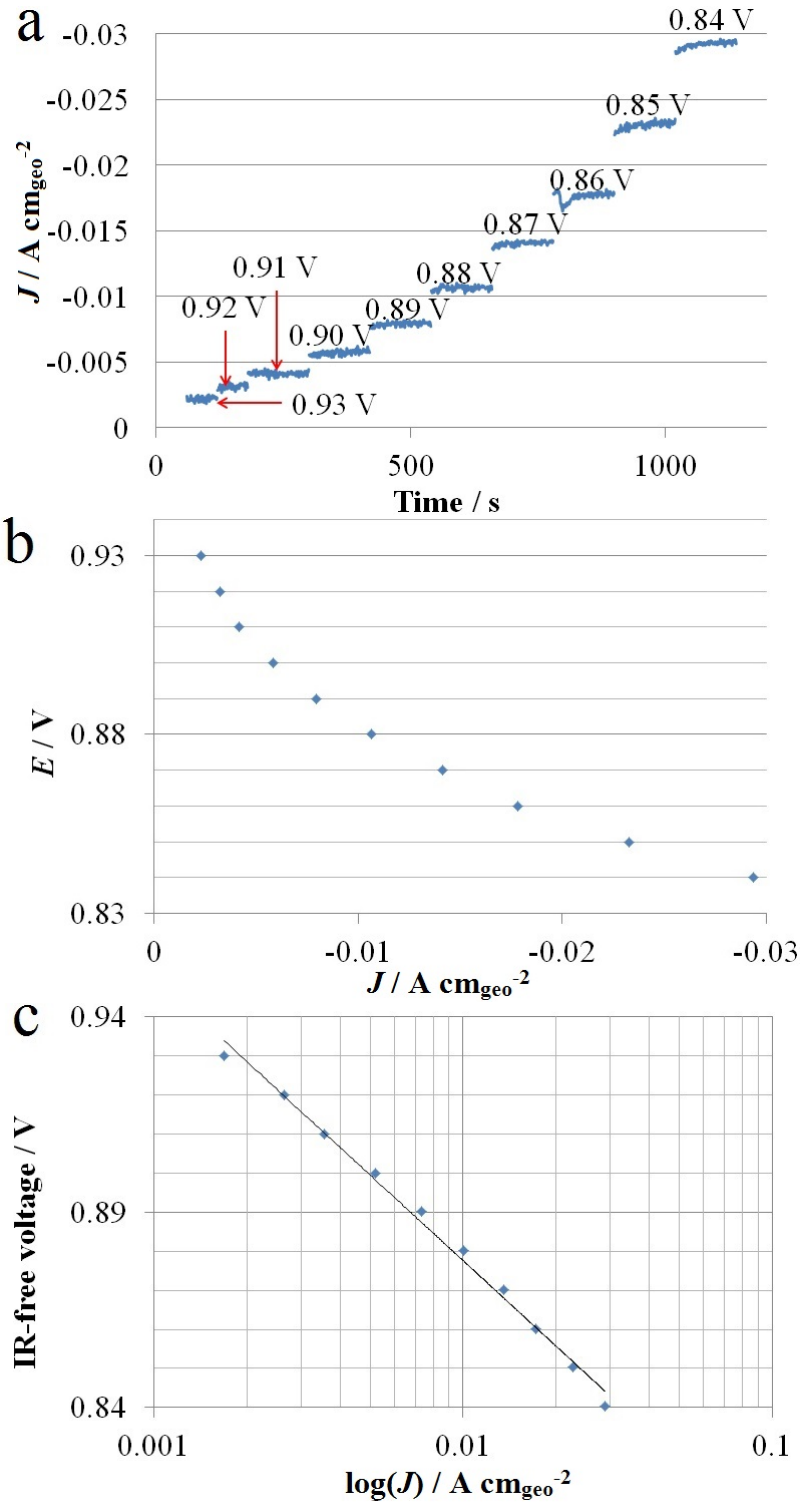

Figure A2.4: Chronoamperometry results (a), E-I pairs graph (b), and corrected E-I logarithmic graph (c) of a commercial catalyst.

References

[1] A. J. Bard and L. R. Faulkner, *Electrochemical Methods: Fundamentals and applications*, John Wiley & Sons, Inc., Weinheim, Germany, 2nd edition, 2001.

[2] S. Trasatti and O. Petrii, *Journal of Electroanalytical Chemistry* **327**, 353 (1992).

[3] F. Maillard, M. Eikerling, O. V. Cherstiouk, S. Schreier, E. Savinova, and U. Stimming, *Faraday Discussions* **125**, 357 (2004).

[4] F. Maillard, S. Schreier, M. Hanzlik, E. R. Savinova, S. Weinkauf, and U. Stimming, *Physical Chemistry Chemical Physics* **7**, 385 (2005).

[5] F. Maillard, E. R. Savinova, and U. Stimming, *Journal of Electroanalytical Chemistry* **599**, 221 (2007).

[6] T. Asset, R. Chattot, J. Nelayah, N. Job, L. Dubau, and F. Maillard, *ChemElectroChem* **3**, 1591 (2016).

[7] N. Job, M. Chatenet, S. Berthon-Fabry, S. Hermans, and F. Maillard, *Journal of Power Sources* **240**, 294 (2013).